Developments and applications of a multi-scale numerical method coupling the Cellular Automaton and Parabolic Thick Needle methods for the prediction of dendritic grain structures

Yijian Wu

PSL★
UNIVERSITÉ PARIS

THÈSE DE DOCTORAT
DE L'UNIVERSITÉ PSL

Préparée à Mines Paris-PSL

Developments and applications of a multi-scale numerical method coupling the Cellular Automaton and Parabolic Thick Needle methods for the prediction of dendritic grain structures

Développements et applications d'une méthode numérique multi-échelle couplant les modèles d'automate cellulaire et de réseau d'aiguilles paraboliques pour la prédiction des structures de grains dendritiques

Soutenue par
Yijian WU
Le 13 décembre 2022

Ecole doctorale n° 364
Sciences Fondamentales et Appliquées

Spécialité
Mécanique numérique et Matériaux

Composition du jury :

Mathis PLAPP
Directeur de recherche, CNRS — *Président*

Henri NGUYEN-THI
Professeur, Aix-Marseille Université — *Rapporteur*

Olga BUDENKOVA
Chargée de recherche, CNRS — *Rapportrice*

Oriane SENNINGER
Chargée de recherche, Mines Paris - PSL — *Encadrante*

Charles-André GANDIN
Directeur de recherche, CNRS — *Directeur de thèse*

MINES PARIS | **PSL★**

Acknowledgements

Contents

General Introduction

Solidification processes play the most important role in metal casting, and the ability to cast metals represents the progress of human culture in a fairly long period of history. For example, the term *Bronze Age* represents the time period from 4000 BC to 1200 BC, and the invention of the Bessemer process leading to the mass production of steel in liquid form is regarded as a key invention of the first industrial revolution [1]. Nowadays, solidification and its control are always remaining of major economic and industrial interest, whereas they are difficult to understand due to their multi-physical aspects: the thermal evolution is heterogeneous and varies with phase transformation in the process; the nucleation of grains is at atomic scale and involves rich physics; the solute diffusion is combined with convection induced by gravity, and convection results in macrosegregation of species; the evolution of thermodynamic phases is anisotropic…

Microstructures formed during solidification processes have a large influence on the properties of cast metals and alloys. A large majority of scientific studies on solidification microstructures are concerned with a kind of very common microstructure called dendrite, including this work. Dendritic growth is driven by the repartition of atoms on both sides of the solid/liquid interface according to the thermodynamic equilibrium. Because of the anisotropy of the solid/liquid interfacial energy, dendrites have principal growth directions corresponding to specific crystal directions. This anisotropy is the reason why dendrites grow with this tree-like shape, which is the origin of their name (*déndron* means tree in Greek) [2].

The morphology of dendritic grains can be columnar or equiaxed. Columnar grains have significant development in one spatial direction, whereas equiaxed grains have similar dimensions in all spatial directions. These two morphologies can coexist in the same ingot, and the Columnar-to-Equiaxed Transition (CET) [3] is a common phenomenon in solidification processes. As this transition impacts the mechanical properties of material, it is necessary to control it during solidification. For example, it has to be eliminated in directional solidification of superalloys (columnar crystals or single crystals) but enhanced in welding processes [4]. The understanding of the CET of alloy can also help for the optimization of grain structures in various solidification processes [5].

In attempts to improve the understanding of the microstructures formed during solidification processes, the Columnar-to-Equiaxed Transition in SOLidification processing (CETSOL) project was launched in 1999 aiming to improve our understanding of the physics governing the formation of the CET in alloy solidification process. Experiments of solidification in the International Space Station (ISS) in microgravity as well as on earth, and different numerical models are being developed and applied for the investigation. The CETSOL project is partially funded by the European Space Agency (ESA) within the frame of its Microgravity Applications Promotion (MAP) program. To date, six phases of CETSOL project have been finished [6]. The last phase, CETSOL-6, from January 2019 to December 2021, based on Contract Change Notice CNN009, was coordinated by ACCESS e.V. and consisted of the following partners:

Academic partners:

- Gerhard Zimmermann (coordinator), Laszlo Sturz, ACCESS e.V. Aachen (Germany)
- Henri Nguyen-Thi, Nathalie Mangelinck-Noel, IM2NP CNRS / Aix-Marseille University (France)
- Charles-André Gandin, Oriane Senninger, CEMEF MINES Paris PSL University (France)
- Shaun McFadden, Antony Robinson, Trinity College Dublin (Ireland)
- Nils Warnken, University of Birmingham (UK)

Associated academic partners:

- Peter Voorhees, Northwestern University Evanston (USA)
- Andras Roosz, University of Miskolc (Hungary)
- Christoph Beckermann, University of Iowa (USA)
- Alain Karma, Northeastern University (USA)

Non-academic partners:

- Etienne Perchat, TRANSVALOR Mougins (France)
- Gerd-Ulrich Grün, HYDRO Aluminium Rolled Products GmbH Bonn (Germany)
- Manfred Grohn, Incaal GmbH Nörvenich (Germany)
- Isabelle Poitrault, ArcelorMittal Industeel Le Creusot (France)

Associated non-academic partners:

- Gabor Balazs, Arconic-Köfem Ltd. (Hungary)
- Tamas Nemeth, Nemak Györ Kft. (Hungary)
- David Toth, INOTAL Aluminiumfeldolgozo (Hungary)

In terms of experiments of the CETSOL project, the solidification of Al-7 wt.% Si samples in microgravity have been completed in the Microgravity Science Laboratory (MSL) on-board the ISS, for dissociating the effect of gravity. The experiments were performed in a Bridgman-type furnace, as shown in Figure 1. The samples were cylinders with a diameter of 7.8 mm and a length of 245 mm, put in a special sample cartridge assembly together with twelve thermocouples positioned along the sample. The samples were fixed, and melting or solidification of the alloy was achieved by moving the furnace along the axis of the sample.
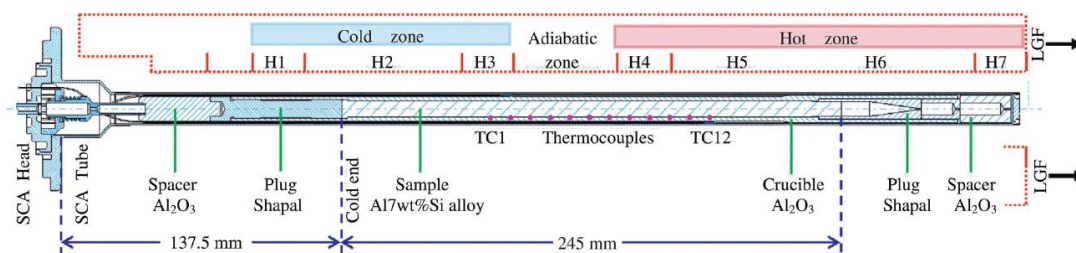
Figure 1 **Schematic setup of the Sample Cartridge Assembly (SCA) inserted in the Low Gradient Furnace (LGF) on board the ISS. The LGF is sketched at its initial position with respect to the SCA. The 12 thermocouples, labeled as TC1 to TC12, are regularly distributed from 72.5mm to 182.5mm from the cold end of the sample. From [7].**

These experiments provide unique data for the CET in Al-7 wt.% Si alloy for purely diffusive solidification conditions, which are helpful for improving numerical models on microstructure formation. Reference experiments were carried out on earth as well, and a notable difference in the genesis and growth of microstructures during solidification by the effect of gravity can be observed (Figure 2). Investigation of CET and equiaxed growth in Al-Cu alloys and investigation of CET in transparent alloys were also carried out.
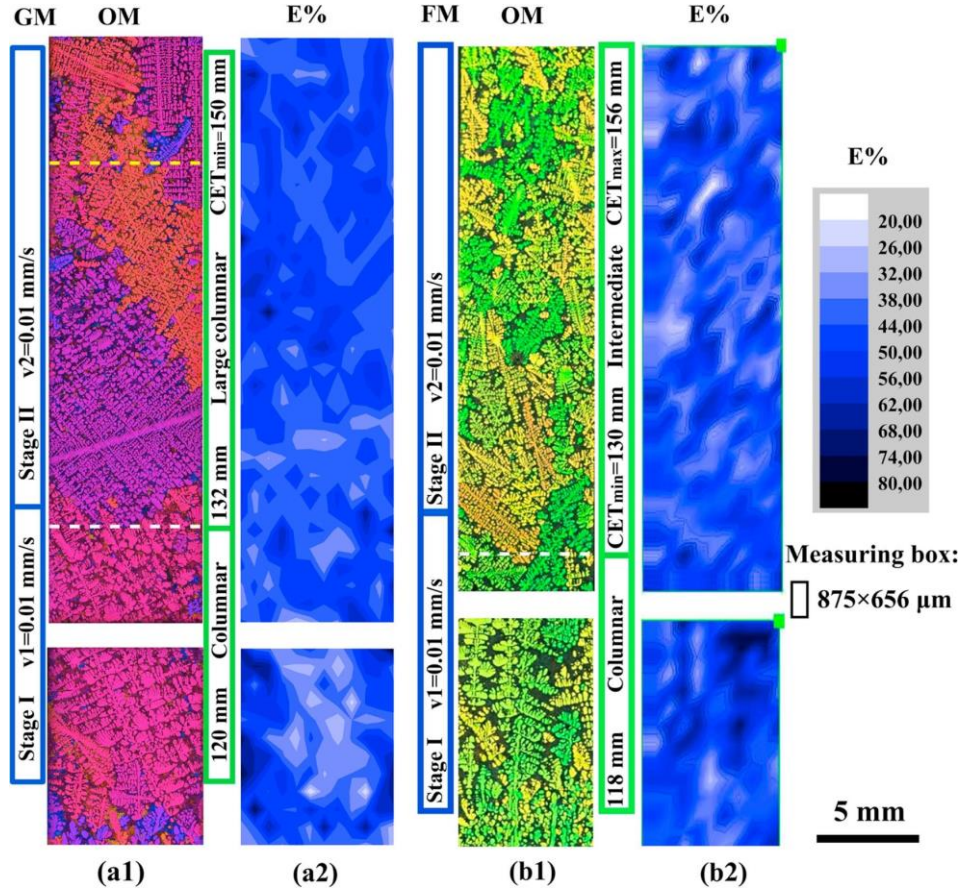
Figure 2 **Microstructure from an optical polarized light microscope (OM) of Al-7 wt.% Si alloys along longitudinal sections in the region of the transition from stage I to stage II for: (a1) the GM (Ground Module) sample from solidification experiment on earth and (b1) the FM (Flight Module) sample from solidification experiment on-board the ISS. Stages I and II are two different stages of solidification with different experimental conditions. During Stage I, the pulling velocity of the sample is $0.01\,\text{mm/s}$ and the initial temperature gradient is about $0.9\,\text{K/mm}$. During Stage II the pulling velocity is identical to Stage I while the temperature gradient decreases continuously due to a cooling down of the hot zone at a cooling rate of $0.067\,\text{K/s}$. (a2) and (b2) are the corresponding eutectic percentage (E%) distribution maps for both samples. The white dashed lines represent the highest position of the columnar grains issued from the initial dendritic zone. The yellow dashed line represents the position defining the CET inception in the GM sample. From [8].**

Numerical models, such as the Cellular Automaton – Finite Element (CAFE) model [9], the Concurrent Columnar Equiaxed Transition (C2ET) model [10], the Dendritic Needle Network (DNN) model [11, 12], have been used for simulating the grain structure of CETSOL solidification experiments, and their predictions on the CET are in reasonable agreement with the experimental measurement.

The team CEMEF MINES Paris is specialized in the modeling of grain structure using the CAFE model that permits to simulate the grain structure during solidification processes. The three-dimensional CAFE model showed encouraging results but was limited for quantitative agreement with the experiment [7], especially due to approximations when considering solute interaction during dendritic growth. The Parabolic Thick Needle (PTN) method [13] is the method used in the DNN model for calculating dendrite tip kinetics, relevant to both steady and unsteady growth. To consider the impact of the solute interaction on dendritic growth, the CAFE model was hereby enriched by coupling the PTN method as growth law. This work was initiated in a two-dimensional model by Romain Fleurisson [14], who was a PhD student in the frame of the CETSOL-5 phase in CEMEF MINES Paris from 2015 to 2019. He implemented the two-dimensional PTN method in the finite element library *cimlib*, studied the influence of numerical parameters, and coupled the PTN method with the CAFE model. This coupling model showed its advantages, but also its shortcomings on huge requirement on computational resources, so its application and development are limited [15].

In the frame of the CETSOL-6 phase, my PhD work aims to improve the efficiency of the two-dimensional Cellular Automaton – Parabolic Thick Needle (CAPTN) method where the resolution of energy is not considered, apply it for investigating the microstructures under directional solidification, and develop the three-dimensional CAPTN model. Chapter 1 presents the state of the art on dendritic growth theories and numerical models. Chapter 2 firstly reviews the algorithm of the PTN method of Fleurisson [14], then present the improvements on the method and their advantages on computational efficiency. Chapter 3 studies the parameters of the PTN model. The parametric study on the two-dimensional model carried out by Fleurisson [14] is recalled, and complementary developments are presented. Then the extension to three dimensions are detailed. Chapter 4 is dedicated to the CAPTN model, concerning its improvements and three-dimensional validation. Equiaxed dendritic grains under isothermal condition are modeled, and compared with theoretical and other numerical models. Chapter 5 focuses on the application of the two-dimensional CAPTN model on investigating the dendritic spacing of a single crystal and the grain boundary of a bi-crystal under directional solidification. It is in the format of an article and is to be submitted.

Chapter 1 Dendritic growth and numerical models of dendrites and grains

Résumé en français

Cette thèse porte sur la modélisation des structures de grain dendritique. Ce premier chapitre présente une étude bibliographique des théories et phénomènes physiques sur la croissance dendritique ainsi que les modèles numériques existant pour modéliser la croissance et les structures de grains dendritiques. Le modèle CAPTN couplant les modèles d'automate cellulaire (Cellular Automaton, CA) et de réseau d'aiguilles paraboliques (Parabolic Thick Needle, PTN) est présenté en détail. Ce modèle a été développé et appliqué pour prédire la structure des grains équiaxes en deux dimensions. Cependant, ce modèle n'était pas efficace numériquement. Cette thèse a pour objectif d'améliorer l'implémentation numérique de ce modèle et de poursuivre son développement vers des applications en trois dimensions.

As the beginning of this thesis, this chapter reviews first the theories on dendritic growth that will be used in the following of the thesis, then the state of the art of the numerical models on dendritic microstructures and grain structures allowing to situate the CAPTN model among the existing models.

1.1   Theories of dendritic growth

1.1.1   Undercooling and supersaturation

Let us consider here a sample of a binary alloy of nominal composition w_0 placed in an isothermal domain at temperature T_∞ lower than the liquidus temperature of the alloy T_L. An exothermal nucleation leads to the growth of a curved solid phase with a solid/liquid interface at temperature T^{ls}, solid composition w^{sl} and liquid composition w^{ls}. The driving force of solidification and the evolution of the solid/liquid interface is the temperature difference $\Delta T = T_L - T^{ls}$, called undercooling. In linear approximation, this undercooling can be divided into four terms [1]

$$\Delta T = \Delta T_C + \Delta T_R + \Delta T_T + \Delta T_K \tag{1.1}$$

ΔT_C is the chemical undercooling due to the diffusion of chemical species in the liquid (see Fig. 1.1). Its origin lies in the difference in solute solubility between the liquid and solid. If the liquidus slope is m, the chemical undercooling can be expressed as

$$\Delta T_C = m\left(w_0 - w^{ls}\right) \tag{1.2}$$

ΔT_R is the curvature undercooling (see Fig. 1.1) due to the curvature of the solid/liquid interface. It is the product of the Gibbs-Thomson coefficient Γ^{sl} and the local curvature at the interface, i.e., $\Delta T_R = 2\Gamma^{sl}/r$ for a sphere of radius r. ΔT_T is the thermal undercooling representing the temperature difference between the liquid at solid/liquid interface and the liquid in the environment. This undercooling requires therefore to define a temperature of reference for the environment and is taken into account when latent heat is released during solidification and heats the solid/liquid interface. ΔT_K is the undercooling due to the atomic attachment kinetics.

For solidification velocities lower than $10\,\mathrm{cm/s}$, it can usually be assumed that the solid/liquid interface is locally in equilibrium state [16], so the kinetic undercooling is not considered. Take the Al-7 wt.% Si alloy under solidification with velocity of $0.2\,\mathrm{mm/s}$ (corresponding to the configuration in the CETSOL project) as an example. Its chemical undercooling is 6.11 K, its curvature undercooling is 0.25 K, and the thermal undercooling can be neglected under this velocity. In the conditions studied in this thesis, ΔT_R, ΔT_T, and ΔT_K are all negligible compared to ΔT_C. Therefore, in the method presented in this thesis, only the chemical undercooling is considered. The solute partition coefficient k is defined as

$$k = \frac{w^{\text{sl}}}{w^{\text{ls}}} \tag{1.3}$$

We define the supersaturation Ω at the interface by

$$\Omega = \frac{w^{\text{ls}} - w_0}{w^{\text{ls}} - w^{\text{sl}}} = \frac{w^{\text{ls}} - w_0}{(1-k)w^{\text{ls}}} \approx \frac{\Delta T}{-m(1-k)w^{\text{ls}}} \tag{1.4}$$

The supersaturation is dimensionless between 0 and 1. In the conditions where the undercooling can be approximated as the chemical undercooling, the supersaturation can be used instead of the undercooling to describe the growth conditions of the structures during solidification.
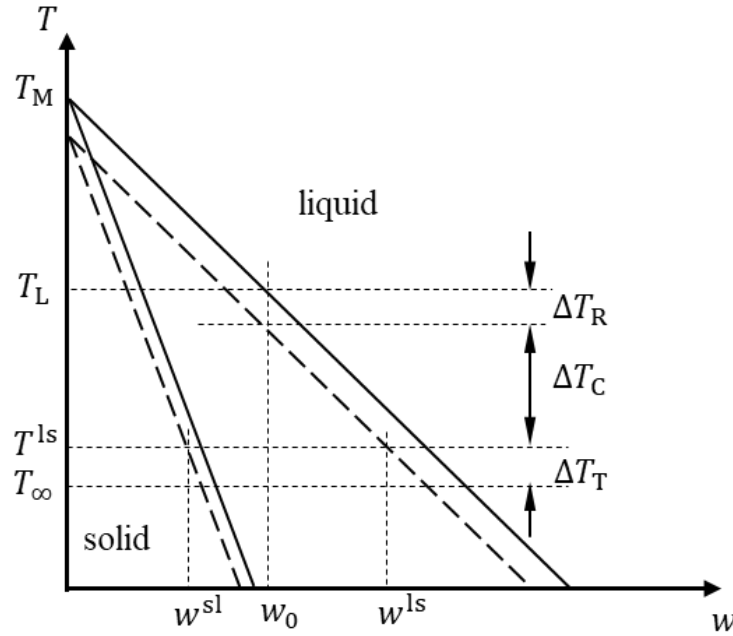
Fig. 1.1   **Linear phase diagram for a binary alloy at constant pressure. ΔT_{C} is the chemical undercooling, ΔT_{R} is the curvature undercooling, and ΔT_{T} is the thermal undercooling. w_0 is the nominal composition of the solute in the alloy, w^{ls} is the solid/liquid interfacial composition in the liquid phase, and w^{sl} is the solid/liquid interfacial composition in the solid phase. T_{M} is the melting temperature for the solvent, T_{L} is the liquidus temperature, and T^{ls} is the temperature at the solid/liquid interface. Redrawn based on [16].**

1.1.2   Parameters describing the dendritic microstructure

The difference in composition between solid and liquid results in the phase transformation by the repartition of atoms on both sides of the solid/liquid interface. The nature and the behavior of the interface between the solid phase and the liquid phase during solidification processes are generally decisive in the formation of grain structures. The solid/liquid interface might be stable or unstable. Imagine there is a small disturbance caused by some physical reasons acting on the interface. The interface is considered stable if this disturbance fades, the interface is considered unstable if this disturbance amplifies, and the interface is considered marginally stable if this disturbance neither fades nor amplifies.

Analytical study [1] on a planar solid/liquid interface stability demonstrates that if the diffusion in solid is neglected, the critical wavelength λ_c to instability is about

$$\lambda_c \approx 2\pi \sqrt{\frac{d_0 D^l}{v^{ls}}} \tag{1.5}$$

with $d_0 = \frac{\Gamma^{sl}}{-m(1-k)w^{ls}}$ the solute capillary length, D^l the solute diffusion coefficient in the liquid, and v^{ls} the velocity of the solid/liquid interface.

Let us assume that the solid has a spherical shape in the stage of nucleation. Once disturbances to the spherical shape can grow, the solid shape starts to show preferred growth directions derived from anisotropy of the solid/liquid interfacial energy [1], which is a result of the regular atomic arrangement in crystal, leading to the growth of dendrite towards preferred directions (as Fig. 1.3). Dendrites along $\langle 1\,0\,0 \rangle$ directions take our interest in this thesis. The tip of a dendrite can be regarded as a paraboloid in three dimensions [17], and its kinetics can be described by tip radius ρ_{tip}, which is the curvature radius at the tip, and tip velocity v_{tip}.
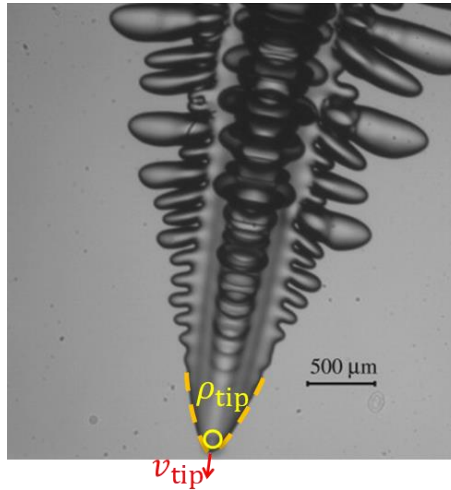
Fig. 1.2   A dendrite of transparent succinonitrile–acetone alloy observed by the high-resolution camera. Its tip is like a paraboloid. From [18].

To determine the morphology of a dendrite, Langer and Müller-Krumbhaar proposed that the dendrite tip radius is equal to the critical wavelength yielding the destabilization of a planar interface λ_c [19]. The so-called marginal stability criterion writes

$$\rho_{tip}^2 v_{tip} = \frac{D^l d_0}{1/(2\pi)^2} \tag{1.6}$$

This widely-used criterion does not take the anisotropy of the interfacial energy into account. It was later replaced by the solvability condition, which was a more mathematically rigorous analysis removing some questionable assumptions in the previous analyses. Karma and Kotlia proposed the microscopic solvability theory for alloys [20], then Ben Amar and Pelcé

generalized it [21]. In the small Peclet number $\text{Pe} = \rho_{\text{tip}} v_{\text{tip}} / (2D^{\text{l}})$ limit, the solvability condition can be expressed as

$$\rho_{\text{tip}}^2 v_{\text{tip}} = \frac{D^{\text{l}} d_0}{\sigma} \tag{1.7}$$

where σ is the selection parameter fixed by the strength of crystalline anisotropy.

A dendritic grain consists of a network of branches from the same initial seed. Primary dendritic arms form along preferred directions, then secondary dendritic arms appear by ramification. The primary dendrite arm spacing λ_1 and the active secondary dendrite arm spacing λ_2 are generally employed for characterizing the network (Fig. 1.3).
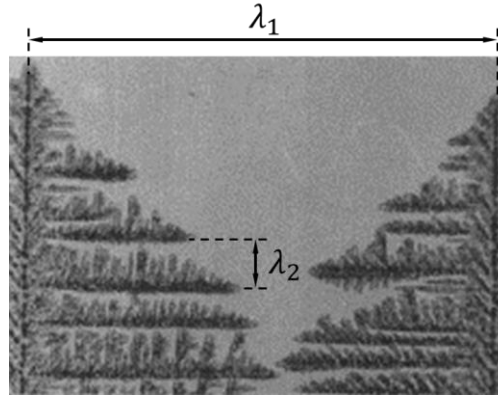
Fig. 1.3   **Photographic illustration of the primary and secondary dendrite arm spacing λ_1 and λ_2. The photo is of camphene (>95% purity, Merck Ltd.), from [22].**

1.1.3   Ivantsov stationary solution

For a single dendritic branch growing at steady state in a semi-infinite domain of nominal composition w_0 imposed in the liquid under constant temperature, if the form of this branch is assumed as parabola in two dimensions or paraboloid in three dimensions, and the composition is uniform as w^{ls} at the solid/liquid interface, the composition field in the liquid can be described by the two-dimensional or three-dimensional Ivantsov solution [23], respectively

$$w_{\text{2D}}^{\text{l}}(\xi) = w_0 + (1 - k)w^{\text{ls}}\sqrt{\pi\text{Pe}}\exp(\text{Pe})\,\text{erfc}(\xi\sqrt{\text{Pe}})$$
$$w_{\text{3D}}^{\text{l}}(\xi) = w_0 + (1 - k)w^{\text{ls}}\,\text{Pe}\,\exp(\text{Pe})\,\text{E}_1(\text{Pe}\,\xi^2) \tag{1.8}$$

with ξ the first parabolic coordinate (see Fig. 1.4), $\text{erfc}(x)$ the complementary error function, and $\text{E}_1(x)$ the exponential integration. The Ivantsov solution was firstly proposed for the thermal diffusion of a pure material, and it was extended later for the chemical diffusion of alloys.

The Ivantsov solution with $\xi = 1$ is the solid/liquid interface, i.e., description of the parabolic branch. According to the definition of undercooling in Eq. (1.4), the Ivantsov solution in Eq. (1.8) can be converted into equations between undercooling and Peclet number when $\xi = 1$

$$\Omega_{2D} = \sqrt{\pi Pe}\,\exp(Pe)\,\,\mathrm{erfc}(\sqrt{Pe})$$
$$\Omega_{3D} = \,Pe\,\exp(Pe)\,E_1(Pe) \tag{1.9}$$

Eq. (1.9) can be rewritten as

$$\Omega_{2D} = \sqrt{\frac{\pi \rho_{\mathrm{tip}} v_{\mathrm{tip}}}{2D^l}}\,\exp\left(\frac{\rho_{\mathrm{tip}} v_{\mathrm{tip}}}{2D^l}\right)\,\mathrm{erfc}\left(\sqrt{\frac{\rho_{\mathrm{tip}} v_{\mathrm{tip}}}{2D^l}}\right)$$
$$\Omega_{3D} = \,\frac{\rho_{\mathrm{tip}} v_{\mathrm{tip}}}{2D^l}\,\exp\left(\frac{\rho_{\mathrm{tip}} v_{\mathrm{tip}}}{2D^l}\right)\,E_1\left(\frac{\rho_{\mathrm{tip}} v_{\mathrm{tip}}}{2D^l}\right) \tag{1.10}$$

if the definition of Pe is taken. For a given supersaturation, Eq. (1.10) and the solvability condition Eq. (1.7) can be solved to get the dendrite tip radius and velocity at the steady state. This theoretical solution is called Ivantsov – Solvability solution in the following, denoted as $\rho_{\mathrm{tip}_{Iv}}$ and $v_{\mathrm{tip}_{Iv}}$.
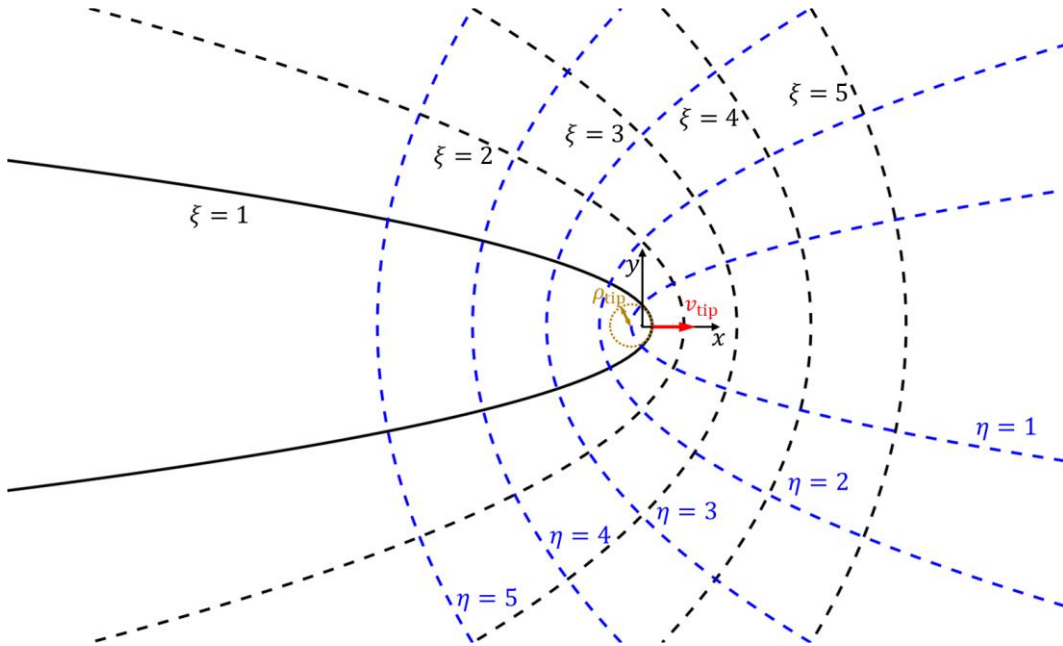
Fig. 1.4   **Parabolic and Cartesian coordinate system. Two sets of parabolas are confocal. The origin of the Cartesian coordinate is at their focus. In Ivantsov solution the solid/liquid interface corresponds to $\xi = 1$. The dendrite tip radius and tip velocity are marked.**

1.1.4   Columnar dendrite, equiaxed dendrite, and Columnar-to-Equiaxed Transition (CET)

There are two typical types of dendritic growth: one is free growth which means the evolution of isolated dendrites in an isotropic infinite undercooled melt, the other is constrained growth where many dendrites grow together under an imposed temperature gradient. These two regimes generate two different morphologies of dendrites: equiaxed dendrites and columnar dendrites. Upon columnar growth dendrites are significantly more developed in one of their principal growth directions. Oppositely equiaxed dendrites grow in all their principal directions of similar dimension. Since the two types of dendrites can coexist in an ingot, the Columnar-to-Equiaxed Transition (CET) is regularly seen in solidification.

The first criterion describing this transition was proposed by Hunt [3]. This criterion is based on the mechanical blocking of the columnar dendrite front by equiaxed grains for a binary alloy. Equiaxed grains are assumed to be nucleated and then to grow in the region in front of the columnar dendrites that is undercooled. If the volume fraction of the equiaxed grains becomes greater than 0.49, the equiaxed grains will block the advancement of the columnar dendrites, yielding the CET.

Gandin [24] studied CET by experiment and numerical approach based on the resolution of the heat flow equation using a two-interface front tracking approach. Two hypotheses of CET are proposed. One is that when the temperature gradient is near zero or even slightly negative along the upward direction, the latent heat released by solidification may remelt some dendritic side branches becoming nuclei of equiaxed grains. The other is the thermal destabilization of the macroscopic interface which means that heat released by some dendrites will influence the growth of dendrite and the primary dendrite arm spacing. Gandin proposed another CET criterion based on the position of the maximum velocity of the columnar dendritic interface according to his study. It should be noticed that Gandin's criterion could only be applied in alloys where no inoculation particles are added to the melt.

Martorano *et al.* [25] proposed another mechanism for CET based on solutal interactions between the equiaxed grains and the advancing columnar front, rather than mechanical blocking. CET will occur if the solute rejected from the equiaxed grains is enough to dissipate the undercooling at the columnar front. They also proposed that the origin of the equiaxed grains may not be heterogeneous nucleation, but rather a breakdown or fragmentation of the columnar dendrites.

Fig. 1.5 is the experimental grain structures observed in the longitudinal section of cylindrical Al-7 wt.% Si ingot obtained by directional solidification over a copper chill [24]. The columnar crystal, the equiaxed crystal, and their transition can be seen.
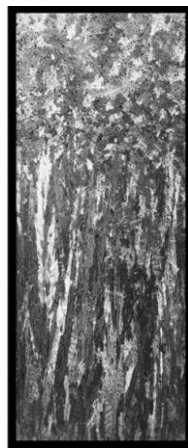
Fig. 1.5   Experimental grain structures observed in the longitudinal section of Al-7 wt.% Si ingot obtained by directional solidification. From [24].

A good understanding of the CET during solidification process is very helpful to the control of the grain structure [5] and of great industrial interest, such as in additive manufacturing [26–28]. The CET is the investigating subject of the CETSOL project.

1.2   Numerical models of dendrites and grains

1.2.1   Phase-Field (PF) method

The PF method is a microscopic computational method describing the growth of the solid phase without its shape known *a priori*. It takes the physics of interface (e.g., curvature and its energy) into account, and is one of the most widely used methods for simulating the evolution of microstructures. In this method, the space is divided into three zones: liquid, solid, and solid/liquid interface. The phase field variable ϕ is employed in order to identify the phase: it keeps constant in each phase and varies continuously at the solid/liquid interface. For example, $\phi = 0$ in solid, $\phi = 1$ in liquid, and $\phi \in (0, 1)$ at the solid/liquid interface. Thus, the solid/liquid interface confined to a narrow region becomes diffuse, and the phases turn into a continuous field [1].

The thickness of the solid/liquid interface is a crucial parameter of the PF method. Extremely fine meshes are employed here to describe its shape and calculate the evolution of phase. A larger thickness permits coarser meshes to be used in this area, so a larger domain can be simulated with the same computational cost. However, this thickness must be limited for ensuring the convergence of simulation results.

The principle of the PF method is seeking to minimize the free energy of the simulation domain with respect to time. It therefore necessitates to solve the thermal and/or solutal transport equation depending on the problem.

In spite of its good accuracy, the application of the PF method on solidification is limited on small simulation domains, due to its enormous requirement on computational resources [14]. For example, in the study of Takaki *et al*., dendritic microstructure is modeled by the three-dimensional PF model on supercomputer TSUBAME2.5 at Tokyo Institute of Technology with 144 GPUs. Fig. 1.6 is one of their results. The computational time for a domain less than 1 mm^3 is about 5.2 days [29].
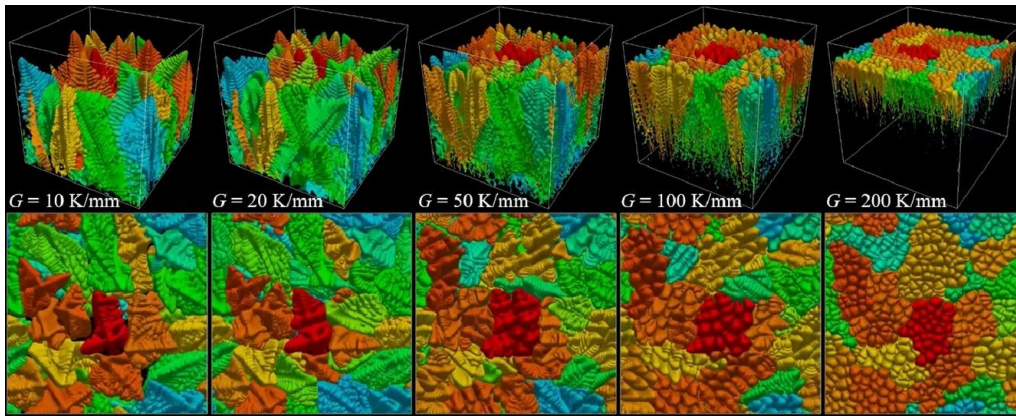
Fig. 1.6   Illustration of three-dimensional PF simulation results of dendritic grains. From [29].

The PF method has been applied in [30] for simulating the CET. This application is only in two dimensions with the moving-domain technique whose moving domain is about 0.004 mm^2. The simulation results qualitatively agrees with the analytical CET criterion of Hunt [3].

1.2.2   Microscopic Cellular Automaton (CA) method

For the sake of a description on dendritic branches, Nastac employed the Cellular Automaton (CA) method for predicting the dendritic morphology controlled by solute diffusion [31], named as microscopic CA method in this manuscript. Afterwards many mathematical models have emerged based on this method for modeling the growth of equiaxed dendrites, columnar dendrites, the CET, and the influence of cooling condition and melt flow, which are summarized in [32].

In the microscopic CA method, the evolution of the solidification interface is governed by the solute balance. The simulation domain is discretized by regular-lattice CA cells, squares in two dimensions and cubes in three dimensions. Each CA cell holds its location information and several variables, such as the concentration, the temperature, the solid fraction, and the crystallographic orientation. A cell can be solid, liquid, or solid/liquid interface. With the growth of dendrites, the solute concentration of the liquid phase in the interface cell increases gradually and diffuses to its neighboring according to the diffusion law. When the solid fraction of the solidification interface cell is greater than unity, it becomes solid and captures the first 4 (resp. 6) nearest-neighboring cells in two dimensions (resp. three dimensions) as interface cells [32]. The definition of neighboring cells can be found in Subsection 1.2.5 and in Fig. 1.13. Simultaneously, the solute diffusion continues in the entire liquid domain.

A three-dimensional microscopic CA model is applied for modeling the microstructures under directional solidification with different temperature gradients in [33], to investigate the influence of physical parameters on the cell-to-dendrite transition in directional solidification. Its results are shown in Fig. 1.7. Each simulation takes less than one day on a personal computer without parallel computation for a simulation domain of 0.03 mm^3. However, the results of the microscopic CA method have limited comparison with dendritic growth theories.
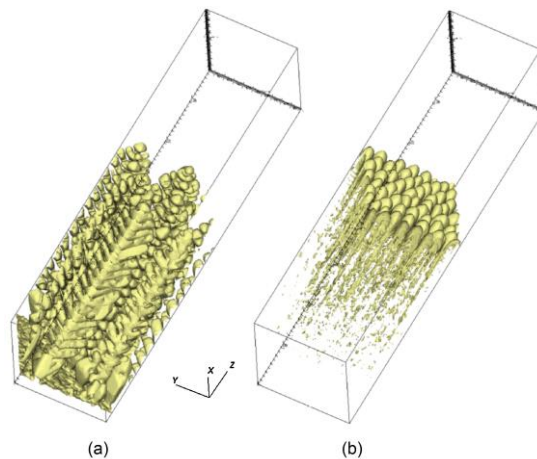
Fig. 1.7   Three-dimensional microscopic CA model simulations of directional solidification: (a) dendritic microstructure at low temperature gradient, (b) cellular microstructure at high temperature gradient. The computational domain is 0.192 mm $\times$ 0.192 mm $\times$ 0.768 mm. From [33].

The microscopic CA method has been applied for modeling the CET in two dimensions, in [34]. The simulation domain is about 12 mm^2. One of its simulation results is shown in

Fig. 1.8. The CET map predicted by the microscopic CA model is consistent with the analytical result of the Hunt model [3]. One of the limits of this work is that the primary dendrite arm spacing is set as a constant, while in the actual solidification process, the primary dendrite arm spacing changes with the thermal condition.
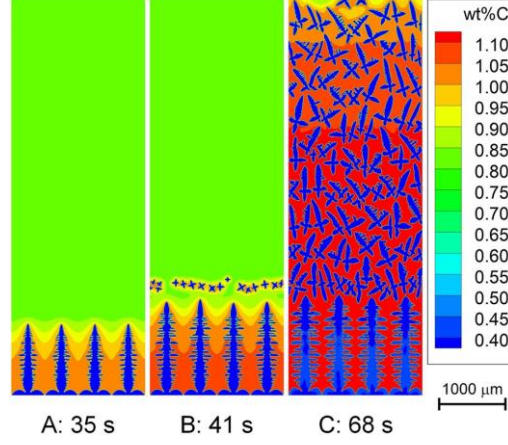
Fig. 1.8   Solidification process of the Fe-0.82C alloy during unidirectional solidification. The temperature gradient is 3 K/mm and the cooling rate is 0.5 K/s. From [34].

1.2.3   Dendritic Needle Network (DNN) and Parabolic Thick Needle (PTN) methods

Proposed by Tourret and Karma in [35], and then enriched in [11–13, 36, 37], the Dendritic Needle Network (DNN) method aims to overtake the numerical limits of the PF method. It models dendritic growth at a scale between the microscopic scale and the mesoscopic scale. Dendrites are regarded as a network of needles. The growing direction of a branch is predefined and fixed during its growth. Each dendrite tip is predefined in parabolic form. This simplified representation of dendrite tip reduces hugely the computational time, making the DNN method able to be applied for larger simulation domains than the PF method.

The method used for calculating the kinetics of a dendrite tip in the DNN method is the Parabolic Thick Needle (PTN) method. In the PTN method, a dendrite tip is represented as a parabola in two dimensions or a paraboloid in three dimensions with radius ρ_{tip} truncated by a cylinder of radius r_{cyl} as in Fig. 1.9. Its growing direction is the $+x$ direction. To be simple, the word "truncating cylinder" is used for both two-dimensional and three-dimensional models. For computing the kinetics of the tip, the solute diffusion equation

$$\frac{\partial w_{\text{PTN}}^{\text{l}}}{\partial t} = D^{\text{l}} \nabla^2 w_{\text{PTN}}^{\text{l}} \tag{1.11}$$

is solved in the liquid to compute the composition field in the liquid $w_{\text{PTN}}^{\text{l}}$. It is assumed that the solid/liquid interface is at thermodynamic equilibrium. Therefore, Dirichlet condition of solid/liquid interfacial composition in the liquid side w^{ls} is imposed at the solid/liquid interface. One should note that the composition w^{ls} is imposed in the parabola as well, so there is no solute conservation in the PTN method.
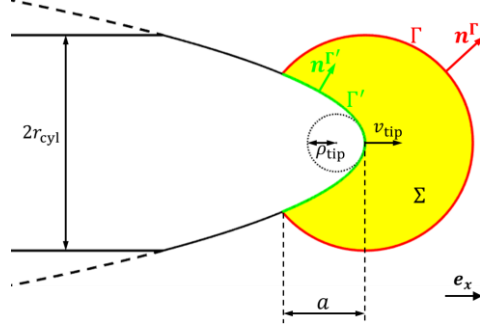
Fig. 1.9   Two-dimensional illustration of the integration contours and area defined by a, used in the calculation of the *Flux Intensity Factor*, and truncating cylinder. The integration on green contour Γ' is converted to integration on yellow surface Σ and red contour Γ. Thus, Σ and Γ compose the integration area for calculating the *Flux Intensity Factor*. Redrawn according to [14].

Neglecting the diffusion in solid, the mass conservation at the solid/liquid interface, also called Stefan condition, can be written as

$$\boldsymbol{v}^* \cdot \boldsymbol{n} = \frac{-D^{\mathrm{l}}}{(1-k)w^{\mathrm{ls}}} \boldsymbol{\nabla} w_{\mathrm{PTN}}^{\mathrm{l}}|^{\mathrm{ls}} \cdot \boldsymbol{n} \tag{1.12}$$

where $\boldsymbol{v}^*$ is the velocity vector of solid/liquid interface, $\boldsymbol{n}$ is the normal vector of solid/liquid interface, and $\boldsymbol{\nabla} w_{\mathrm{PTN}}^{\mathrm{l}}|^{\mathrm{ls}}$ is the gradient of composition field in the liquid at solid/liquid interface. Assuming that the growth of the dendritic branch is quasi-stationary, $\boldsymbol{v}^* \cdot \boldsymbol{e_x} = v_{\mathrm{tip}}$ with $\boldsymbol{e_x}$ the unit vector of the growth direction [14].

In two dimensions integrating Eq. (1.12) along the contour of parabolic dendrite tip Γ' defined by the integration distance a (see Fig. 1.9, a is the distance along the axis of the branch between the dendrite tip and the farthest point on the contour Γ' from the dendrite tip) yields a direct relation between ρ_{tip} and v_{tip},

$$\rho_{\mathrm{tip}} v_{\mathrm{tip}}^2 = \frac{2D^{\mathrm{l}^2} \mathcal{F}_{\mathrm{2D}}^2}{d_0} \tag{1.13}$$

$\mathcal{F}_{\mathrm{2D}}$ in Eq. (1.13), named as *Flux Intensity Factor* (FIF), is defined as

$$\mathcal{F}_{\mathrm{2D}} = \frac{-1}{4\sqrt{a/d_0}\,(1-k)w^{\mathrm{ls}}} \int_{\Gamma'} \boldsymbol{\nabla} w_{\mathrm{PTN}}^{\mathrm{l}} \cdot \boldsymbol{n}^{\Gamma'}\, \mathrm{d}\Gamma' \tag{1.14}$$

In numerical implementation (such as the finite difference method [11–13, 36, 37] and the finite element method [14]), the composition gradient on the parabola is difficult to evaluate with good precision because extremely fine meshes need to be applied to the contour Γ', thus, Eq. (1.14) is transferred by the divergence theorem into

$$\mathcal{F}_{\mathrm{2D}} = \frac{-1}{4\sqrt{a/d_0}\,(1-k)w^{\mathrm{ls}}} \left(\int_{\Gamma} \boldsymbol{\nabla} w_{\mathrm{PTN}}^{\mathrm{l}} \cdot \boldsymbol{n}^{\Gamma}\, \mathrm{d}\Gamma + \frac{1}{D^{\mathrm{l}}} \iint_{\Sigma} \boldsymbol{v_{\mathrm{tip}}} \cdot \boldsymbol{\nabla} w_{\mathrm{PTN}}^{\mathrm{l}}\, \mathrm{d}\Sigma \right) \tag{1.15}$$

where Γ is the outer contour and Σ is the surface, as illustrated in Fig. 1.9.

In three dimensions integrating Eq. (1.12) along the surface of parabolic dendrite tip Γ' leads to

$$\rho_{\text{tip}} v_{\text{tip}} = D^{\text{l}} \mathcal{F}_{\text{3D}} \tag{1.16}$$

with

$$\mathcal{F}_{\text{3D}} = \frac{-1}{2\pi a(1-k)w^{\text{ls}}} \iint_{\Gamma'} \boldsymbol{\nabla} w^{\text{l}}_{\text{PTN}} \cdot \boldsymbol{n}^{\boldsymbol{\Gamma'}} \, d\Gamma' \tag{1.17}$$

and its form for implementation is

$$\mathcal{F}_{\text{3D}} = \frac{-1}{2\pi a(1-k)w^{\text{ls}}} \left(\iint_{\Gamma} \boldsymbol{\nabla} w^{\text{l}}_{\text{PTN}} \cdot \boldsymbol{n}^{\boldsymbol{\Gamma}} \, d\Gamma + \frac{1}{D^{\text{l}}} \iiint_{\Sigma} \boldsymbol{v_{\text{tip}}} \cdot \boldsymbol{\nabla} w^{\text{l}}_{\text{PTN}} \, d\Sigma \right) \tag{1.18}$$

Combining the solvability condition Eq. (1.7) and Eq. (1.13) or (1.16), ρ_{tip} and v_{tip} can be obtained. Because of its consideration on the composition field in the liquid in the vicinity of the tip, the PTN method is relevant for computing dendrite tip kinetics at both steady and unsteady state.

The DNN method is implemented by the finite difference method [11–13, 35–37], so as the PTN method. Parametric studies [13, 38] have shown that the kinetics is dependent with the integration distance and the mesh size. To date, the simulation domain of the DNN method can reach up to 100 mm^3. The three-dimensional DNN model has been applied for simulating the CET of the experiments under microgravity on-board the International Space Station in the framework of CETSOL project. However, the solid fraction generated during the growth is not modeled and so the coupling of the microstructure evolution with resolution of energy is currently not possible. In the DNN simulation, the temperature field is imposed as the temperature measured from the CETSOL experiments. Fig. 1.10 is one of its results, demonstrating that the columnar front is completely blocked by the growth of equiaxed grains from inoculant particles. The start, the end, and the length of the CET are predicted accurately with the three-dimensional DNN model [12].
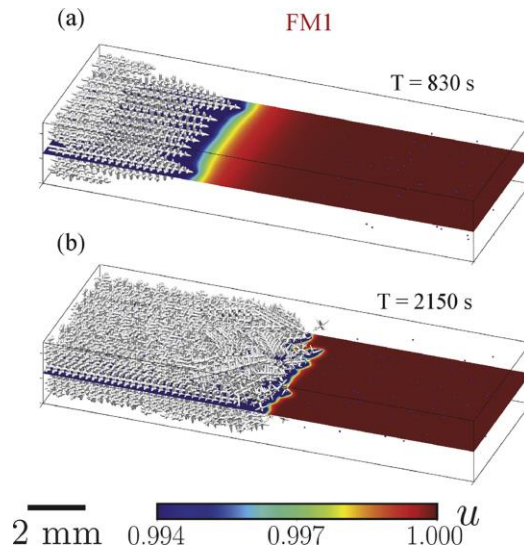
Fig. 1.10   **Illustration of the three-dimensional DNN simulation under imposed temperature field for investigating the CET. Snapshots at (a) $t = 830$ s and (b) $t = 2150$ s of three-dimensional DNN simulation results for one sample of CETSOL experiments in microgravity. From [12].**

17

1.2.4   Grain Envelope method

Also named as the "mesoscopic phase-field" method, the grain envelope method was initially proposed by Steinbach et al. in [39] and then improved in [40]. It describes the dendritic grain by its envelope but not its solid/liquid interface in order to save computational resources.

The envelope of a grain is a virtual smooth surface connecting all its active dendrite tips, so the envelope growth kinetics can be calculated from the kinetics of dendrite tips. A confocal envelope is defined with a distance from the principal envelope, as schematized by Fig. 1.11. The stagnant film is defined by the liquid between the grain envelope and the confocal grain envelope. The composition field in the stagnant film is regarded as Ivantsov-like composition field, under the assumption that the theory determining dendritic growth is valid for all orders' tips and the interactions at the tip scale is independent of the interactions at grain scale. The growth of the dendrite tips is determined by the solvability theory and the local supersaturation in the vicinity of the envelope. The solute mass balance is resolved over the entire domain. Within the envelope, the solid/liquid interface is assumed at thermodynamic equilibrium [41].
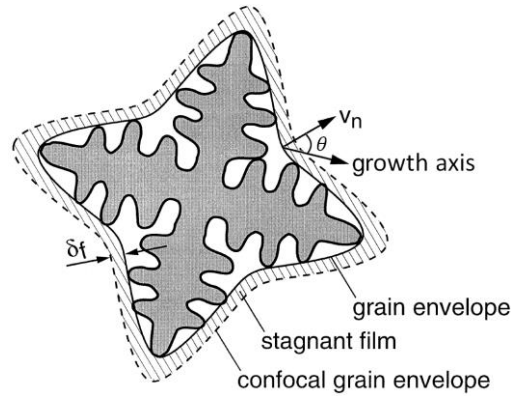
Fig. 1.11   Illustration of the grain envelope defined by active dendrite tips, the stagnant film, and the confocal grain envelope in the grain envelope method. From [39].

The grain envelope model was recently enriched with the volume-average fluid flow equation in two dimensions, and the columnar and equiaxed dendritic growth under the influence of flow was investigated [41]. The computational cost of the grain envelope simulations is about two orders of magnitude lower than that of PF [42]. Three-dimensional grain envelope model has also been developed, while its simulation domain is generally in the order of 1 mm^3 [43]. Fig. 1.12 is an example of three-dimensional grain envelope simulation during equiaxed solidification in a thin sample.

To our knowledge, the grain envelope method has not been applied for modeling the CET.
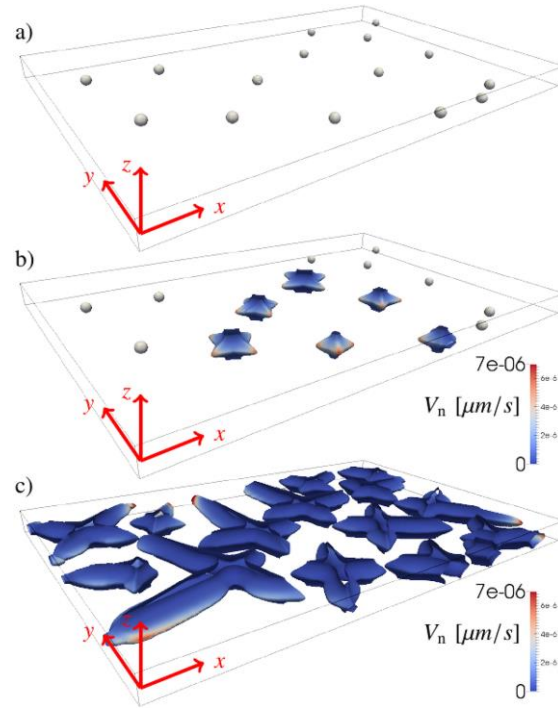
Fig. 1.12   **Three-dimensional snapshots of the grain envelope simulation of 15 equiaxed grains during equiaxed solidification in a thin sample at three different times. The color map indicates the normal growth velocity of the envelopes, V_{n}. From [43].**

1.2.5   Cellular Automaton – Finite Element (CAFE) method

Initially introduced by Rappaz and Gandin [44], the mesoscopic CA method is used for the prediction of the grain structure by modeling the grain envelopes on a cellular grid. This method is able to simulate the grain structure evolution during solidification processes at the scale of 1000 cm^3 [45]. In the rest of this thesis, only this mesoscopic CA method is concerned, so it is simply called the CA method.

The simulation domain is covered by equal-size CA cells, usually squares in two dimensions and cubes in three dimensions, and they are aligned as grid. Their edge length is called CA cell size, denoted as l_{CA}. Each cell has its neighbors that are the cells having common point, common edge, or common surface with it. Consider a cell v, which is with black solid contours in Fig. 1.13. In two dimensions, the cells having a common edge with cell v are its first nearest cells, as the red cells in Fig. 1.13a, and the cells having a common point with cell v are its second nearest cells, as the green cells in Fig. 1.13a; in three dimensions, the cells having a common surface with cell v are its first nearest cells, as the red cells in Fig. 1.13b, the cells having a common edge with cell v are its second nearest cells, as the green cells in Fig. 1.13b, and the cells having a common point with cell v are its third nearest cells, as the yellow cells in Fig. 1.13b. There are two commonly used neighborhoods. Von Neumann neighborhood is composed by the first nearest cells (4 cells in two dimensions, 6 cells in three dimensions); Moore neighborhood is composed by the first and second nearest cells in two dimensions (8 cells) and first, second, and third nearest cells in three dimensions (26 cells) [46]. In the following of this thesis, Moore neighborhood is adopted.
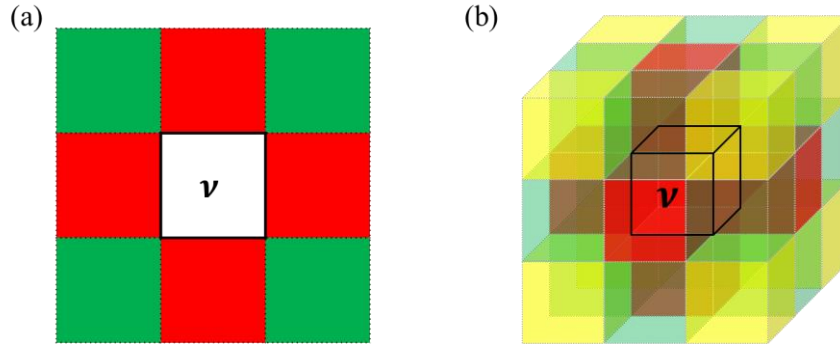
Fig. 1.13   Illustration of two-dimensional and three-dimensional CA cell and its neighbors. For the cell ν with black solid contours, (a) in two dimensions, the red cells having a common edge with it are its first nearest cells, and the greem cells having a common point with its are its second nearest cells; (b) in three dimensions, the red cells having a common surface with it are its first nearest cells, the green cells having a common edge with it are its second nearest cells, and the yellow cells having a common point with it are its third nearest cells.

The evolution of grain structure in the solidification process is modeled by the transition of CA cell state. There are three different cell states: liquid, mushy, and solid. A CA cell in mushy state has a growing envelope. During the solidification process, the envelope captures neighboring cells in liquid state, then these captured cells turn into mushy state and bear their own envelopes (Fig. 1.14). A CA cell will turn into solid state if all its neighbors are in mushy state or solid state (Fig. 1.15). In this way, the propagation of grain is modeled.
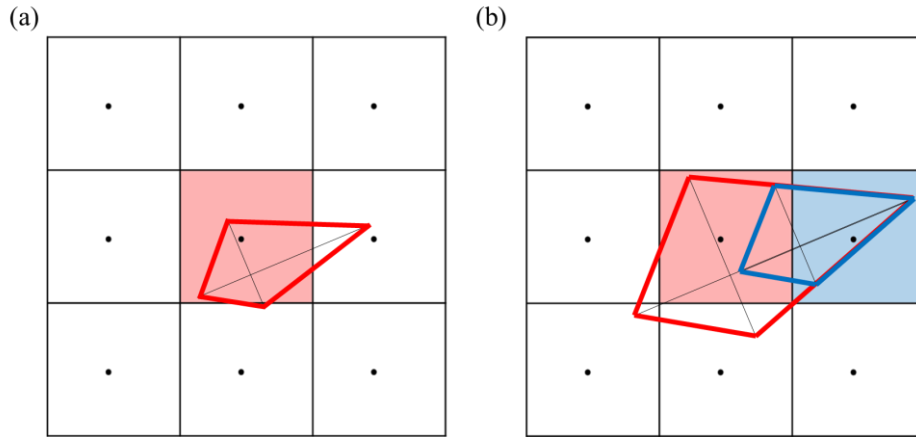
Fig. 1.14   Illustration of capture process in the two-dimensional CA method. The red cell is in mushy state, and its envelope is the red quadrilateral. (a) All its neighboring cells are in liquid state. (b) At this moment the center of the blue cell is included within the red envelope, so this blue cell is captured by the red envelope, leading to the creation of the blue envelope.

The grain envelope is an orthodiagonal quadrilateral in two dimensions (Fig. 1.14) and an orthodiagonal octahedron in three dimensions, i.e., diagonals are perpendicular to each other. The growth of the envelope is determined by analytical laws calculating the velocity of its apices, such as the Ivantsov – Solvability solution, depending on the temperature at the apices (when the temperature field is non-uniform, the apices of an envelope may have different velocities, so the envelope can be an irregular quadrilateral or octahedron). These analytical growth laws are under strong assumptions such as growth at steady state [23]. Therefore, the

CA method does not consider solute interactions between grains unless macrosegregation is accounted for [9]. However, in this configuration, solute interaction remains very approximate.
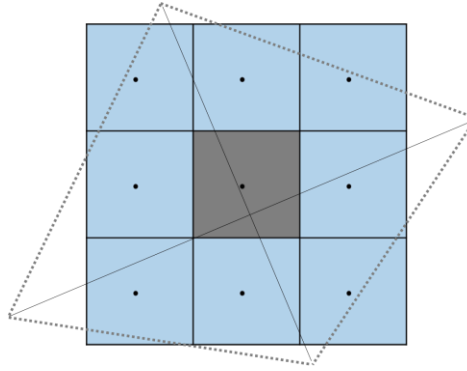
Fig. 1.15   Illustration of transition into solid state of a CA cell in two dimensions. The gray envelope belongs to the gray cell at center. At this moment, all its neighbors are captured (Moore neighborhood is adopted), so the gray cell is turned into solid state, and its envelope is no longer needed.

Fig. 1.14 illustrates the capture process of the CA method. The red quadrilateral is the envelope of the red cell in mushy state in Fig. 1.14a, and all its white neighboring cells are in liquid state. At a moment the center of the right cell (colored in blue in Fig. 1.14b) is contained within the red envelope, so it is captured by the red envelope and becomes mushy. This capture induced the creation of the blue envelope associated to the blue cell, which is homothetic to the red envelope, linked to the same grain and retaining its preferred growing directions, as shown in Fig. 1.14b. The size of the newly born blue envelope is determined by the CA cell size and the length of the capturing edge of the red envelope at the moment of capture [47].

With the implementation of the microsegregation laws for computing the solid fraction generated during grain growth, the CA method has been coupled with the Finite Element (FE) resolution of energy and solute mass in the simulation domain, as the Cellular Automaton – Finite Element (CAFE) method, for taking thermal and solutal evolution during the solidification process into account. As the continuity of the initial work [48], the thermal coupling was introduced in [49], the macrosegregation was introduced in [50], and Wang-Beckermann microsegregation model was introduced in [51]. The two-dimensional and three-dimensional CAFE models have been developed and implemented in the CEMEF finite element library *cimlib* [45].

Fig. 1.16a is the simulation result of the three-dimensional CAFE model on the solidification grain structure of one sample of CETSOL project, and Fig. 1.16b is the experimental grain structure of the sample observed in a longitudinal metallographic cross section. The Gaussian nucleation law is applied in the entire domain, with nuclei density 5×10^{10} m^{-3}, and mean (4 K) and standard deviation (0.5 K) of nucleation undercooling. Qualitative comparison between the CAFE simulation and experimental observation is reached, while there is still some deviation at the CET position [7]. Possible reasons are that the grains are only considered as envelopes, and the CAFE model is poor at describing dendrite kinetics at unsteady state for its use of analytical growth laws on grain envelopes.
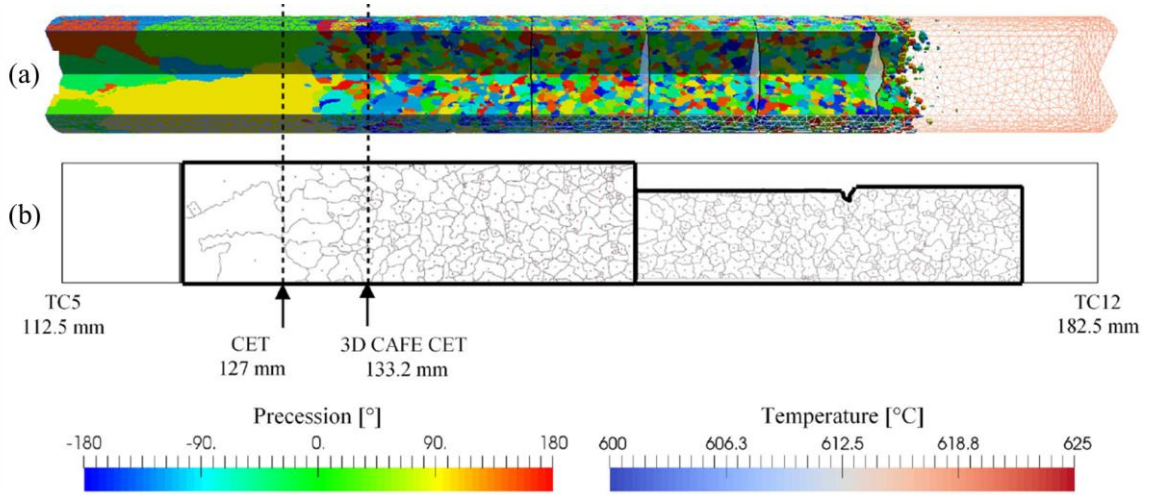
Fig. 1.16   Three-dimensional CAFE simulation of the solidification grain structure of one sample from the CETSOL experiment between thermocouples TC5 (112.5 mm) and TC12 (182.5 mm). A quarter of the cylinder was removed by postprocessing to offer an exploded view at (a) the equiaxed structure forming at $t = 2400$ s. The position of the CET favorably compares with the (b) experimental grain structure observed in a longitudinal metallographic cross section. From [7].

1.2.6   Cellular Automaton – Parabolic Thick Needle (CAPTN) coupling method

Since the PTN method is relevant to calculating dendritic growth at unsteady state by the composition field in the vicinity of the tip, and the CA method is relevant to modeling grain structures and can be coupled with resolution of energy, their complementary advantages have motivated their coupling in the so-called Cellular Automaton – Parabolic Thick Needle (CAPTN) method. This method was initiated in the thesis of Fleurisson [14] at CEMEF in two dimensions for binary alloys. Its principle is to associate a parabola with radius of curvature ρ_{tip} to each growing branch of the envelopes of the CA model and to calculate the tip velocity v_{tip} of the branches by the PTN method on these parabolas. A review of this coupling will be found in Section 4.1

Fleurisson has implemented the PTN method in the CEMEF finite element library *cimlib*. The description of the integration area as a circle by the integration distance a of the DNN method [36] has been maintained in this implementation. Same as the finite difference implementation in the DNN method, this finite element implementation of the PTN method requires a fine mesh size at least in the vicinity of the parabola tips, so an adaptive heterogeneous mesh, called PTN mesh, is used [14]. But a major limitation of this strategy is that it costs a large amount of computational time for very frequent reconstruction of mesh to maintain the fine mesh at the solid/liquid interface [15]. Section 2.1 is a summary of this implementation and its computational cost. A parametric study analyzing the convergence of the PTN model to the Ivantsov – Solvability solution as a function of the minimum mesh size and the integration distance has also been carried out [14]. This study is summarized at the beginning of Chapter 3. Fleurisson has adapted the CA method to the CAPTN coupling, in particular on how to capture adjacent cells (see Section 4.1).

This CAPTN model can be coupled to a resolution of mass and heat transfer over the resolution domain in the same way as the CAFE model. A two-dimensional CAPTN – FE

simulation of the growth of an equiaxed grain in a circular domain was performed and compared to its corresponding CAFE simulation [15]. It has been shown that if the thermal evolutions of the two models are consistent, the kinetics of the primary branches of the grain are different. In particular, the solute interaction of the branches with the edge of the domain is observed in the CAPTN – FE simulation, while it is not considered in the CAFE simulation. Fig. 1.17 shows the simulation results at four different times of the growth of an equiaxed dendritic grain by the coupling CAPTN – FE method on the (a) PTN, (b) CA, and (c) FE meshes.

In spite of its encouraging first results, this method necessitates numerical improvements. It is too costly in terms of computational resources. Neither the CAPTN method nor the CAPTN – FE method has been developed in three dimensions [15].

Remark: to our knowledge, among the models for dendrites and grain structures mentioned above, the PF method and the microscopic CA method have been applied for modeling the CET in two dimensions, the DNN method and the CAFE method have been applied for modeling the CET in three dimensions. Some other models not aiming at predicting individual grain envelopes can also predict the CET, such as the volume averaging method [52, 53]. These models are not introduced in details since the numerical models studied in this thesis aim to predict the grain structures.
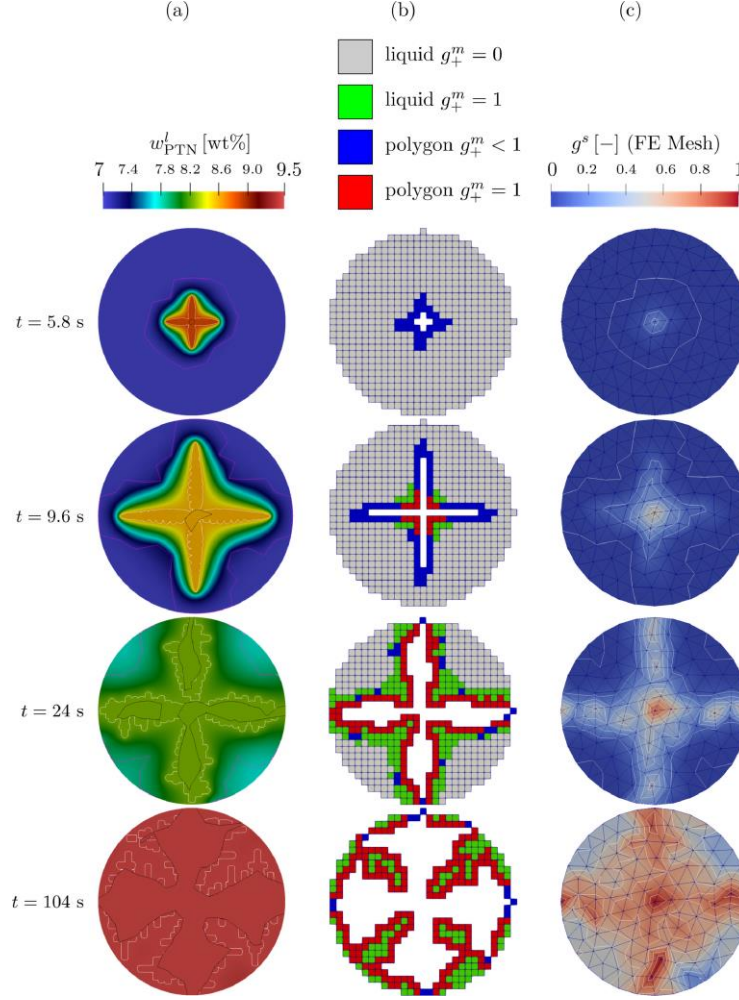
Fig. 1.17   **Two-dimensional CAPTN – FE simulation for an equiaxed dendritic grain. Evolution of the (a) PTN composition field w_{PTN}^l, (b) CA mush fraction g_+^m and cell state, with deallocated cells (white parts) and (c) FE volume fraction of solid g^s at four different times. From [15].**

1.3   Conclusion

Solidification processes involve many physical phenomena, and the microstructures formed during solidification processes have large influence on the properties of casting metals and alloys. Dendrite, as a very common microstructure, is studied in this thesis. Some physical theories and phenomena on dendritic growth as well as numerical models for dendrites and dendritic grain structures were reviewed in this chapter. Table 1.1 is a summary of the numerical models on the application on modeling the CET. Fleurisson [14] implemented the PTN method in the finite element library and initiated the multi-scale coupling CAPTN model. The CAPTN model has been applied for predicting the structure of the equiaxed grains and has shown encouraging results. However, the CAPTN model was only two-dimensional, not computationally efficient. Furthermore, even though the CAPTN model has been compared with the CAFE model at mesoscopic scale [15], some evaluations on dendritic microstructures are still missing.

In the following of this thesis, first the PTN model will be improved in particular on computational efficiency; then the PTN model will be developed into three dimensions and its

parameters will be studied; next the CAPTN model will be improved, developed into three dimensions, and evaluated by other microscopic numerical models; finally, the two-dimensional CAPTN model will be applied for investigating the microstructures produced under directional solidification.

Table 1.1   Numerical models and their application on the modeling of the CET. The individual grain envelope means the model has description on dendrites or grains. The maximum domain size as well as the reference is for the application on the CET, so for the models without application on the CET, these two items are blank.

Model	Individual grain envelope	Application on the CET	Maximum domain size	Reference
PF	✓	✓	$0.004 \ mm^2$	[30]
Microscopic CA	✓	✓	$12 \ mm^2$	[34]
Grain envelope	✓	✗		
DNN	✓	✓	$192 \ mm^3$	[12]
CAFE	✓	✓	$3345 \ mm^3$	[7]
CAPTN (– FE)	✓	✗		
Volume averaging	✗	✓	$1.27 \times 10^8 \ mm^3$	[53]

Chapter 2   Improvements on the PTN finite element implementation

Résumé en français

    Le temps de calcul de chaque module de l'algorithme original du modèle PTN est analysé. Le remaillage prend la majorité du temps de calcul. Pour augmenter l'efficacité du calcul, une nouvelle stratégie de maillage adaptatif visant à diminuer la fréquence de remaillage est proposée. Cette stratégie se fonde sur la structure octree et la méthode de requête orthogonale pour trouver rapidement les nœuds appartenant à un certain domaine. L'algorithme amélioré permet d'économiser énormément de temps de calcul dans la simulation bidimensionnelle. Ce résultat satisfaisant encourage l'application de la méthode CAPTN et son développement en trois dimensions.

This chapter is dedicated to the PTN finite element implementation. The original PTN implementation [14] before this thesis is reviewed, and its shortcomings on computation efficiency are pointed out. As improvements, a new adaptive meshing strategy is proposed, and the octree structure and the orthogonal query method involve into the implementation. The effects of the improvements are shown in the end.

2.1   Review on the finite element implementation of the PTN method

2.1.1   PTN algorithms

To illustrate the two-dimensional finite element implementation of the PTN method [14], it is applied here for simulating the growth of a single dendritic branch (see Fig. 2.1). The simulation domain is a square with edge length L_D along x and y axes. The origin of the coordinate locates at the left-down corner of the domain. A single dendritic branch grows from left to right (in $+x$ direction). Its root stays at $(0, L_D/2)$. The position of the tip is $(L_{init}, L_D/2)$ initially and then evolves to $(x_{tip}, L_D/2)$ with time. Its tip radius and tip velocity are ρ_{tip} and v_{tip}, respectively. The parabolic form of the branch can be described mathematically using a formula by tip position, root position, and tip radius: $(y - L_D/2)^2 + 2\rho_{tip}(x - x_{tip}) = 0$.
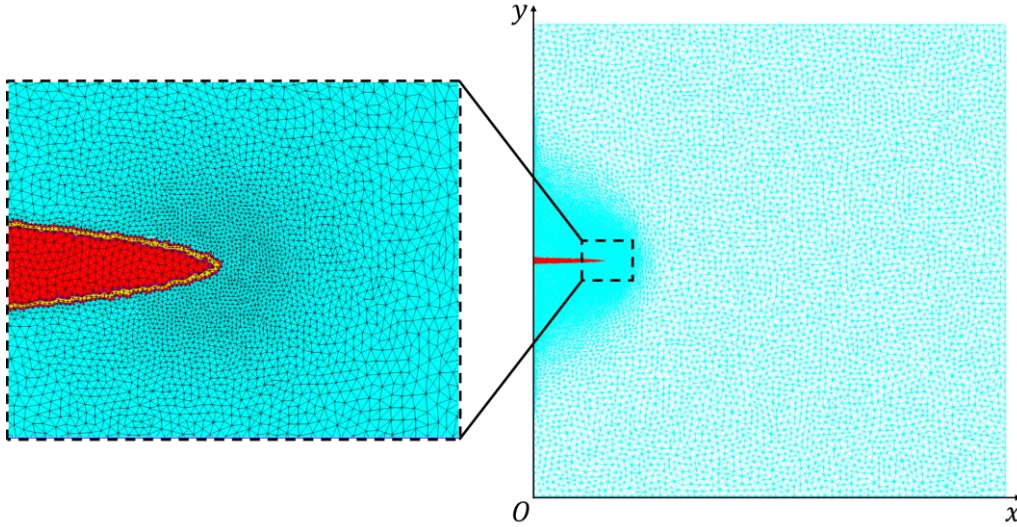
Fig. 2.1   **Illustration of the adaptive heterogeneous PTN mesh used by Fleurisson [14]. On the right the mesh is represented by wireframe. On the left is the enlargement of the box with black dashed contours, and the mesh is represented by surface with edges. The nodes in yellow elements with minimum mesh size h_{min} are at solid/liquid interface; the nodes in red elements with mesh size h_{solid} are in the solid. The mesh is heterogeneous in the cyan liquid area, and its size is smaller where the magnitude of composition gradient is larger.**

This method is implemented by the finite element method on an unstructured finite element mesh of simplex (triangle in two dimensions), as shown in Fig. 2.1. This mesh is called "PTN mesh" in the following part of the thesis. A nodal field $\delta_{\in parabola}$ is employed for indicating whether a node belongs to the parabola or to the liquid: $\delta_{\in parabola} = 0$ for

nodes in the liquid, and $\delta_{\in\text{parabola}} = 1$ for nodes belonging to the parabola [1]. The algorithm for calculating this field will be introduced in the *Dirichlet Condition* module. The elements having some nodes belonging to the parabola and some nodes belonging to the liquid are regarded as the solid/liquid interface (colored in yellow in Fig. 2.1).

An adaptive heterogeneous meshing strategy was proposed in [14] for a good description of the composition field near the dendrite tip and the computation efficiency, as shown in Fig. 2.1. Nodes of the elements at the solid/liquid interface are equipped with isotropic mesh with minimum mesh size $h_{\min}$ (nodes in yellow elements in Fig. 2.1); nodes belonging to the parabola are equipped with isotropic mesh with mesh size h_{solid} (nodes in red elements in Fig. 2.1). h_{solid} is greater than $h_{\min}$ for reducing the number of elements. An anisotropic mesh is generated for liquid nodes (nodes in cyan elements in Fig. 2.1) by an anisotropic metric based on the composition field using a geometric error estimator [54]

$$\Lambda_k = \min\left(\max\left(\frac{c}{\epsilon}|\lambda_k|, \frac{1}{h_{\max}^2}\right), \frac{1}{h_{\min}^2}\right) \tag{2.1}$$

In the framework of the eigenvectors of the Hessian of composition field, the diagonal values Λ_k of the metric are functions of eigenvalues λ_k of the Hessian of composition field, of the minimum mesh size $h_{\min}$ and maximum mesh size $h_{\max}$, of the maximum estimated interpolation error accepted ϵ, and of the geometric parameter $c = \frac{1}{2}\left(\frac{dim}{dim+1}\right)^2$ with dim the spatial dimension of the problem (2 or 3) [14]. Thus, the mesh size in the liquid is between $h_{\min}$ and $h_{\max}$, and is smaller where the magnitude of composition gradient is greater.

The two physical fields used in the PTN method are the temperature field T and the liquid composition field $w_{\text{PTN}}^{\text{l}}$. These fields are implemented as nodal fields. As for the DNN method, the composition on nodes belonging to the parabola is imposed to the liquidus composition of the tip w^{ls} (as described in the *Dirichlet Condition*). Therefore, there is no solute conservation in the PTN method. $w_{\text{PTN}}^{\text{l}}$ is imposed to the nodes with $\delta_{\in\text{parabola}} = 1$ as a Dirichlet condition.

The algorithm of the PTN method can be briefly presented by the flow chart in Fig. 2.2.

Initialization is the module at the very beginning of the method. In this module the initial values of fields and parameters are set. Composition Dirichlet condition is imposed to the nodes belonging to the parabola, which will be detailed in the module *Dirichlet Condition*. The temperature field is uniform. The initial tip radius is the one of Ivantsov – Solvability solution, and the initial tip velocity is 0. The initial composition field in the liquid can be either uniform or Ivantsov solution.

Resolution of Solute Diffusion solves the diffusion equation Eq. (1.11), with boundary conditions to calculate the composition field in the liquid at time t. The composition boundary conditions are no-flux boundary condition at the simulation domain edges and Dirichlet

---

[1] For the cases with more than one branch in the simulation, $\delta_{\in\text{parabola}} = j$ where j is the number of the branch and $j \in \{1, 2, 3, \dots\}$.

boundary condition given by *Initialization* for the first time step or by *Dirichlet Condition* at time $t - \Delta t$ for other time steps.

Remeshing judges whether the current mesh needs to be reconstructed based on some remeshing criteria, and if so, a remeshing operation will be launched on the PTN mesh, and the fields of the old mesh will be interpolated to the new mesh. Since the anisotropy of the mesh corresponds to the composition field in the liquid and the position of the parabola, as the dendrite grows a certain distance, a new heterogeneous mesh adapting to the new composition field and the parabola should be constructed. The remeshing criteria are as follows. Once at least one of them is satisfied, *Remeshing* will be carried out.

- The tip of a parabola has passed more than one element of size $h_{\min}$ since last *Remeshing*.

- A parabola is calculated by the PTN method for the first time.[1]

- 25 time steps have passed since last *Remeshing*.[2]
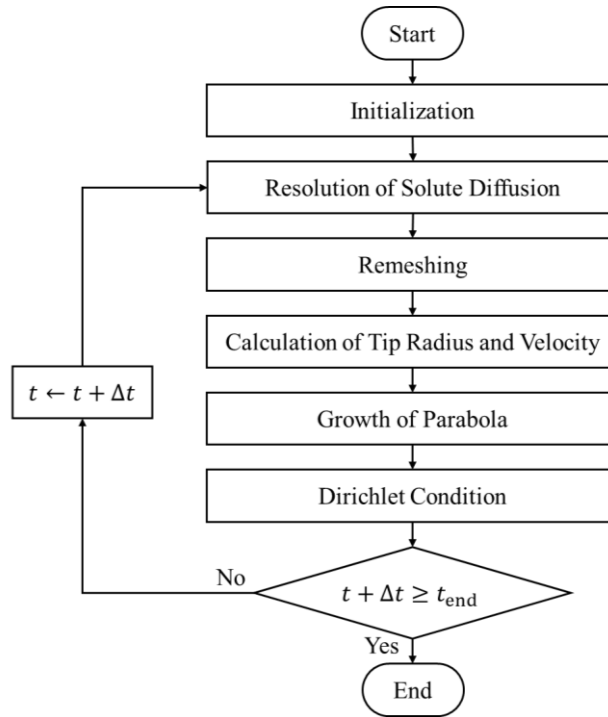
Fig. 2.2   Algorithm modules of the PTN method. The modules in the temporal loop take our interest in the following.

Calculation of Tip Radius and Velocity calculates first the *Flux Intensity Factor* by integration, then the tip radius and velocity at time $t + \Delta t$. In order to identify the elements on which an integration should be carried out, all elements of the PTN mesh are gone through,

---

[1] In the PTN simulation presented in this chapter, *Remeshing* is carried out at the beginning of the simulation.

[2] 25 is a quite arbitrary number aiming at the branch with decreasing velocity and increasing radius. In the PTN simulation presented in this chapter, this criterion is not reached.

and the distance from each node to the tip of the parabola is calculated. According to this, an elementary field indicating that an element belongs to the integration surface Σ or integration contour Γ is deduced. An element is considered to belong to the contour Γ if at least one node of this element is contained in the integration circle, whose radius is determined by the integration distance a and tip radius, and at least one other node of this element is not in the circle. Besides, any node contained in the parabola is not considered as in the circle. An element belongs to the surface Σ if all its nodes are contained in the integration circle but not contained in the parabola. Definitions for a, Γ, and Σ are illustrated in Fig. 1.9. The gradient of composition on the elements belonging to Γ and Σ is computed based on $w_{\text{PTN}}^{\text{l}}$. The area of element $d\Sigma$, the length of the arc of the integration circle contained in the element $d\Gamma$, as well as unit outside normal vector $\boldsymbol{n}^{\Gamma}$ are calculated. Then the contribution to the *Flux Intensity Factor* of related elements are calculated, as in Eq. (1.15). Once the *Flux Intensity Factor* is known by summing all contribution, the tip radius and tip velocity can be deduced from Eq. (1.7) and Eq. (1.13).

Growth of Parabola gets the position and shape of parabola at time $t + \Delta t$ based on its tip radius and velocity at time $t + \Delta t$ and its position at time t.

Dirichlet Condition tags the nodes inside the parabolas (nodes in the red area in Fig. 2.1) at $t + \Delta t$ with the Boolean $\delta_{\in\text{parabola}}^{t+\Delta t} = 1$, and imposes the liquidus composition w^{ls} on these nodes. This becomes a part of the boundary condition in *Resolution of Solute Diffusion*. To identify the nodes belonging to the parabola, all elements of the PTN mesh are gone through for computing the distance from each node to the middle of the root and the tip of the parabola (Point M in Fig. 2.12). For each node with distance not greater than $\sqrt{2\rho_{\text{tip}}L + L^2/4}$ (L is the distance between the root and the tip of the parabola, as in Fig. 2.12), its coordinates are used for verifying if the node is in the parabola or not. Since the composition in the solid has no influence on the composition in the liquid, for the simplicity of implementation, all nodes belonging to the parabola are given $w^{\text{ls}} = (T - T_{\text{M}})/m$ as composition Dirichlet condition, with T the temperature of the tip of the parabola, T_{M} the melting point, and m the liquidus slope.

A *Time Ending* criterion is applied to stop the loop: if the simulation time exceeds t_{end}, the loop will stop and go to the end.

The algorithm mentioned here (detailed in [14]) is called original algorithm in the following. The integration distance a is a fixed model parameter. Parametric studies on a and minimum mesh size h_{min} have been carried out by Fleurisson [14], which will be summarized at the beginning of Section 3.1.

2.1.2   Computational time

A two-dimensional PTN simulation of Al-7 wt.% Si alloy for $\Omega = 0.1$ by the original algorithm is launched on 2 CPU cores. The CPUs used in this thesis are of type Intel® Xeon® E5-2680V4 2.40GHz. The composition in liquid is initialized as the Ivantsov solution.

Material properties are listed in Table 2.1; simulation parameters are listed in Table 2.2. Under this supersaturation, the tip radius and tip velocity from the Ivantsov – Solvability solution are $\rho_{\text{tip}_{\text{Iv}}} = 2.45 \times 10^{-2}\text{mm}$ and $v_{\text{tip}_{\text{Iv}}} = 8.90 \times 10^{-4}\text{mm/s}$, respectively. The simulation domain is a square whose edge length is 135 mm, about $40D^{\text{l}}/v_{\text{tip}_{\text{Iv}}}$, so that the simulation could correspond to the growth in a semi-infinite space. The initial length of the branch is 20 mm, giving a tip initial position at $\left(6D^{\text{l}}/v_{\text{tip}_{\text{Iv}}}, 20D^{\text{l}}/v_{\text{tip}_{\text{Iv}}}\right)$. The maximum mesh size is around $0.6D^{\text{l}}/v_{\text{tip}_{\text{Iv}}}$. All these parameters are chosen as in the thesis of Fleurisson [14]. In this test, the simulation time is 5100 s. During this period, the tip moves forward about $1.35D^{\text{l}}/v_{\text{tip}_{\text{Iv}}}$, and the final tip radius and velocity at 5100 s are $\rho_{\text{tip}} = 2.55 \times 10^{-2}\text{mm}$ and $v_{\text{tip}} = 8.23 \times 10^{-4}\text{mm/s}$.

Table 2.1   Material properties of Al-7 wt.% Si [16].

Variable	Name	Unit	Value
Nominal composition in Al	w_0	wt. % Si	7
Diffusion coefficient	D^{l}	$\text{mm}^2 \cdot \text{s}^{-1}$	3×10^{-3}
Partition coefficient	k		0.13
Liquidus slope	m	$\text{K} \cdot \text{wt.}\%^{-1}$	−6.5
Melting temperature	T_{M}	K	933.6
Gibbs Thomson coefficient	Γ^{sl}	$\text{K} \cdot \text{mm}$	1.96×10^{-4}
Marginal stability coefficient	σ		$1/(4\pi^2)$

Table 2.2   Simulation parameters used for the original algorithm, for Al-7 wt.% Si alloy with supersaturation $\Omega = 0.1$.

Variable	Name	Unit	Value
Minimum PTN mesh size	h_{min}	$\rho_{\text{tip}_{\text{Iv}}}$	1
PTN mesh size in solid	h_{solid}	h_{min}	2
Maximum PTN mesh size	h_{max}	h_{min}	82
Integration distance	a	h_{min}	10
Time step	Δt	s	1

The accumulated computational time of each PTN module is depicted in Fig. 2.3, and the total computational time, i.e., the sum of the computational time of these five modules, is 2756 s. *Remeshing* consumes 70.5% of the total computational time, because mesh building is a time-costing process and it is too frequent: in this simulation of 5100 time steps there are 197 times of *Remeshing*. To raise the computational efficiency, an indispensable step is to reduce the frequency of *Remeshing*. A new adaptive meshing strategy will be introduced in the next section. In the PTN implementation, it is necessary to find the nodes locating in the parabola or the integration area. All nodes are scanned for the queries, which is not efficient.

The query on nodes will also be used in the new meshing strategy. In order to avoid a systematic scan over all nodes or elements in the simulation domain, the octree structure and orthogonal query method will be employed. They will be introduced in Subsection 2.2.1 and their applications on *Remeshing*, *Dirichlet Condition*, and *Calculation of Tip Radius and Velocity* will be presented in Subsection 2.2.2, 2.2.3, and 2.2.4, respectively. The evaluation of the improvements will be presented in Subsection 2.2.5.
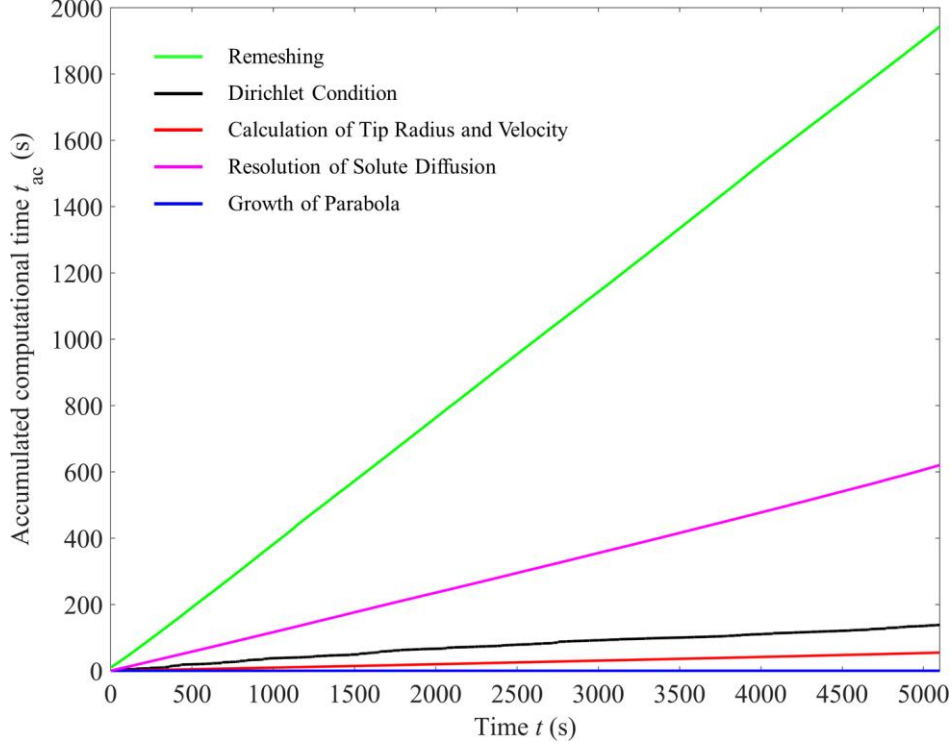
Fig. 2.3   **Accumulated computational time for each PTN module of the original algorithm for a two-dimensional PTN simulation on 2 CPU cores. *Remeshing* consumes 70.5% of the total computational time.**

2.2   Octree and orthogonal query

2.2.1   Theory

Orthogonal query [55] is a quick-query algorithm to report quickly the points in a range that is a d-dimensional axis-parallel box. This range is named as orthogonal query range. This query algorithm is efficient because it is based on a tree data structure. In the PTN model, the octree data structure is applied to divide the mesh domain.

An octree [56] is a tree data structure where each internal child has eight children. A three-dimensional space can be recursively subdivided into eight octants, so an octree is often used to represent this kind of partition. Each child represents a space and its eight octants. The subdivided region may be a cuboid or a sphere, or an arbitrary shape.

A quadtree [55], shown in Fig. 2.4, is the two-dimensional analog of octree. Each of its internal child has four children and corresponds to a two-dimensional space and its four quadrants. In our current two-dimensional case, a quadtree structure is applied; but to be simple on words, here these kinds of structure are also called "octree".

There are two parameters used for creating an octree structure: its maximum number of levels and the threshold of element number in a child for subdivision (in general, it is not satisfactory to subdivide a child with only small number of elements). Fig. 2.4 is an octree with 4 levels and the subdivision is carried out only on children with at least 16 elements. The numbers in each block is the number of elements of each block. Green blocks in the third level will not be divided since they each have less than 16 elements. Red blocks in the fourth level will not be divided either since the fourth level is its deepest division.
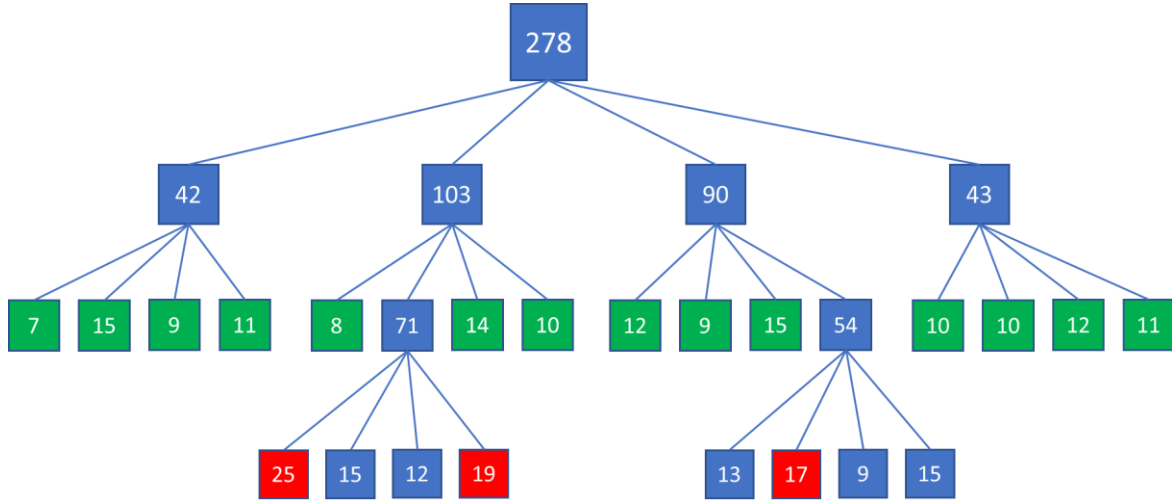
Fig. 2.4   Illustration of the two-dimensional octree (quadtree) data structure. This tree has 4 levels. The subdivision only acts on the blocks with at least 16 elements. The number in each block is the number of elements of each block. Green blocks in the third level will not be divided since they each have less than 16 elements. Red blocks in the fourth level will not be divided either since the fourth level is its deepest division.

Because the Cartesian coordinate system is used, the subdivided region of the octree is chosen as a rectangle. The edges of all rectangles are axis-parallel, so a rectangle can be defined by two characteristic vertices: vertex inferior V_{inf} $(x_{\text{inf}}, y_{\text{inf}})$ and vertex superior V_{sup} $(x_{\text{sup}}, y_{\text{sup}})$, as in Fig. 2.5. x_{inf} and y_{inf} are the minimum of x and y coordinates of the vertices of the rectangle; x_{sup} and y_{sup} are the maximum of x and y coordinates of the vertices of the rectangle.
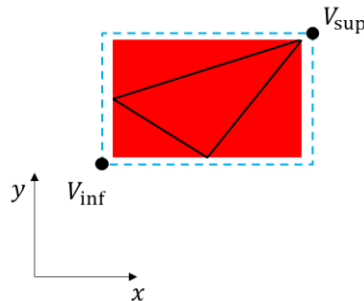
Fig. 2.5   Illustration of an axis-parallel containing rectangle of a triangle with extension. The red axis-parallel rectangle contains the triangle with black solid edges. The rectangle with light blue dashed edges is created based on the red rectangle with extension. It is the containing rectangle of the triangle. This rectangle with light blue dashed edges is defined by vertex inferior V_{inf} and vertex superior V_{sup}.

For the orthogonal query, the relative position of two rectangles needs to be analyzed, hence two functions are employed: intersection and inclusion. Rectangle A is intersected with Rectangle B if they have common area or common segment or common point. Rectangle A is included in Rectangle B if Rectangle A is entirely a part of Rectangle B. If Rectangle A is intersected with Rectangle B, then Rectangle B is intersected with Rectangle A; vice versa. If Rectangle A is included in Rectangle B, then they are definitely intersected with each other. In all the four cases in Fig. 2.6, Rectangle A and Rectangle B are intersected with each other; in particular, in Fig. 2.6a Rectangle A is included in Rectangle B, and in Fig. 2.6c Rectangle B is included in Rectangle A.

An arbitrary shape can be included in an axis-parallel rectangle. The minimum x and y coordinate and the maximum x and y coordinate of the shape are denoted as $x_{\min}$, $y_{\min}$, $x_{\max}$, $y_{\max}$, respectively. If the vertex inferior V_{inf} and the vertex superior V_{sup} of an axis-parallel rectangle are defined by $(x_{\min}, y_{\min})$ and $(x_{\max}, y_{\max})$, then this rectangle includes the shape. However, some points or edges of the shape will locate exactly on the edge of this rectangle. To ensure that all of the shape is fully located inside this rectangle (but not on the edge of this rectangle), an extension factor f_{ext} is applied on the rectangle

$$x_{\mathrm{inf}} = x_{\min} - f_{\mathrm{ext}} \cdot (x_{\max} - x_{\min})$$

$$y_{\mathrm{inf}} = y_{\min} - f_{\mathrm{ext}} \cdot (y_{\max} - y_{\min})$$

$$x_{\mathrm{sup}} = x_{\max} + f_{\mathrm{ext}} \cdot (x_{\max} - x_{\min})$$

$$y_{\mathrm{sup}} = y_{\max} + f_{\mathrm{ext}} \cdot (y_{\max} - y_{\min})$$

This rectangle is called the containing rectangle of the shape, as in Fig. 2.5.
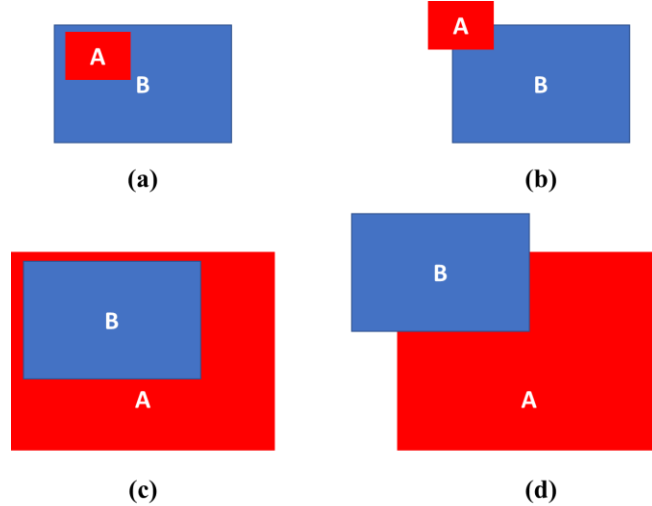
Fig. 2.6   **Illustration of the two relations of location: intersection and inclusion. In all these four cases, Rectangle A is intersected with Rectangle B, and Rectangle B is intersected with Rectangle A as well. In particular, in (a) Rectangle A is included in Rectangle B, and in (c) Rectangle B is included in Rectangle A. In (b) and (d) there is only intersection not inclusion.**

Now the octree is applied to the PTN mesh. A mesh will be constructed with an octree once it is created. The total mesh area has its containing rectangle that is the first level of the

octree. The content of a child of the octree is a set of simplexes (in the two-dimensional case, a simplex is a triangle; in the three-dimensional case, a simplex is a tetrahedron) of this mesh whose containing rectangles are intersected with the region corresponding to the child. One should note that a simplex is regarded intersected with a rectangular region if the containing rectangle of the simplex is intersected with the rectangular region.

In order to guarantee that all the nodes of the mesh locate inside at least one of the deepest-level rectangular region of the octree, the extension factor f_{ext} is also applied in the construction of subdivided regions, i.e., for any subdivision of the octree, the region of a child is a bit larger than a quarter of the region of the parent.

The orthogonal query range is an axis-parallel rectangle, denoted as Rectangle R. The objective of orthogonal query is to find all simplexes in the query range R. The algorithm of orthogonal query is demonstrated in Fig. 2.7. For the parent without child (Line 3), if the rectangular region of this parent is intersected with Rectangle R (Line 4), then all simplexes in this parent will be reported (Line 5). For the parent of octree with children (Line 6), for each of its child (Line 7), if the rectangular region of this child is included in Rectangle R (Line 9), then all simplexes related to this child will be reported (Line 10); if the rectangular region of this child is intersected with but not included in Rectangle R (Line 8, 11), then do the same thing on its each child as on the parent (Line 12), recursively. After all queries, a list of simplex numbers will be reported, after sorting and deleting repeated ones (Line 13, 14). All simplexes in the query range are reported. However, some other simplexes not in the query range are also reported because they are in the last-level child of the octree.

Orthogonal query (query range, parent)

1.   **Input:** query range, parent
2.   **Output:** list of simplex number
3.   **if** the parent has NO child
4.   **if** its domain is intersected with the query range
5.   add all simplex numbers of this parent to the list
6.   **else**
7.   **for** each child i of the parent
8.   **if** domain of child i is intersected with the query range
9.   **if** domain of child i is included by the query range
10.   add all simplex numbers of child i to the list
11.   **else**
12.   **Orthogonal query (query range, child i)**
13.   sort the simplex numbers reported by **Orthogonal query**
14.   delete the repetitive simplex numbers due to the extension

Fig. 2.7   Recursive algorithm of the orthogonal query method.

Fig. 2.8a is an illustration of orthogonal query on mesh. The rectangle with black solid edges is the orthogonal query range. The mesh has a five-level octree structure, and the color dashed lines represent the subdivisions (here only the subdivisions related to the orthogonal query are drawn). The mesh itself is the first level, and the dark red (magenta, green, blue,

resp.) represents the first (second, third, fourth, resp.) level. For the sake of clarity, the children of octree are named by 0, 1, 2, 3 in each level, and a number is added behind for each subdivision, as shown in Fig. 2.8b.
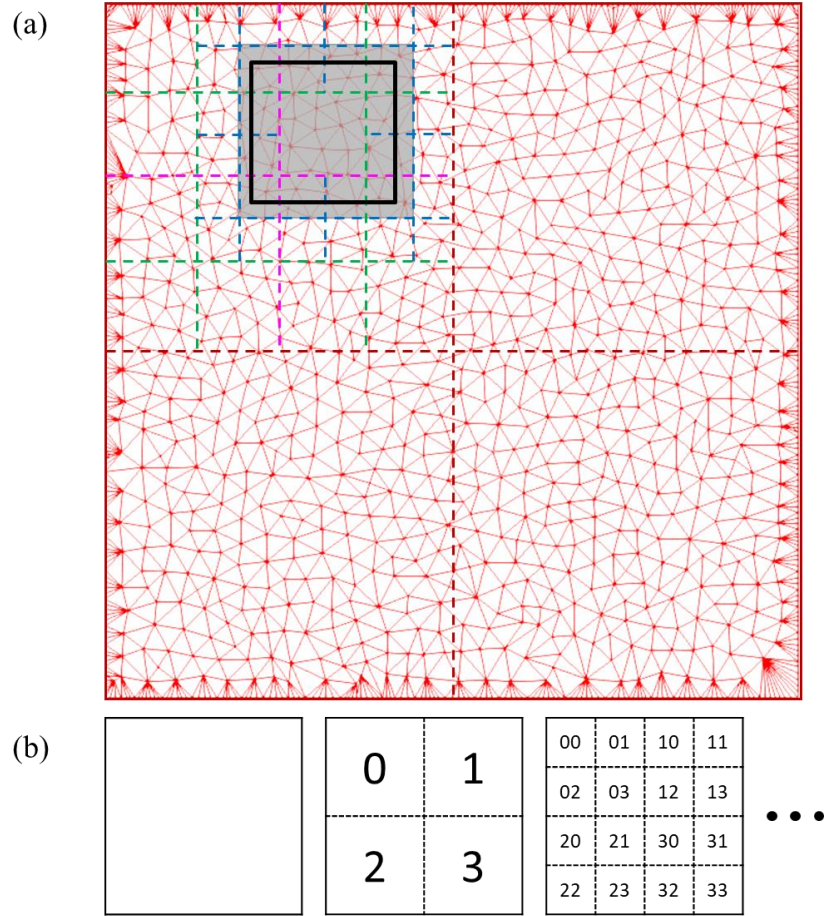
Fig. 2.8   **(a) Illustration of orthogonal query on a meshing domain. The rectangle with black solid edges is the orthogonal query range. Dark red, magenta, green, and blue dashed lines represent the first, second, third, and fourth subdivision, respectively. Only the ones involving into this orthogonal query are drawn. The gray zone is the orthogonal query result based on this octree. It is larger than the orthogonal query range. All simplexes in this gray zone are reported as result. (b) Nomenclature of the octree structure used in this thesis. The children of the octree are named by 0, 1, 2, and 3 for the top left, top right, bottom left, and bottom right in each level, and a number is added behind for each new subdivision.**

The orthogonal query processes are as follows.

(i)   The orthogonal query range is included in the mesh. Orthogonal query is launched on its children: Children 0, 1, 2, 3.

(ii)   Only Child 0 is intersected with the orthogonal query range, so another orthogonal query is launched on its children: Children 00, 01, 02, 03.

(iii)   Children 00, 01, 02, 03 are all intersected with the orthogonal query range, so another orthogonal query is launched on their children.

(iv)   Children 001, 003, 010, 011, 012, 013, 021, 030, 031 are intersected with the orthogonal query range; in particular, Child 012 is included in the orthogonal query

range. So, another orthogonal query is launched on all their children except for Child 012. All elements in Child 012 are reported.

(v)   Children 0013, 0031, 0033, 0102, 0103, 0112, 0130, 0132, 0211, 0300, 0301, 0310 are intersected with the orthogonal query range. Since this is the last level of the octree structure, all elements in these children are reported.

As its result, all elements in the gray zone are reported. The above example does not account for the extension of the subdivision, explaining the absence of the repetitive simplexes found (Line 14 in Fig. 2.7).

2.2.2   New adaptive meshing strategy

To guarantee that the mesh follows the form of the dendritic branch, the original algorithm needs to rebuild the mesh nearly every two time steps, which costs enormous computational time. In order to save computational time, it is indispensable to reduce the frequency of *Remeshing*. Since in the PTN method a branch has a known trajectory, the part of mesh used for computing its kinetics can also be predefined. Based on this, a new adaptive meshing strategy is proposed: the idea is to place a box with minimum mesh size h_{min} in front of the tip, along its growth direction, as the rectangle with blue dashed edges in Fig. 2.9. This permits to compute the *Flux Intensity Factor* with a good precision at every time step in certain duration while not proceeding with remeshing.

The integration area is a part of circle, drawn in yellow and red in Fig. 2.9. Its radius at the creation time of the fine-mesh box, denoted as R_{integ}^{c}, is determined by the integration distance a, which is a constant in the current code, and tip radius at this time ρ_{tip}^{c}

$$R_{integ}^{c} = \sqrt{a^2 + 2\rho_{tip}^{c} a} \qquad (2.2)$$

The distance from the dendrite tip to the back edge of the fine-mesh box is l_{b}, and the distance from the dendrite tip to the center of the fine-mesh box tip is l. Hence, the length of the fine-mesh box is $2(l + l_{b})$. This length impacts the frequency of *Remeshing*: the greater the length is, the less frequently the reconstruction of mesh occurs. However, in order to limit the number of elements, the fine-mesh box should not be too long. Half of its height, denoted as H, is greater than the radius of integration area at this time. Meshes in the solid (resp. liquid) are homogeneous with mesh size h_{solid} (resp. h_{max}). To have good transition between different mesh sizes, two transitional areas TA1 and TA2 are defined based on the distance of nodes to the walls of the fine-mesh box. These transitional areas are also helpful to the reconstruction of the mesh, which will be detailed in Subsection 3.1.1. Meshes in these two transitional areas are isotropic and homogeneous with different mesh sizes, h_1 and h_2, respectively. If mesh belongs to different areas with different sizes, its size is determined by the smallest one.

The integration area for calculating the *Flux Intensity Factor* of the tip must always stay in the fine-mesh box, so this heterogeneous PTN mesh needs to be reconstructed if at least one of the following criteria is satisfied:

- A parabola employs the PTN method for the first time.

- The tip of a parabola has passed more than a distance l_R since last remeshing [1].

- The radius of integration area, which varies with tip radius, is greater than $0.95H$.

These criteria are only suitable for the simulation with a single branch. Its generalization for multi-branch cases will be discussed in Subsection 4.3.2.
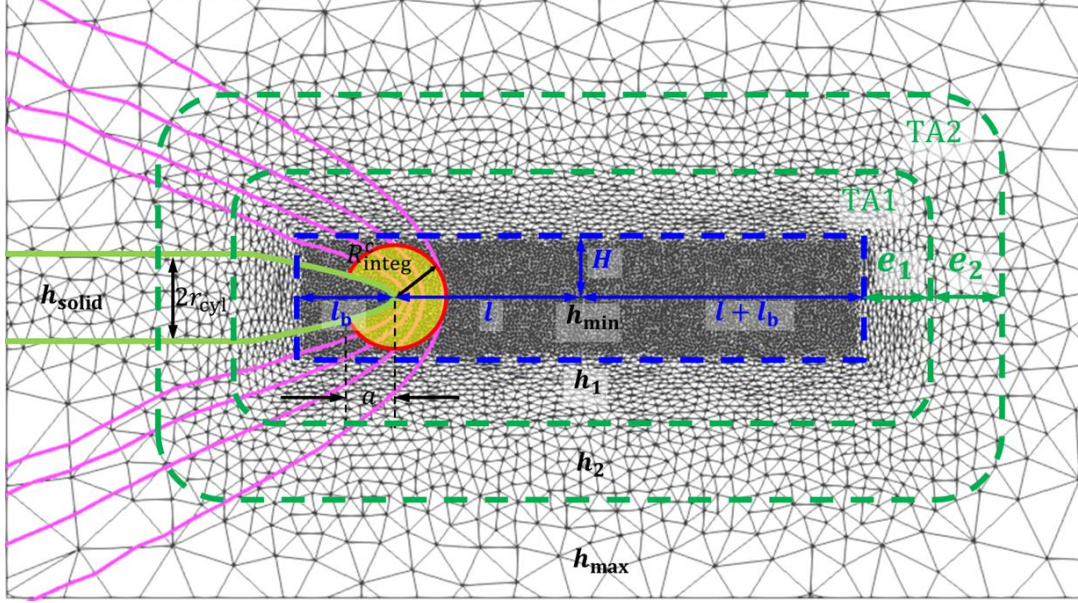
Fig. 2.9   **New adaptive heterogeneous PTN mesh. The dendritic branch with its integration area is represented by green solid line and yellow area with red solid contour. Magenta lines are the iso-composition lines in the liquid. At this moment the adaptive mesh is constructed. Meshes in the fine-mesh box with blue dashed edges have minimum mesh size $h_{\min}$ for calculating the kinetics of the tip. The distance from the dendrite tip to the back edge of the fine-mesh box is l_b, and the distance from the dendrite tip to the center of the fine-mesh box tip is l. Its half height is H. Meshes in the solid have homogeneous mesh size h_{solid}, and meshes in the liquid have homogeneous mesh size $h_{\max}$. Transitional Area 1 (TA1) is in the smaller round corner rectangle with dark green dashed edges and outside the fine-mesh box. Its thickness is e_1. Meshes in it are isotropic and homogeneous with mesh size h_1. Transitional Area 2 (TA2) has a thickness of e_2 from TA1, i.e., the area between the two round corner rectangles with dark green dashed edges. Meshes in it are isotropic and homogeneous with mesh size h_2.**

A nodal field $\delta_{\in\text{fine-mesh box}}$ indicating the nodes belonging to the fine-mesh box is defined. The orthogonal query is employed for finding nodes in the fine-mesh box. In general cases, the fine-mesh box is oriented with the axis of the dendritic branch and thus not aligned with the frame axes, so an orthogonal query range must be determined. In Fig. 2.10 the blue box is the fine-mesh box determined above. Point *A* and *B* are the midpoints of the two edges respectively. $\overrightarrow{AB}$ is the growing direction of the dendrite. A simple way to determine the orthogonal query range is to first draw a circle at the center of the blue box whose diameter equals to the length of the diagonal of the blue box (i.e., the red circle in Fig. 2.10), then

---

[1] The selection of the value of l_R will be discussed in Subsection 3.1.1.

determine the square along axes at the same center circumscribing around the circle (i.e., the black square in Fig. 2.10). This square is its orthogonal query range.
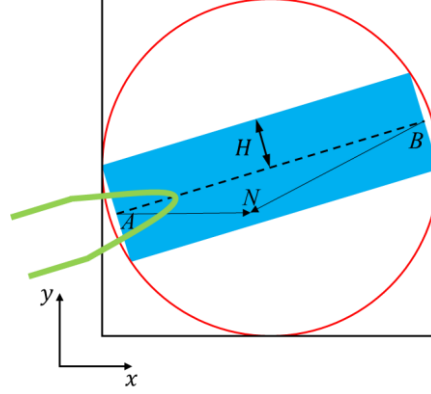
Fig. 2.10   Illustration of the algorithm on finding nodes in the blue box with the help of orthogonal query. The green branch is the dendritic branch. This blue box represents the fine-mesh box mentioned above, i.e., the rectangle with blue dashed edges in Fig. 2.9. Point *A* and *B* are the midpoints of the two edges and $\overrightarrow{AB}$ is the growing direction of the dendrite. The red circle is at the center of the blue box and its diameter equals to the length of the diagonal of the blue box. The square with black solid edges is the axis-parallel circumscribing square of the red circle. This square is the orthogonal query range. For a node *N*, if its distance to line AB is not greater than the mid height of the blue box, *H*, and both $\overrightarrow{AN} \cdot \overrightarrow{AB} \geq 0$ and $\overrightarrow{BN} \cdot \overrightarrow{AB} \leq 0$ are satisfied, this node locates in the blue box.

The algorithm for determining $\delta_{\in\text{fine-mesh box}}$ is shown in Fig. 2.11. The orthogonal query reports quickly all nodes belonging to it (Line 5 in Fig. 2.11). Then for each of these nodes, its distance to line *AB* is calculated (Line 8 in Fig. 2.11). For a node *N*, if its distance to line AB is not greater than the half height of the blue box, *H* (Line 9 in Fig. 2.11), and both $\overrightarrow{AN} \cdot \overrightarrow{AB} \geq 0$ and $\overrightarrow{BN} \cdot \overrightarrow{AB} \leq 0$ are satisfied (Line 12 in Fig. 2.11), this node is in the blue box. Although all illustrations are two-dimensional here, this algorithm is suitable for three-dimensional model as well, with two-dimensional box and circle replaced by three-dimensional cylinder and sphere.

1. **Inputs:** Parabolas
2. **Outputs:** $\delta_{\in\text{fine-mesh box}}$
3. **for** each parabola j
4.   creation of the square as orthogonal query range
5.   search of the elements intersected with the square
6.   **for** each element i in the result of orthogonal query
7.   **for** each node N of element i
8. $d[N]$: distance of node l to segment AB
9.   **if** $d[N] \leq H$
10. $c_1[N] \leftarrow \overrightarrow{AN} \cdot \overrightarrow{AB}$
11. $c_2[N] \leftarrow \overrightarrow{BN} \cdot \overrightarrow{AB}$
12.   **if** $c_1[N] \geq 0$ && $c_2[N] \leq 0$: node N is in the fine-mesh box of parabola j
13. $\delta_{\in\text{fine-mesh box}}[N] \leftarrow j+1$

Fig. 2.11   Algorithm of finding nodes in the fine-mesh box with minimum mesh size.

The efficiency of this improved adaptive meshing strategy will be presented in Subsection 2.2.5.

2.2.3   Application to *Dirichlet Condition*

The essential step in the algorithm of *Dirichlet Condition* is to identify the nodes belonging to the parabolas. In the original algorithm, all elements need to be scanned for calculating distance from their nodes to the middle of the root and the tip of the parabola (Point *M* in Fig. 2.12), called "the middle of the parabolic branch". The calculation on the elements very far from the parabola is a waste of time. The orthogonal query method is now used for raising computational efficiency by reducing the number of elements involved in the calculation. The orthogonal query range is determined similarly as before: it is an axis-parallel square whose center locates on the middle of the parabolic branch and whose edge length is $2\sqrt{2\rho_{\text{tip}}L + L^2/4}$ with ρ_{tip} and L respectively the tip radius and the length of the parabolic branch, as shown in Fig. 2.12. If the parabola is truncated, the circle and square do not change.
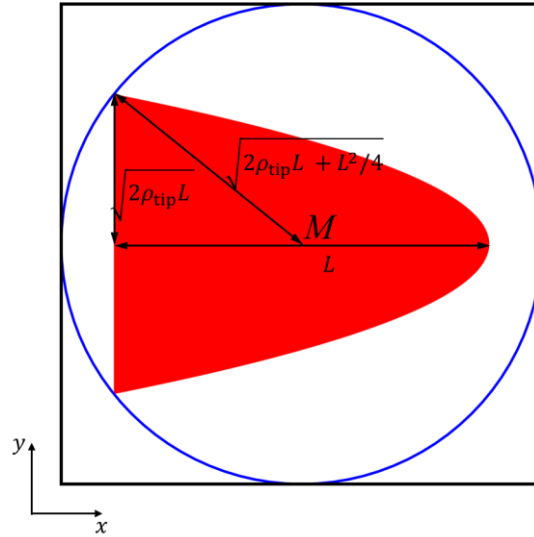
Fig. 2.12   Illustration of the orthogonal query range in *Dirichlet Condition*. Point *M* is the midpoint at the growing axis. The blue circle is centered at *M* and passes through the farthest edge points of the non-truncated parabola (so its radius equals $\sqrt{2\rho_{\text{tip}}L + L^2/4}$). The black square that is the axis-parallel circumscribing square of the blue circle is the orthogonal query range. If the parabola is truncated, the circle and the square do not change.

The improved algorithm of *Dirichlet Condition* by using the orthogonal query method is shown in Fig. 2.13. As inputs, T is the nodal temperature field on the PTN mesh, and "parabolas" means the tip coordinates, root coordinates, and tip radius of each parabola. As outputs, $\delta_{\in\text{parabola}}$ is a nodal field identifying nodes belonging to parabolas, and $w_{\text{PTN}}^{\text{ls}}$ is the composition of nodes belonging to parabolas. For each parabola, the matrix of changing lab framework to the framework of this parabola is computed. With the help of the orthogonal query method, the number of elements considered is reduced. A list of elements will be reported by orthogonal query (Line 6 in Fig. 2.13). For each element in the list, each node is tested if it locates in a circle of center given by the middle of the parabolic branch and of

radius given by $\sqrt{2\rho_{\mathrm{tip}}L + L^2/4}$ (Line 13, 14). If a node is in this circle (the blue circle in Fig. 2.12), its coordinates in the coordinate framework associated with the parabola are calculated (Line 15 in Fig. 2.13) for judging whether it is inside the parabola. For a node inside the parabola, the value of $\delta_{\in\mathrm{parabola}}$ is given as the index of the parabola (Line 17 in Fig. 2.13). The temperature of the dendrite tip is obtained by locating the element containing the tip and interpolating the temperature field. The interfacial composition in liquid calculated from the tip temperature and a linearized phase diagram is given to the nodes belonging to this branch.

1.   **Inputs:** T, parabolas
2.   **Outputs:** $\delta_{\in\mathrm{parabola}}$, w_{PTN}^{l}
3.   **for** each parabola j
4. $F_{j\to\mathrm{lab}}$: change of frame, from local frame to lab frame
5.   creation of the square for orthogonal query
6.   search of the elements intersected with the square
7.   **for** each element i in the result of orthogonal query
8.   **if** ALL of its nodes are in the parabola: $\delta_{\in\mathrm{parabola}} \neq 0$
9.   **continue**
10.   **for** each node l of element i
11.   **if** node l is in the parabola: $\delta_{\in\mathrm{parabola}} \neq 0$
12.   **continue**
13. $d[l]$: distance of node l to point M
14.   **if** $d[l]^2 < 2\rho_{\mathrm{tip}_j}L_j + L_j{}^2/4$
15. $f[l] \leftarrow y_{\mathrm{local\ frame\ }j}^2 + 2\rho_{\mathrm{tip}_j}\left(x_{\mathrm{local\ frame\ }j} - L_j\right)$
16.   **if** $f[l] \leq 0$: node l is in the parabola j
17. $\delta_{\in\mathrm{parabola}}[l] \leftarrow j + 1$
18.   **for** each node l of the domain
19.   **if** its tip temperature T_j is unknown
20.   location of the element containing the tip of parabola j
21.   interpolation of T_j: the temperature of the tip of parabola j
22.   **for** each node l of the domain
23.   **if** $\delta_{\in\mathrm{parabola}}[l] > 0$
24. $w_{\mathrm{PTN}}^{l}[l] \leftarrow w^{\mathrm{ls}} \leftarrow \left(T_j - T_{\mathrm{M}}\right)/m$

Fig. 2.13   **Improve algorithm of *Dirichlet Condition* for the PTN method.**

Fig. 2.14 shows the elements reported by the orthogonal query (in green and red) and elements belonging to the parabola (in red). In this example the maximum number of levels of the octree structure is limited to 12 and subdivision is carried out only on children with at least 256 elements. The mesh near the dendrite tip is finer. Because of the threshold of element number in a child for subdivision, the number of levels of subdivision near the tip is greater than that far away the tip, and the regions of the children at the last level of the octree near the dendrite tip are smaller in area. Therefore, the regions reported by the orthogonal query are not the same in area. This yields that the reported shape is not a rectangle. 34184 elements are reported by the orthogonal query, whereas in the total simulation domain there are 78523 elements: only 43.5% of the elements go into the loop from Line 7 to Line 17 in Fig. 2.13. The efficiency of this improvement will be presented in Subsection 2.2.5.

One has to note that this *Dirichlet Condition* algorithm is only suitable for the PTN and CAPTN model when the temperature field is uniform. If the temperature is non-uniform, this algorithm is no longer relevant, and its generalization will be discussed in Subsection 4.3.1.
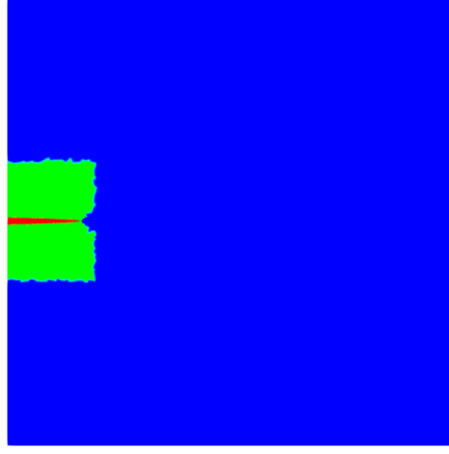
Fig. 2.14   Elements of orthogonal query results and parabola. The green and red zones are the elements reported by the orthogonal query; the red parabola contains the elements whose nodes are imposed to Dirichlet condition. In the simulation domain there are 78523 elements. The number of levels of the octree structure is limited to 12 and subdivision is carried out only on children with at least 256 elements. 34184 elements are reported by the orthogonal query.

2.2.4   Application to *Calculation of Tip Radius and Velocity*

The calculation of dendrite tip kinetics necessitates computing the *Flux Intensity Factor* in the integration area. The algorithm of *Calculation of Tip Radius and Velocity* is improved as well with the employment of the orthogonal query method in a similar way. Its query range is chosen as an axis-parallel square whose center is at the tip of the parabola and whose edge length equals $2R_{\text{integ}}$, where

$$R_{\text{integ}} = \sqrt{2\rho_{\text{tip}}a + a^2} \tag{2.3}$$

is the radius of its integration area for *Flux Intensity Factor*, so the integration area is entirely included in this query range, as shown in Fig. 2.15.

The improved algorithm of *Calculation of Tip Radius and Velocity* is shown in Fig. 2.16. Here the arguments are for the current time step t by default, and to be simple, their superscript t is omitted; on the contrary, arguments for the previous time step are noted by superscript $t - \Delta t$. As inputs, $\delta_{\in\text{parabola}}$ is a nodal field identifying that nodes belong to parabolas, w_{PTN}^{1} is the composition field composition, T is the nodal temperature field on the PTN mesh, and "parabolas" means the tip coordinates, root coordinates, and radius of each parabola. As outputs, ρ_{tip} and v_{tip} are the tip radius and velocity of each branch.

For each parabola, the matrix of changing lab framework to the framework of this parabola is computed (Line 4 in Fig. 2.16). The orthogonal query method reports the elements located in the query range (Line 5 in Fig. 2.16) that will be browsed in the following. If none of the nodes of the element is in liquid area (a node is in liquid area at $t - \Delta t$ if

$\delta^{t-\Delta t}_{\in\text{parabola}} = 0$), this element will be passed out. The distance of each node to the tip of the parabola is calculated (Line 10 in Fig. 2.16), if none of the nodes locates in the integration area, i.e., its distance to the tip of the parabola is greater than the radius of integration area, this element will be passed out; else, this element donates its contribution to the *Flux Intensity Factor*. For an element contributing to the calculation of *Flux Intensity Factor*, its composition gradient will be calculated if it is unknown (Line 13 in Fig. 2.16). Then it is distinguished whether the element is on the boundary Γ of the integration area or in the surface Σ (as defined in Fig. 1.9), by regarding if at least one of its nodes are out of the integration area (Line 14 in Fig. 2.16). In the two-dimensional model, for the simplicity of implementation, the integration in Eq. (1.15) is modified as

$$\mathcal{F}' = \frac{-1}{4\sqrt{a}(1-k)w^{\text{ls}}} \left(\int_{\Gamma} \boldsymbol{\nabla} w^{\text{l}}_{\text{PTN}} \cdot \boldsymbol{n}^{\boldsymbol{\Gamma}} \; \mathrm{d}\Gamma + \frac{1}{D^{\text{l}}} \iint_{\Sigma} \boldsymbol{v}_{\text{tip}} \cdot \boldsymbol{\nabla} w^{\text{l}}_{\text{PTN}} \; \mathrm{d}\Sigma \right) = \frac{1}{\sqrt{d_0}} \mathcal{F} \quad (2.4)$$

The contributions of the elements to this modified *Flux Intensity Factor* $\mathcal{F}'$ of parabola j are accumulated as $\mathcal{F}'_j$. The temperature of the tip of parabola is interpolated with the help of a logarithmic locator, which is able to find the element of PTN mesh containing the tip of the parabola (Line 20 in Fig. 2.16). This logarithmic locator is also based on the octree discussed above while it is an application of point query. After calculating the interfacial composition of the tip in the liquid w^{tip} and the capillary distance d_0, the new tip radius and velocity can be obtained by combining the Solvability condition (Eq. (1.7)).
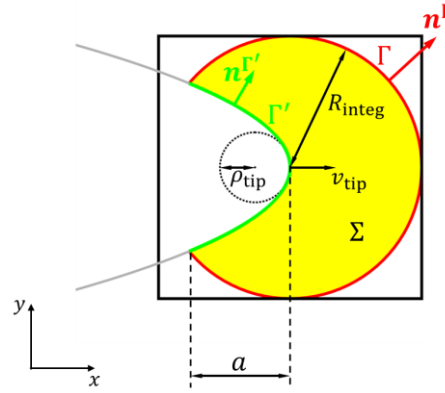
Fig. 2.15   **Illustration of the orthogonal query range in *Calculation of Tip Radius and Velocity*. The dendrite tip is drawn with its integration area, i.e., the partial circle in yellow and its red arc. The axis-parallel square with black solid edges outside the integration area is the orthogonal query range. Its center is at the tip of parabola and its edge length is the diameter of the partial circle, i.e. $2R_{\text{integ}}$.**

Fig. 2.17 shows the elements reported by the orthogonal query (in green, yellow, and red) and elements belonging to the integration area (in yellow and red). In this example the number of levels of the octree structure is limited as no larger than 12 and subdivision is carried out only on children with at least 256 elements as well. 2144 elements are reported by the orthogonal query, whereas in the total simulation domain there are 78523 elements: only 2.7% elements go into the loop from Line 6 to Line 18 in Fig. 2.16. The efficiency of this improvement will be presented in Subsection 2.2.5.

1.   **Inputs:** $\delta^{t-\Delta t}_{\in \text{parabola}}$, $w^{\text{l}}_{\text{PTN}}$, T, parabolas
2.   **Outputs:** $\rho_{\text{tip}}, v_{\text{tip}}$
3.   **for** each parabola j
4. | $F_{j \to \text{lab}}$: change of frame, from local frame to lab frame
5. | orthogonal query of the elements located in the square
6. | **for** each element i in the result of orthogonal query
7. | | **if** all nodes of element i are solid, i.e. $\delta^{t-\Delta t}_{\in \text{parabola}} \neq 0$
8. | | | **continue**
9. | | **for** each node l of element i
10. | | | $d[l]$: distance of node l to the dendritic tip
11. | | **if** a node is in the integration area, i.e. $\exists\, l, d[l] \leq R_{\text{integ } j}$
12. | | | **if** $\nabla w^{\text{l}}_{\text{PTN}}$ hasn't been calculated for element i
13. | | | | compute $\boldsymbol{\nabla} w^{\text{l}}_{\text{PTN}}$
14. | | | **if** at least one node is not in the integration area
15. | | | | $\mathcal{F}'_{ij} \leftarrow \boldsymbol{\nabla} w^{\text{l}}_{\text{PTN}} \cdot \boldsymbol{n}^{\Gamma} d\Gamma \,/\, (4\sqrt{a})$ // integration on contour Γ
16. | | | **else**
17. | | | | $\mathcal{F}'_{ij} \leftarrow \boldsymbol{\nabla} w^{\text{l}}_{\text{PTN}} \cdot M_{j \to \text{lab}} \boldsymbol{v_{\text{tip}}}^{t-\Delta t}_{j} A_i \,/\, (D^{\text{l}} 4\sqrt{a})$ // integration on area Σ
18. | | | $\mathcal{F}'_j \leftarrow \mathcal{F}'_j + \mathcal{F}'_{ij}$
19. **for** each parabola j
20. | location of the element containing the tip of parabola j
21. | interpolation of T_j: the temperature of the tip of parabola j
22. | $w^{\text{tip}}_j \leftarrow (T_j - T_{\text{M}})/m$: composition of the solid/liquid interface
23. | $d_{0\,j}$: capillary distance, function of w^{tip}_j
24. | $\mathcal{F}'_j \leftarrow -\mathcal{F}'_j \,/\, ((1-k)w^{\text{tip}}_j)$
25. | $\rho_{\text{tip}\,j} \leftarrow \left(\dfrac{d_{0\,j}^2}{2\sigma^2 \mathcal{F}'^2_j} \right)^{1/3}$
26. | $v_{\text{tip}\,j} \leftarrow D^{\text{l}} \left(\dfrac{4\sigma \mathcal{F}'^4_j}{d_{0\,j}} \right)^{1/3}$

Fig. 2.16   **Improve algorithm of two-dimensional *Calculation of Tip Radius and Velocity*.**
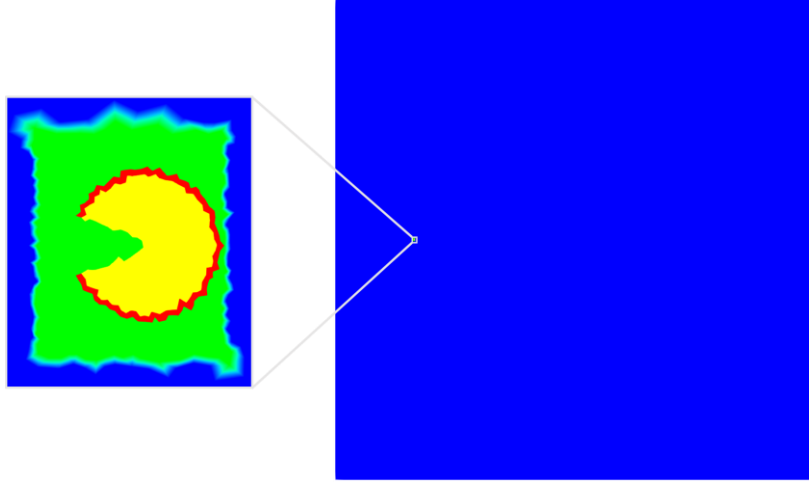
Fig. 2.17 **Elements of orthogonal query results and integration area. The green, yellow, and red zones are the elements reported by the orthogonal query; the yellow area and red contour correspond to integration area Σ and Γ defined in Fig. 1.9 respectively. In the simulation domain there are 78523 elements. The number of levels of the octree structure is limited to 12 and subdivision is carried out only on children with at least 256 elements. 2144 elements are reported by the orthogonal query. On the left is an enlargement of the corresponding part on the right.**

2.2.5   Reduction on computational time

The same simulation as Section 2.1 is redone on 2 cores with improved algorithms employing the orthogonal query method on *Remeshing*, *Dirichlet Condition*, and *Calculation of Tip Radius and Velocity*. Its simulation parameters are listed in Table 2.3, keeping the same minimum mesh size, mesh size in the solid, maximum mesh size, integration distance, time step, and simulation time. The tip radius and tip velocity from the Ivantsov – Solvability solution are $\rho_{\text{tip}_{\text{Iv}}} = 2.45 \times 10^{-2}$ mm and $v_{\text{tip}_{\text{Iv}}} = 8.90 \times 10^{-4}$ mm/s .The distance l is defined based on the diffusion length under Ivantsov – Solvability solution, denoted as $\delta_{\text{d}_{\text{Iv}}}$, which will be introduced in Subsection 3.1.2. Here $\delta_{\text{d}_{\text{Iv}}} = 0.67$ mm (i.e., $\delta_{\text{d}_{\text{Iv}}}/\rho_{\text{tip}_{\text{Iv}}} \approx 28$).

The final tip radius and velocity at 5100 s calculated by the improved PTN algorithm are $\rho_{\text{tip}} = 2.52 \times 10^{-2}$ mm and $v_{\text{tip}} = 8.46 \times 10^{-4}$ mm/s. The computational time for each PTN module of the improved algorithm is depicted in Fig. 2.18 with dashed curves, in comparison with the computational time of the original algorithm with solid curves. The curves of original algorithm are just those in Fig. 2.3. The numbers of elements of the two algorithms are not too different: 93148 and 85060 elements at the last time step for the original and improved algorithm, respectively. Even so, the reducing on computational time is dramatic. The improved *Remeshing* consumes only 53 s, saving 97.3% time of the original *Remeshing*, because it is only launched 4 times in 5100 time steps. The employment of orthogonal query helps *Dirichlet Condition* and *Calculation of Tip Radius and Velocity* to save 41.2% and 50.4% of its computational time, respectively. There is no algorithmic improvement on *Resolution of Solute Diffusion* or *Growth of Parabola*. The computational time of *Growth of Parabola* does not change; however, the computational time of *Resolution of Solute Diffusion* decreases a little. This decrease of time can be explained by the fact that the number of elements of the improved algorithm is a little smaller than that of the original algorithm, so

the time for solving diffusion equation on the mesh is saved a little. In total, for this simulation, the original algorithm consumes 2756 s while the improved algorithm consumes only 768 s : 72.1% of the computational time is saved. This great improvement on computational efficiency will permit the model to be applied for more complicated two-dimensional and three-dimensional cases.

Table 2.3   Simulation parameters for the improved algorithm, for Al-7 wt.% Si alloy with supersaturation $\Omega = 0.1$.

Variable	Name	Unit	Value
Minimum PTN mesh size	$h_{\min}$	$\rho_{\mathrm{tip}_{\mathrm{Iv}}}$	1
PTN mesh size in TA1	h_1	$h_{\min}$	3
PTN mesh size in TA2	h_2	$h_{\min}$	10
PTN mesh size in solid	h_{solid}	$h_{\min}$	2
Maximum PTN mesh size	$h_{\max}$	$h_{\min}$	82
Integration distance	a	$h_{\min}$	10
Time step	Δt	s	1
Distance from the tip to the center of the rectangle with $h_{\min}$ at its creation	l	$\delta_{\mathrm{d}_{\mathrm{Iv}}}$	1
Distance from the tip to the back boundary of the rectangle with $h_{\min}$ at its creation	l_{b}	a	1.2
Half height of the rectangle with $h_{\min}$	H	$R^{\mathrm{c}}_{\mathrm{integ}}$	1.5
Distance passed by the tip between two *Remeshings*	l_{R}	l	1.9
TA1 thickness	e_1	l	1
TA2 thickness	e_2	l	1

It should be emphasized that all these improvements on algorithm are suitable for the three-dimensional model as well, only with changes in dimension, for example: the rectangular box with minimum mesh size becomes a cylinder, the circle and axis-parallel square become a sphere and axis-parallel cube.

Besides of the computational time, kinetics obtained by the original and improved algorithm at 5100 s are comparative. Further analyses on the kinetics will be discussed in Section 3.1.
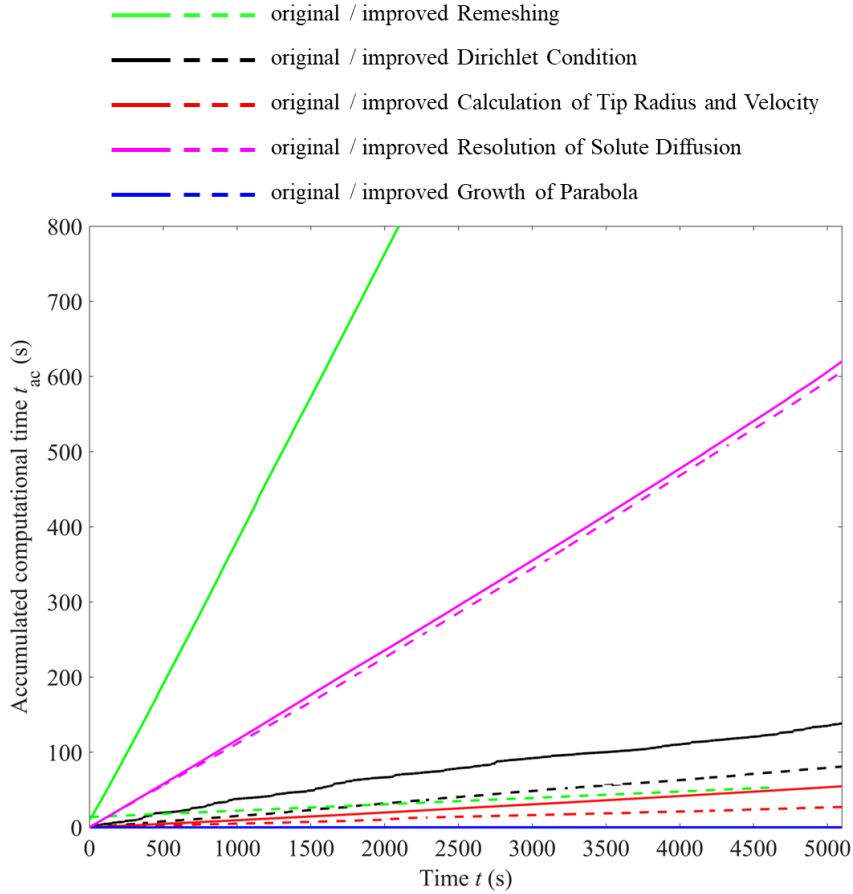
Fig. 2.18   Accumulated computational time of PTN modules for original (solid curves) and improved (dashed curves) algorithms. The curves of original algorithm are just those in Fig. 2.3. The original *Remeshing* (the green solid curve) consumes 2756 s, out of the scale limit of this figure. The improved *Remeshing* consumes only 53 s: 2.7% of the original. The employment of orthogonal query helps *Dirichlet Condition* (black curves) to save 41.2% of its computational time, and *Calculation of Tip Radius and Velocity* (red curves) to save 50.4% of its computational time.

2.3   Conclusion

The original algorithm and implementation of the PTN method [14] were reviewed briefly at the beginning of this chapter, and the computational time of each module was analyzed. *Remeshing* consumed enormous time. To raise the computation efficiency, the octree structure and orthogonal query method have been employed in *Remeshing*, *Dirichlet Condition*, and *Calculation of Tip Radius and Velocity* for seeking the nodes in a certain domain quickly, and a new adaptive meshing strategy aiming to decrease the frequency of *Remeshing* have been proposed. The improved algorithm saves huge amount of computational time in the two-dimensional as-example simulation. This satisfactory result encourages the application of the CAPTN method and its three-dimensional development.

Algorithmic improvements in this chapter does not change the simulation results on kinetics. The kinetics of the original and improved algorithms will be further compared in the next chapter.

Chapter 3   Parametric studies of the PTN method

Résumé en français

   La cinétique calculée par l'algorithme amélioré du modèle PTN et celle calculée par l'algorithme original sont quasiment identiques en deux dimensions, attestant que l'algorithme amélioré n'influence pas la cinétique. La longueur de diffusion d'une branche dendritique sous la solution d'Ivantsov est définie. Celle-ci est utilisée pour dimensionner la distance d'intégration et la dimension de la boîte des mailles fines dans la suite de cette thèse. On observe que lorsque la distance d'intégration est trop grande, la cinétique calculée est divergente. Ce phénomène est expliqué mathématiquement. Les paramètres numériques du modèle PTN sont ensuite étudiés en trois dimensions. Dans une certaine gamme de valeurs, une distance d'intégration plus grande et une taille de maille minimale plus petite améliorent la précision de la cinétique. Le pas de temps a une toute petite influence sur la cinétique en régime permanent, et le cylindre tronquant la parabole ne doit pas croiser la zone d'intégration pour ne pas influencer la cinétique des branches dendritiques.

This chapter shows the studies on PTN method parameters. The calculated kinetics of the improved and original two-dimensional PTN methods are compared. A new observation that the kinetics will be divergent when the integration distance is too large is explained mathematically. The parametric studies on the two-dimensional PTN method are extended to the three-dimensional PTN method.

3.1 Two-dimensional PTN parameters in isothermal condition

Fleurisson has analyzed the influence of the parameters, including the minimum mesh size $h_{\min}$, integration distance a, and radius of truncating cylinder r_{cyl}, on the results of the two-dimensional PTN method [14]. A single dendritic branch of Al-7 wt.% Si alloy growing under constant supersaturation in a large simulation domain is modeled with the two-dimensional PTN method. The initial composition field $w_{\mathrm{PTN}}^{\mathrm{l}}$ in the liquid is taken equal to the Ivantsov solution. In these conditions, the dendrite tip kinetics evolves towards a steady state that should theoretically correspond to the Ivantsov – Solvability solution, introduced in Subsection 1.1.3.

As shown in Fig. 3.1, it is observed that steady-state tip radius and tip velocity converge towards the Ivantsov – Solvability solution for small $h_{\min}/\rho_{\mathrm{tip_{Iv}}}$ and large $a/h_{\min}$. The smaller $h_{\min}/\rho_{\mathrm{tip_{Iv}}}$ and the larger $a/h_{\min}$ are, the smaller difference between the calculated results at steady state and the Ivantsov – Solvability solution is, and the higher its computational cost is. In terms of r_{cyl}, if the truncating cylinder intersects with the integration area, it does influence the results; otherwise, it does not have noticeable impact on the results. Fleurisson has also demonstrated that the prediction on kinetics becomes less precise when the supersaturation increases [15].
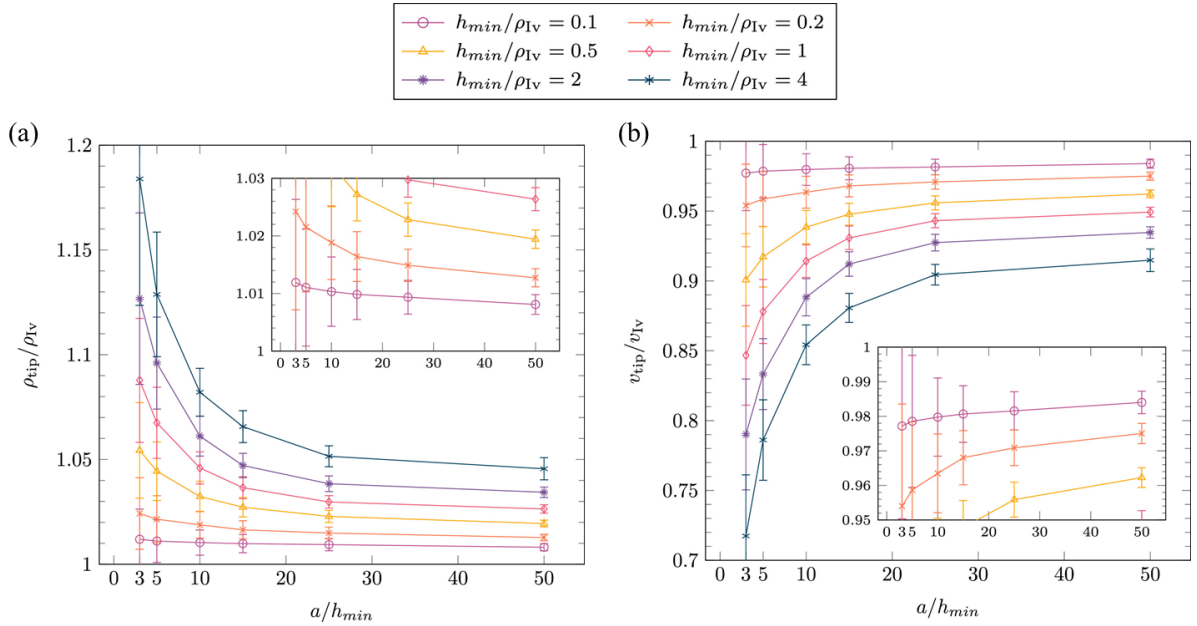
Fig. 3.1   **Evolution of the steady-state dimensionless kinetics (a) $\rho_{\mathrm{tip}}/\rho_{\mathrm{tip_{Iv}}}$ and (b) $v_{\mathrm{tip}}/v_{\mathrm{tip_{Iv}}}$ of a dendrite tip of Al-7 wt.% Si alloy in two dimensions under supersaturation $\Omega = 0.1$ with $a/h_{\min}$ for various values of $h_{\min}/\rho_{\mathrm{tip_{Iv}}}$. From [15]. The notations ρ_{Iv} and v_{Iv} in the figure correspond to $\rho_{\mathrm{tip_{Iv}}}$ and $v_{\mathrm{tip_{Iv}}}$ in this thesis.**

These studies are regarded as a reliable reference for the PTN model. The improved algorithm does not change the method of calculating the kinetics, therefore the kinetics from the improved algorithm should be the same as that from the original algorithm. This is validated by comparing the PTN simulation results from two algorithms for a case mentioned in [14].

3.1.1   Comparison on kinetics between the original and improved algorithm

The same simulations for a single dendritic branch of Al-7 wt.% Si alloy growing under constant supersaturation $\Omega = 0.1$ as Subsection 2.1.2 and 2.2.5 are used for comparing the kinetics calculated by the original and improved algorithm. The simulation domain is a square of 135 mm $\times$ 135 mm. The branch is rooted at the middle of the left domain edge and grows towards the right. Its initial length is 20 mm. The composition in the liquid is initialized as the Ivantsov solution. In this case, the tip radius, tip velocity, and diffusion length at dendrite tip from Ivantsov – Solvability solution (to see Subsection 3.1.2) are $\rho_{\text{tip}_{\text{Iv}}} = 2.4 \times 10^{-2}$mm, $v_{\text{tip}_{\text{Iv}}} = 8.9 \times 10^{-4}$mm/s, and $\delta_{\text{d}_{\text{Iv}}} = 0.67$ mm, respectively. The simulation time is 5100 s.

The kinetics computed by the simulation using the original algorithm and the improved algorithm are compared. The normalized tip radius and tip velocity at every time step are plotted in Fig. 3.2: (a) is from the original algorithm, and (b) is from the improved algorithm. The normalization is achieved by dividing the Ivantsov – Solvability solution under the same supersaturation. At the first time step, the kinetics is initialized by the Ivantsov – Solvability solution, so the dimensionless kinetics equals to 1. The composition field in the liquid is initialized as the Ivantsov solution, so the kinetics is close to its steady state from the beginning. The PTN method is employed as the growth law just from the second time step. The improved algorithm gives very similar kinetics to the original algorithm, indicating that the improved algorithm keeps the same precision on results. Thus, the studies on parameters in [15] are valid for the improved algorithm as well.
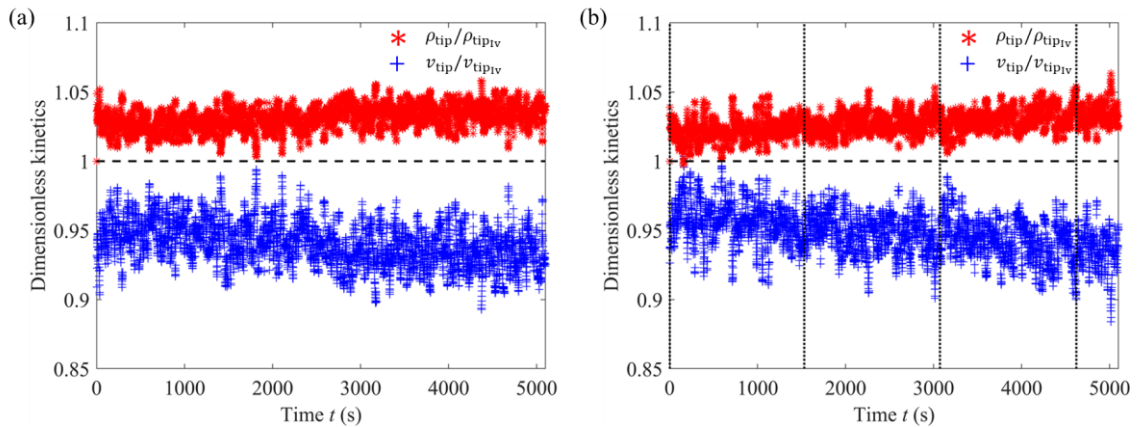
Fig. 3.2   **Tip radius and velocity normalized by the Ivantsov – Solvability solution, computed in the simulations by the (a) original and (b) improved algorithm. Vertical dotted lines in (b) are the moments when the mesh is reconstructed in the improved algorithm. The kinetics is initialized by the Ivantsov – Solvability solution and the composition field is initialized by the Ivantsov solution. The improved algorithm gives very similar kinetics to the original algorithm. In 5100 seconds, the kinetics have not arrived at steady state.**

Vertical dotted lines in Fig. 3.2b are the moments when the mesh is reconstructed in the improved algorithm. The moments of reconstructing the mesh in the original algorithm are not plotted in the Fig. 3.2a because there are 197 times of *Remeshing*, too many to present in the figure. The mesh with branch, integration area, iso-composition contours, and the definition of fine-mesh box at the time step just before ($t = 3071$ s) and after ($t = 3072$ s) *Remeshing* are shown in Fig. 3.3a and Fig. 3.3b, respectively.
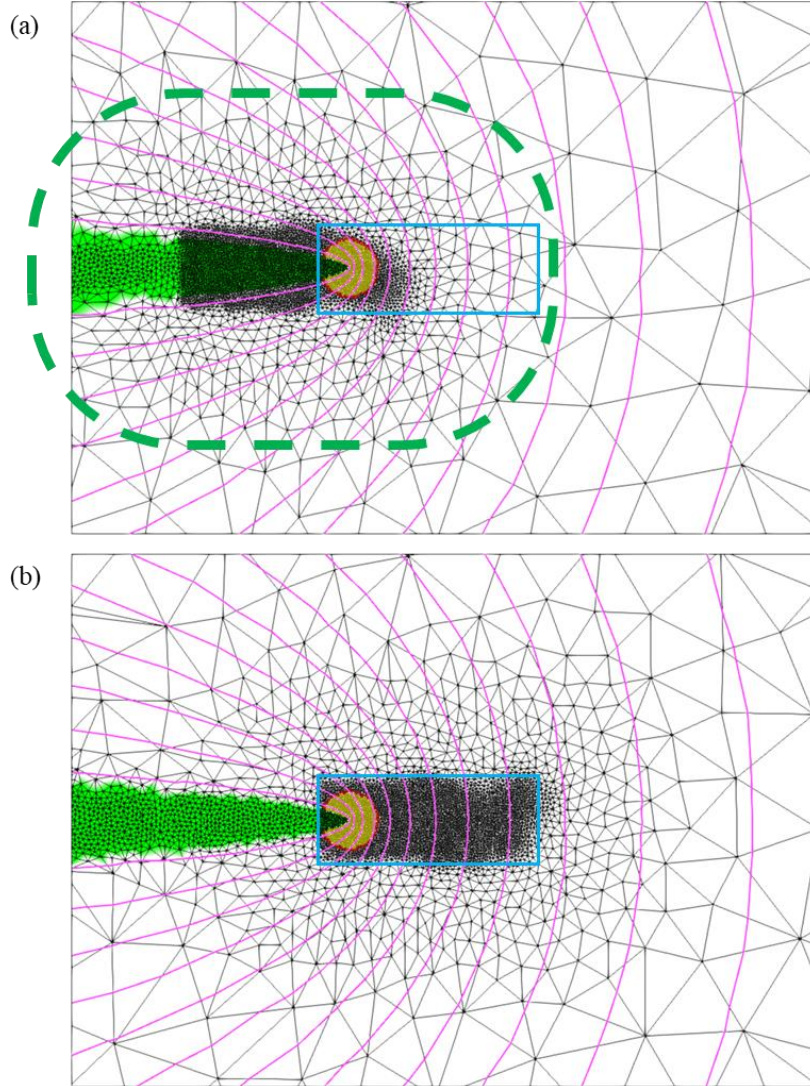
Fig. 3.3 **Mesh with dendritic branch, integration area, and iso-composition contours before and after *Remeshing*, for the two-dimensional PTN simulation of a single dendritic branch of Al-7 wt.% Si alloy with supersaturation $\Omega = 0.1$. (a) is at $t = 3071$ s, the last time step before *Remeshing*, and (b) is at $t = 3072$ s, the first time step after *Remeshing*. The dendritic branch is in green; the integration area is in yellow and its contour is in red; the iso-composition contours are in magenta, from 7.10 wt.% Si to 7.65 wt.% Si, every 0.05 wt.% Si. The blue rectangle is the theoretical position of the fine-mesh box with minimum mesh size at the moment of constructing the mesh in (b). The round corner rectangle with dark green dashed edges in (a) is the larger transitional area (TA2) before *Remeshing*.**

The areas with minimum mesh size are not exact rectangles, especially on the right side, for the reason that their definition is based on the coarse mesh of the last time step. The transitional areas (introduced in Subsection 2.2.2, and the larger transitional area TA2 in Fig.

3.3a is shown by the round corner rectangle with dark green dashed edges) can partly solve this problem, besides ensure good transition between minimum mesh size and maximum mesh size. If the elements with the maximum mesh size are involved in the description of the blue box, which is not the current case, the mesh will no doubt become much worse.

Supposing at steady state the tip radius remains as $\rho_{\text{tip}_{\text{Iv}}}$ and the radius of the integration area R_{integ} is such that $R_{\text{integ}} < 0.95H$. In this case the integration area will go out of the fine-mesh box if the tip has passed

$$l_{R_{\max}} = 2l + l_{\text{b}} - R_{\text{integ}} \tag{3.1}$$

since last *Remeshing*. With the parameters in Table 2.3, $l_{R_{\max}} \approx 2.04l$. In the simulation $l_R = 1.9l < l_{R_{\max}}$ is used so as to reconstruct the mesh before the integration area enters the poorly defined zone near the right boundary of the blue box. If the integration area always stays in the area with minimum mesh size, the influences of *Remeshing* on the composition field and kinetics will be negligible. In Fig. 3.2b, there is little extra fluctuation at the moments when *Remeshing* occurs.

The mesh sizes in the transitional areas, h_1 and h_2, hardly influence the calculation on kinetics if their values are reasonably chosen. This will be manifested in Section 4.5, by the comparison of the kinetics calculated by the adaptive heterogeneous mesh and the kinetics calculated by the homogeneous mesh (all mesh sizes are equal to $h_{\min}$).

3.1.2   Diffusion length under Ivantsov – Solvability solution

As mentioned above, Fleurisson uses the minimum mesh size $h_{\min}$ to nondimensionalize the integration distance a. However, the integration area used for calculating the solute flux is rather linked with the composition field, so it is better to use a physical length related to the composition for nondimensionalizing the integration distance.

The diffusion length at a parabolic tip under Ivantsov solution is proposed. It is denoted as $\delta_{\text{d}_{\text{Iv}}}$, as firstly mentioned in Subsection 2.2.5. Suppose that a single dendritic branch grows in a semi-infinite domain. The form of the branch is assumed as a parabola. At steady state, the composition field in the liquid follows Ivantsov solution as Eq. (1.8). In two dimensions, the tip of the parabolic branch is at $(x, y) = \left(\rho_{\text{tip}_{\text{Iv}}}/2, 0\right)$, and the relation of parabolic coordinate and Cartesian coordinate is (as shown in Fig. 1.4)

$$\rho_{\text{tip}_{\text{Iv}}}\xi^2 = x + \sqrt{x^2 + y^2}, \qquad \rho_{\text{tip}_{\text{Iv}}}\eta^2 = -x + \sqrt{x^2 + y^2}$$

At x axis, $y = 0$, $\xi = \sqrt{2x/\rho_{\text{tip}_{\text{Iv}}}}$, so

$$w_{\text{2D}}^{\text{l}}(x) = w_0 + (1 - k)w^{\text{ls}}\sqrt{\pi\text{Pe}}\,\exp(\text{Pe})\,\text{erfc}\left(\sqrt{\text{Pe}\cdot 2x/\rho_{\text{tip}_{\text{Iv}}}}\right) \tag{3.2}$$

Referring to the definition of the diffusion length of a planar front, the diffusion length at the dendrite tip along its growing direction is defined as twice of the intersection of the tangent of the composition along the x axis at the solid/liquid interface and the nominal

composition, as shown in Fig. 3.4. The derivative of the composition at the dendrite tip along x axis is

$$\left.\frac{\mathrm{d}w_{2\mathrm{D}}^{\mathrm{l}}}{\mathrm{d}x}\right|_{x=\frac{\rho_{\mathrm{tip}_{\mathrm{Iv}}}}{2}} = -2(1-k)w^{\mathrm{ls}}\mathrm{Pe}/\rho_{\mathrm{tip}_{\mathrm{Iv}}} \tag{3.3}$$

so the diffusion length is

$$\delta_{\mathrm{d}_{\mathrm{Iv}}} = \frac{w_0 - w^{\mathrm{ls}}}{-2(1-k)w^{\mathrm{ls}}\mathrm{Pe}/\rho_{\mathrm{tip}_{\mathrm{Iv}}}} \times 2 = \frac{2\Omega D^{\mathrm{l}}}{v_{\mathrm{tip}_{\mathrm{Iv}}}} \tag{3.4}$$

For the three-dimensional case, even if the composition field is different from that of two dimensions, the diffusion length takes the same formula as Eq. (3.4). Fig. 3.5 demonstrates the evolution of two-dimensional and three-dimensional diffusion length and tip radius of a dendrite tip of Al-7 wt.% Si alloy at steady state with supersaturation Ω. For $\Omega \leq 0.5$ in two dimensions and $\Omega \leq 0.3$ in three dimensions, which are satisfied by all the studies in this thesis, $\delta_{\mathrm{d}_{\mathrm{Iv}}} > \rho_{\mathrm{tip}_{\mathrm{Iv}}}$ always stands. Under the same supersaturation, the three-dimensional characteristic lengths are much smaller than the two-dimensional ones, and the ratio of $\delta_{\mathrm{d}_{\mathrm{Iv}}}$ to $\rho_{\mathrm{tip}_{\mathrm{Iv}}}$ in three dimensions is smaller than in two dimensions.
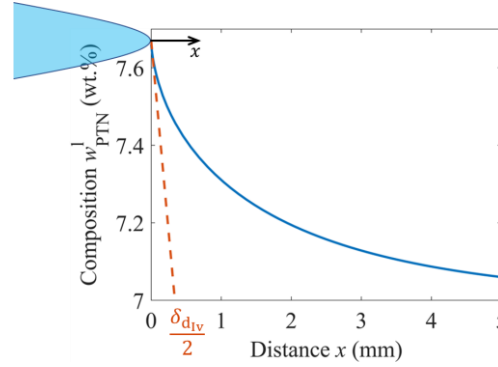
Fig. 3.4   **Two-dimensional illustration of the definition of diffusion length at steady state for Al-7 wt.% Si alloy with supersaturation $\Omega = 0.1$. The intersection of the tangent of the composition at the dendrite tip along the x axis and the nominal composition is half of its diffusion length, $\delta_{\mathrm{d}_{\mathrm{Iv}}}/2$.**
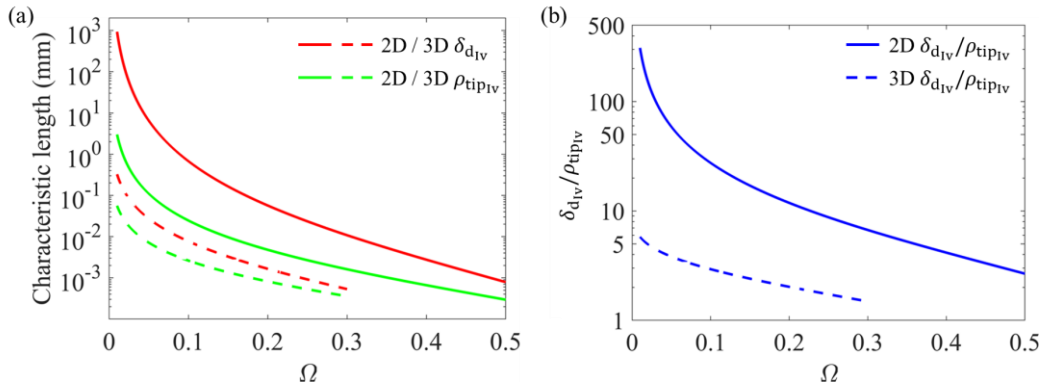
Fig. 3.5   **Evolution of two-dimensional (solid curves) and three-dimensional (dashed curves) diffusion length and tip radius of a dendrite tip of Al-7 wt.% Si alloy at steady state with supersaturation. (a) Diffusion length is in red and tip radius is in green. The characteristic length axis is in log scale. (b) shows the ratio of diffusion length and tip radius.**

3.2   Integration distance and convergence on kinetics

3.2.1   Observation of convergence limit

The influence of the integration distance a on kinetics has been investigated in [15], and a general conclusion is that the greater the integration distance is, the more accurate the kinetics is. However, in our study, it is observed that, as shown below, if the integration distance is too large, the kinetics may be divergent and not physical.

PTN simulations for Al-7 wt.% Si alloy with supersaturation $\Omega = 0.1$ have been carried out with different integration distance: $a/\delta_{d_{Iv}} \in \{0.1, 0.2, 0.5, 1, 2, 5, 20, 25, 30\}$. Fig. 3.6 illustrates the branch and integration area of (a) $a = \delta_{d_{Iv}}$, (b) $a = 5\delta_{d_{Iv}}$, and (c) $a = 25\delta_{d_{Iv}}$. Other parameters are the same as Table 2.3.
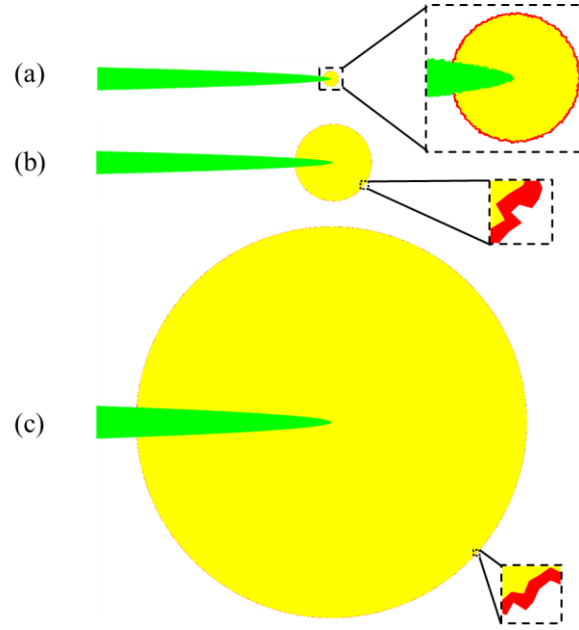
Fig. 3.6   Illustration of the dendritic branch with its integration area in PTN simulations for a single dendrite tip with integration distance (a) $a = \delta_{d_{Iv}}$, (b) $a = 5\delta_{d_{Iv}}$, (c) $a = 25\delta_{d_{Iv}}$. Branches are green, integration areas are yellow in the surface and red on the contour (to see the enlarging figures). The tiny red elements can be seen in the enlargements.

Fig. 3.7 shows the evolution of kinetics at steady state with integration distance for $a/\delta_{d_{Iv}} \leq 20$. The tip radius and velocity are normalized by the Ivantsov – Solvability solution, their standard deviations are represented by error bars, and the integration distance is normalized by the diffusion length at steady state. In this range, the kinetics keeps improving as a increases. However, for $a/\delta_{d_{Iv}} \in \{25, 30\}$ there is not any steady state for the kinetics: the kinetics becomes divergent. Fig. 3.8 demonstrates (a) the convergent kinetics of the simulation with $a = 5\delta_{d_{Iv}}$ and (b) the divergent kinetics of the simulation with $a = 25\delta_{d_{Iv}}$. In the divergent case, although the initial kinetics and composition field are the same as the theoretical steady-state solution, the tip velocity drops dramatically, then increases slightly, finally increases dramatically. This interesting phenomenon will be explained in the next subsection.
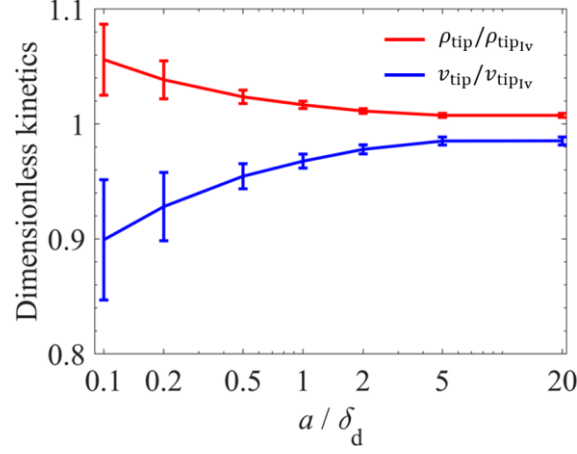
Fig. 3.7   **Evolution of dimensionless kinetics of a dendrite tip of Al-7 wt.% Si alloy in two dimensions under supersaturation $\Omega = 0.1$ with integration distance a, for $a \leq 20\delta_{d_{Iv}}$. The tip radius and velocity are normalized by the Ivantsov – Solvability solution, the error bars are their standard deviation, and the integration distance is normalized by the diffusion length at steady state. In this range, that greater the integration distance is, the more precise the kinetics is.**
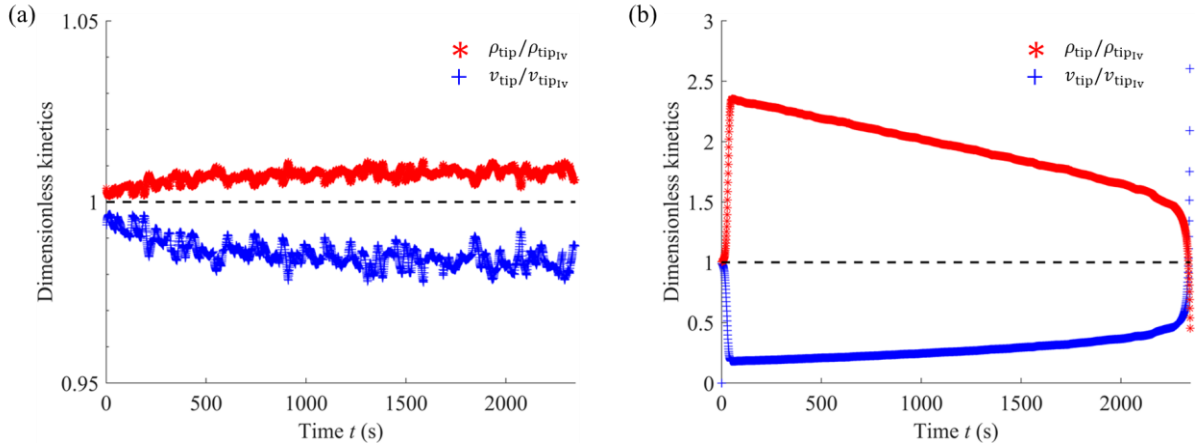
Fig. 3.8   **Dimensionless kinetics of a dendrite tip of Al-7 wt.% Si alloy in two dimensions under supersaturation $\Omega = 0.1$ with (a) $a = 5\delta_{d_{Iv}}$ and (b) $a = 25\delta_{d_{Iv}}$. Kinetics in (a) is convergent while kinetics in (b) is divergent.**

3.2.2 Theoretical explanation

The divergence of kinetics for very large integration distance can be explained by the following deduction. By combining Eq. (1.7) and Eq. (1.15), an expression of the tip velocity can be obtained

$$v_{\text{tip}} = D^{\text{l}} \left(\frac{4\sigma}{d_0} \left(-\frac{1}{(1-k)w^{\text{ls}}} \cdot \frac{1}{4\sqrt{a}} \left(\int_\Gamma \boldsymbol{\nabla} w_{\text{PTN}}^{\text{l}} \cdot \boldsymbol{n}^{\boldsymbol{\Gamma}} \mathrm{d}\Gamma + \frac{v_{\text{tip}}}{D^{\text{l}}} \iint_\Sigma \boldsymbol{e}_{\boldsymbol{x}} \cdot \boldsymbol{\nabla} w_{\text{PTN}}^{\text{l}} \, \mathrm{d}\Sigma \right) \right) \right)^4 \right)^{\frac{1}{3}} \quad (3.5)$$

To be simple, Eq. (3.5) is noted as $v_{\text{tip}} = f(v_{\text{tip}})$. This is also the explicit formula used in the current model for calculating the tip velocity of time t based on the tip velocity of time $t - \Delta t$

$$v_{\text{tip}}^t = f(v_{\text{tip}}^{t-\Delta t})$$

59

Suppose that the branch grows at steady state with velocity $v_{\text{tip}}^{\text{s}}$. Then $v_{\text{tip}}^{t} = v_{\text{tip}}^{t-\Delta t} = v_{\text{tip}}^{\text{s}}$, and $v_{\text{tip}}^{\text{s}} = f(v_{\text{tip}}^{\text{s}})$ stands. If there is a small error Δv^{R} on the velocity on the right-hand side, then there will be an error Δv^{L} on the left-hand side as well, i.e.,

$$v_{\text{tip}}^{\text{s}} + \Delta v^{\text{L}} = f(v_{\text{tip}}^{\text{s}} + \Delta v^{\text{R}}) \tag{3.6}$$

By Taylor's theorem,

$$f(v_{\text{tip}}^{\text{s}} + \Delta v^{\text{R}}) \approx f(v_{\text{tip}}^{\text{s}}) + f'(v_{\text{tip}}^{\text{s}})\Delta v^{\text{R}} \tag{3.7}$$

From Eq. (3.6) and Eq. (3.7), there is

$$f'(v_{\text{tip}}^{\text{s}}) \approx \frac{\Delta v^{\text{L}}}{\Delta v^{\text{R}}} \tag{3.8}$$

The derivative of f, i.e., the right-hand side of Eq.(3.5), at $v_{\text{tip}} = v_{\text{tip}}^{\text{s}}$ can be calculated under the assumption that all other parameters are independent with v_{tip}, so

$$f'(v_{\text{tip}}^{\text{s}}) = -\frac{\sqrt{2}}{3(1-k)w^{\text{ls}}\sqrt{a\rho_{\text{tip}}^{\text{s}}}} \iint_{\Sigma} \boldsymbol{e}_x \cdot \nabla w_{\text{PTN}}^{\text{l}} \, \mathrm{d}\Sigma \tag{3.9}$$

with $\rho_{\text{tip}}^{\text{s}}$ the tip radius at steady state. Eq. (3.9) is regarded a function of a, denoted as $C(a)$, indicating the convergence of the explicit formula.

$$C(a) = f'(v_{\text{tip}}^{\text{s}}) \approx \frac{\Delta v^{\text{L}}}{\Delta v^{\text{R}}} \tag{3.10}$$

Theoretically, if $C(a)$ is greater than 1, an error on the velocity on the right-hand side will lead to a greater error on the velocity on the left-hand side in Eq. (3.6), then the calculated velocity will go further and further away from the correct solution, meaning that this formula is divergent.

If the composition field in the liquid at steady state is equal to the Ivantsov solution (see Subsection 1.1.3), and the steady-state tip radius and velocity are just $\rho_{\text{tip}_{\text{Iv}}}$ and $v_{\text{tip}_{\text{Iv}}}$, then the integrated part of Eq. (3.9) can be calculated mathematically

$$\boldsymbol{e}_x \cdot \nabla w = \frac{\partial w}{\partial x} = \frac{\partial w}{\partial \xi}\frac{\partial \xi}{\partial x} = -\frac{(1-k)w^{\text{ls}}\text{Pe}\exp(\text{Pe})}{\rho_{\text{tip}_{\text{Iv}}}}\exp\left(-\frac{\text{Pe}\left(x+\sqrt{x^2+y^2}\right)}{\rho_{\text{tip}_{\text{Iv}}}}\right)\left(\frac{x+\sqrt{x^2+y^2}}{x^2+y^2}\right)^{\frac{1}{2}}$$

Eq. (3.9) can be converted as

$$C(a) = \frac{\sqrt{2}\,\text{Pe}\exp(\text{Pe})}{3\rho_{\text{tip}_{\text{Iv}}}\sqrt{a}}\iint_{\Sigma}\exp\left(-\frac{\text{Pe}\left(x+\sqrt{x^2+y^2}\right)}{\rho_{\text{tip}_{\text{Iv}}}}\right)\left(\frac{x+\sqrt{x^2+y^2}}{x^2+y^2}\right)^{\frac{1}{2}}\mathrm{d}x\mathrm{d}y \tag{3.11}$$

where the upper half of the integration surface can be expressed as

$$\frac{1}{2}\Sigma_{\mathrm{u}}: \begin{cases} y: 0 \to \sqrt{R_{\mathrm{integ}}^2 - \left(x - \frac{\rho_{\mathrm{tip_{Iv}}}}{2}\right)^2}, \text{for } x \in \left[\frac{\rho_{\mathrm{tip_{Iv}}}}{2}, R_{\mathrm{integ}} + \frac{\rho_{\mathrm{tip_{Iv}}}}{2}\right] \\ y: \sqrt{-2\rho_{\mathrm{tip_{Iv}}}\left(x - \frac{\rho_{\mathrm{tip_{Iv}}}}{2}\right)} \to \sqrt{R_{\mathrm{integ}}^2 - \left(x - \frac{\rho_{\mathrm{tip_{Iv}}}}{2}\right)^2}, \text{for } x \in \left[-a + \frac{\rho_{\mathrm{tip_{Iv}}}}{2}, \frac{\rho_{\mathrm{tip_{Iv}}}}{2}\right] \end{cases}$$

and the lower half of the integration surface can be expressed as

$$\frac{1}{2}\Sigma_{\mathrm{l}}: \begin{cases} y: -\sqrt{R_{\mathrm{integ}}^2 - \left(x - \frac{\rho_{\mathrm{tip_{Iv}}}}{2}\right)^2} \to 0, \text{for } x \in \left[\frac{\rho_{\mathrm{tip_{Iv}}}}{2}, R_{\mathrm{integ}} + \frac{\rho_{\mathrm{tip_{Iv}}}}{2}\right] \\ y: -\sqrt{R_{\mathrm{integ}}^2 - \left(x - \frac{\rho_{\mathrm{tip_{Iv}}}}{2}\right)^2} \to -\sqrt{-2\rho_{\mathrm{tip_{Iv}}}\left(x - \frac{\rho_{\mathrm{tip_{Iv}}}}{2}\right)}, \text{for } x \in \left[-a + \frac{\rho_{\mathrm{tip_{Iv}}}}{2}, \frac{\rho_{\mathrm{tip_{Iv}}}}{2}\right] \end{cases}$$

with $R_{\mathrm{integ}} = \sqrt{a^2 + 2\rho_{\mathrm{tip_{Iv}}}a}$. See Fig. 3.9 for illustration.
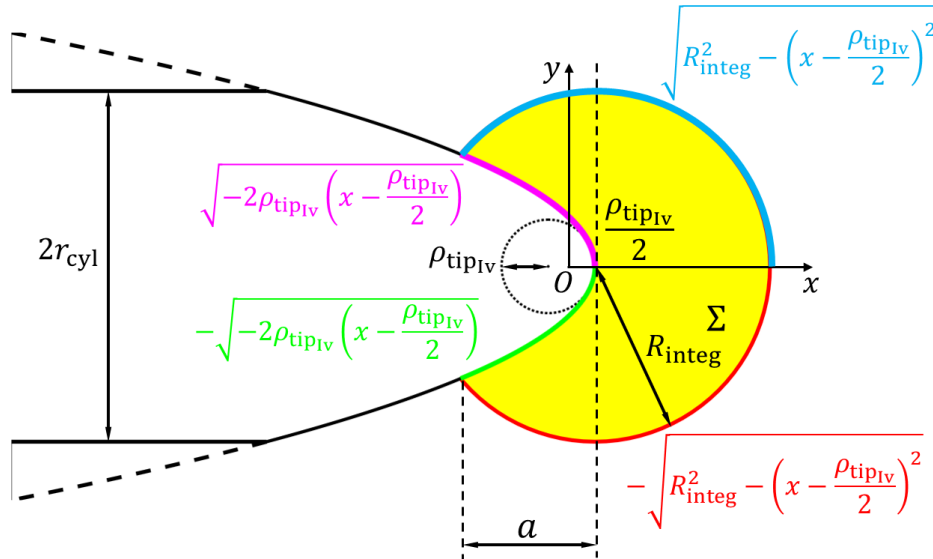
Fig. 3.9   Illustration of the integration surface Σ. The yellow integration surface is divided into upper half part and lower half part by the x axis. Tip coordinate is $\left(\frac{\rho_{\mathrm{tip_{Iv}}}}{2}, 0\right)$. Formulas correspond to the curve in the same color.

The two-dimensional curve of $C(a)$ by Eq. (3.11) for Al-7 wt.% Si alloy with $\Omega = 0.1$ is plotted in Fig. 3.10a. a is also nondimensionalized by $\delta_{\mathrm{d_{Iv}}}$. $C(a)$ increases from 0 to more than 1 with the increase of $a/\delta_{\mathrm{d_{Iv}}}$. For $a/\delta_{\mathrm{d_{Iv}}} \leq 5$, $C(a)$ is smaller than unity, the kinetics is convergent as indicated in Fig. 3.7. For $a/\delta_{\mathrm{d_{Iv}}} = 20$, even if $C(a)$ is a little greater than unity, the kinetics is also convergent. This might be because in the deduction of Eq. (3.11) the composition field is regarded as Ivantsov solution and the tip radius and tip velocity are regarded as Ivantsov – Solvability condition, but in the reality, they are not. For $a/\delta_{\mathrm{d_{Iv}}} \in \{25, 30\}$, $C(a)$ gets further from unity, so the kinetics becomes divergent.

In summary, $C(a)$ deduced from Ivantsov solution is fairly consistent with the divergence of kinetics observed in the simulations, while the criterion $C(a) < 1$ is a little bit stricter than the reality due to the strong assumption in the mathematical deduction. It can be used as an advance test on the choice of integration distance a: with $C(a) \geq 1$ there is risk of divergence on kinetics, and a might be too large.
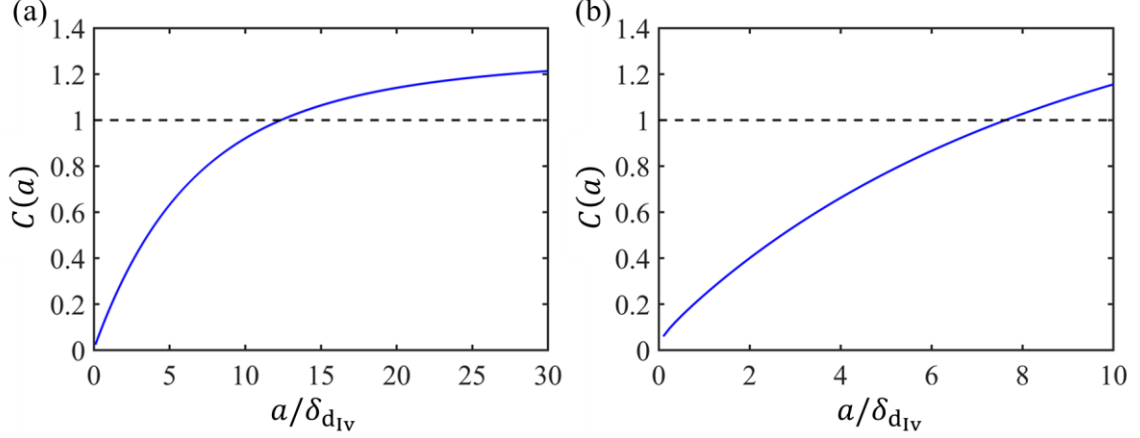
Fig. 3.10   **Evolution of the convergence of kinetics with a under Ivantsov – Solvability solution for Al-7 wt.% Si alloy with supersaturation $\Omega = 0.1$, by mathematical deduction, in (a) two dimensions and (b) three dimensions. $C(a)$ is monotonic increase with a. $C(a) > 1$ has risk of divergence.**

In terms of the three-dimensional model, the same convergence-to-divergence phenomena are observed as the integration distance a increases, and its theoretical explanation follows the same logic, except that Eq. (3.5) should match with the three-dimensional equations

$$v_{\text{tip}} = \frac{D^{\text{l}}\sigma}{d_0}\left(\frac{-1}{2\pi a(1-k)w^{\text{ls}}}\right)^2 \left(\iint_{\Gamma} \nabla w_{\text{PTN}}^{\text{l}} \cdot \boldsymbol{n}^{\Gamma} \, d\Gamma + \frac{v_{\text{tip}}}{D^{\text{l}}}\iiint_{\Sigma} \boldsymbol{e_x} \cdot \nabla w_{\text{PTN}}^{\text{l}} \, d\Sigma\right)^2 \quad (3.12)$$

It is assumed that all other parameters are independent with v_{tip} and the branch grows at steady state with velocity $v_{\text{tip}}^{\text{s}}$. $v_{\text{tip}}^{\text{s}} = f(v_{\text{tip}}^{\text{s}})$ stands. The influence of disturbance can be expressed as $v_{\text{tip}}^{\text{s}} + \Delta v^{\text{L}} = f(v_{\text{tip}}^{\text{s}} + \Delta v^{\text{R}})$. So

$$\frac{\Delta v^{\text{L}}}{\Delta v^{\text{R}}} \approx f'(v_{\text{tip}}^{\text{s}}) = C(a) = -\frac{1}{\pi a \rho_{\text{tip}}(1-k)w^{\text{ls}}}\iiint_{\Sigma} \boldsymbol{e_x} \cdot \nabla w_{\text{PTN}}^{\text{l}} \, d\Sigma \quad (3.13)$$

Suppose that the composition field in the liquid at steady state is equal to the Ivantsov solution, and the steady-state tip radius and velocity are just $\rho_{\text{tip}_{\text{Iv}}}$ and $v_{\text{tip}_{\text{Iv}}}$. Taking the three-dimensional form of Eq. (1.8) into Eq. (3.13) yields

$$C(a) = \frac{\text{Pe}\exp(\text{Pe})}{\pi a \rho_{\text{tip}_{\text{Iv}}}}\iiint_{\Sigma} \exp\left(-\frac{\text{Pe}(x + \sqrt{x^2 + r^2})}{\rho_{\text{tip}_{\text{Iv}}}}\right) \cdot \left(\sqrt{x^2 + r^2}\right)^{-\frac{1}{2}} \cdot 2\pi r \, dr \, dx \quad (3.14)$$

where the integration zone can be expressed as

$$\Sigma:\begin{cases} r:0 \to \sqrt{R_{\text{integ}}^2 - \left(x - \dfrac{\rho_{\text{tip}_{\text{Iv}}}}{2}\right)^2}, \text{for } x \in \left[\dfrac{\rho_{\text{tip}_{\text{Iv}}}}{2}, R_{\text{integ}} + \dfrac{\rho_{\text{tip}_{\text{Iv}}}}{2}\right] \\ \\ r:\sqrt{-2\rho_{\text{tip}_{\text{Iv}}}\left(x - \dfrac{\rho_{\text{tip}_{\text{Iv}}}}{2}\right)} \to \sqrt{R_{\text{integ}}^2 - \left(x - \dfrac{\rho_{\text{tip}_{\text{Iv}}}}{2}\right)^2}, \text{for } x \in \left[-a + \dfrac{\rho_{\text{tip}_{\text{Iv}}}}{2}, \dfrac{\rho_{\text{tip}_{\text{Iv}}}}{2}\right] \end{cases}$$

The curve of three-dimensional $C(a)$ for Al-7 wt.% Si alloy with $\Omega = 0.1$ is plotted in Fig. 3.10b. The same as in two dimensions, $C(a)$ increases from 0 to more than 1 with the increase of $a/\delta_{d_{\text{Iv}}}$. In our further observation of three-dimensional simulations (not shown here), the simulations with $a/\delta_{d_{\text{Iv}}} \in \{1, 2, 5, 7\}$ have convergent results, whereas the simulation with $a/\delta_{d_{\text{Iv}}} = 10$ has divergent results. This observation corresponds well to the explanation: results are convergent if $C(a) < 1$; results are divergent if $C(a) > 1$.

The evolutions of $a/\delta_{d_{\text{Iv}}}$ with Ω at $C(a) = 1$ in two-dimensional and three-dimensional models are drawn in Fig. 3.11. $a/\delta_{d_{\text{Iv}}}\big|_{C(a)=1}$ decreases with Ω, indicating that at high supersaturation the choice of a is more limited. Besides, in both two-dimensional and three-dimensional models, large integration distance means large consumption on computational resource, therefore in the real simulation it is rare to use a large integration distance. In the following simulations the choice of a guarantees the convergence of kinetics.
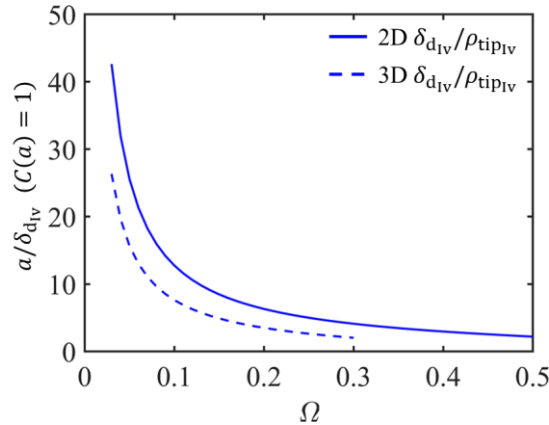
Fig. 3.11   Evolution of the value of $a/\delta_{d_{\text{Iv}}}$ with Ω at $C(a) = 1$, in two-dimensional and three-dimensional models.

3.3   Three-dimensional PTN parameters in isothermal condition

The three-dimensional PTN model has also been developed. Its parameters are to be investigated as the same way as the two-dimensional model. For this, the growth of a single dendritic branch of Al-7 wt.% Si alloy under constant temperature with supersaturation $\Omega = 0.062$ is studied. The velocity of Ivantsov – Solvability solution at this temperature is $0.02\ \text{mm/s}$, corresponding to the minimum pulling velocity in the CETSOL project experiments. Physical parameters from Ivantsov – Solvability solution are given in Table 3.1. The initial length of the branch is $15\delta_{d_{\text{Iv}}}$, long enough for any integration distance investigated. The initial composition in the liquid is the nominal composition $w_0 = 7\ \text{wt.}\%$,

leading to a long transient to arrive at its steady-state growth [1]. The simulation domain is a cube, and the branch grows from its bottom. In this section we are only interested in its steady-state kinetics that will be compared with the Ivantsov – Solvability solution, so the length of the cube must be large enough for the branch arriving at steady state: it is hereby chosen as 3 mm $\approx 160\delta_{d_{Iv}}$. The simulation time is set as 140 s. The integration distance a, the minimum mesh size $h_{\min}$, the time step Δt, and the radius of truncating cylinder r_{cyl} are the parameters investigated in this section.

Table 3.1   Physical parameters from Ivantsov – Solvability solution, for Al-7 wt.% Si alloy with supersaturation $\Omega = 0.062$.

Variable	Name	Unit	Value
Tip radius	$\rho_{tip_{Iv}}$	mm	5.27×10^{-3}
Tip velocity	$v_{tip_{Iv}}$	mm·s^{-1}	2×10^{-2}
Diffusion length	$\delta_{d_{Iv}}$	mm	1.87×10^{-2}

The integration distance is nondimensionalized by the diffusion length of a parabolic branch under Ivantsov – Solvability solution. The minimum mesh size is nondimensionalized by the tip radius of Ivantsov – Solvability solution, and the time step is nondimensionalized by the quotient of the minimum mesh size divided by the tip velocity of Ivantsov – Solvability solution, hence introducing the parameters α, γ, and τ

$$a = \frac{1}{\alpha}\delta_{d_{Iv}} \tag{3.15}$$

$$h_{\min} = \gamma\rho_{tip_{Iv}} \tag{3.16}$$

$$\Delta t = \tau\frac{h_{\min}}{v_{tip_{Iv}}} \tag{3.17}$$

For the sake of precision on kinetics, the truncating cylinder should not intersect with the integration area [14], so a minimum applicable radius of truncating cylinder at steady state r_{cyl}^{min} is defined as the distance from the intersection of the circle contour of the integration area with the parabola to the axis of the branch, under the assumption that its growth follows the Ivantsov – Solvability solution:

$$r_{cyl}^{min} = \sqrt{2a\rho_{tip_{Iv}}} \tag{3.18}$$

r_{cyl} is then nondimensionalized by r_{cyl}^{min}, hence introducing the parameter β:

$$r_{cyl} = \beta r_{cyl}^{min} \tag{3.19}$$

Simulation parameters are given in Table 3.2.

---

[1] We remind that for the above two-dimensional simulations the initial composition field was set to the Ivantsov solution.

Table 3.2   Simulation parameters of three-dimensional PTN simulation for Al-7 wt.% Si alloy with supersaturation $\Omega = 0.062$.

Variable	Name	Unit	Value
Minimum PTN mesh size	$h_{\min}$	$\rho_{\text{tip}_{\text{Iv}}}$	γ
PTN mesh size in TA1	h_1	$h_{\min}$	2
PTN mesh size in TA2	h_2	$h_{\min}$	5
PTN mesh size in solid	h_{solid}	$h_{\min}$	5
Maximum PTN mesh size	$h_{\max}$	$h_{\min}$	20
Integration distance (Eq. (3.4) for $\delta_{\text{d}_{\text{Iv}}}$)	a	$\delta_{\text{d}_{\text{Iv}}}$	$1/\alpha$
Radius of truncating cylinder (Eq. (3.18) for $r_{\text{cyl}}^{\min}$)	r_{cyl}	$r_{\text{cyl}}^{\min}$	β
Time step	Δt	$h_{\min}/v_{\text{tip}_{\text{Iv}}}$	τ
Distance from the tip to the center of the box with $h_{\min}$ at its creation	l	$\delta_{\text{d}_{\text{Iv}}}$	10
Distance from the tip to the end of the box with $h_{\min}$ at its creation	l_{b}	a	1.2
Half height of the rectangle with $h_{\min}$ (Eq. (2.2) for $R_{\text{integ}}^{\text{c}}$)	H	$R_{\text{integ}}^{\text{c}}$	1.5
Distance passed by the tip between two *Remeshings*	l_{R}	l	1.6
TA1 thickness	e_1	l	1
TA2 thickness	e_2	l	1

3.3.1   Three-dimensional PTN simulation results and computational time

The dendrite tip radius and tip velocity of the simulation with parameters $\alpha = 1/3$, $\gamma = 0.5$, $\tau = 0.5$, and $\beta = \infty$ (the branch is not truncated by the cylinder), normalized by the Ivantsov – Solvability solution, are shown in Fig. 3.12, where the kinetics is plotted every 10 time steps. At the first time step, the tip is given radius and velocity of Ivantsov – Solvability solution for initialization, so the normalized kinetics is unity. In the following time steps its kinetics is calculated by the PTN method. At the beginning its growth is unsteady: large composition gradient near the solid/liquid interface in the vicinity of the tip yields large solute flux, so the tip velocity is large and tip radius is small. The growth closely approaches steady state gradually. At the end of simulation, the tip is near the boundary, which has considerable effect on the composition field in liquid in the vicinity of the tip, so the tip velocity gets smaller and the tip radius gets greater. There is fluctuation on the kinetics for numerical reasons. The dotted vertical lines are the moments when *Remeshing* occurs, and there is tiny extra fluctuation at these *Remeshing* moments. Since the evolution of kinetics is smooth overall, the tiny extra fluctuation is considered acceptable, as well as the current *Remeshing* strategy.

The composition field on the cross section at $(1.5\ \text{mm}, 1.5\ \text{mm}, 1.5\ \text{mm})$ with $+x$ direction, in the above-mentioned simulation at $t = 100\ \text{s}$, is depicted by wireframe in Fig. 3.13a. Dirichlet condition is imposed to all nodes belonging to the paraboloid. Finer meshes are employed near the tip. Fig. 3.13b is an enlargement of the meshes in the rectangle with black dashed edges, where the branch (in green) and the integration area (in yellow and red)

are overlapped. The integration area locates in the fine-mesh box with minimum mesh size $h_{\min}$. The meshes for transitional areas, solid, and liquid can be easily identified. It demonstrates the aptness of the improved meshing strategy for three-dimensional PTN model.
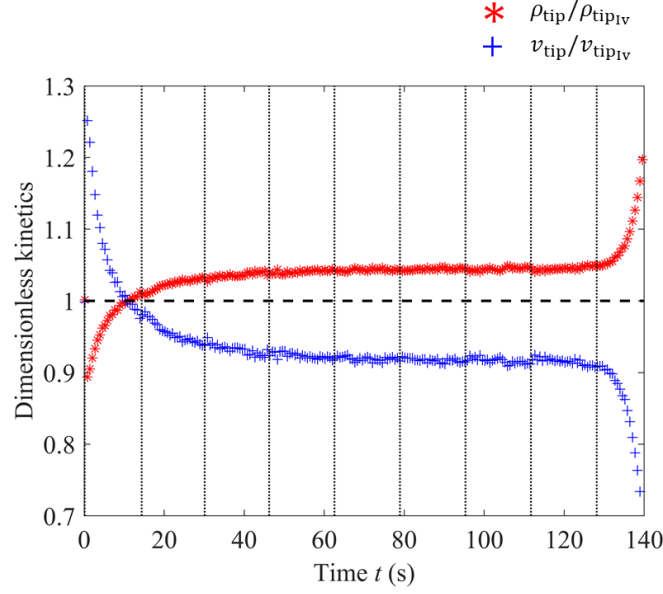
Fig. 3.12   **Evolution of normalized tip radius and tip velocity for the three-dimensional PTN simulation of Al-7 wt.% Si alloy with supersaturation $\Omega = 0.062$, with parameters $\alpha = 1/3, \gamma = 0.5, \tau = 0.5$, and $\beta = \infty$. Vertical dotted lines are the moments when the mesh is reconstructed. The kinetics is plotted every 10 time steps.**
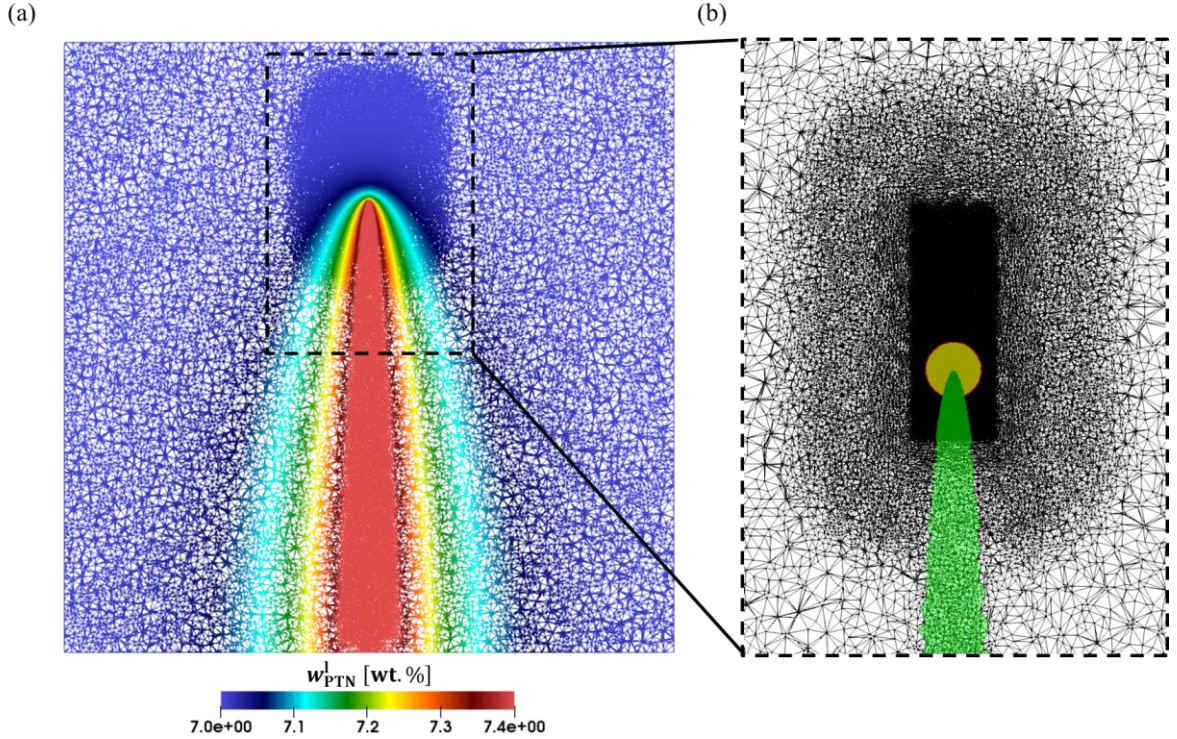
Fig. 3.13   **Simulation outputs at $t = 100$ s on the cross section at $(1.5\ mm, 1.5\ mm, 1.5\ mm)$ with $+x$ direction, for three-dimensional PTN simulation of a single dendritic branch of Al-7 wt.% Si alloy with supersaturation $\Omega = 0.062$, with parameters $\alpha = 1/3, \gamma = 0.5, \tau = 0.5$, and $\beta = \infty$. (a) is the composition field. (b) is an enlargement of the meshes in the rectangle with black dashed edges in (a). The branch (in green) and the integration area (in yellow and red) are overlapped.**

The accumulated computational time of each PTN module of this simulation, launched on 32 CPU cores, is plotted by curves in Fig. 3.14. The total computational time of the five modules is 57730 s. *Remeshing* consumes 88% of the total computational time, *Resolution of Solute Diffusion* consumes 10% of the total computational time, *Calculation of Tip Radius and Velocity* and *Dirichlet Condition* both consume 1% of the total computational time, and *Growth of Parabola* hardly consumes computational time. This is the same conclusion as the two-dimensional PTN model.
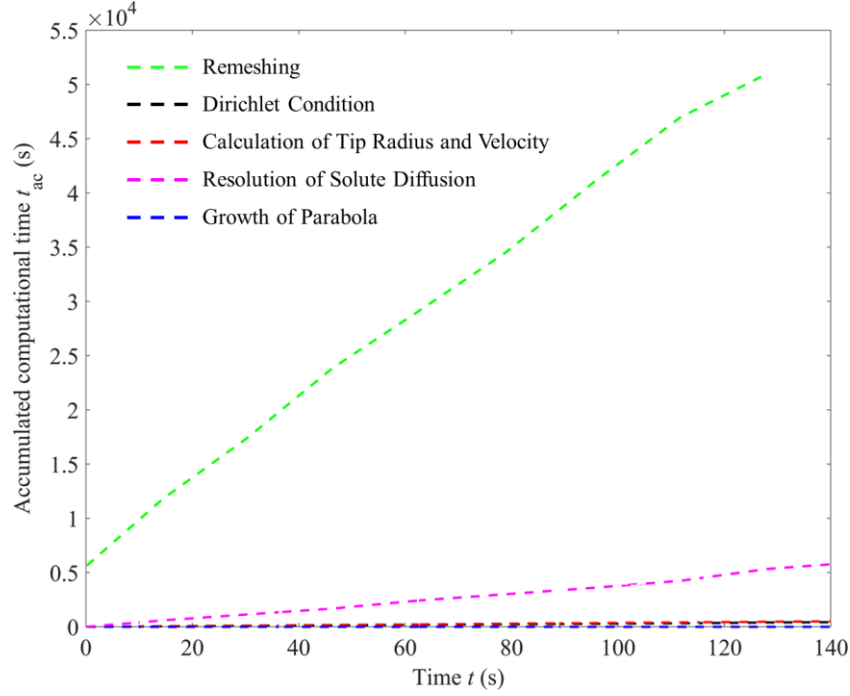
Fig. 3.14   **Accumulated computational time of each PTN module in the three-dimensional PTN simulation mentioned in Subsection 3.3.1, launched on 32 CPU cores. *Remeshing* consumes most of the computational time.**

3.3.2   Influence of the integration distance and minimum mesh size

In a first part, the integration distance a and the minimum mesh size $h_{\min}$ are studied. The branch is not truncated by the cylinder, i.e., $\beta = \infty$. The dimensionless time step is fixed as $\tau = 0.5$. Since three-dimensional simulation consumes lots of computational resource, the investigating ranges of α and γ are not as large as two-dimensional ones, but they are still sufficient to reveal their influence. Two series of simulations are launched on 32 CPU cores. For Series I, $\gamma = 0.5$, and for Series II, $\gamma = 1$. Their parameters, computational time, and number of elements at $t = 100$ s are listed in Table 3.3. The Series I, $\gamma = 0.5$, $\alpha = 1/3$ is the simulation discussed in Subsection 3.3.1, but its computational time in the Table 3.3, 1086 minutes, is larger than the sum of the accumulated computational time of the five PTN modules in Fig. 3.14 because the computational time listed in the Table 3.3 includes other modules of the simulation such as loading and partitioning of the mesh.

Kinetics closely approaches steady state between 60 s and 100 s for all the simulations reported in Table 3.3. The mean value and standard deviation of $\rho_{\text{tip}}/\rho_{\text{tip}_{\text{Iv}}}$ and $v_{\text{tip}}/v_{\text{tip}_{\text{Iv}}}$ in this period are computed for all the simulations, and they are plotted in Fig. 3.15 as solid

curves for Series I and dashed curves for Series II. The same conclusion as the study of two-dimensional model [14] is obtained: larger integration distance and smaller minimum mesh size will bring steady-state results closer to Ivantsov – Solvability solution and smaller fluctuation, with higher computational cost. One should note that the difference between the steady-state kinetics and the Ivantsov – Solvability solution is larger in three dimensions than in two dimensions. For example, the two-dimensional steady-state velocity with $\alpha = 1$ and $\gamma = 1$ is about $94\%v_{\text{tip}_{\text{Iv}}}$ [15], whereas the three-dimensional steady-state velocity with $\alpha = 1$ and $\gamma = 1$ is about $77\%v_{\text{tip}_{\text{Iv}}}$. This may be because that the ratio $\delta_{\text{d}_{\text{Iv}}}/\rho_{\text{tip}_{\text{Iv}}}$ is smaller in three dimensions than in two dimensions, as shown in Fig. 3.5. Since $h_{\min} = \rho_{\text{tip}_{\text{Iv}}}$, the composition field is worse described by the mesh in three dimensions.

Table 3.3   **Parameters (various α and γ, with $\tau = 0.5$ and $\beta = \infty$), computational time, and number of elements at $t = 100$ s for three-dimensional PTN simulation of a single dendritic branch of Al-7 wt.% Si alloy with supersaturation $\Omega = 0.062$. These simulations are run on 32 CPU cores.**

Series	Parameters		Computational time (min)	Number of elements
	γ	α		
		1/5	3052	2.62×10^7
		1/3	1086	1.07×10^7
I	0.5	1/2	499	6.42×10^6
		1	305	3.95×10^6
		2	174	3.17×10^6
		1/7	492	6.41×10^6
		1/5	212	3.10×10^6
II	1	1/3	79	1.25×10^6
		1/2	52	7.33×10^5
		1	36	4.23×10^5

It has to be noted that although Series I and II have the same dimensionless time step τ, they do not have the same time step. Since the minimum mesh size of Series II is twice of the minimum mesh size of Series I, according to the definition of τ, the time step of Series II is also twice of the time step of Series I. For the same simulation time, Series I have twice loop numbers than Series II. Nevertheless, the times of *Remeshing* are the same because *Remeshing* does not depend on loop numbers, and its computational time almost determines the total computational time, it is therefore reasonable to compare the total computational time of the two series.

Since both increasing the integration distance a and decreasing the minimum mesh size $h_{\min}$ are able to improve the precision on kinetics, it is interesting to compare their consumption on computational resources. From the steady-state kinetics depicted in Fig. 3.15, and information in Table 3.3, Series I with $\alpha = 1$ and Series II with $\alpha = 1/5$ have very similar steady-state kinetics, whereas the former consumes more computational resources;

Series I with $\alpha = 1/2$ and Series II with $\alpha = 1/7$ consumes similar computational resources, whereas the former has better kinetics. There is not a universal conclusion on this subject. However, it is clear that even for a single dendritic branch, the three-dimensional PTN simulation can be resource-costing. A trade-off between accuracy and computational cost must be considered for three-dimensional CAPTN simulations with many dendritic branches, as shown in Chapter 4.

Fig. 3.15   **Steady-state dimensionless kinetics of three-dimensional PTN simulations of a single dendritic branch of Al-7 wt.% Si alloy with supersaturation $\Omega = 0.062$, with different integration distance and minimum mesh size. The α axis is in log scale. There are two series of simulations: Series I represented by solid curves for $\gamma = 0.5$ and Series II represented by dashed curves for $\gamma = 1$. Error bars represent their standard deviations.**

3.3.3   Influence of the time step

Simulations with different time steps, $\alpha = 1/3$, $\beta = \infty$, $\gamma = 0.5$, $\tau \in \{0.5, 1, 2, 10, 50\}$ are launched for investigating the influence of time step. Their steady-state kinetics are plotted in Fig. 3.16.

Fig. 3.16   **Steady-state dimensionless kinetics of three-dimensional PTN simulations of a single dendritic branch of Al-7 wt.% Si alloy with supersaturation $\Omega = 0.062$, with different time step. Error bars represent their standard deviations.**

The time step has very small influence on the steady-state kinetics. This is because at steady state, the composition field remains stable in the parabolic frame of dendrite, and in the PTN algorithm (Fig. 2.2) the composition field is solved before calculating dendritic kinetics. However, the tip velocity increases and tip radius decreases slightly with the time step, indicating that the composition fields under different time steps have small difference with each other. Moreover, for describing the dendritic growth at unsteady state, the time step should be small enough for good temporal discretization.

3.3.4   Influence of the radius of truncating cylinder

Using a cylinder for truncating the parabolic branch permits to avoid the branches with non-physical thickness, and in the simulations of solidification, the employment of the truncating cylinder is indispensable [14]. It is therefore important to study the influence of the radius of truncating cylinder r_{cyl} on kinetics for the following developments. This kind of study has been done in two dimensions [14], so now we focus on three dimensions.

The previous simulation with parameters $\alpha = \frac{1}{3}$, $\gamma = 0.5$, and $\tau = 0.5$ is reused for studying the influence of the radius of truncating cylinder, whereas the radius of truncating cylinder is imposed as $\beta = 0.5$, 2.0, and 5.0, respectively. Fig. 3.17 shows the relation of truncating cylinder and integration area at steady state in the simulation with (a) $\beta = 0.5$ and (b) $\beta = 2$. At steady state, if $\beta < 1$, the truncating cylinder will intersect with the integration area.
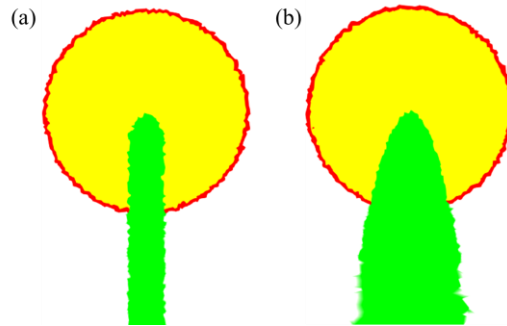
Fig. 3.17   Simulation outputs of (a) $\beta = 0.5$ and (b) $\beta = 2$ at steady state. Dendritic branches are in green, integration areas are in yellow and red. For $\beta < 1$, the truncating cylinder intersects with its integration area.

Their steady-state kinetics are depicted in Fig. 3.18 with error bars representing standard deviations. $\beta = \infty$ means there is no truncating cylinder. Same as two-dimensional cases, $\beta < 1$ yields bad calculation on kinetics and $\beta > 1$ hardly influences the dendritic kinetics. However, even though $\beta > 1$, the composition Dirichlet condition changes with β, so the composition field may have small change. This explains the small difference on kinetics between $\beta = 2$, 5, and ∞. In the following simulations, $r_{cyl} = 2r_{cyl}^{min}$ is chosen.
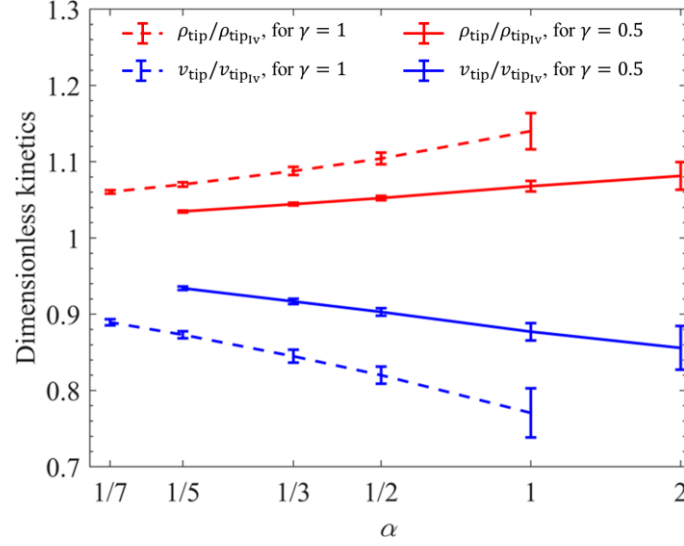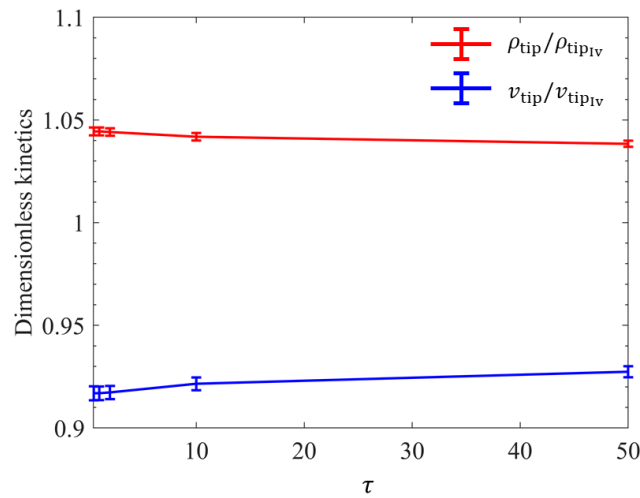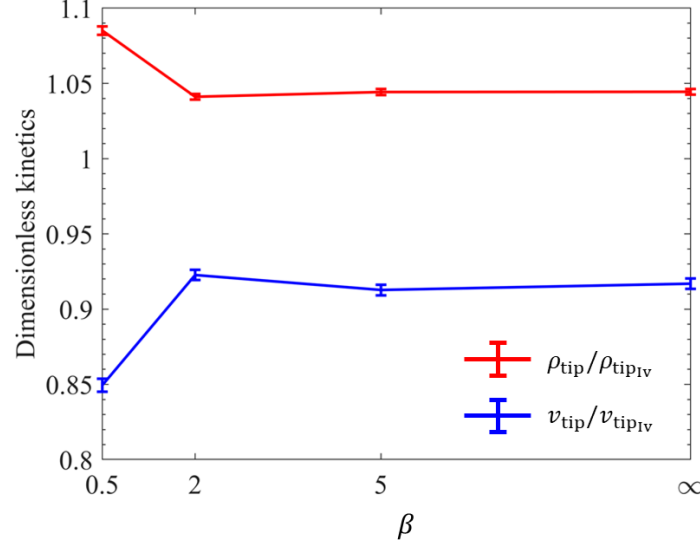
Fig. 3.18   Steady-state dimensionless kinetics of three-dimensional PTN simulations of a single dendritic branch of Al-7 wt.% Si alloy with supersaturation $\Omega = 0.062$, with different radius of truncating cylinder. β axis is in log scale. $\beta = \infty$ means there is no truncating cylinder. Error bars represent their standard deviations.

3.4   Conclusion

This chapter was dedicated to the parametric study of the PTN model. The kinetics calculated by the improved algorithm has been compared with the kinetics calculated by the original algorithm in two dimensions. They are almost the same, attesting that the improved algorithm does not influence the kinetics. Thus, the parametric study of two-dimensional PTN model [14] is valid to the improved algorithm as well. The diffusion length of a dendritic branch under Ivantsov solution has been defined. It is used for nondimensionalizing the integration distance and the dimension of the fine-mesh box in the rest of this thesis. It is observed that when the integration distance is too large the kinetics will be divergent. This phenomenon has been explained by mathematical deduction. For the three-dimensional PTN model, parametric studies on integration distance, minimum mesh size, time step, and radius of truncating cylinder have been carried out. These studies are equivalent to the two-dimensional parametric studies [14], and the conclusion is similar to that of two-dimensional model: in certain range, larger integration distance and smaller minimum mesh size improve the kinetics precision, time step has tiny influence on steady-state kinetics, and the truncating cylinder should not intersect with the integration area. These studies are important reference for parameters in the following studies.

Chapter 4   Improvements and evaluations of the CAPTN model

Résumé en français

    La première implémentation du modèle CAPTN a été faite avant cette thèse. Des améliorations algorithmiques ont été réalisées au cours de cette thèse. Ces améliorations permettent de choisir une loi de croissance de la pointe appropriée en fonction de la longueur de la branche physique, d'éliminer les branches tertiaires superposant sa branche primaire, d'activer un pourcentage de branches latérales, d'imposer une condition de Dirichlet de la composition en fonction de la température locale du nœud, et d'appliquer la stratégie de maillage adaptatif hétérogène pour la méthode PTN. Toutes ces améliorations sont valables en deux dimensions et trois dimensions. Le modèle tridimensionnel CAPTN est évalué en modélisant un grain équiaxe croissant à une sursaturation constante. La cinétique obtenue par ce modèle est en bon accord avec celle obtenue par le modèle PF (Phase-Field) et le modèle DNN (Dendritic Needle Network). En particulier, pour un domaine de simulation de même taille, le modèle CAPTN prend moins de temps que le modèle DNN.

Since the PTN method is developed to describe dendritic growth and the Cellular Automaton (CA) method aims at modeling grain structures and can be coupled with large scale solution for heat and mass transfers, their complementary advantages have motivated their coupling in the so-called Cellular Automaton – Parabolic Thick Needle (CAPTN) method. This coupling was firstly proposed by Fleurisson in his thesis [14]. Section 4.1 is a recall of it. Section 4.2 and 4.3 will focus on the adaptations of the CA and PTN methods for building the CAPTN method. Then the validation of the three-dimensional method will be presented in Sections 4.4 and 4.5.

4.1   Review on the coupling of the PTN and the CA methods

4.1.1   The CA method adapted to the PTN coupling

In the CA method, dendritic grains are approximated as orthodiagonal quadrilaterals in two dimensions or orthodiagonal octahedrons in three dimensions, called envelopes, at the scale of automaton cells (see Fig. 4.1).
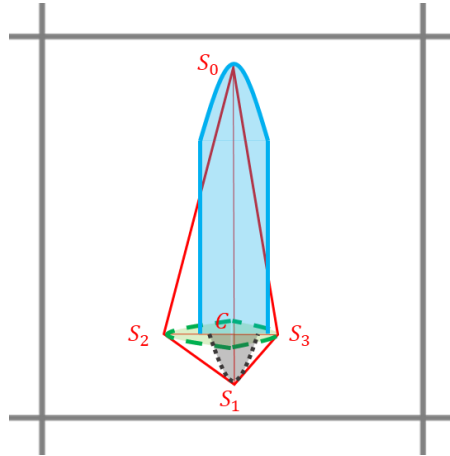
Fig. 4.1   Illustration of the principle of the CAPTN method. The red orthodiagonal quadrilateral is the envelope associated to the square edge CA cell. Its center is denoted as C, and its four apices are denoted as S_0, S_1, S_2, and S_3. Suppose it is created by upward capture. CS_0 is its principal branch, CS_1 is its opposite branch, and CS_2 and CS_3 are its side branches. The principal branch associates a truncated parabola in blue. The opposite branch has a gray parabola but never grows. Side branches have green parabolas.

For an envelope associated to a CA cell, its center C and apices $S_i, i \in [0, 3]$ consist of the principal growing directions of the grain. The segments between the center and the apex $CS_i, i \in [0, 3]$ are called envelope branches. The orientations of the branches correspond to the crystallographic directions $\langle 1\ 0 \rangle$. Grain growth is thus modeled by the growth of envelope branches that eventually capture neighboring cells. In the classical CA method, a CA cell in the liquid state will be captured if its cell center is contained within an envelope (mentioned in Subsection 1.2.5). In the CAPTN method, however, this rule has been adjusted. Many parabolas are not created (for example, the branches towards the solid do not associate parabolas. This will be mentioned in Subsection 4.1.2), therefore the envelope will not grow in all directions. It will be impossible to contain the centers of all its adjacent cells in the liquid state within the envelope. Moreover, with the strong solute interaction added by the

PTN method, the advance of the apices in the adjacent cells may be more constrained, such as the secondary branches with slower growth. To limit these problems, the capture is facilitated: in the two-dimensional CAPTN model, a CA cell in liquid state will be captured if its circumscribed circle is intersected by the envelope. The capture method is illustrated in Fig. 4.2. In Fig. 4.2a, a red envelope associated to the red cell grows. Other white cells are in liquid state. As it grows, the envelope will intersect with the blue circle that circumscribes the blue cell located above the red cell (Fig. 4.2b). The blue cell is then captured, inducing the creation of its own envelope with the same orientation of the branches as the capturing envelope. Then the two envelopes continue to grow (Fig. 4.2b). Later, the red envelope also reaches the green circle, hence capturing the green cell located on its right, and a similar state change of the green cell and initialization of a green envelope take place (Fig. 4.2c). A CA cell can be captured only once. Even later the blue envelope enters into the green circle but will not capture the green cell again.
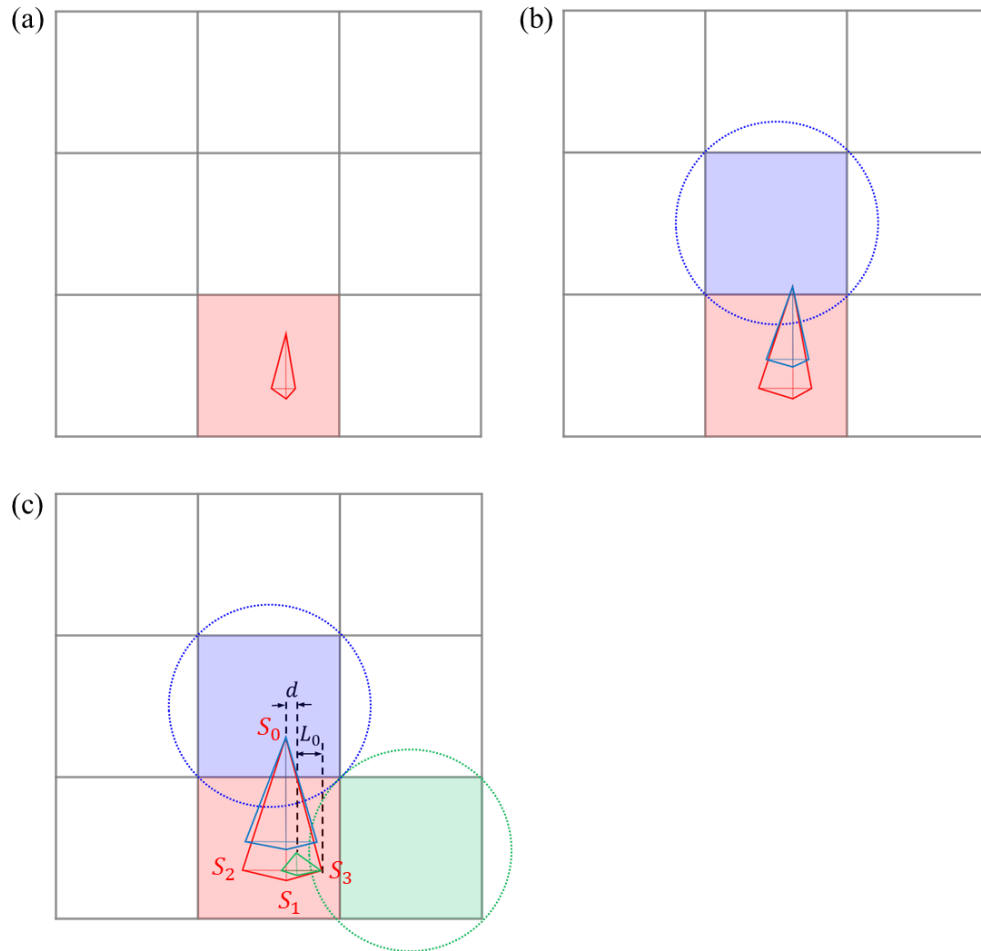
Fig. 4.2   **Illustration of the capture algorithm, the state change, and the selection of side branches in the CAPTN method. Cells in colors are in mushy state, and cells in white are in liquid state. (a) At the beginning the red cell in mushy state has its envelope drawn in red. (b) The red envelope grows and intersect with the blue circle, so the blue cell is captured, inducing the blue envelope. (c) The red and blue envelopes continue to grow. The red envelope first reaches the green circle, therefore the green cell is captured by it. The four envelope branches of the red envelope are named from S_0 to S_3. S_0 and S_3 are the capturing branches for the blue and green envelope, respectively. The distance between the upward branch of the red and green envelope is defined as d. The length of the rightward branch of the green envelope is defined as L_0.**

The way that the capturing envelope enters in the circumscribed circle permits to identify a capturing branch (S_0 for the blue envelope and S_3 for the green envelope in Fig. 4.2c), which is propagated by the new envelope. The corresponding branch of the new envelope is called "principal branch". Its opposite branch is called "opposite branch" and the other branches are called "side branches". The positions of side branches are imposed by the capture methodology. Take the green envelope in Fig. 4.2c as an example. Imagine that this is the moment when the green cell is captured and the green envelope is created. The length of its principal branch, which is the rightward branch, denoted as L_0, is equal to half of the length of the edge S_1S_3 of the red envelope [15]. One has to note that the envelope center can be out of its corresponding cell, such as the blue and green envelopes in Fig. 4.2c.

4.1.2   Branches growth velocity

The principle of the CAPTN method is to compute the growth velocity of envelope branches by using the PTN method. Fig. 4.1 is an illustration in two dimensions. This CA cell is in mushy state, so it has a growing envelope. Envelope branches are regarded as dendritic arms. Each envelope branch associates a parabola (maybe truncated, according to the thickness of the parabola, such as the upward branch in Fig. 4.1): the branch is just the axis of its parabola, and the branch and the parabola (maybe truncated) have the same length. The tip of the parabola is at the apex of the envelope. Thus, the description of the morphology of a parabola necessitates the center of the envelope, the apex of the envelope, and its tip radius.

The CA method stores all the information about envelopes, such as coordinates of centers and apices. The PTN method owns tip radius and velocity for each parabola. The envelope information is transferred to the PTN method for building parabolas on the PTN mesh for all branches growing on the CA grid. Dirichlet condition is imposed to them in order to compute the composition field in the liquid. Then the velocity of each tip is calculated from solute flux in the PTN method. This velocity returns to the CA method as the growing velocity of its corresponding apex.

For envelopes created by the capture of a cell, the principal branch is the continuity of the already existing capturing branch. As the opposite branch is towards the existing capturing branch, it cannot grow. Thus, no parabola is associated to this branch and its growth velocity is imposed to zero. The initial length of side branches is limited to the thickness of the principal branch parabola. In order to avoid perturbation of the growth of the principal branch due to the growth of side branches, the growth of the side branches is allowed only when the principal branch reaches a sufficient length. This length will be defined later in Subsection 4.2.1.

4.1.3   Deactivation of parabolas

As the grain propagates on the CA grid, the number of parabolas will become large. This will increase the complexity of computation, especially in the current PTN meshing strategy because a fine-mesh box is used for each parabola. It is certain that all these parabolas are not useful for calculation. As mentioned before, the opposite branch of an envelope is never built. Due to the facilitation on the capture, a geometric estimation of the maximum length that a

branch will definitively capture neighboring cell is selected. Branches are limited to this maximal length: if the length of a branch exceeds twice of the diagonal of the CA cell ($2\sqrt{2}l_{CA}$ in two dimensions, $2\sqrt{3}l_{CA}$ in three dimensions), this branch is stopped so no more parabola is associated to it. Moreover, once a CA cell is deallocated for all its neighboring cells are captured, its envelope information will be discarded, hence any parabola will no longer be associated with it.

4.2   Improvements on the CA method for adapting to the CAPTN method

For the coupling of the CA method and the PTN method, some basic managements on both methods have been done by Fleurisson [14]. Nevertheless, further investigations and applications showed shortcomings. The CA method is improved as follows for better adapting to the CAPTN method.

4.2.1   Activation of side branches

Let's consider the two envelopes in Fig. 4.3. The red envelope belongs to Cell μ, and its branches are named as S_0^μ, S_1^μ, S_2^μ, and S_3^μ. Each branch is associated with a parabola (maybe truncated). This envelope captured Cell ν, inducing the creation of the green envelope belonging to Cell ν. The branches of the green envelope are named as S_0^ν, S_1^ν, S_2^ν, and S_3^ν. S_0^ν and S_0^μ are defined by the same apex, and their associated parabolas have the same tip radius and tip velocity. S_1^ν is the opposite branch, so it has no associated parabola. S_2^ν and S_3^ν are side branches. They could be regarded as tertiary branches of the primary branches S_2^μ and S_3^μ. The growth of tertiary branches is allowed only when the distance from them to their primary branch is greater than $2r_{cyl}$. S_2^ν and S_3^ν will thus be eliminated if the distance from them to S_2^μ and S_3^μ, denoted as d in Fig. 4.3, is not greater than $2r_{cyl}$ (r_{cyl} is the radius of truncating cylinder). This is achieved in order to avoid that the branch along S_2^ν (or S_3^ν) will overlap the branch along S_2^μ (or S_3^μ) unphysically in the future. This is also illustrated in Fig. 4.2c.
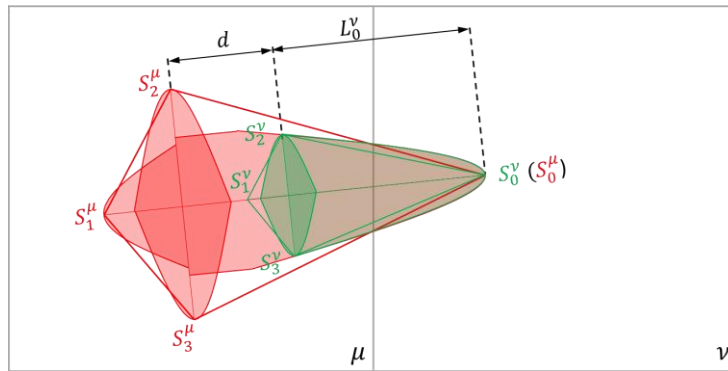
Fig. 4.3   **Illustration of two envelopes associated with parabolas in the CAPTN method. The red envelope belongs to CA Cell μ, and its apices are named as S_0^μ, S_1^μ, S_2^μ, and S_3^μ. Each branch is associated with a red parabola (maybe truncated). This envelope captured the CA Cell ν, inducing the creation of the green envelope belonging to Cell ν. The apices of the green envelope are named as S_0^ν, S_1^ν, S_2^ν, and S_3^ν. S_0^ν and S_0^μ are the same point, and their associated parabolas have the same tip radius and tip velocity. S_1^ν is the opposite branch, so it has no associated parabola. S_2^ν and S_3^ν are side branches, associating their own parabola. The distance between S_2^μ (or S_3^μ) and S_2^ν (or S_3^ν) is denoted as d. The length of S_0^ν is denoted as L_0^ν.**

Other side branches are permitted to grow with some delay after the time of capture, because on the one hand the formation of secondary branches behind the primary tip only occurs from a sufficient distance to have enough supersaturation due to the solute rejected by the primary tip [18, 57], and on the other hand this avoid hindering the growth of the principal branch. In the CAPTN model, when the length of the principal branch is greater than $3r_{\text{cyl}}$ or the maximal length (twice of the diagonal of the CA cell), side branches may start to grow. As illustrated in Fig. 4.3, the length of the principal branch of the green envelope is denoted as L_0^v. If $L_0^v > \min(3r_{\text{cyl}}, 2\sqrt{2}l_{\text{CA}})$ in two dimensions or $L_0^v > \min(3r_{\text{cyl}}, 2\sqrt{3}l_{\text{CA}})$ in three dimensions, S_2^v and S_3^v may start to grow.

It is also possible to allow only part of the side branches to grow, with the help of a random number in the current code. Each side branch is associated with a random number between 0 and 1. If its random number is smaller than a chosen threshold sb [1], then this side branch will grow when the length of its principal branch satisfies the condition; otherwise it never grows. In this way, $sb\%$ or so of the side branches will grow in the simulation. This part activation of the side branches operation saves computational resources by reducing the number of branches. This will be demonstrated in Subsection 4.4.2.

One should note that the CAPTN model does not aim at simulating the secondary dendrite arm spacing but only the primary dendrite arm spacing, so the number of secondary branches must be large enough to simulate branching.

4.2.2   Selection of growth law based on the physical length of branch

As mentioned above, the PTN method necessitates an integration area for calculating the solute flux. Thus, a branch must be at least longer than its integration distance a (currently it is a constant) to employ the PTN method as its growth law. In the CAPTN simulations there may be branches shorter than a, such as seeds or new-born side branches. To select appropriate growth law for a certain branch, a first idea is to test its length. If a branch is longer than $1.3a$, it will employ the PTN method as growth law; otherwise, it will grow following another growth law (e.g., the Ivantsov – Solvability solution).

At the beginning of this thesis, the only available length for describing a branch was the envelope branch length that is the distance from the apex to the center of the envelope. This length is however not relevant to be used for the test. Indeed, a dendritic branch may be described by several super-imposed envelope branches due to the discretization of CA cells and the capture algorithm. This is found in Fig. 4.2b when considering the upward branches. Envelopes with associated upward parabolas are illustrated in Fig. 4.4. The blue envelope was born from capture. According to the definition of envelope branch in the CAPTN method, the blue envelope has its own upward branch, called "blue branch". The upward branch of the red envelope is called "red branch". These two branches share the same tip position, the same growing direction, and the same radius. They differ by their lengths (because their roots are different). Evidently the blue branch that does not exist physically is a part of the red branch.

---

[1] $sb \in [0, 1]$, so in the following $sb\% \in [0, 100]$.

The envelope branch length of the blue branch is L_1 and the envelope branch length of the red branch is L_2. If they are used for selecting the growth law, there might be a conflict. Suppose that $L_1 > 1.3a$ and $L_2 < 1.3a$. The kinetics of the red branch will be calculated by the PTN method whereas the kinetics of the blue branch will be calculated by another law, hence the two physically same tips will have different radii and velocities!
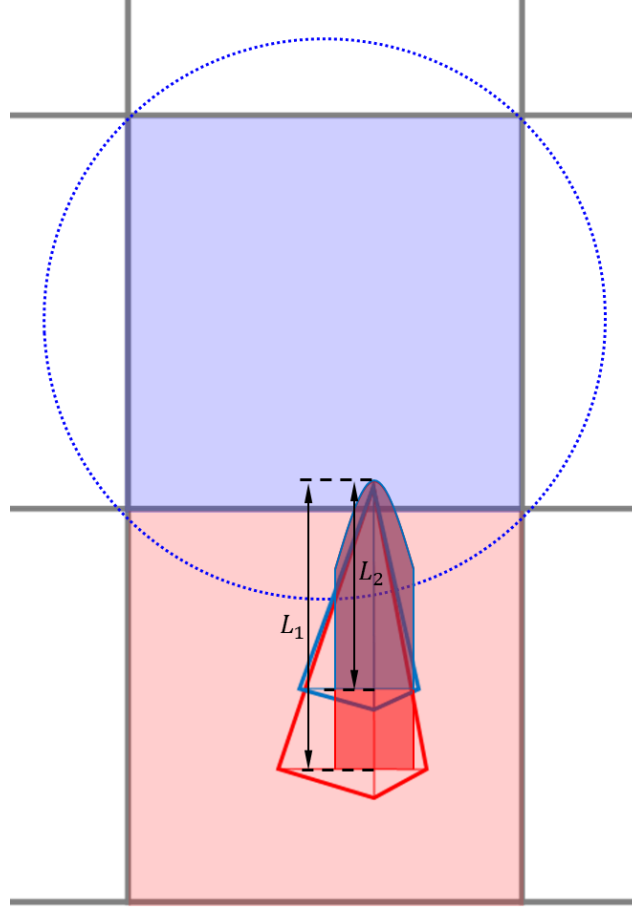
Fig. 4.4   CA envelopes from Fig. 4.2b associated with upward branches. The blue (resp. red) truncated parabola with length L_1 (resp. L_2) associates with the upward envelope branch of the blue (resp. red) envelope. They correspond to the same physical dendritic branch.

In order to reconcile this conflict, a new parameter L_{phy} is introduced. It is the physical length of a branch, i.e., the distance from the tip to the root of a physical branch. The blue branch and the red branch therefore have the same physical length L_{phy}. In Fig. 4.4, if the red envelope is a seed, then L_{phy} will just be L_1. In terms of implementation, during the capture, L_{phy} of the principal branch is inherited from that of the capturing branch.

Now the selection criterion for the PTN method can be established with the help of L_{phy}: for a dendritic branch in the CAPTN method, if $L_{\text{phy}} > 1.3a$, the PTN method will be employed as its growth law; otherwise it is a short branch and there are two cases.

- For a new seed, such as an equiaxed grain, all its branches can grow. Tip radius and tip velocity of each branch are initialized by the Ivantsov – Solvability solution (see Subsection 1.1.3) based on the CA cell temperature. Every branch keeps this tip radius

and tip velocity for growing, until their physical lengths exceed $1.3a$. Then the PTN method is employed as the growth law.

- For an envelope born from capture, when side branches start to grow, their tip radii and tip velocities are initialized by those of the principal branch at this time, and their tip positions are just at the solid/liquid interface of the principal branch. They keep this kinetics for growing until their physical lengths exceed $1.3a$, then the PTN method is used.

In both cases, once a dendritic branch starts to grow, its associated parabola will be created, and composition Dirichlet boundary condition will be imposed to the parabola. During its growth before the employment of the PTN method, the composition field in the liquid of its surroundings evolves as well, ensuring the composition field in the vicinity of the tip will be derivable when the PTN method is used for the first time.

4.3   Improvements on the PTN algorithm for adapting to the CAPTN method

The CAPTN method can be applied for modeling more complex cases than the PTN method (presented in Chapter 2 and Chapter 3), such as dendritic growth with side branches under non-uniform temperature. Non-uniform temperature field will complicate the composition Dirichlet condition on branches. More branches will challenge the remeshing strategy mentioned above that is valid for a single branch. In attempts to adapt the PTN method to the CA method for modeling these cases, its algorithms necessitate adjustments.

4.3.1   *Dirichlet Condition* using local temperature

The *Dirichlet Condition* algorithm introduced in Subsection 2.2.3 determines the solid/liquid interfacial composition by the temperature of the tip and impose it to all nodes belonging to the corresponding branch. It is suitable for CAPTN simulation under isothermal condition. For the CAPTN simulations under non-isothermal condition, this algorithm is not relevant.

A dendritic branch may contain several same-direction envelope branches due to the capture algorithm, as illustrated in Fig. 4.4. Moreover, non-growing envelopes can remain in the simulation because of the fact that all its neighboring cells are not captured. Since in the previous algorithm (Fig. 2.13) the interfacial composition is determined by the tip temperature, this yields discontinuous solid/liquid interfacial composition along the growing direction of the branch. Fig. 4.5a is the composition field of a single branch of succinonitrile-0.4 wt.% acetone under upward temperature gradient. The white grid is the CA grid, and the thicker white contour is the branch depicted by the PTN mesh. The discontinuity of composition in the solid is not physical and, as Dirichlet boundary condition, will influence the composition field in the liquid.

To solve this problem, the *Dirichlet Condition* algorithm is improved for the CAPTN method: the solid/liquid interfacial composition at each node in the solid is determined by the local temperature of the node. There is already a nodal temperature field on the PTN mesh, so this improvement does not bring in extra complicated implementation work. In addition, there

is no more need to interpolate the temperature at the tip position. The improved algorithm is explained in Fig. 4.6. Here the length of parabola j, denoted as L_j, is the length of the envelope branch. The difference with the algorithm in Fig. 2.13 starts at Line 18.

$$w^{\mathrm{l}}_{\mathrm{PTN}}\,[\mathbf{wt.}\,\%]$$
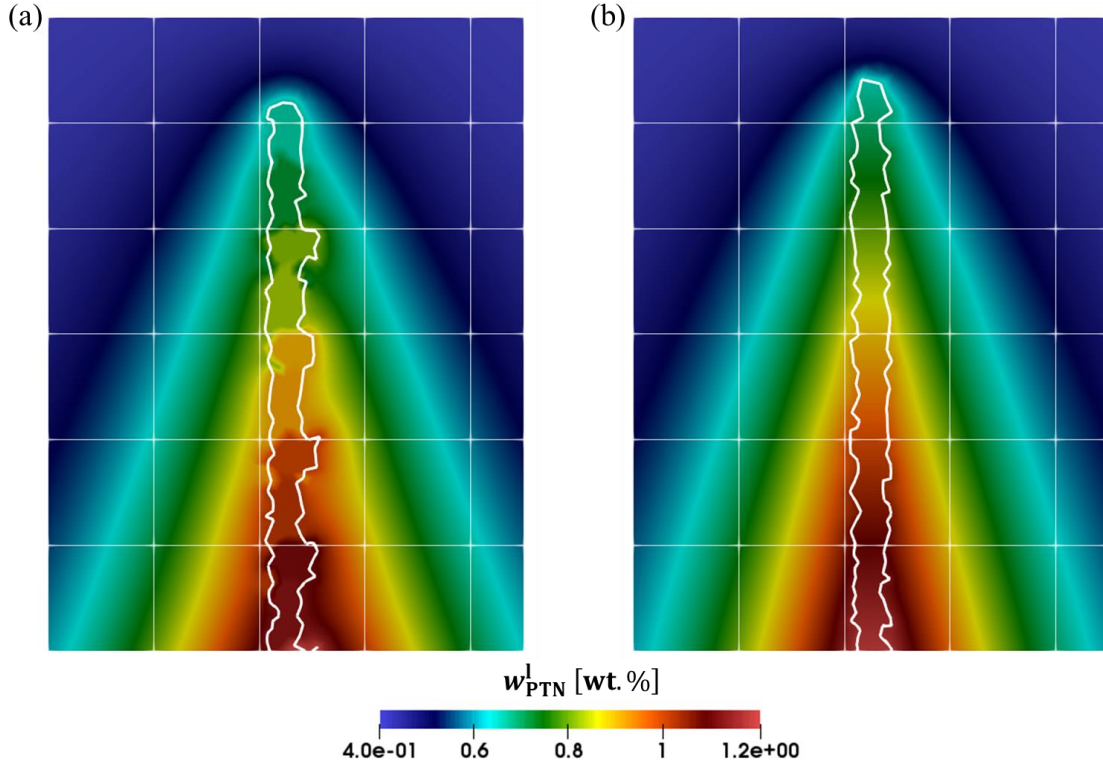
Fig. 4.5   **Composition field in the solid and liquid in a two-dimensional CAPTN simulation of a single branch of succinonitrile-0.4 wt.% acetone growing under upward temperature gradient. The white grid is the CA grid. The truncated parabola is enclosed by the thicker white contour. Its nodes are imposed to interfacial composition by (a) the previous *Dirichlet Condition* algorithm using tip temperature and (b) the new *Dirichlet Condition* algorithm using local temperature.**

Fig. 4.5b presents the composition field of the same case calculated by the new *Dirichlet Condition* algorithm. The composition field in the solid (the part enclosed by thicker white curve) is now continuous. The composition field in the liquid is better calculated.

1.   **Inputs:** T, parabolas
2.   **Outputs:** $\delta_{\in\text{parabola}}$, $w_{\text{PTN}}^{\text{ls}}$
3.   **for** each parabola j
4. $\quad F_{j\to\text{lab}}$: change of frame, from local frame to lab frame
5. $\quad$ creation of the square for orthogonal query
6. $\quad$ search of the elements intersected with the square
7. $\quad$ **for** each element i in the result of orthogonal query
8. $\quad\quad$ **if** ALL of its nodes are in the parabola:$\delta_{\in\text{parabola}} \neq 0$
9. $\quad\quad\quad$ **continue**
10. $\quad\quad$ **for** each node l of element i
11. $\quad\quad\quad$ **if** node l is in the parabola:$\delta_{\in\text{parabola}} \neq 0$
12. $\quad\quad\quad\quad$ **continue**
13. $\quad\quad\quad$ $d[l]$: distance of node l to point M
14. $\quad\quad\quad$ **if** $d[l]^2 < 2\rho_{\text{tip}_j} L_j + L_j^2/4$
15. $\quad\quad\quad\quad$ $f[l] \leftarrow y_{\text{local frame } j}^2 + 2\rho_{\text{tip}_j}\left(x_{\text{local frame } j} - L_j\right)$
16. $\quad\quad\quad\quad$ **if** $f[l] \leq 0$: node l is in the parabola j
17. $\quad\quad\quad\quad\quad$ $\delta_{\in\text{parabola}}[l] \leftarrow j + 1$
18. **for** each node l of the domain
19. $\quad$ **if** $\delta_{\in\text{parabola}}[l] > 0$
20. $\quad\quad$ $w_{\text{PTN}}^{\text{ls}}[l] \leftarrow (T[l] - T_{\text{M}})/m$

Fig. 4.6   Improved *Dirichlet Condition* algorithm using local temperature. As inputs, *T* is the nodal temperature field on the PTN mesh, and "parabolas" means the tip coordinates, root coordinates, and radius of each parabola. As outputs, $\delta_{\in\text{parabola}}$ is a nodal field identifying that nodes belong to parabolas, and $w_{\text{PTN}}^{\text{ls}}$ is the composition of nodes belonging to parabolas. From Line 18, it is different from the algorithm in Fig. 2.13 where the solid/liquid interfacial composition is computed by tip temperature: now the local temperature of nodes in the solid is involved for computing its solid/liquid interfacial composition directly. See Fig. 2.12 for schematic illustration.

4.3.2   Remeshing criteria for multi-branch dendritic grain

In the CAPTN simulation there are generally more than one dendritic branch, so the remeshing criteria for a single branch proposed in Subsection 2.2.2 must be generalized.

If a branch is created for the first time, for example a side branch is determined to grow, then the mesh near this branch will be reconstructed locally. This operation is performed by the local remeshing function equipped in the finite element library, which allows the mesh generator to act on part of the mesh. The local remeshing area is defined the same way as the fine-mesh box but with different arguments. It includes the transitional areas of this branch, so the fine-mesh box and transitional areas of this branch will be reconstructed during local remeshing.

If the radius of integration area of a branch is greater than $0.95H$ (H is the half-height of the fine-mesh box), then the local remeshing will also be applied for this branch: its fine-mesh box and transitional areas will be reconstructed based on its current position and morphology.

During the simulation, at each time step, the maximum velocity among all tips is stored as $\max(v_{tip})$. The mesh will be totally reconstructed (called total remeshing) if the accumulated distance of $\max(v_{tip})\Delta t$ since last total remeshing is greater than l_R (l_R is a parameter defined in the simulation. It is introduced in Subsection 2.2.2). This criterion is stricter than the one of the PTN method; it is adopted for the simplicity of implementation because $\max(v_{tip})$ is an already existing output. It is however less economical on computation. A potential improvement might be to introduce a variable for each branch to record the distance passed since its last local remeshing. If this distance is greater than l_R, the local remeshing around this branch will be launched.

4.4   Application of the three-dimensional CAPTN model at steady state

The first application of the three-dimensional CAPTN model aims at modeling an equiaxed dendritic Al-7 wt.% Si alloy grain growing in a melt maintained at constant temperature with supersaturation $\Omega = 0.062$ (the same thermal condition as that of a single branch in the PTN model in Section 3.3). The tip radius, tip velocity, and diffusion length of Ivantsov – Solvability condition are $\rho_{\mathrm{tip}_\mathrm{Iv}} = 5.27 \times 10^{-3}$ m, $v_{\mathrm{tip}_\mathrm{Iv}} = 2 \times 10^{-2}$ mm/s, and $\delta_{\mathrm{d}_\mathrm{Iv}} = 1.87 \times 10^{-2}$ mm, respectively. This dendritic grain has six primary branches, and may be with or without side branches. Simulations are run on 64 CPU cores. The cubic simulation domain is of 6^3 mm$^3 \approx \left(320\delta_{\mathrm{d}_\mathrm{Iv}}\right)^3$ with minimum coordinates $(0, 0, 0)$ mm and maximum coordinates $(6, 6, 6)$ mm. The simulation time is set to 100 s. The CA cell size is 0.2 mm. The CA grid is aligned with the domain and begins from $(0, 0, 0)$ mm, therefore the center of the domain, $(3, 3, 3)$ mm, is just at the corner of the CA cells. The grain with six branches of 0.02 mm $\approx 1.07\delta_{\mathrm{d}_\mathrm{Iv}}$ initial length is placed at position $(3.1, 3.1, 3.1)$ mm. The grain does not locate in the center of the domain because it should not be on the face or corner of the CA cell in this model. The initial composition in the liquid is the nominal composition $w_0 = 7$ wt. %. Other simulation parameters are listed in Table 4.1. The velocities of the primary branches at steady state are investigated. They are normalized by the Ivantsov – Solvability solution.

Table 4.1   **Simulation parameters of three-dimensional CAPTN simulation for Al-7 wt.% Si alloy equiaxed grain with supersaturation $\Omega = 0.062$.**

Variable	Name	Unit	Value
Minimum PTN mesh size	$h_{\min}$	$\rho_{\text{tip}_{\text{Iv}}}$	1 or 1.5
PTN mesh size in TA1	h_1	$h_{\min}$	2
PTN mesh size in TA2	h_2	$h_{\min}$	5
PTN mesh size in solid	h_{solid}	$h_{\min}$	5
Maximum PTN mesh size	$h_{\max}$	$h_{\min}$	20
Integration distance (Eq. (3.4) for $\delta_{d_{\text{Iv}}}$)	a	$\delta_{d_{\text{Iv}}}$	3
Radius of truncating cylinder (Eq. (3.18) for $r_{\text{cyl}}^{\min}$)	r_{cyl}	$r_{\text{cyl}}^{\min}$	2
Time step	Δt	$h_{\min}/v_{\text{tip}_{\text{Iv}}}$	1
Distance from the tip to the center of the box with $h_{\min}$ at its creation	l	$\delta_{d_{\text{Iv}}}$	10
Distance from the tip to the end of the box with $h_{\min}$ at its creation	l_{b}	a	1.2
Half height of the rectangle with $h_{\min}$ (Eq. (2.2) for $R_{\text{integ}}^{\text{c}}$)	H	$R_{\text{integ}}^{\text{c}}$	1.5
Distance passed by the tip between two *Remeshings*	l_{R}	l	1.6
TA1 thickness	e_1	l	1
TA2 thickness	e_2	l	1

4.4.1   Equiaxed grain without side branches

First only the six primary branches are allowed to grow and any other side branch does not grow, controlled by letting $sb = 0$. In this case the CA cell size does not influence the steady-state kinetics. The minimum mesh size is set equal to the tip radius of the Ivantsov – Solvability solution $h_{\min} = \rho_{\text{tip}_{\text{Iv}}}$. The orientation of the grain is defined by Euler angles. First the Euler angles are equal to $(0°, 0°, 0°)$. This simulation takes 308 minutes. Fig. 4.7a is the computed structure at $t = 100$ s. Branches are presented by red elements contained in the truncated parabola using cylinder of radius r_{cyl}. The solid part near the tips is depicted by elements with minimum mesh size $h_{\min}$. The other solid part is depicted by elements with larger mesh size h_{solid}, so its description is less precise. Captured CA cells are shown by yellow wireframe. Primary branches are denoted by their crystal directions [1 0 0], [$\bar{1}$ 0 0], [0 1 0], [0 $\bar{1}$ 0], [0 0 1], and [0 0 $\bar{1}$]. The composition field on the crystal plane (1 0 0) at the same time is shown in Fig. 4.7b by wireframe. It can be observed clearly that there is a fine-mesh box near each tip. The normalized velocities of the six primary branches are plotted in Fig. 4.8a. The six primary branches have nearly the same velocity due to the symmetry of the system. Fig. 4.8b displays the minimum and maximum velocities among the six primary branches at each time step, which are indeed the envelope of the curves in Fig. 4.8a. The black dashed line with the gray zone is the average with standard deviation of the dimensionless velocity of a single dendritic branch growing under the same condition calculated by the PTN method with the same parameters in Table 4.1, between 60 s and 100 s, corresponding to the results in Fig. 3.15.

Fig. 4.7   **(a) Three-dimensional view of dendritic microstructure and (b) composition field on the cross section for three-dimensional CAPTN simulation of an equiaxed Al-7 wt.% Si alloy grain with Euler angles $(0°, 0°, 0°)$ growing under constant temperature with supersaturation $\Omega = 0.062$, at $t = 100$ s. Simulation parameters are $\alpha = 1/3$, $\beta = 2$, $\gamma = 1$, and $\tau = 1$. In (a) the dendritic branches are presented by red elements and the captured CA cells are presented by yellow wireframe. Primary branches are denoted by crystal directions $[1\,0\,0]$, $[\bar{1}\,0\,0]$, $[0\,1\,0]$, $[0\,\bar{1}\,0]$, $[0\,0\,1]$, and $[0\,0\,\bar{1}]$. (b) is the composition field by wireframe on the crystal plane $(1\,0\,0)$.**

Fig. 4.8   **Dimensionless velocities of the six primary branches of an equiaxed Al-7 wt.% Si alloy grain with Euler angles $(0°, 0°, 0°)$ growing under constant temperature with supersaturation $\Omega = 0.062$. Simulation parameters are $\alpha = 1/3$, $\beta = 2$, $\gamma = 1$, and $\tau = 1$. (a) Velocities of six primary branches are plotted. (b) The maximum and minimum velocity of each time step among the six primary branches are plotted. The velocity between 60 s and 100 s of a single branch growing in the same condition with the same simulation parameters is also plotted: the black dashed line is its mean value and the gray zone represents its standard deviation, corresponding to the results in Fig. 3.15.**

As mentioned above, the dimensionless velocity equals unity for initialization. The initial length of branch is about $0.37a$, so its velocity remains $v_{\text{tip}_{\text{Iv}}}$ until its physical branch length L_{phy} exceeds $1.3a$. At $t = 2.75$s $L_{\text{phy}} > 1.3a$, the PTN method begins to be used. The composition field in the vicinity of a tip is influenced by other branches, so its velocity falls down. As the branches grow, the influence of other primary branches becomes weaker and

weaker. After some time the velocities tend towards steady state. The velocity between 60 s and 100 s of this six-branch CAPTN simulation is nearly the same as the velocity between 60 s and 100 s of the single-branch PTN simulation. This shows that the three-dimensional CAPTN model retrieves expected results for the growth conditions, with the same deviation from the Ivantsov – Solvability solution.

The influence of the orientation of the grain is then investigated. An equiaxed grain with a misorientation of $(20°, 20°, 20°)$ in Euler angles is modeled. Fig. 4.9a shows its branches (in red) and captured CA cells (in yellow wireframe) at $t = 100$ s. Primary branches are also denoted by crystal directions. The composition field on the crystal plane $(1\,0\,0)$ at the same time is depicted in Fig. 4.9b by wireframe. Normalized velocities of the six primary branches and their extreme values at every time step are plotted in Fig. 4.10. Compared with Fig. 4.8, there is no noticeable difference on the velocities of primary branches, demonstrating that the CAPTN model is good at computing dendritic growth of any orientation. However, the number of captured CA cells in the simulation with misorientation is greater compared with the number of captured CA cells without misorientation, as illustrated in Fig. 4.7a and Fig. 4.9a. In terms of computational time, the simulation with misorientation takes 328 minutes, only a little (6.5%) longer than the simulation without misorientation.
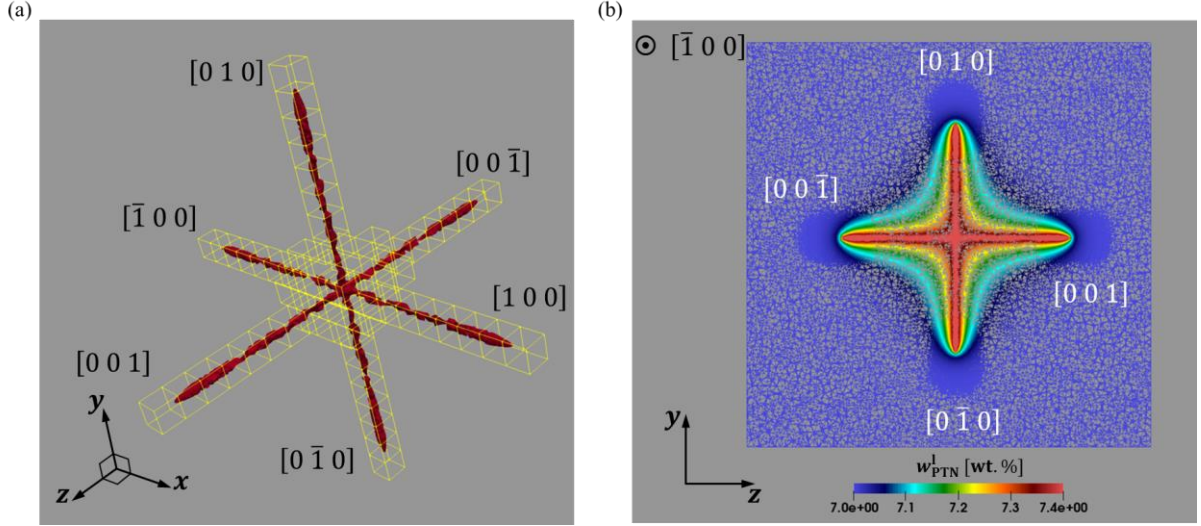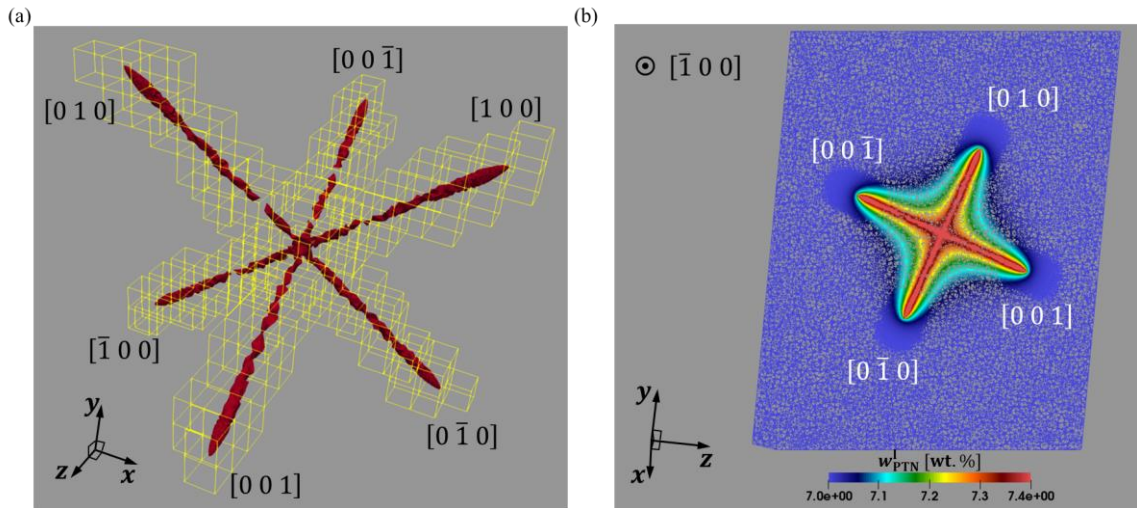

Fig. 4.9   (a) Three-dimensional view of dendritic microstructure and (b) composition field on the cross section for three-dimensional CAPTN simulation of an equiaxed Al-7 wt.% Si alloy grain with a misorientation of $(20°, 20°, 20°)$ in Euler angles growing under constant temperature with supersaturation $\Omega = 0.062$, at $t = 100$ s. Simulation parameters are $\alpha = 1/3$, $\beta = 2$, $\gamma = 1$, and $\tau = 1$. In (a) the dendritic branches are presented by red elements and the captured CA cells are presented by yellow wireframe. Primary branches are denoted by crystal directions $[1\,0\,0]$, $[\bar{1}\,0\,0]$, $[0\,1\,0]$, $[0\,\bar{1}\,0]$, $[0\,0\,1]$, and $[0\,0\,\bar{1}]$. (b) is the composition field by wireframe on the crystal plane $(1\,0\,0)$.
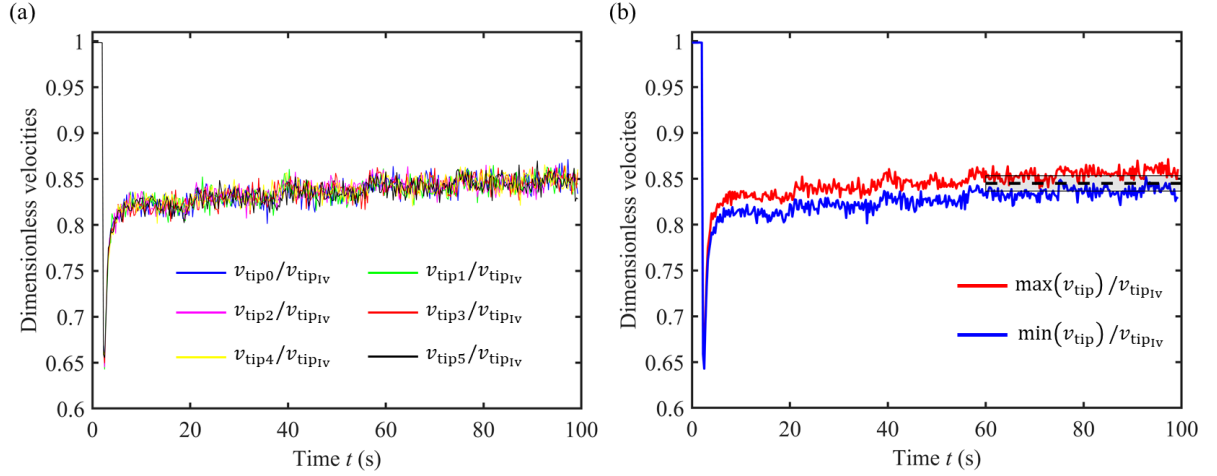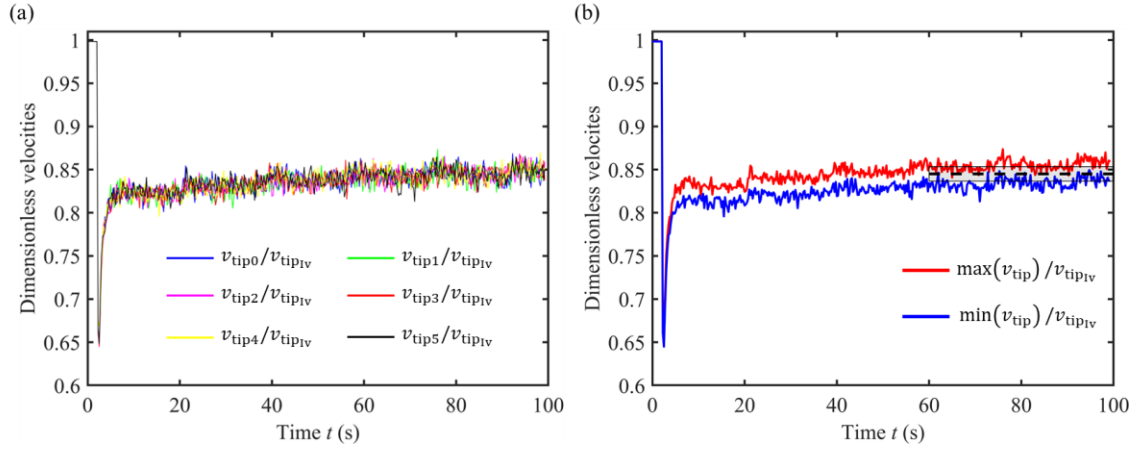
Fig. 4.10   **Dimensionless velocities of primary branches of an equiaxed Al-7 wt.% Si alloy grain with a misorientation of $(20°, 20°, 20°)$ in Euler angles with cellular grids growing under constant temperature with supersaturation $\Omega = 0.062$. Simulation parameters are $\alpha = 1/3$, $\beta = 2$, $\gamma = 1$, and $\tau = 1$. (a) Velocities of six primary branches are plotted. (b) The maximum and minimum velocity of each time step among the six primary branches are plotted. The velocity between 60 s and 100 s of a single branch growing in the same condition with the same simulation parameters is also plotted: the black dashed line is its mean value and the gray zone represents its standard deviation, corresponding to the results in Fig. 3.15.**

4.4.2   Equiaxed grain growth with side branches

In this part, the simulation of an equiaxed dendritic Al-7 wt.% Si alloy grain growing with supersaturation $\Omega = 0.062$ presented previously in Subsection 4.4.1 is retaken but the growth of side branches is allowed. The minimum mesh size is set to $1.5\rho_{\text{tip}_{\text{Iv}}}$ for the sake of a trade-off between precision and consumption of computational resource. The percentage of activated side branches is set to $sb\% \in \{0\%, 20\%, 50\%, 100\%\}$.

The dendritic microstructure and the composition field on the crystal plane $(1\ 0\ 0)$ at $t = 100$ s are exhibited in Fig. 4.11 and Fig. 4.12, respectively. When no side branch is activated, i.e., $sb\% = 0\%$, as shown in Fig. 4.11a, the branches are not fully depicted by red elements. Compared to Fig. 4.7a, part of the primary branches is vanished because larger mesh size is used. This effect can be also seen in Fig. 4.12a. The solid part near the tips is well depicted, guaranteeing the calculation of kinetics. When more side branches are activated, the description of branches becomes better, and more CA cells are captured (yellow wireframe in Fig. 4.11). When all side branches are activated, i.e., $sb\% = 100\%$, there is discontinuity of description of branches by red elements in the center of the grain in Fig. 4.11d. This is due to the deallocation of CA cells. Fig. 4.13 is the two-dimensional view of CA cells on the crystal plane $(1\ 0\ 0)$ at $t = 100$ s. Blue CA cells are in liquid state. Red CA cells are in mushy state. White CA cells are in solid state and deallocated since all their neighboring cells are captured by other branches and in mushy or solid state. One should note that the three-dimensional Moore neighborhood (see Subsection 1.2.5) is applied for deallocation. In the two-dimensional view it seems that some red cells should be deallocated, but all their neighboring cells are not captured in the three-dimensional view.

The computational time and number of elements at $t = 100\,\text{s}$ for simulations with different $sb\%$ are listed in Table 4.2. The requiring computational resources increase with the number of activated side branches.

Table 4.2   **Computational time and number of elements at $t = 100\,\text{s}$ for three-dimensional CAPTN simulation of an equiaxed Al-7 wt.% Si alloy grain along cellular grids growing under constant temperature with supersaturation $\Omega = 0.062$, with different percentage of side branches activated ($sb\%$). Simulations are run on 64 CPU cores.**

$sb\%$	Computational time (min)	Number of elements
0%	91	2.20×10^6
20%	1470	2.07×10^7
50%	3995	3.30×10^7
100%	5064	5.76×10^7
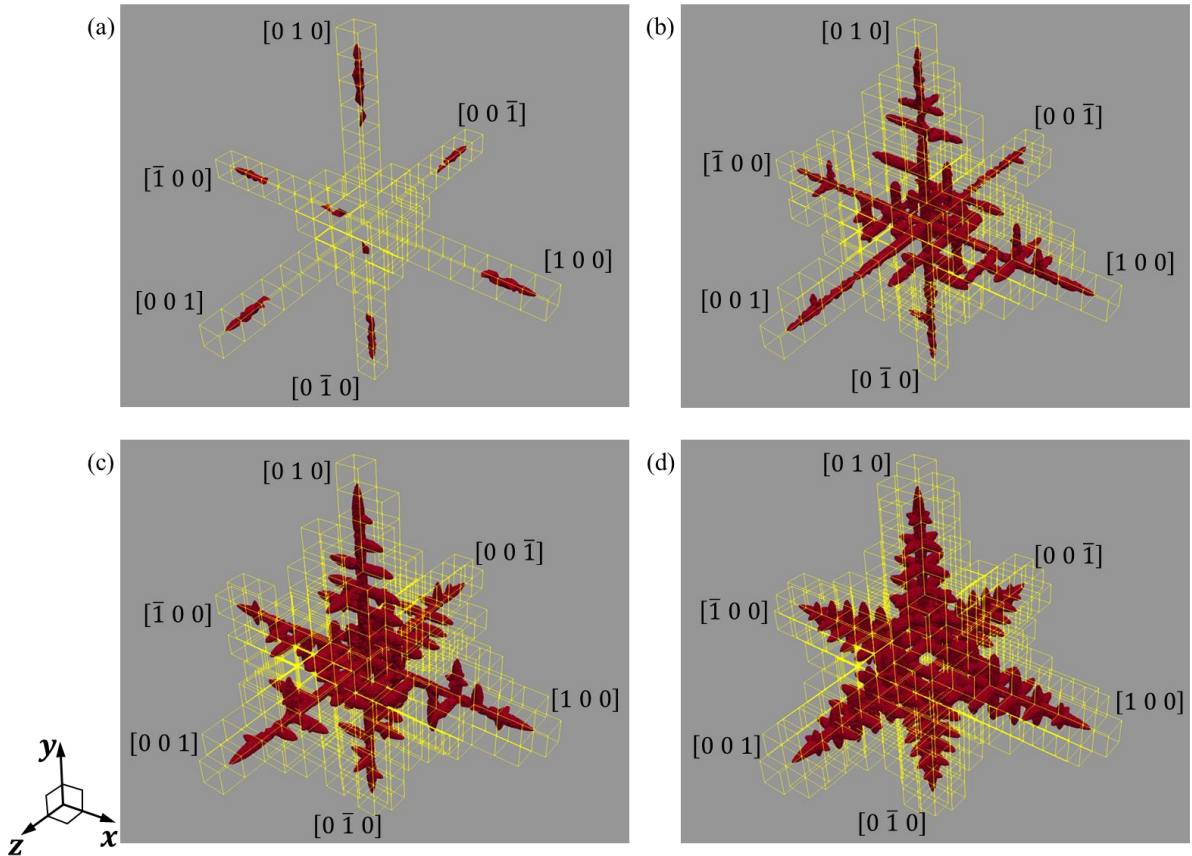
Fig. 4.11   **Three-dimensional view of dendritic microstructure for three-dimensional CAPTN simulation of an equiaxed Al-7 wt.% Si alloy grain with Euler angles $(0°, 0°, 0°)$ growing under constant temperature with supersaturation $\Omega = 0.062$, at $t = 100\,\text{s}$, with different percentage of side branches activated: (a) $sb\% = 0\%$, (b) $sb\% = 20\%$, (c) $sb\% = 50\%$, (d) $sb\% = 100\%$. Simulation parameters are $\alpha = 1/3$, $\beta = 2$, $\gamma = 1.5$, and $\tau = 1$. The dendritic branches are presented by red elements and the captured CA cells are presented by yellow wireframe. Primary branches are denoted by crystal directions $[1\,0\,0]$, $[\bar{1}\,0\,0]$, $[0\,1\,0]$, $[0\,\bar{1}\,0]$, $[0\,0\,1]$, and $[0\,0\,\bar{1}]$.**
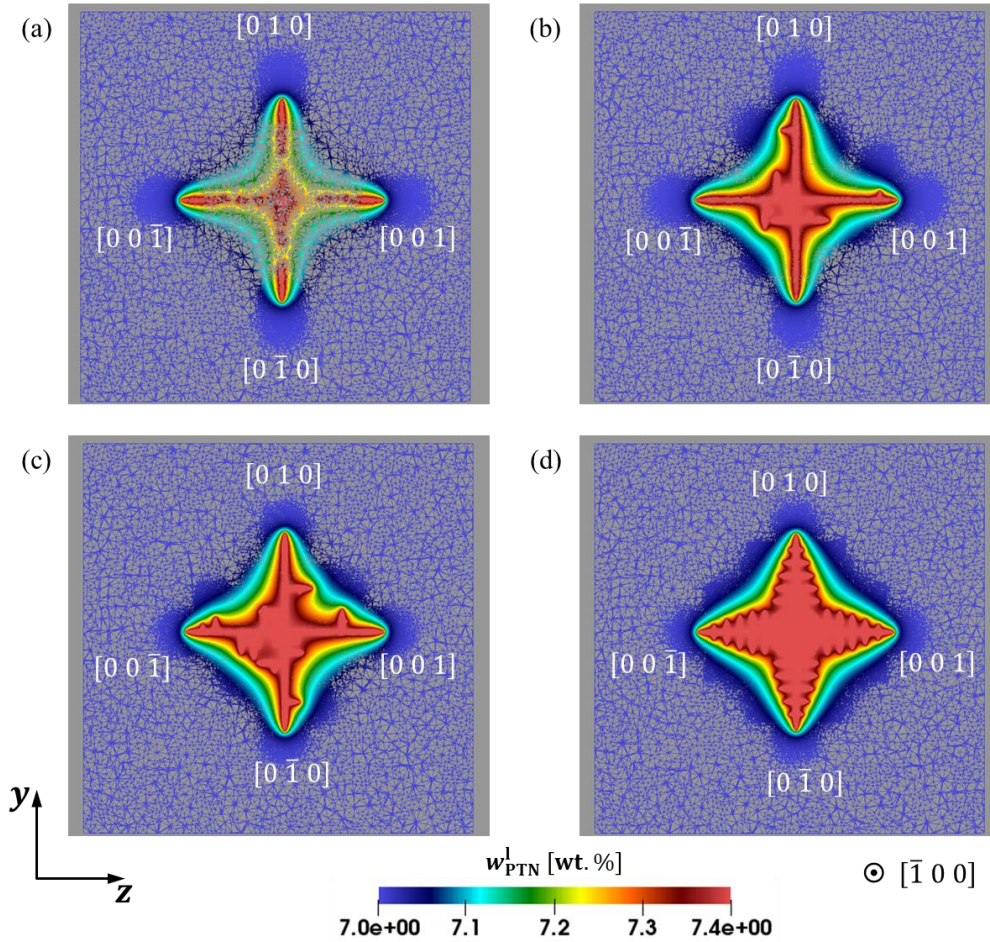
Fig. 4.12   Composition field by wireframe on the crystal plane $(1\,0\,0)$ for three-dimensional CAPTN simulation of an equiaxed Al-7 wt.% Si alloy grain with Euler angles $(0°, 0°, 0°)$ growing under constant temperature with supersaturation $\Omega = 0.062$, at $t = 100$ s, with different percentage of side branches activated: (a) $sb\% = 0\%$, (b) $sb\% = 20\%$, (c) $sb\% = 50\%$, (d) $sb\% = 100\%$. Simulation parameters are $\alpha = 1/3$, $\beta = 2$, $\gamma = 1.5$, and $\tau = 1$.
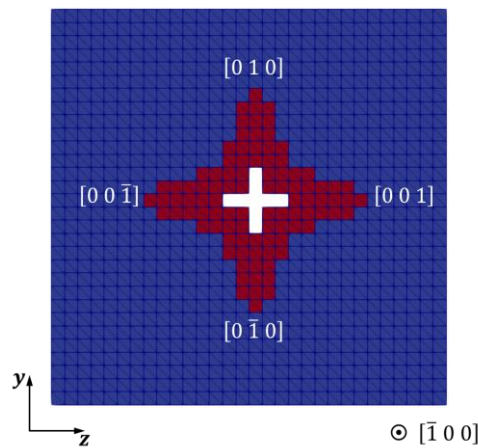
Fig. 4.13   CA cells on the crystal plane $(1\,0\,0)$ for three-dimensional CAPTN simulation of an equiaxed Al-7 wt.% Si alloy grain with Euler angles $(0°, 0°, 0°)$ growing under constant temperature with supersaturation $\Omega = 0.062$, at $t = 100$ s, with all side branches activated $(sb\% = 100\%)$. Simulation parameters are $\alpha = 1/3$, $\beta = 2$, $\gamma = 1.5$, and $\tau = 1$. Corresponding to Fig. 4.11d and Fig. 4.12d. Blue CA cells are in liquid state. Red CA cells are in mushy state. White CA cells in the center are in solid state and deallocated, so no envelope or parabola is associated with them.

The composition field in the liquid evolves with the number of activated side branches. As shown in Fig. 4.12, the more side branches are activated, the weaker the gradient is in the vicinity of the tip of the primary branches. This evolution yields an evolution of kinetics of the primary branches. The normalized velocities of the six primary branches and their maximum and minimum values at each time step of these simulations are plotted in Fig. 4.14. It is observed that there is slight decrease on the velocity between $60\,\text{s}$ and $100\,\text{s}$ with the increase of the activated side branches, which is consistent with the fact that side branches may slow down the growth of the primary branches by influencing the composition field at their surroundings.

$sb\% = 50\%$

(e)

(f)

$sb\% = 100\%$

(g)

(h)
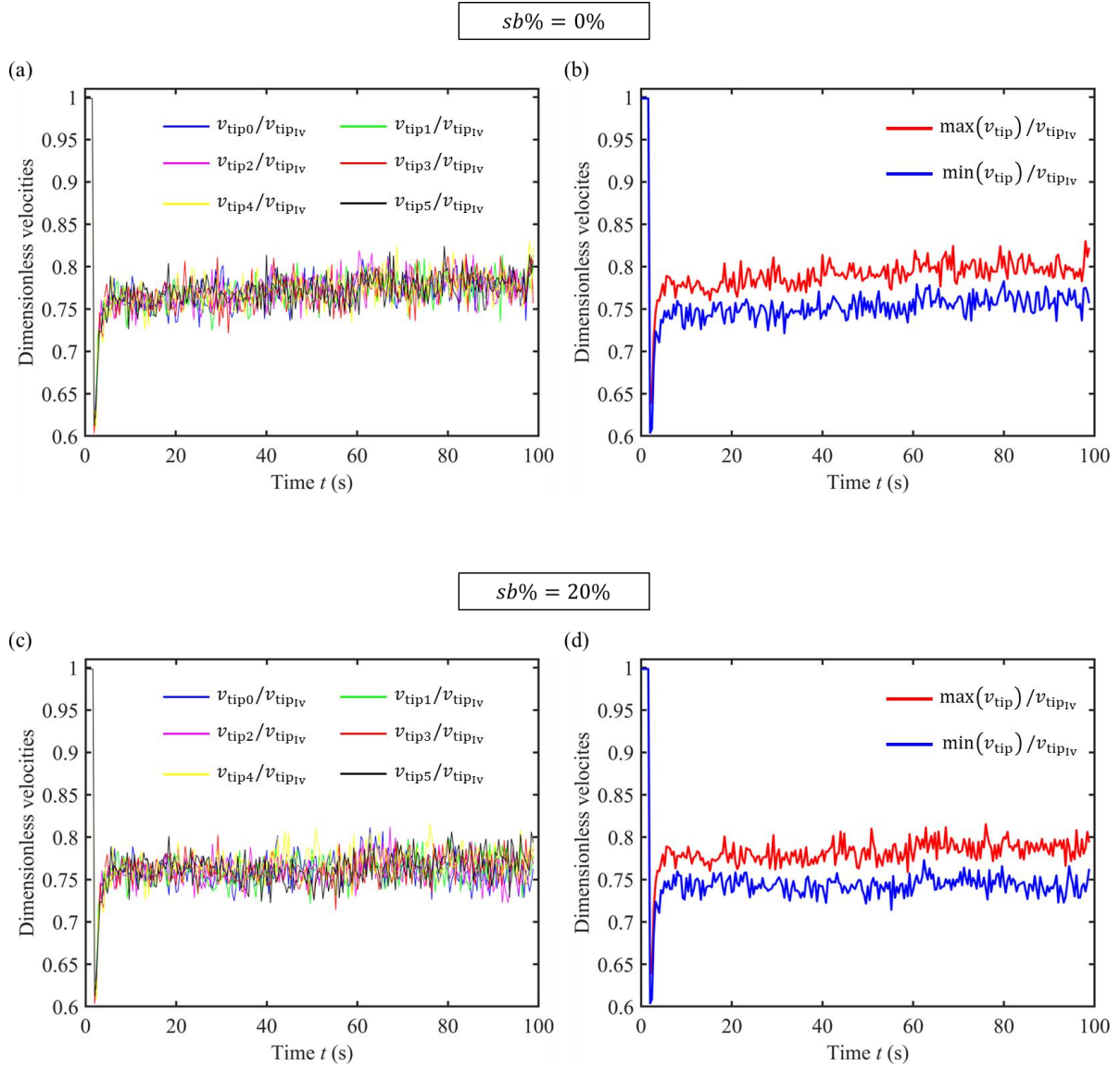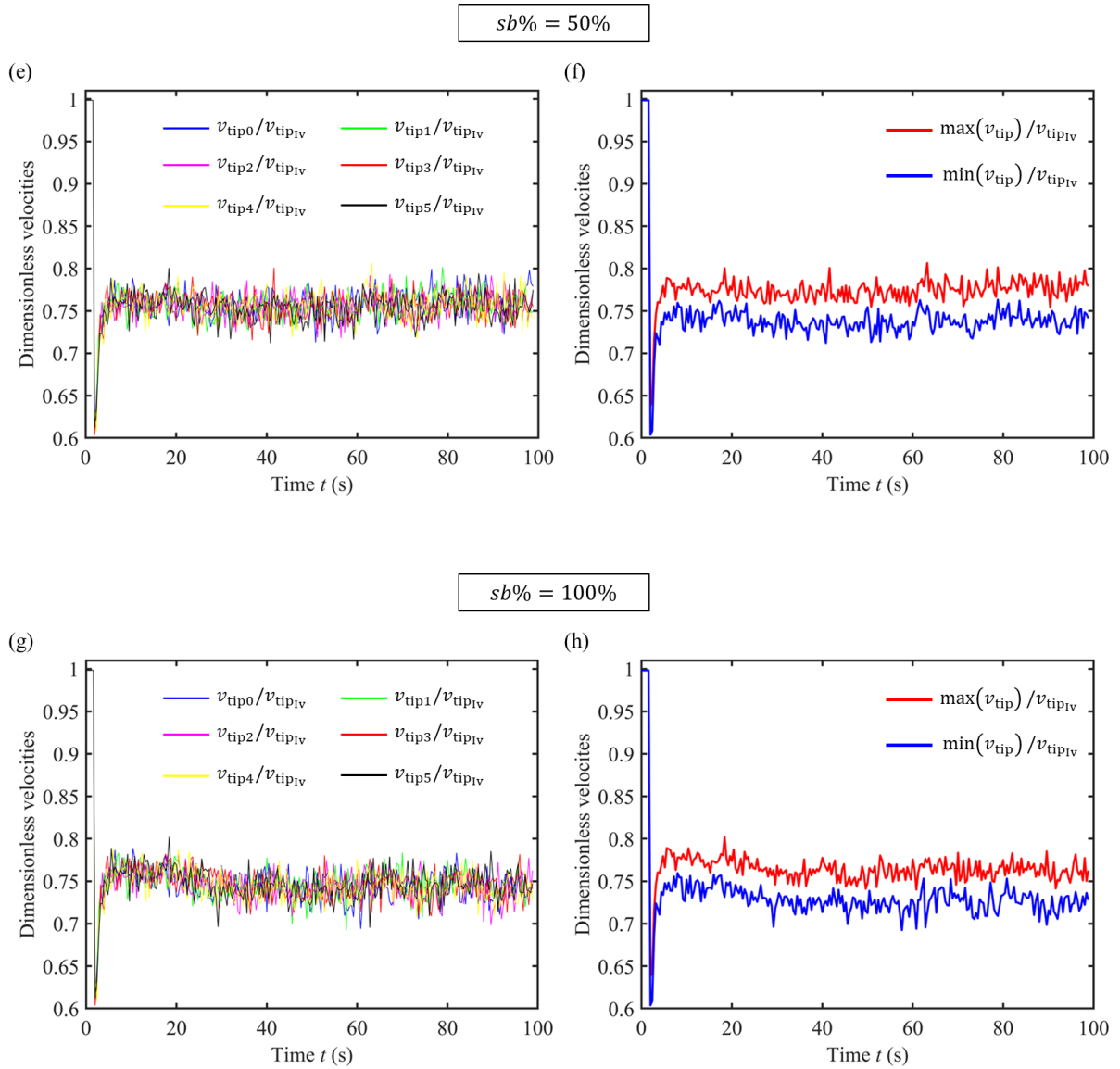
Fig. 4.14   Dimensionless velocities of primary branches of an equiaxed Al-7 wt.% Si alloy grain with Euler angles $(0°, 0°, 0°)$ growing under constant temperature with supersaturation $\Omega = 0.062$, with different percentage of side branches activated: (a, b) $sb\% = 0\%$, (c, d) $sb\% = 20\%$, (e, f) $sb\% = 50\%$, (g, h) $sb\% = 100\%$. Simulation parameters are $\alpha = 1/3, \beta = 2, \gamma = 1.5$, and $\tau = 1$. In the left figures (a, c, e, g) velocities of six primary branches are plotted. In the right figures (b, d, f, h) the maximum and minimum velocity of each time step among the six primary branches are plotted, which are the envelopes of the curves in their corresponding left figures.

The influence of the orientation of the grain is investigated as well. An equiaxed grain with 100% side branches and orientation $(20°, 20°, 20°)$ in Euler angles is modeled. Simulation parameters are the same as those in Table 4.1 with $h_{\min} = 1.5\rho_{\text{tip}_{\text{Iv}}}$. Fig. 4.15a shows its branches (in red) and captured CA cells (in yellow wireframe) at $t = 100\ \text{s}$. Primary branches are also denoted by crystal directions. The composition field on the crystal plane $(1\ 0\ 0)$ at the same time is depicted in Fig. 4.15b by wireframe. Normalized velocities of the six primary branches and their extreme values at every time step are plotted in Fig. 4.16. The kinetics of the six branches are very similar. There is no noticeable difference on the steady-state velocities of primary branches between Fig. 4.14h and Fig. 4.16b,

demonstrating once again that the CAPTN model is relevant to computing dendritic growth of any orientation due to its finite element implementation with unstructured tetrahedral mesh.
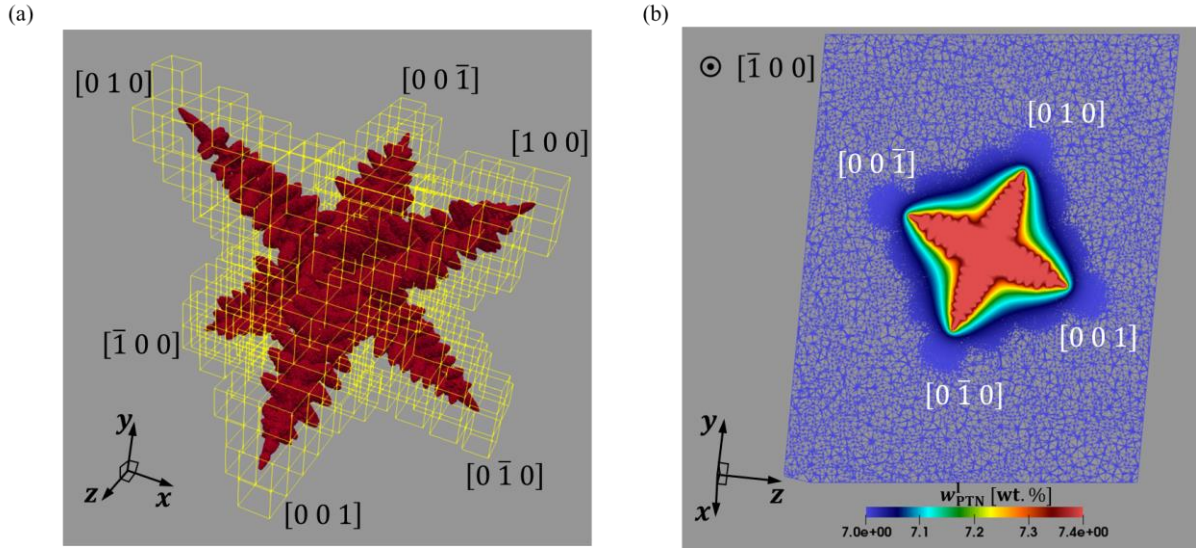
Fig. 4.15 **(a) Three-dimensional view of dendritic microstructure and (b) composition field on the cross section for three-dimensional CAPTN simulation of an equiaxed Al-7 wt.% Si alloy grain with a misorientation of $(20°, 20°, 20°)$ in Euler angles, whose side branches are all activated, growing under constant temperature with supersaturation $\Omega = 0.062$, at $t = 100$ s. Simulation parameters are $\alpha = 1/3$, $\beta = 2$, $\gamma = 1.5$, and $\tau = 1$. In (a) the dendritic branches are presented by red elements and the captured CA cells are presented by yellow wireframe. Primary branches are denoted by crystal directions $[1\,0\,0]$, $[\bar{1}\,0\,0]$, $[0\,1\,0]$, $[0\,\bar{1}\,0]$, $[0\,0\,1]$, and $[0\,0\,\bar{1}]$. (b) is the composition field by wireframe on the crystal plane $(1\,0\,0)$.**
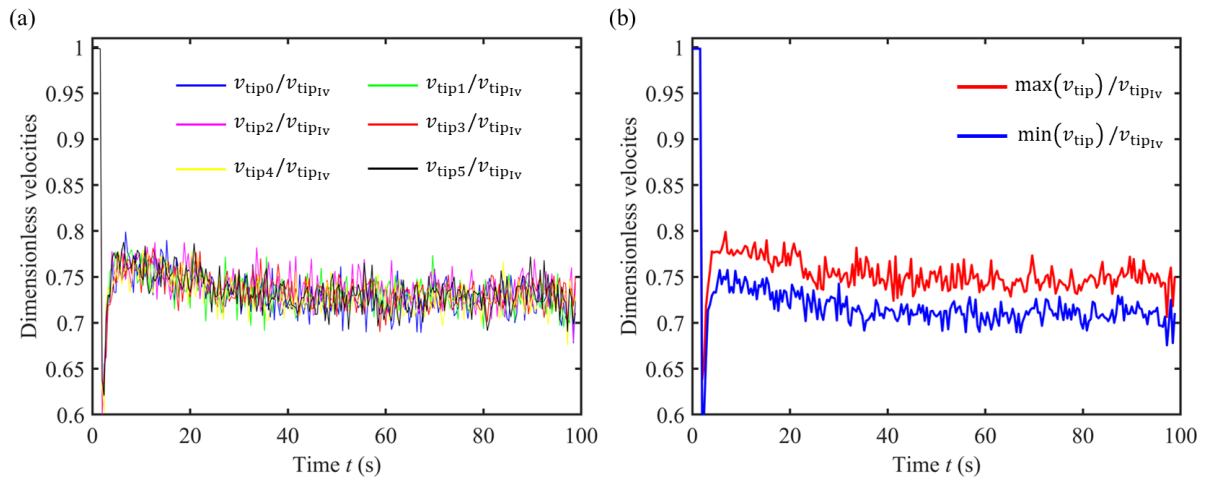
Fig. 4.16 **Dimensionless velocities of primary branches of an equiaxed Al-7 wt.% Si alloy grain with a misorientation of $(20°, 20°, 20°)$ in Euler angles, whose side branches are all activated, growing under constant temperature with supersaturation $\Omega = 0.062$. Simulation parameters are $\alpha = 1/3$, $\beta = 2$, $\gamma = 1.5$, and $\tau = 1$. (a) Velocities of six primary branches are plotted. (b) The maximum and minimum velocity of each time step among the six primary branches are plotted.**

However, there are more captured CA cells in the misoriented case than in the well-oriented case, leading to an increase of side branches since each captured CA cell may produce a set of (4 in three dimensions) side branches. At $t = 100$ s, there are 989 active

branches that have non-zero velocity in the misoriented simulation, whereas 370 active branches in the well-oriented simulation. The computational time is of large difference: the misoriented simulation takes 12617 minutes and the well-oriented simulation takes 5064 minutes for running while using the same hardware.

4.5   Application of the three-dimensional CAPTN model at unsteady state

The CAPTN model is now evaluated by comparing its prediction of equiaxed grain growth to the DNN simulations and PF simulations [58]. Both the DNN model and the PF model are implemented by the finite difference method on an isotropic homogeneous cubic grid.

In the DNN and PF simulations, an equiaxed dendritic grain grows under supersaturation of 0.05 and 0.25 in a cubic domain with nominal composition in the liquid. Its growth is unsteady at the beginning, then reaches or closely approaches steady state, and becomes unsteady at the end with smaller velocity due to the effect of the boundary of the simulation domain. Parameters are all nondimensionalized by physical parameters such as $\rho_{\mathrm{tip_{Iv}}}$ and $v_{\mathrm{tip_{Iv}}}$. The solvability constant σ used in the DNN model is obtained from the PF studies: $\sigma = 0.0165$ for $\Omega = 0.05$ and $\sigma = 0.0135$ for $\Omega = 0.25$. In the DNN simulations, the growth of side branches is not allowed. The DNN and PF results were shared by Thomas Isensee and Damien Tourret.

The CAPTN model is employed for modeling the same cases. An equiaxed grain with six primary branches without side branches is placed at the center of a cubic domain along domain edges. The temperature is uniform and fixed, corresponding to the supersaturation. The initial branch lengths in the DNN simulations are not identical for different mesh sizes for a given supersaturation; in the CAPTN simulations the initial branch length is imposed identically as the largest initial branch length in the DNN simulations for the same supersaturation. It satisfies $L_{\mathrm{phy}} > 1.3a$ and allows the PTN method to be used from the first time step. The initial composition in the liquid is the nominal composition $w_0 = 7\%$. The CA cell size does not influence the kinetics. It is chosen as 0.3 mm for $\Omega = 0.05$ and 0.01 mm for $\Omega = 0.25$. The CAPTN model employs the adaptive heterogeneous meshing strategy, so its mesh size is characterized by the minimum mesh size h_{min}. The same dimensionless parameters for the DNN model are used except for the edge length of the simulation domain. The PF and DNN simulations model only 1/8 of the domain with symmetric boundary condition on the three faces comprising the grain center and non-flux boundary condition on the other three faces, whereas the CAPTN simulations model the entire domain with only non-flux boundary condition on its six faces, so the edge length of the CAPTN simulation domain L_{D} is twice the edge length of PF and DNN simulation domains. In the CAPTN simulation the six branches have very similar kinetics, so in the following analyses only the branch of $+x$ direction is investigated.
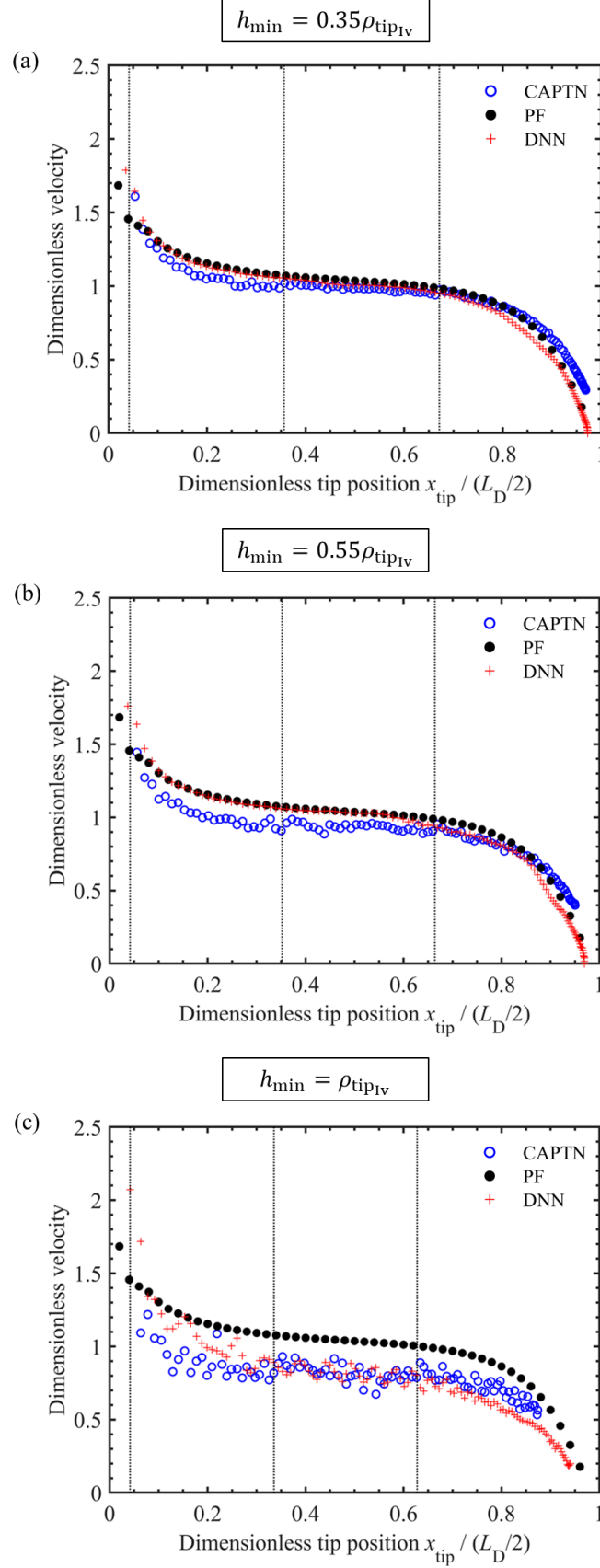
The material properties of Al-7 wt.% Si alloy are used for defining all dimensional parameters in the CAPTN simulations. For $\Omega = 0.05$, parameters are listed in Table 4.3.

Table 4.3   Parameters of simulation of an equiaxed grain without side branch growing under constant temperature with supersaturation $\Omega = 0.05$.

Variable	Name	Unit	Value
Solvability constant	σ	1	0.0165
Tip radius from Ivantsov – Solvability solution	$\rho_{\text{tip}_{\text{Iv}}}$	mm	1.097×10^{-2}
Tip velocity from Ivantsov – Solvability solution	$v_{\text{tip}_{\text{Iv}}}$	mm/s	7.155×10^{-3}
Diffusion length from Ivantsov – Solvability solution	$\delta_{\text{d}_{\text{Iv}}}$	mm	4.193×10^{-2}
Minimum PTN mesh size	h_{min}	$\rho_{\text{tip}_{\text{Iv}}}$	0.35 or 0.55 or 1
Integration distance (Eq. (3.4) for $\delta_{\text{d}_{\text{Iv}}}$)	a	$\delta_{\text{d}_{\text{Iv}}}$	0.566
Radius of truncating cylinder (Eq. (3.18) for $r_{\text{cyl}}^{\text{min}}$)	r_{cyl}	$r_{\text{cyl}}^{\text{min}}$	2
Edge length of simulation domain	L_{D}	mm	2.10
Simulation time	t_{end}	s	150
Time step	Δt	s	0.5
PTN mesh size in TA1	h_1	h_{min}	2
PTN mesh size in TA2	h_2	h_{min}	5
PTN mesh size in solid	h_{solid}	h_{min}	5
Maximum PTN mesh size	h_{max}	h_{min}	10
Distance from the tip to the center of the box with h_{min} at its creation	l	$\delta_{\text{d}_{\text{Iv}}}$	5
Distance from the tip to the end of the box with h_{min} at its creation	l_{b}	a	1.2
Half height of the rectangle with h_{min} (Eq. (2.2) for $R_{\text{integ}}^{\text{c}}$)	H	$R_{\text{integ}}^{\text{c}}$	1.5
Distance passed by the tip between two *Remeshings*	l_{R}	l	1.6
TA1 thickness	e_1	l	1
TA2 thickness	e_2	l	1

The evolution of tip velocity with tip length is plotted in Fig. 4.17. The tip velocity is always normalized by $v_{\text{tip}_{\text{Iv}}}$, the tip velocity of Ivantsov – Solvability condition, under the same supersaturation. The tip position is normalized by half the domain edge length of the CAPTN model. PF results are identical in all subfigures. Fig. 4.17a (Fig. 4.17b, Fig. 4.17c, resp.) shows the DNN results with mesh size equal to $0.35\rho_{\text{tip}_{\text{Iv}}}$ ($0.55\rho_{\text{tip}_{\text{Iv}}}$, $\rho_{\text{tip}_{\text{Iv}}}$, resp.) and the CAPTN results using adaptive heterogeneous mesh with minimum mesh size equal to $0.35\rho_{\text{tip}_{\text{Iv}}}$ ($0.55\rho_{\text{tip}_{\text{Iv}}}$, $\rho_{\text{tip}_{\text{Iv}}}$, resp.). Vertical dotted lines indicate the moments when the adaptive heterogeneous mesh is reconstructed in the CAPTN model. The impact of reconstructing the mesh on tip velocity is observed to be very small. The CAPTN results are in good agreement with the DNN results, and they both reproduce similar kinetics with the PF result when their characteristic mesh size is equal to $0.35\rho_{\text{tip}_{\text{Iv}}}$ or $0.55\rho_{\text{tip}_{\text{Iv}}}$. For mesh size equal to $\rho_{\text{tip}_{\text{Iv}}}$, the CAPTN and DNN results are more fluctuating than those with smaller mesh size. They follow the tendency of the PF result but are significantly smaller than it. One

should note that the transient kinetics at the early-stage growth and the solute interaction in the end are well predicted by all the models. With the classical CA model this is unfeasible: the tip velocity will keep $v_{\text{tip}_{\text{Iv}}}$ during the simulation.

$$h_{\min} = 0.35\rho_{\text{tip}_{\text{Iv}}}$$

(a)

$$h_{\min} = 0.55\rho_{\text{tip}_{\text{Iv}}}$$

(b)

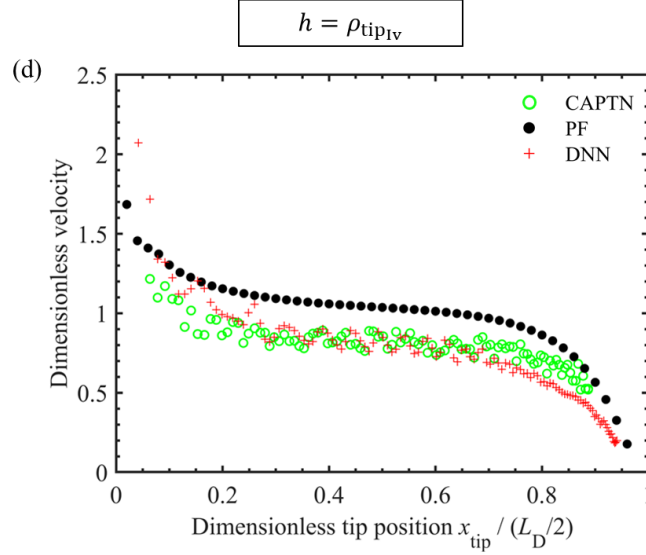$$h_{\min} = \rho_{\text{tip}_{\text{Iv}}}$$

(c)

Fig. 4.17   **Evolution of tip velocity with tip position for an equiaxed grain growing under supersaturation $\Omega = 0.05$ from the PF, DNN, and CAPTN models. The tip velocity is normalized by $v_{\text{tip}_{\text{Iv}}}$. The tip position is normalized by half of the domain edge length of the CAPTN model. PF results in the four figures are the same, while DNN and CAPTN results are from different meshes. The mesh size in the DNN model and the minimum mesh size in the CAPTN model equal (a) $0.35\rho_{\text{tip}_{\text{Iv}}}$, (b) $0.55\rho_{\text{tip}_{\text{Iv}}}$, and (c) $\rho_{\text{tip}_{\text{Iv}}}$. Vertical dotted lines indicate the moments when the adaptive heterogeneous mesh is reconstructed in the CAPTN model. In (d) the CAPTN model uses an homogeneous mesh, whose mesh size is the same as the mesh size in the DNN model, equal to $\rho_{\text{tip}_{\text{Iv}}}$.**

To demonstrate the effect of the adaptive heterogeneous meshing strategy on improving computational efficiency, another CAPTN simulation using isotropic homogeneous mesh with mesh size equal to $\rho_{\text{tip}_{\text{Iv}}}$ is accomplished as well. Its result is presented by green hollow circles in Fig. 4.17d. The PTN mesh does not need to be reconstructed during the simulation. There is no significant difference from the CAPTN results using adaptive mesh (Fig. 4.17c). The composition fields at $t = 75$ s on the cross section passing the grain center for the two meshes are shown by wireframe in Fig. 4.18. Fields are similar but their numbers of elements are not in the same order of magnitude. Computational time and number of elements for different CAPTN simulations are listed in Table 4.4. They are all launched on a CPU with 32 cores. It is exciting that the computational time of the CAPTN simulation with adaptive heterogeneous meshing strategy is less than 1% of that of the CAPTN simulation with isotropic homogeneous mesh [1].

The CAPTN simulations with adaptive heterogeneous meshing strategy take 13 minutes for $h_{\text{min}} = \rho_{\text{tip}_{\text{Iv}}}$ and 60 minutes for $h_{\text{min}} = 0.55\rho_{\text{tip}_{\text{Iv}}}$. As comparison, the DNN simulation with constant mesh size equal to $\rho_{\text{tip}_{\text{Iv}}}$ takes less than 4 minutes, and the one with constant mesh size equal to $0.55\rho_{\text{tip}_{\text{Iv}}}$ takes 50 minutes, on a single GPU GeForce RTX 2080 Ti with 4352 cores. One should remind that the simulation domains of the CAPTN simulations are eight times bigger than the simulation domains of the DNN simulations. So in short, the

---

[1] The homogeneous mesh is prepared before the simulation, so the mesh preparation time is not included in the computational time.

CAPTN simulation with $h_{\min} = \rho_{\text{tip}_{\text{Iv}}}$ takes $13/(8 \times 4) = 41\%$ of the computational time of the DNN simulation, and the CAPTN simulation with $h_{\min} = 0.55\rho_{\text{tip}_{\text{Iv}}}$ takes $60/(8 \times 50) = 15\%$ of the computational time of the DNN simulation.
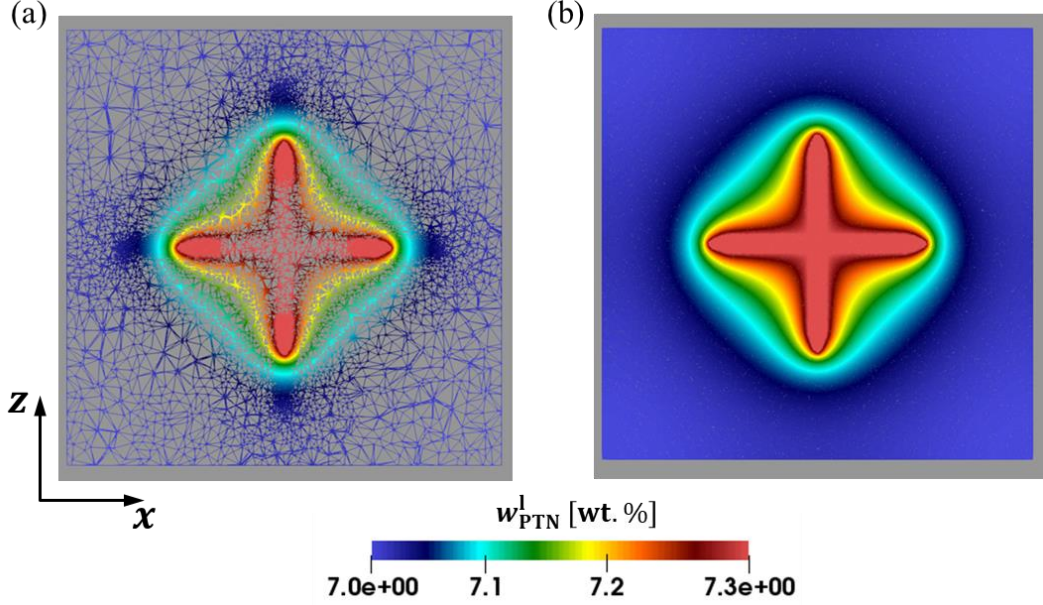
Fig. 4.18   **Composition field on the center cross section presented by wireframe, for the three-dimensional CAPTN simulation of an equiaxed grain without side branches growing under supersaturation $\Omega = 0.05$, by using (a) adaptive heterogeneous mesh with $h_{\min} = \rho_{\text{tip}_{\text{Iv}}}$ and (b) isotropic homogeneous mesh with mesh size $h = \rho_{\text{tip}_{\text{Iv}}}$. Their results are the blue hollow circles in Fig. 4.17c and Fig. 4.17d.**

Table 4.4   **Computational time and number of elements at $t = 75$ s for three-dimensional CAPTN simulation of an equiaxed grain along cellular grids growing under supersaturation $\Omega = 0.062$, with different meshes. Simulations are run on 32 CPU cores.**

CAPTN simulation	Computational time (min)	Number of elements
Adaptive heterogeneous mesh with $h_{\min} = 0.35\rho_{\text{tip}_{\text{Iv}}}$	251	6.80×10^6
Adaptive heterogeneous mesh with $h_{\min} = 0.55\rho_{\text{tip}_{\text{Iv}}}$	60	1.71×10^6
Adaptive heterogeneous mesh with $h_{\min} = \rho_{\text{tip}_{\text{Iv}}}$	13	2.53×10^5
Isotropic homogeneous mesh with $h = \rho_{\text{tip}_{\text{Iv}}}$	1451	9.70×10^7

The simulations for $\Omega = 0.25$ are analyzed in a similar way. Parameters are listed in Table 4.5. Fig. 4.19a exhibits the DNN results with mesh size equal to $0.2\rho_{\text{tip}_{\text{Iv}}}$ and the CAPTN results using adaptive heterogeneous mesh with minimum mesh size equal to $0.2\rho_{\text{tip}_{\text{Iv}}}$. Fig. 4.19b exhibits the DNN results with mesh size equal to $0.3\rho_{\text{tip}_{\text{Iv}}}$ and the CAPTN results using adaptive heterogeneous mesh with minimum mesh size equal to $0.3\rho_{\text{tip}_{\text{Iv}}}$. Vertical dotted lines indicate the moments when the adaptive heterogeneous mesh is

reconstructed in the CAPTN model. The PF result is regarded as reference. It is observed that the CAPTN model and the DNN model both reproduce better kinetics with smaller mesh size.

Table 4.5   Parameters of simulation of an equiaxed grain without side branch growing under constant temperature with supersaturation $\Omega = 0.25$.

Variable	Name	Unit	Value
Solvability constant	σ	1	0.0135
Tip radius from Ivantsov – Solvability solution	$\rho_{tip_{Iv}}$	mm	9.923×10^{-4}
Tip velocity from Ivantsov – Solvability solution	$v_{tip_{Iv}}$	mm/s	8.743×10^{-1}
Diffusion length from Ivantsov – Solvability solution	$\delta_{d_{Iv}}$	mm	1.716×10^{-3}
Minimum PTN mesh size	h_{min}	$\rho_{tip_{Iv}}$	0.2 or 0.3
Integration distance (Eq. (3.4) for $\delta_{d_{Iv}}$)	a	$\delta_{d_{Iv}}$	0.979
Radius of truncating cylinder (Eq. (3.18) for r_{cyl}^{min})	r_{cyl}	r_{cyl}^{min}	2
Edge length of simulation domain	L_D	mm	0.068
Simulation time	t_{end}	s	0.054
Time step	Δt	s	4.5×10^{-5}
PTN mesh size in TA1	h_1	h_{min}	2
PTN mesh size in TA2	h_2	h_{min}	5
PTN mesh size in solid	h_{solid}	h_{min}	5
Maximum PTN mesh size	h_{max}	h_{min}	10
Distance from the tip to the center of the box with h_{min} at its creation	l	$\delta_{d_{Iv}}$	5
Distance from the tip to the end of the box with h_{min} at its creation	l_b	a	1.2
Half height of the rectangle with h_{min} (Eq. (2.2) for R_{integ}^c)	H	R_{integ}^c	1.5
Distance passed by the tip between two *Remeshings*	l_R	l	1.6
TA1 thickness	e_1	l	1
TA2 thickness	e_2	l	1

Although the CAPTN model and the DNN model have similar method for calculating the kinetics, the CAPTN model gives slightly less precise results than the DNN model. This may be caused by their differences on mesh simplex. Indeed, the CAPTN model employs linear tetrahedral elements while the DNN model employs linear hexahedral elements. It is known from literature that linear tetrahedral elements yield less precise results than linear hexahedral elements of the same mesh size [59–62].
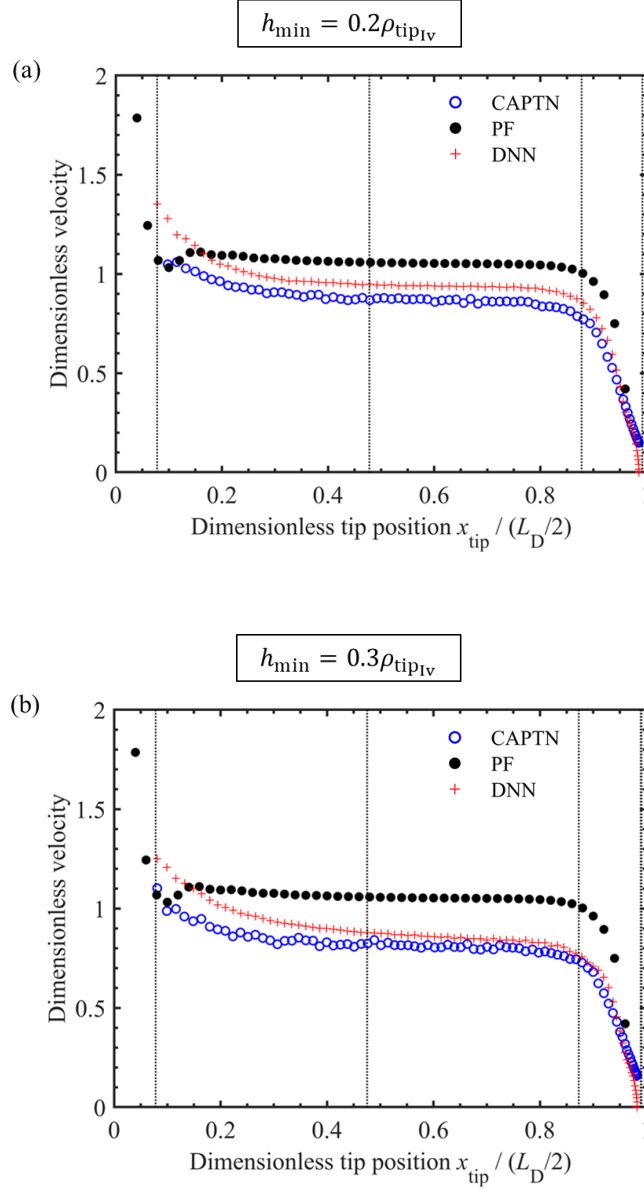
Fig. 4.19 **Evolution of tip velocity with tip position for an equiaxed grain growing under supersaturation $\Omega = 0.25$ from the PF, DNN, and CAPTN models. The tip velocity is normalized by $v_{\text{tip}_{Iv}}$. The tip position is normalized by half of the domain edge length of the CAPTN model. PF results in the two figures are the same, while DNN and CAPTN results are from different meshes. The mesh size in the DNN model and the minimum mesh size in the CAPTN model equal (a) $0.2\rho_{\text{tip}_{Iv}}$ and (b) $0.3\rho_{\text{tip}_{Iv}}$. Vertical dotted lines indicate the moments when the adaptive heterogeneous mesh is reconstructed in the CAPTN model.**

4.6   Conclusion

This chapter is dedicated to the multi-scale coupling CAPTN model and its application to three-dimensional configurations of dendritic growth. The first-time implementation of this model by Fleurisson [14] was reviewed. In this thesis, the adaptation of both the CA method and the PTN method to the CAPTN method has been improved. The CAPTN method has been actually able to choose appropriate tip growth law depending on the physical branch length, to eliminate tertiary branches overlapping its primary branch, to activate a percentage of side branches, to impose composition Dirichlet condition depending on node's local

temperature, and to apply the adaptive heterogeneous PTN meshing strategy mentioned in Subsection 2.2.2. All of these improvements are usable in both two dimensions and three dimensions.

The three-dimensional CAPTN model has been evaluated by modeling an equiaxed alloy grain growing at constant supersaturation, at steady state with the PTN method, and at unsteady state with the DNN method and the PF method. Thanks to the finite element implementation of the PTN method, grain orientation does not affect the kinetics of primary branches. Side branches do have small impact on the kinetics of primary branches. For the simulation domain with the same size, the CAPTN model takes less time than the DNN model.

Until now the evaluation of the CAPTN model under isothermal condition has been accomplished. In the next chapter the two-dimensional CAPTN model will be applied on predicting columnar dendritic grain structures under temperature gradient.

References

[1] J. A. Dantzig and M. Rappaz, *Solidification*, 1st version. Lausanne, Switzerland: EPFL Press, 2009.

[2] W. Kurz, D. J. Fisher, and R. Trivedi, "Progress in modelling solidification microstructures in metals and alloys: dendrites and cells from 1700 to 2000," *Int. Mater. Rev.*, vol. 64, no. 6, pp. 311–354, Aug. 2019.

[3] J. D. Hunt, "Steady state columnar and equiaxed growth of dendrites and eutectic," *Mater. Sci. Eng.*, vol. 65, no. 1, pp. 75–83, Jul. 1984.

[4] W. Kurz, C. Bezençon, and M. Gäumann, "Columnar to equiaxed transition in solidification processing," *Sci. Technol. Adv. Mater.*, vol. 2, no. 1, p. 185, Mar. 2001.

[5] R. Lenart and M. Eshraghi, "Modeling columnar to equiaxed transition in directional solidification of Inconel 718 alloy," *Comput. Mater. Sci.*, vol. 172, p. 109374, Feb. 2020.

[6] G. Zimmermann *et al.*, "CETSOL-6 Final Report," 2022.

[7] G. Zimmermann *et al.*, "Columnar and Equiaxed Solidification of Al-7 wt.% Si Alloys in Reduced Gravity in the Framework of the CETSOL Project," *JOM*, vol. 69, no. 8, pp. 1269–1279, Jun. 2017.

[8] Y. Z. Li, N. Mangelinck-Noël, G. Zimmermann, L. Sturz, and H. Nguyen-Thi, "Comparative study of directional solidification of Al-7 wt% Si alloys in Space and on Earth: Effects of gravity on dendrite growth and Columnar-to-equiaxed transition," *J. Cryst. Growth*, vol. 513, pp. 20–29, May 2019.

[9] T. Carozzani, C.-A. Gandin, H. Digonnet, M. Bellet, K. Zaidat, and Y. Fautrelle, "Direct Simulation of a Solidification Benchmark Experiment," *Metall. Mater. Trans. A*, vol. 44, no. 2, pp. 873–887, Feb. 2013.

[10] R. P. Mooney *et al.*, "Concurrent model for sharp and progressive columnar to equiaxed transitions validated by directional solidification experiments processed in microgravity conditions," *Comput. Mater. Sci.*, vol. 210, p. 111436, Jul. 2022.

[11] P.-A. Geslin, C.-H. Chen, A. M. Tabrizi, and A. Karma, "Dendritic needle network modeling of the Columnar-to-Equiaxed transition. Part I: two dimensional formulation and comparison with theory," *Acta Mater.*, vol. 202, pp. 42–54, Jan. 2021.

[12] C.-H. Chen, A. M. Tabrizi, P.-A. Geslin, and A. Karma, "Dendritic needle network modeling of the Columnar-to-Equiaxed Transition. Part II: three dimensional formulation, implementation and comparison with experiments," *Acta Mater.*, vol. 202, pp. 463–477, Jan. 2021.

[13] D. Tourret and A. Karma, "Three-dimensional dendritic needle network model for alloy solidification," *Acta Mater.*, vol. 120, pp. 240–254, Nov. 2016.

[14] R. Fleurisson, "Modélisation multi-échelle parallélisée pour la prédiction de structures de grains dendritiques couplant les éléments finis, un automate cellulaire et un réseau de paraboles," PhD thesis, Paris Sciences et Lettres, 2019.

[15] R. Fleurisson, O. Senninger, G. Guillemot, and C.-A. Gandin, "Hybrid Cellular Automaton - Parabolic Thick Needle model for equiaxed dendritic solidification," *J. Mater. Sci. Technol.*, 2022.

[16] W. Kurz and D. J. Fisher, *Fundamentals of Solidification*, 4th Revised Edition. Uetikon-Zuerich, Switzerland: TRANS TECH PUBLICATIONS LTD, 1998.

[17] A. Papapetrou, "Investigations on the dendrite growth of crystals," *Z. Für Krist. - Cryst. Mater.*, vol. 92, no. 1–6, pp. 89–130, Jun. 1935.

[18] A. J. Melendez and C. Beckermann, "Measurements of dendrite tip growth and sidebranching in succinonitrile–acetone alloys," *J. Cryst. Growth*, vol. 340, no. 1, pp. 175–189, Feb. 2012.

[19] J. S. Langer and H. Müller-Krumbhaar, "Theory of dendritic growth—I. Elements of a stability analysis," *Acta Metall.*, vol. 26, no. 11, pp. 1681–1687, Nov. 1978.

[20] A. Karma and B. G. Kotliar, "Pattern selection in a boundary-layer model of dendritic growth in the presence of impurities," *Phys. Rev. A*, vol. 31, no. 5, pp. 3266–3275, May 1985.

[21] M. Ben Amar and P. Pelcé, "Impurity effect on dendritic growth," *Phys. Rev. A*, vol. 39, no. 8, pp. 4263–4269, Apr. 1989.

[22] E. Çadırlı, N. Maraslı, B. Bayender, and M. Gündüz, "Dependency of the microstructure parameters on the solidification parameters for camphene," *Mater. Res. Bull.*, vol. 35, no. 6, pp. 985–995, Apr. 2000.

[23] G. P. Ivantsov, "Temperature field around a spherical, cylindrical and needle-crystals which grows in supercooled melt," *Dokl Akad Nauk SSSR*, vol. 58, pp. 567–569, 1947.

[24] Ch.-A. Gandin, "From constrained to unconstrained growth during directional solidification," *Acta Mater.*, vol. 48, no. 10, pp. 2483–2501, Jun. 2000.

[25] M. A. Martorano, C. Beckermann, and C.-A. Gandin, "A solutal interaction mechanism for the columnar-to-equiaxed transition in alloy solidification," *Metall. Mater. Trans. A*, vol. 34, no. 8, pp. 1657–1674, Aug. 2003.

[26] H. Li *et al.*, "Columnar to equiaxed transition in additively manufactured CoCrFeMnNi high entropy alloy," *Mater. Des.*, vol. 197, p. 109262, Jan. 2021.

[27] M. Qi *et al.*, "Columnar to equiaxed transition during β heat treatment in a near β alloy by laser additive manufacture," *J. Mater. Res. Technol.*, vol. 13, pp. 1159–1168, Jul. 2021.

[28] P. Liu, Z. Wang, Y. Xiao, M. F. Horstemeyer, X. Cui, and L. Chen, "Insight into the mechanisms of columnar to equiaxed grain transition during metallic additive manufacturing," *Addit. Manuf.*, vol. 26, pp. 22–29, Mar. 2019.

[29] T. Takaki, S. Sakane, M. Ohno, Y. Shibuta, T. Aoki, and C.-A. Gandin, "Competitive grain growth during directional solidification of a polycrystalline binary alloy: Three-dimensional large-scale phase-field study," *Materialia*, vol. 1, pp. 104–113, Sep. 2018.

[30] A. Badillo and C. Beckermann, "Phase-field simulation of the columnar-to-equiaxed transition in alloy solidification," *Acta Mater.*, vol. 54, no. 8, pp. 2015–2026, May 2006.

[31] L. Nastac, "Numerical modeling of solidification morphologies and segregation patterns in cast dendritic alloys," *Acta Mater.*, vol. 47, no. 17, pp. 4253–4262, Nov. 1999.

[32] W. Wang, S. Luo, and M. Zhu, "Numerical Simulation of Three-Dimensional Dendritic Growth of Alloy: Part I—Model Development and Test," *Metall. Mater. Trans. A*, vol. 47, no. 3, pp. 1339–1354, Mar. 2016.

[33] L. Wei, X. Lin, M. Wang, and W. Huang, "Low artificial anisotropy cellular automaton model and its applications to the cell-to-dendrite transition in directional solidification," *Mater. Discov.*, vol. 3, pp. 17–28, Mar. 2016.

[34] W. Wang, Z. Wang, S. Yin, S. Luo, and M. Zhu, "Numerical simulation of solute undercooling influenced columnar to equiaxed transition of Fe-C alloy with cellular automaton," *Comput. Mater. Sci.*, vol. 167, pp. 52–64, Sep. 2019.

[35] D. Tourret and A. Karma, "Multiscale dendritic needle network model of alloy solidification," *Acta Mater.*, vol. 61, no. 17, pp. 6474–6491, Oct. 2013.

[36] D. Tourret, M. M. Francois, and A. J. Clarke, "Multiscale dendritic needle network model of alloy solidification with fluid flow," *Comput. Mater. Sci.*, vol. 162, pp. 206–227, May 2019.

[37] T. Isensee and D. Tourret, "Convective effects on columnar dendritic solidification – A multiscale dendritic needle network study," *Acta Mater.*, vol. 234, p. 118035, Aug. 2022.

[38] D. Tourret, L. Sturz, A. Viardin, and M. Založnik, "Comparing mesoscopic models for dendritic growth," *IOP Conf. Ser. Mater. Sci. Eng.*, vol. 861, no. 1, p. 012002, May 2020.

[39] I. Steinbach, C. Beckermann, B. Kauerauf, Q. Li, and J. Guo, "Three-dimensional modeling of equiaxed dendritic growth on a mesoscopic scale," *Acta Mater.*, vol. 47, no. 3, pp. 971–982, Feb. 1999.

[40] I. Steinbach, H.-J. Diepers, and C. Beckermann, "Transient growth and interaction of equiaxed dendrites," *J. Cryst. Growth*, vol. 275, no. 3, pp. 624–638, Mar. 2005.

[41] A. Viardin, M. Založnik, Y. Souhar, M. Apel, and H. Combeau, "Mesoscopic modeling of spacing and grain selection in columnar dendritic solidification: Envelope versus phase-field model," *Acta Mater.*, vol. 122, pp. 386–399, Jan. 2017.

[42] A. Viardin, Y. Souhar, M. Cisternas Fernández, M. Apel, and M. Založnik, "Mesoscopic modeling of equiaxed and columnar solidification microstructures under forced flow and buoyancy-driven flow in hypergravity: Envelope versus phase-field model," *Acta Mater.*, vol. 199, pp. 680–694, Oct. 2020.

[43] A. Olmedilla, M. Založnik, and H. Combeau, "Quantitative 3D mesoscopic modeling of grain interactions during equiaxed dendritic solidification in a thin sample," *Acta Mater.*, vol. 173, pp. 249–261, Jul. 2019.

[44] M. Rappaz and Ch.-A. Gandin, "Probabilistic modelling of microstructure formation in solidification processes," *Acta Metall. Mater.*, vol. 41, no. 2, pp. 345–360, Feb. 1993.

[45] T. Carozzani, "Développement d'un modèle 3D Automate Cellulaire-Éléments Finis (CAFE) parallèle pour la prédiction de structures de grains lors de la solidification d'alliages métalliques," PhD thesis, Paris, ENSMP, 2012.

[46] M. Mitchell, "Computation in Cellular Automata: A Selected Review | Santa Fe Institute," in *Nonstandard Computation*, 1998, pp. 95–140.

[47] Ch.-A. Gandin and M. Rappaz, "A 3D Cellular Automaton algorithm for the prediction of dendritic grain growth," *Acta Mater.*, vol. 45, no. 5, pp. 2187–2195, May 1997.

[48] Ch.-A. Gandin and M. Rappaz, "A coupled finite element-cellular automaton model for the prediction of dendritic grain structures in solidification processes," *Acta Metall. Mater.*, vol. 42, no. 7, pp. 2233–2246, Jul. 1994.

[49] Ch.-A. Gandin, J.-L. Desbiolles, M. Rappaz, and Ph. Thevoz, "A three-dimensional cellular automation-finite element model for the prediction of solidification grain structures," *Metall. Mater. Trans. A*, vol. 30, no. 12, pp. 3153–3165, Dec. 1999.

[50] G. Guillemot, Ch.-A. Gandin, and M. Bellet, "Interaction between single grain solidification and macrosegregation: Application of a cellular automaton—Finite element model," *J. Cryst. Growth*, vol. 303, no. 1, pp. 58–68, May 2007.

[51] Ch.-A. Gandin, S. Mosbah, Th. Volkmann, and D. M. Herlach, "Experimental and numerical modeling of equiaxed solidification in metallic alloys," *Acta Mater.*, vol. 56, no. 13, pp. 3023–3035, Aug. 2008.

[52] S. Sachi, "Coupling solidification model with CALPHAD data for the prediction of macrosegregation and solidification structures," PhD thesis, Université de Lorraine, 2022.

[53] H. Ettroudi, "Modélisation numérique multi-échelle des structures de solidification, de la macroségrégation et de la Transition Colonnaire-Equiaxe," PhD thesis, Université Paris sciences et lettres, 2021.

[54] M. Hamide, "Modélisation numérique du soudage à l'arc des aciers," PhD thesis, École Nationale Supérieure des Mines de Paris, 2008.

[55] M. de Berg, O. Cheong, M. van Kreveld, and M. Overmars, *Computational Geometry: Algorithms and Applications*, 3rd ed. Berlin Heidelberg: Springer-Verlag, 2008.

[56] D. Meagher, "Geometric modeling using octree encoding," *Comput. Graph. Image Process.*, vol. 19, no. 2, pp. 129–147, Jun. 1982.

[57] Y. Couder, J. Maurer, R. González-Cinca, and A. Hernández-Machado, "Side-branch growth in two-dimensional dendrites. I. Experiments," *Phys. Rev. E*, vol. 71, no. 3, p. 031602, Mar. 2005.

[58] T. Isensee, D. Tourret, A. Viardin, L. Sturz, and M. Založnik, "Benchmark simulations of multiscale models for dendritic growth in alloys under isothermal and directional conditions," ICASP 6, oral presentation, Jun. 2022.

[59] W. Wang, Y. Cao, and T. Okaze, "Comparison of hexahedral, tetrahedral and polyhedral cells for reproducing the wind field around an isolated building by LES," *Build. Environ.*, vol. 195, p. 107717, May 2021.

[60] A. O. Cifuentes and A. Kalbag, "A performance study of tetrahedral and hexahedral elements in 3-D finite element structural analysis," *Finite Elem. Anal. Des.*, vol. 12, no. 3, pp. 313–318, Dec. 1992.

[61] A. Karimi, R. Grytz, S. M. Rahmati, C. A. Girkin, and J. C. Downs, "Analysis of the effects of finite element type within a 3D biomechanical model of a human optic nerve head and posterior pole," *Comput. Methods Programs Biomed.*, vol. 198, p. 105794, Jan. 2021.

[62] S. C. Tadepalli, A. Erdemir, and P. R. Cavanagh, "Comparison of hexahedral and tetrahedral elements in finite element analysis of the foot and footwear," *J. Biomech.*, vol. 44, no. 12, pp. 2337–2343, Aug. 2011.

[63] A. Pineau, G. Guillemot, D. Tourret, A. Karma, and C.-A. Gandin, "Growth competition between columnar dendritic grains – Cellular automaton versus phase field modeling," *Acta Mater.*, vol. 155, pp. 286–301, Aug. 2018.

[64] E. Dorari, K. Ji, G. Guillemot, C.-A. Gandin, and A. Karma, "Growth competition between columnar dendritic grains – The role of microstructural length scales," *Acta Mater.*, vol. 223, p. 117395, Jan. 2022.

Chapter 5   Application of the two-dimensional CAPTN model

This chapter focuses on the application of the two-dimensional CAPTN model on investigating the primary dendrite arm spacing of a single crystal and the grain boundary orientation of a bi-crystal under directional solidification. It is in the format of an article and is to be submitted.

Résumé en français

Ce chapitre est rédigé sous la forme d'un article qui a été soumis à un journal pour publication. Cet article présente les avancées et les optimisations de calcul sur le modèle CAPTN qui couple les méthodes de l'automate cellulaire (CA) et de réseau d'aiguilles paraboliques (PTN). Ce modèle CAPTN bidimensionnel optimisé est évalué sur sa capacité à reproduire l'espacement des bras dendritiques primaires et l'angle d'orientation des joints de grains entre deux grains d'orientations différentes, développés dans la croissance directionnelle avec un gradient de la température constant G et une vitesse isotherme constante v_L. Il est montré que le modèle CAPTN peut reproduire la sélection de grains entre les branches primaires et la création de nouvelles branches à partir des branches tertiaires tant que la taille des cellules est suffisamment petite pour modéliser les interactions de soluté entre les branches. Dans ces conditions, les simulations convergent vers une distribution des branches primaires qui dépend de l'histoire des branches dendritiques, en accord avec les résultats expérimentaux et la théorie. Contrairement au modèle CA classique, l'angle d'orientation des joints de grains obtenu dans les simulations CAPTN est stable avec la taille des cellules et en bon accord avec les études PF précédentes pour différents gradients de la température. De plus, l'angle d'orientation des joints de grains suit une loi exponentielle avec le rapport G/v_L.

Simulation of dendritic grain structures with Cellular Automaton - Parabolic Thick Needle model

Y. Wu [(1)], O. Senninger [(1)]*, Ch.-A. Gandin[(1)]

(1) Mines Paris, PSL University, Center for material forming (CEMEF), UMR CNRS, 06904 Sophia Antipolis, France

Abstract

This article presents advances and computing optimizations on the CAPTN model which couples the Cellular Automaton (CA) and the Parabolic Thick Needle (PTN) methods. This optimized CAPTN model is evaluated on its ability to reproduce two physical quantities developed during directional growth in a constant temperature gradient G with isotherm velocity v_L: the interdendritic primary spacing and the grain boundary orientation angle between two grains of different orientations. It is shown that the CAPTN model can reproduce the grain selection between primary branches and creation of new branches from tertiary branches as long as cell size is sufficiently small to model solute interactions between branches. In these conditions, simulations converge toward a distribution of primary branches which depends on the history of the branching events, in agreement with experimental results and the theoretical $G^{-b}v_L^{-c}$ power law. Contrary to the classical CA model, the grain boundary orientation angle obtained in CAPTN simulations is stable with cell size and in good agreement with previous phase field studies for various gradients. Moreover, the grain boundary orientation angle is found to follow an exponential law with the ratio G/v_L.

Keywords: dendritic growth; modeling; CAPTN model; primary dendrite arm spacing; grain boundary orientation

1. Introduction

The numerical prediction of the dendritic grain structure developed in solidification processes is of scientific and industrial interest [1]. To be predictive, models have to

---

*Corresponding author

Email address: `oriane.senninger@minesparis.psl.eu` (O. Senninger [(1)])

reproduce physical phenomena involved in dendritic grain growth on wide range of spatial scale. However, such detailed models require heavy computation resources and are limited to small simulation domains.

The Dendritic Needle Network (DNN) and the Parabolic Thick Needle (PTN) methods aim to overtake these numerical limits by approximating dendritic branches to parabolas truncated by cylinders [2, 3, 4]. Solute diffusion and convection are solved in the liquid phase and dendrite tip growth velocities are computed from the integration of the solute composition gradient in the vicinity of dendrite tips. With the original methodologies, the DNN method is implemented on Graphics Processing Units (GPUs) using the finite difference method. Simulation domains can reach up to 100 mm^3 [5]. However, the solid fraction generated during grain growth was not modeled with this method and so the coupling of the microstructure evolution with thermal resolution was not achieved.

The Cellular Automaton (CA) method goes a step further in the approximation by limiting the modeling to the grain envelopes [6, 7]. The simulation domain is covered by a regular lattice of cubic cells named CA grid. The grain envelopes develop on the CA grid. Within each CA cell, the dendritic microstructure is simplified by an orthodiagonal quadrilateral (orthodiagonal octahedron in 3D), with half diagonals representing the length of the dendrite arms. Their lengths are aligned with the $< 1\ 0 >$ (resp. $< 1\ 0\ 0 >$) in 2D (resp. 3D) directions [8]. The growth is computed using analytical laws and the local temperature and composition fields, based on theoretical stationary dendrite tip kinetics models. This approach therefore does not consider solute interactions between grains. The implementation of microsegregation laws in the model permits to compute the solid fraction generated during grain growth and so to couple the modeling of the microstructure evolution to Finite Element (FE) resolution of the energy on the simulation domain [7, 9, 10]. This coupling is called the CAFE method and permits the modeling of grain structures developed in several liters components [9].

The complementary advantages of the CA and PTN methods have motivated their coupling in the so called CAPTN model [11]. The PTN method is used to compute the dendrite tip velocity at the apices of the polygons (polyhedrons in 3D) located in each CA cell. A first coupling has been performed with a FE implementation of the PTN model using adaptive mesh. It has been shown that this CAPTN method gives a description of equiaxed grain growth with a higher precision than the classical CAFE model. However, the strategy developed for the PTN implementation requires much heavier computational resources.

In this article, a new strategy is presented in Section 2 that limits the frequency of remeshing and so reduces drastically the computation time of the CAPTN model. A parametric study is performed in Section 3.1 to analyze the convergence of the model toward the theoretical kinetics in stationary state for an isolated dendrite tip. The model is then evaluated on its ability to reproduce two physical quantities developed during directional growth in a constant temperature gradient with a constant isotherm velocity: the primary dendrite arm spacing in Section 3.2 and the grain boundary orientation angle between two grains of different orientations in Section 3.3. Results are compared with CA simulations and with Phase-Field (PF) results [12].

2. Model description

The CAPTN model uses a FE implementation of the PTN method with an adaptive mesh keeping track of the growing parabolic dendrite tips. However, this mesh is updated very frequently, which is numerically time consuming. In this paper, a new remeshing strategy is proposed. It is described in Section 2.1.2. The CAPTN model is first applied using a frozen temperature approximation. Section 2.2 presents the coupling between the CA and PTN methods and its improvements compared to the previous implementation.

2.1. PTN finite element implementation

2.1.1. PTN theory and implementation

The PTN method [2, 3] is based on the approximation of dendrite branches as parabolas of curvature radius ρ_{tip} truncated by cylinders of radius r_{cyl} (represented in light green in Fig 1). To compute the growth velocity of tips, v_{tip}, solute diffusion is solved in the liquid around tips to obtain the liquid composition field, w^l_{PTN}. For this, the composition at solid/liquid interfaces is imposed to the liquid composition w^{ls} corresponding to the temperature of the tip, T_{tip}, i.e., $w^{ls} = (T_{tip} - T_M)/m$, where T_M is the melting temperature for the solvent, and m is the liquidus slope.

Equations (1a) and (1b) give the relations between ρ_{tip} and v_{tip}:

$$\rho_{tip}^2 v_{tip} = \frac{D^l d_0}{\sigma} \tag{1a}$$

$$\rho_{tip} v_{tip}^2 = \frac{2 \, D^{l2} \mathcal{F}^2}{d_0} \tag{1b}$$

where D^l is the interdiffusion coefficient in the liquid, $d_0 = -\Gamma^{ls}/m(1-k)w^{ls}$ is the solute capillary length, Γ^{ls} is the Gibbs-Thomson coefficient of the interface, and k is the segre-
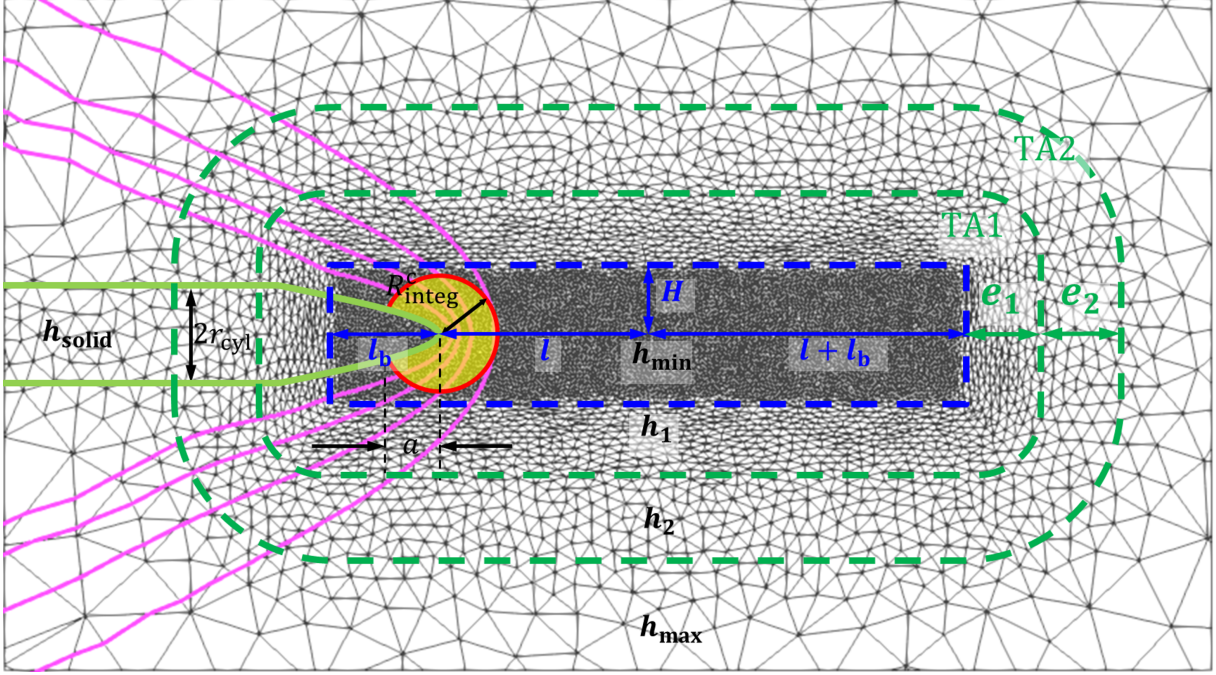
Figure 1: Sketch of the FE implementation of the PTN method. The truncated parabola (light green) moves in a liquid with solute isocomposition lines in pink. The integration area (surface Σ in yellow with its contour Γ in red) is a truncated disk of radius R_{integ} defined by the a parameter. The adaptive mesh generated for this branch is presented as a gray wireframe. The minimum mesh area with its dimensional parameters (l_b, l, and H) is delimited by the blue dashed box. The edge of the two transitional areas TA1 and TA2 of parameters e_1 and e_2 is marked with green dashed lines. The mesh size parameters h_{min}, h_{solid}, h_1, h_2, and h_{max} in each zone are written in black.

gation coefficient. The constant σ is the dendrite tip selection parameter. The quantity $\mathcal{F}$ in Eq. (1b) is called Flux Intensity Factor (FIF). To compute this quantity, an integration area of surface Σ (in yellow in Fig 1) and contour Γ (in red in Fig 1), parameterized with parameter a, which is the distance along the axis of the branch between the dendrite tip and the intersection of the contour Γ with the parabola, is defined in front of the tip. This integration area is a disk truncated by the parabola with its tip located at the center of the disk. Its radius R_{integ} is therefore $R_{integ} = \sqrt{a^2 + 2\,\rho_{tip}\,a}$. The FIF is thus computed at each time step using Eq. (2) where v_{tip} in the equation is taken at previous time step.

$$\mathcal{F} \approx \frac{-1}{4\sqrt{a/d_0}(1-k)w^{ls}} \left(\int_\Gamma \nabla w^l_{PTN} \cdot \mathbf{n} \mathrm{d}\Gamma + \frac{1}{D^l} \iint_\Sigma \mathbf{v_{tip}} \cdot \nabla w^l_{PTN} \mathrm{d}\Sigma \right) \qquad (2)$$

Values of integration parameter a are discussed in Section 3.1. A first FE implementation with adaptive mesh (called PTN mesh) has been described in Ref [11]. In this implementation, a minimum mesh size h_{min} was imposed at the solid/liquid interface, and the

mesh in the liquid was adapted to the solute composition gradient. This meshing strategy is efficient to compute (ρ_{tip}, v_{tip}) while limiting the number of elements in the mesh. However, it necessitates to remesh very frequently, which is numerical time consuming (see section 3.1). In this article, a new mesh strategy is proposed to limit the remeshing frequency without degrading the precision on the growth velocity.

2.1.2. Finite element metric and improved remeshing strategy

As for the first finite element implementation [11], the mesh size in the liquid far from parabolas is set to a maximum value h_{max}, because there is no need to compute the composition gradient ∇w^l_{PTN} with high resolution in this region. In addition, the mesh size in areas corresponding to the internal part of parabolas is set to a value h_{solid} (see Fig 1). In order to limit the remeshing frequency and to ensure a fine mesh in the integration area at each time step, a rectangular box is defined in front of each parabola using the orthogonal query method [13, 14]. This box, which is aligned with the predefined parabola trajectory, will be crossed by the growing branch and recreated as soon as the integration area reaches its edge. Parameters defining the dimensions and position of the box (half-height H, minimum length behind the tip l_b, total box length $2l + 2l_b$) are reported in Fig 1. These parameters are defined according to the dimensions of the integration area of the parabola at the time of creation of the box, identified by a c exponent in the followings. In simulations presented in Section 3, these parameters are scaled as $H = 1.5 R^c_{integ}$, $l_b = 1.2 a^c$, and $l = 10 \delta_{d_{Iv}}$ where $\delta_{d_{Iv}}$ is the diffusion length along the growth direction at stationary state. The definition of $\delta_{d_{Iv}}$ is given in Appendix 4. The mesh in this box has minimum mesh size h_{min}.

To facilitate the transitional from h_{max} to h_{min} at the creation of the box, two transition areas TA1 and TA2 of thickness e_1 and e_2 and mesh size h_1 and h_2 are defined (Fig 1). The choice of values of mesh size in the various regions of the simulation domain (h_{min}, h_{max}, h_{solid}, h_1 and h_2) is a compromise between the precision and the necessity to limit the number of elements in the simulation domain. This study will be detailed in Section 3 as part of a convergence study.

2.2. CAPTN method

This section is a recall of the CAPTN coupling and the adaptation of the CA model to this coupling [11]. Some improvements are also presented.

2.2.1. CA model adapted to the PTN coupling

The CA model aims at predicting the grain structure generated during solidification processes. This method is based on the approximation of dendritic grains as orthodiagonal quadrilaterals (resp. orthodiagonal octahedrons) in 2D (resp. in 3D) at the scale of CA cells (see Fig 2). The diagonals of the polygon are aligned with the dendrite branches. Grain growth is thus modeled by the growth of the branches which eventually capture neighboring cells by entering in their circumscribed circle. A new polygon attached to the captured cell is therefore created with the same diagonal orientation as the capturing polygon. The way the capturing polygon enters in the circumscribed circle of the captured neighboring cell permits to identify a capturing branch (S_0^μ for the green cell ν and S_2^μ for the blue cell ζ in Fig 2), which is propagated by the new polygon. This branch of the new polygon is called "principal branch" (S_0^ν for the green envelope, and S_0^ζ for the blue envelope). The branch opposite to this branch is called "opposite branch" (S_1^ν for the green envelope, and S_1^ζ for the blue envelope) and the two other branches are called "side branches" (S_2^ν and S_3^ν for the green envelope, and S_2^ζ and S_3^ζ for the blue envelope). One should note that the center of the polygon can be out of its corresponding cell.

2.2.2. Branches growth velocity

The principle of the CAPTN model is to compute the growth velocity of polygon branches by using the PTN method. A parabola truncated by a cylinder is thus defined on the PTN mesh for each branch growing on the CA grid (see Fig 2). For polygons created by the capture of a cell, the principal branch is the continuity of the already existing capturing branch. Therefore, its parabola is the same as the one of the capturing branch. Opposite branches are towards the existing branches, they can not grow, hence there is no parabola associated to the opposite branches. The initial length of side branches is limited to the thickness of the principal branch parabola. As shown in Fig 2, for the green polygon, the initial length of S_2^ν and S_3^ν are limited to the thickness of S_0^ν. In order to avoid perturbation of the growth of the principal branch due to the growth of side branches, the growth of side branches is permitted only when the length of the principal branch L_0^ν is such that $L_0^\nu > \min(3\,r_{cyl}, 2\sqrt{2}\,l_{CA})$. Their initial velocity is set to the velocity of the principal branch at this time. However, the PTN method can be applied to compute the growth velocity of a branch only if this branch is longer than the integration distance a. In this model, the PTN method is used to compute the velocity of a branch if its length is greater than $1.3\,a$. Before this, its kinetics is equal to the one at last time step. Nevertheless, this methodology can lead to the creation of branches which are very close
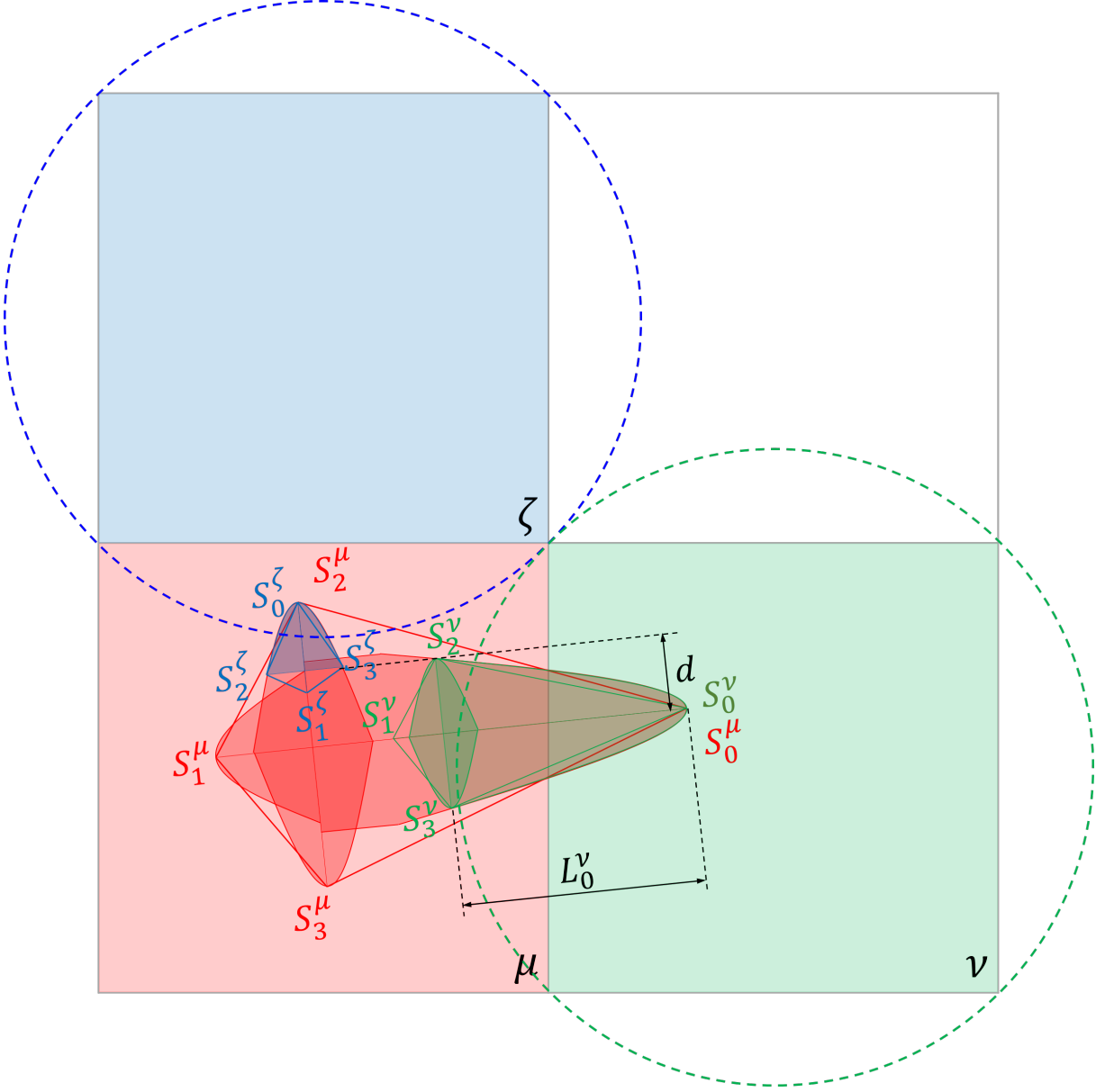
Figure 2: Process of grain propagation on the CA grid. The S_0^μ branch of the red polygon (resp. S_2^μ) associated to the red cell μ enters in the circumscribed circle of the green (resp. blue) cell ν (resp. ζ), leading to the creation of the green (resp. green) polygon and the switch of the cell state from liquid to containing growing dendritic branches. The length of the principal branch of the green polygon, S_0^ν, is denoted as L_0^ν. The distance between the principle branch of the red polygon S_0^ν and side branch of the blue polygon S_3^ζ is defined as d. A parabola is associated to each branch except for the opposite branches (S_1^ν for the green envelope, and S_1^ζ for the blue envelope) and the eliminated side branches (S_2^ζ and S_3^ζ for the blue envelope, if $d < 2\,r_{cyl}$).

115

to already existing branches growing in the same direction (an example is given in Fig 2 with branches identified by the distance d). In order to avoid such non-physical events, branches at a distance lower than $2\,r_{cyl}$ from an already existing branch growing in the same direction are not allowed to grow. In Fig 2, $d < 2\,r_{cyl}$, so S_2^ζ and S_3^ζ of the blue polygon cannot grow, so they do not have associated parabolas.

When a polygon associated to a cell has captured all its neighboring cells, the polygon associated to the cell is suppressed. In this case, the PTN mesh is coarsened to a mesh size equal to h_{max}.

3. Applications

The capacity of the CAPTN model to capture physical quantities of the columnar growth of dendrites is studied. For this, the growth of dendritic grains in a constant temperature gradient $G = \boldsymbol{G} \cdot \hat{\boldsymbol{z}}$ with isotherms moving at constant velocity $v_L = \boldsymbol{v_L} \cdot \hat{\boldsymbol{z}}$ is modeled, where $\hat{\boldsymbol{z}}$ is the unit vector in the vertical direction. As the model precision depends on the choice of numerical parameters, in particular those involved in the FE implementation of the PTN model, this section starts with a study of the convergence of the PTN model to theoretical kinetics in Section 3.1. The CAPTN model is then evaluated on its ability to reproduce primary dendrite arm spacing in Section 3.2 and grain boundary orientation angle in Section 3.3. This study is performed on a succinonitrile - 1.3wt.% acetone alloy whose properties are given in Table 1.

Table 1: Properties of the succinonitrile - 1.3wt.% acetone alloy

Quantity	Variable	Value	Unit	Ref
Nominal composition	w_0	1.3	wt.%	
Interdiffusion coefficient in liquid	D^l	1.270×10^{-9}	$m^2 \cdot s^{-1}$	[15]
Segregation coefficient	k	0.1		[15]
Liquidus slope	m	-3.02	$K \cdot wt\%^{-1}$	[16]
Liquidus temperature	T_L	327.314	K	[16]
Gibbs-Thomson coefficient	Γ^{ls}	6.4×10^{-5}	$K \cdot mm$	[17]
Selection parameter	σ	0.057		[12]

For all simulations, the initial temperature at the bottom of the simulation domain is equal to the liquidus temperature T_L (Table 1). At any time t and position z, the temperature is computed as $T(t,z) = T_L + G(z - z_0) - G \cdot v_L(t - t_0)$, with z_0 and t_0 the lowest coordinate of the simulation domain and the initial time, respectively.

116

3.1. Analyze of numerical parameters

As seen in Section 2.1, the FE implementation of the PTN model necessitates to calibrate numerical variables. Simulations presented in Sections 3.2 and 3.3 analyse the growth of columnar dendritic grains. In theory, the steady state of an isolated dendrite tip aligned with the temperature gradient is such that its velocity is equal to v_L and its curvature radius corresponds to the solution of Eq. (1a) with w^{ls} corresponding to the Ivantsov solution w^{ls}_{Iv} [18, 11]. In this configuration, the radius of curvature is written as $\rho_{tip_{Iv}}$ and the tip undercooling ΔT_{tip} is equal to $\Delta T_{Iv} = -m(w^{ls}_{Iv} - w_0)$.

In order to calibrate numerical parameters for simulations, a single parabolic branch is placed in a box of 20×20 mm². It is aligned with a temperature gradient $G = 0.475$ K $\cdot$ mm^{-1} and a constant isotherm velocity $v_L = 0.086$ mm $\cdot$ s^{-1}. In these conditions, the theoretical curvature radius and undercooling of the tip are given in Table 2 for three values of the velocity.

Table 2: Ivantsov solutions for different isotherm velocities using the material parameters listed in Table 1

v_L (mm $\cdot$ s^{-1})	Ω	$\rho_{tip_{Iv}}$ (mm)	$\delta_{d_{Iv}}$ (mm)	ΔT_{Iv} (K)
0.043	0.2988	2.620×10^{-3}	0.0176	1.4441
0.086	0.3386	1.805×10^{-3}	0.0099	1.7208
0.172	0.3811	1.242×10^{-3}	0.0056	2.0496

The Numerical parameters influencing the kinetics of the tip and analyzed in this section are the integration parameter a, the minimum mesh size h_{min} and the time step Δt. Other parameters are scaled using parameters given in Table 3. The integration parameter a has to be big enough to compute the solute gradient in front of the tip with a good precision. It is therefore scaled as $a = \frac{\delta_{d_{Iv}}}{\alpha}$ where α is a dimensionless constant and

$$\delta_{d_{Iv}} = 2\Omega D^l/v_L \tag{3}$$

the diffusion length along the growth direction of the Ivanstov solution. Ω is the supersaturation, defined as $\Omega = [w^{ls}_{Iv} - w_0]/[(1 - k)w^{ls}_{Iv}]$. The minimum mesh size h_{min} has to be small enough to describe the parabolic branch tip and the solute composition field around the tip. Similarly, the time step Δt has to be small enough to keep track of the solute composition field. These quantities are thus scaled such that $h_{min} = \gamma \rho_{tip_{Iv}}$ and $\Delta t = \tau \frac{h_{min}}{v_L}$ with γ and τ being dimensionless parameters.

117

Fig 3 presents the average undercooling ΔT_{tip} and curvature radius ρ_{tip} computed at steady state for different values of parameters α, γ and τ. Error bars represent the standard deviation of ΔT_{tip} and ρ_{tip} at steady state. For each curve, other parameters are set to the value 0.5. It is observed that whereas the parameter τ has almost no influence on results, the variation of the minimum mesh size with γ has a large effect on the precision of the simulation. It is also observed that numerical parameters have a higher influence on the precision of the undercooling than on the curvature radius.

Taking the same simulation domain and parameters $\alpha = 0.5$, $\gamma = 1$ and $\tau = 1$, the simulation using the PTN mesh described in Ref [11] takes 14 hours on 8 CPU processors to displace the tip by 9.25 mm, with 2714 times of remeshing, whereas it only takes 2 hours for the same number of processors to displace it by the same distance with the new meshing strategy, with only 93 times of remeshing. The simulation time is therefore drastically reduced with the new mesh strategy.

For a balance between accuracy and the efficiency of computation, dimensionless parameters are set to $\alpha = 0.5$, $\gamma = 1.5$ and $\tau = 1$ for simulations in Sections 3.2 and 3.3. The undercooling of this selection of parameters is $1.928\,\mathrm{K}$ in average with standard deviation $6.551 \times 10^{-4}\,\mathrm{K}$, and the curvature radius of this selection of parameters is $1.775 \times 10^{-3}\,\mathrm{mm}$ in average with standard deviation $2.484 \times 10^{-5}\,\mathrm{mm}$. These results are the same as the results of $\alpha = 0.5$, $\gamma = 1.5$ and $\tau = 0.5$ in Fig 3, which are $1.924\,\mathrm{K}$ in average with standard deviation $4.972 \times 10^{-4}\,\mathrm{K}$ for undercooling, and $1.776 \times 10^{-3}\,\mathrm{mm}$ in average with standard deviation $2.624 \times 10^{-5}\,\mathrm{mm}$ for radius curvature. Other numerical parameters are set to values given in Table 3. The minimum value of the steady state radius of truncating cylinder is $r_{cyl}^{min} = \sqrt{2\,a\,\rho_{tip_{Iv}}}$. If the radius of truncating cylinder r_{cyl} is greater than r_{cyl}^{min}, the kinetics of the branch is not influenced by the truncation [3, 11]. Thus, in our application, r_{cyl} is fixed as $r_{cyl} = 2\,r_{cyl}^{min}$.

3.2. Primary dendritic arm spacing for a single crystal

The spacing developed between primary branches during directional growth is a complex phenomenon. Experimental studies on various alloys [16, 19, 20] have shown that for a given temperature gradient and isotherms velocity, this spacing is not unique and can vary along the solidification front, giving a λ_1 distribution limited by two values λ_1^{min} and λ_1^{max}. This result has been retrieved in simulations using cellular automaton [21] and DNN methods [22]. This possible range of λ_1 values has been proved theoretically by Warren and Langer [23] who have shown that the spacing between primary branches is history dependent. Analytical studies using more restrictive assumptions [24, 25] predict
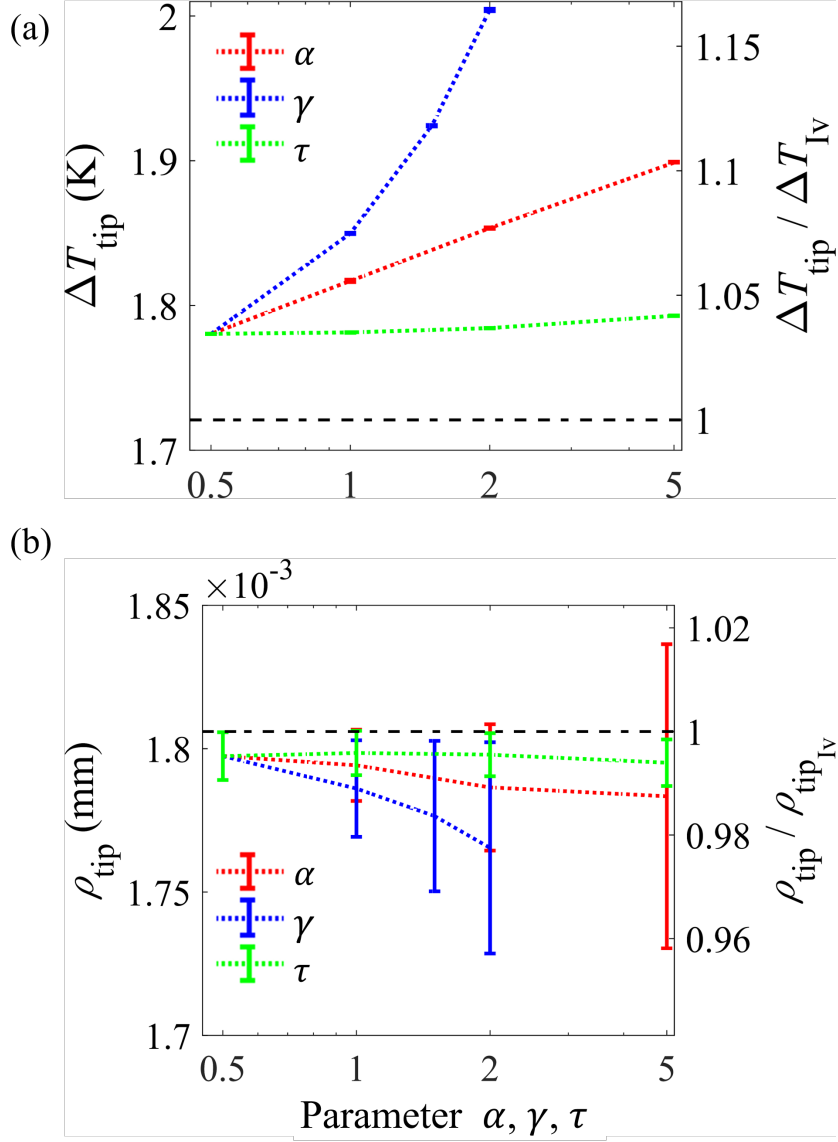
118

Figure 3: Evolution of steady state quantities (a) ΔT_{tip} and $\Delta T_{tip}/\Delta T_{Iv}$ and (b) $\rho_{tip_{Iv}}$ and $\rho_{tip}/\rho_{tip_{Iv}}$ according to numerical parameters (red) α, (blue) γ, and (green) τ for a single parabolic branch aligned with a constant temperature gradient $G = 0.475 \text{ K} \cdot \text{mm}^{-1}$ and a constant isotherm velocity $v_L = 0.086 \text{ mm} \cdot \text{s}^{-1}$. Black dashed lines correspond to Ivantsov solutions presented in Table 2. For each curve, only one parameter is varied, while the others are maintained to their minimum value, 0.5.

Table 3: Simulation parameters used in Sections 3.2 and 3.3

Variable	Name	Unit	Value
Minimum PTN mesh size	h_{min}	$\rho_{tip_{Iv}}$	1.5
PTN mesh size in TA1	h_1	h_{min}	3
PTN mesh size in TA2	h_2	h_{min}	10
PTN mesh size in solid	h_{solid}	h_{min}	10
Maximum PTN mesh size	h_{max}	h_{min}	50
Integration distance	a	$\delta_{d_{Iv}}$	2
Distance from the tip to the center of the fine mesh rectangle at its creation	l	$\delta_{d_{Iv}}$	10
Distance from the tip to the end of the fine mesh rectangle at its creation	l_b	a	1.2
Half height of the fine mesh rectangle	H	R^c_{integ}	1.5
TA1 thickness	e_1	l	1
TA2 thickness	e_2	l	1

that for isotherms velocities higher than a transition rate $v_{tr} = GD^l/[(1/k - 1)mw_0]$, the primary spacing should evolve as $\lambda_1 \propto v_L^{-1/4} G^{-1/2}$. In experimental studies, dependencies according to $\lambda_1 \propto v_L^{-b} G^{-c}$ with scattered values of coefficients b and c have been found.

The CAPTN model is now used to demonstrate its capability to model the branching of dendrites and the solute interaction between dendrite branches, hence yielding a stable selection of the primary dendrite arm spacing during directional growth. To analyze this, a single seed with 5 μm branch length aligned with the temperature gradient is placed at the bottom center of a box of 10×17 mm^2 in width and height. During the simulation, the grain captures neighboring CA cells and propagates on the whole width of the domain, forming a network of dendrite branches which then grow vertically, leading to a selection of primary branches. An example of the dendrite network generated during a CAPTN simulation is presented in Fig 4. The spreading of the grain on the simulation domain through secondary branches can clearly be observed on the bottom part of the domain. Elimination and creation of tertiary branches can also be spotted during grain growth.

Fig 5 shows the solidification front at $t = 135$ s for the same simulation. CA cells containing a growing polygon, i.e., with at least one liquid neighboring cell, are presented in white empty squares and the solute composition field is presented as wireframe on the PTN mesh. The area with fine mesh defined in Section 2.1 can be observed in front of each parabolic tip with a liquid composition close to the alloy nominal composition (in blue). Inside branches, the composition is imposed by the Dirichlet condition to the liquidus composition corresponding to the local temperature. One can also observe the coarse mesh on the lower part of the image, as CA cells are deallocated.

To measure primary dendrite arm spacing in simulations, a thickness δy of the solidification front is defined from the position of the highest primary branch. This thickness
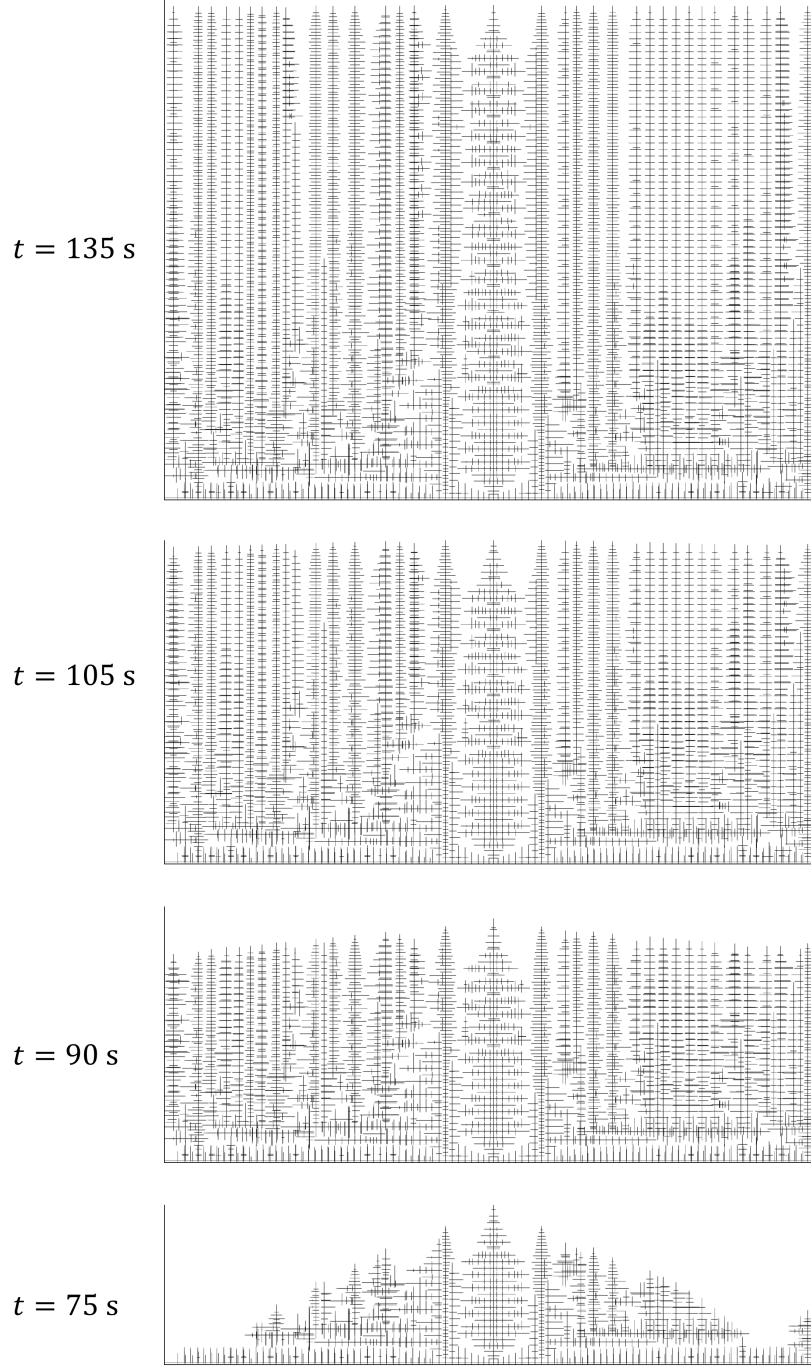
$t = 135$ s

$t = 105$ s

$t = 90$ s

$t = 75$ s

Figure 4: Dendrite needle network at different times ($t = 75$ s, $t = 90$ s, $t = 105$ s, and $t = 135$ s) in a CAPTN simulation for $G = 0.475$ K $\cdot$ mm^{-1}, $v_L = 0.086$ mm $\cdot$ s^{-1} and $l_{CA} = 0.1$ mm. The domain width is 10 mm.
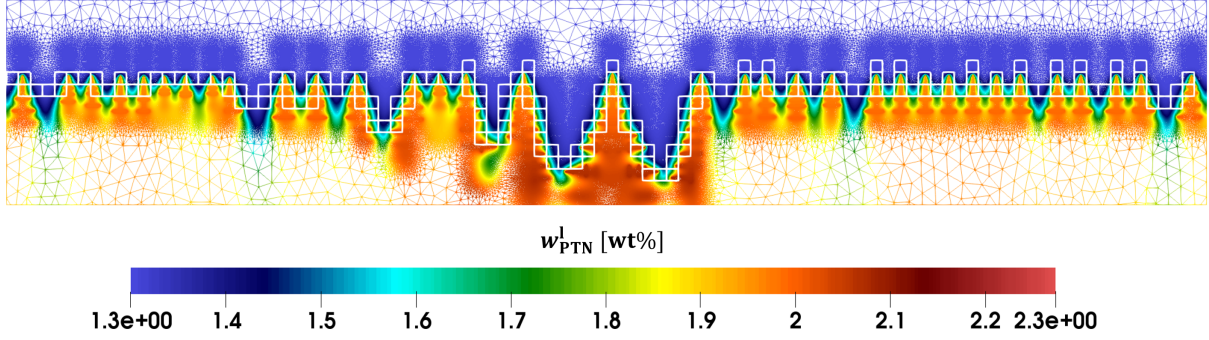
121

Figure 5: Wireframe of solute composition field in the liquid phase at the solidification front at $t = 135$ s in a CAPTN simulation for $G = 0.475$ K$\cdot$mm^{-1}, $v_L = 0.086$ mm$\cdot$s^{-1} and $l_{CA} = 0.1$ mm. CA cells containing a growing polygon are represented as white squares. The domain width is 10 mm.

is taken as $\delta y = 1/2\bar{\lambda}_1$, where $\bar{\lambda}_1$ is the average value of λ_1 measured in the simulation. The spacing between branches with tip aligned with the gradient located in this thickness is then measured. This measurement is recursive until the $\bar{\lambda}_1$ used for δy is the same as the $\bar{\lambda}_1$ measured at this time. Fig 6 (a) shows the distribution of measured λ_1 for various cell size and Fig 7 (a) shows the evolution of the average λ_1, and of the maximum and minimum value of λ_1 with l_{CA} for $G = 0.475$ K$\cdot$mm^{-1} and $v_L = 0.086$ mm$\cdot$s^{-1}. It can be observed on Figures 4 and 5 for $l_{CA} = 0.1$ mm that the primary spacing around the central branch corresponding to the initial position of the seed is quite large. This spacing is the highest measured value in Fig 6 (a). This large spacing can be related to the solute distribution around secondary branches in Fig 5 at the beginning of the simulation preventing the growth of tertiary branches and so limiting the filling by new tertiary branches. Furthermore, the spacing between primary branches far from the center of the simulation domain (edge branches set apart) is quite small and close to $\lambda_1 \approx 0.2$ mm. These side areas have similar histories with almost no elimination of branches during growth.

It is observed in Fig 6 (a) and Fig 7 (a) that the distribution of λ_1 converges toward a distribution with an average value $\bar{\lambda}_1$ around 0.26 mm with the decrease of cell size. As this value is lower than 0.4, it seems logical that the simulation using $l_{CA} = 0.4$ mm is not capable to predict this spacing as the spacing between branches is artificially constrained with this parameter value.

Figures 6 (b) and (c) show the evolution of the distribution of λ_1 with the temperature gradient and isotherm velocity respectively. In addition, Figures 7 (b) and (c) present the evolution of λ_1^{min}, $\bar{\lambda}_1$ and λ_1^{max} according to these two values. These studies use a CA cell size $l_{CA} = 0.1$ mm.
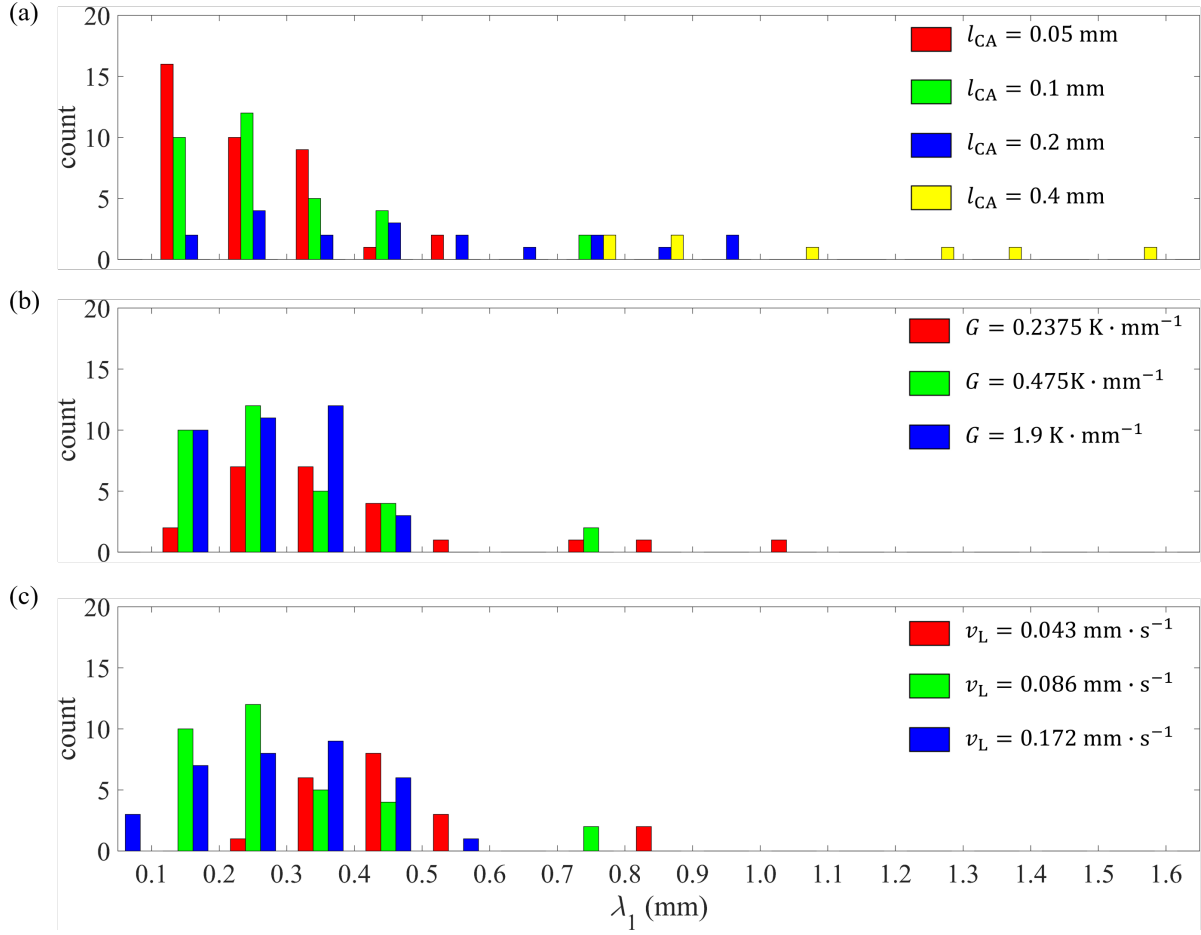
122

Figure 6: Distribution of λ_1 according to (a) cell size for $G = 0.475$ K $\cdot$ mm^{-1} and $v_L = 0.086$ mm $\cdot$ s^{-1}, (b) temperature gradient for $l_{CA} = 0.1$ mm and $v_L = 0.086$ mm $\cdot$ s^{-1} (c) isotherm velocity for $l_{CA} = 0.1$ mm and $G = 0.475$ K $\cdot$ mm^{-1}

It can be observed that the average value of λ_1 tends to decrease with both G and v_L. Moreover, theoretical laws proportional to $G^{-1/2}$ and $v_L^{-1/4}$ are respectively reported in Figures 7 (b) and (c). It can be observed that whereas the $v_L^{-1/4}$ dependency fits quite well the evolution of $\bar{\lambda}_1$ with v_L, the $G^{-1/2}$ dependency seems to overestimate the variation of $\bar{\lambda}_1$ with the temperature gradient. It is also observed that the variation of temperature gradient has a stronger effect on the range of λ_1 values compared to the velocity, with an enhanced variation between λ_1^{max} and λ_1^{min} at low G compared to high G.

3.3. Diverging grain boundary orientation angle for a bi-crystal

The inclination of the grain boundary between two grains with different inclinations growing in a constant temperature gradient G with a constant isotherm velocity v_L has
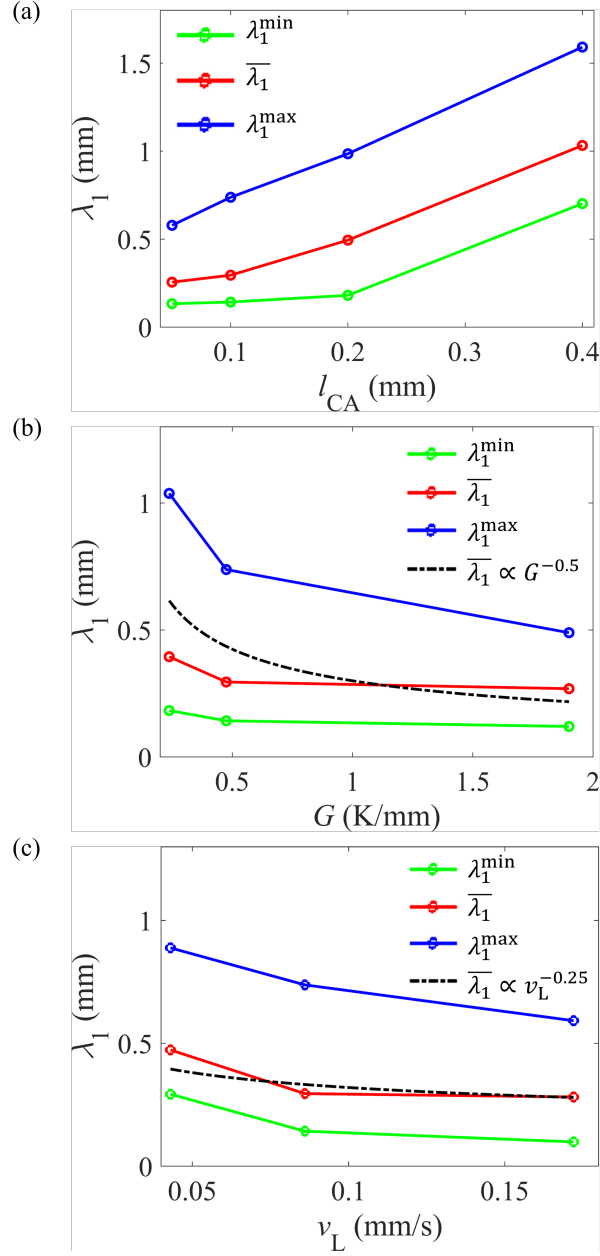
123

Figure 7: λ_1^{min}, $\bar{\lambda}_1$ and λ_1^{max} according to (a) cell size for $G = 0.475$ K $\cdot$ mm^{-1} and $v_L = 0.086$ mm $\cdot$ s^{-1}, (b) temperature gradient for $l_{CA} = 0.1$ mm and $v_L = 0.086$ mm $\cdot$ s^{-1} (c) isotherm velocity for $l_{CA} = 0.1$ mm and $G = 0.475$ K $\cdot$ mm^{-1}. Black lines are theoretical laws with $G^{-0.5}$ (b) and $v_L^{-1/4}$ (c) dependencies fitted on $\bar{\lambda}_1$ simulation values.

124

been studied using PF and CA methods [7, 12, 26, 27, 28]. It has been shown that the value of the angle of the grain boundary is contained between two theoretical limits: the Favorably Oriented Grain (FOG) [12, 28, 29] and the Geometrical Limit (GL) [12, 28]. The angle θ_D of the grain boundary formed by the diverging primary directions of two grains with inclinations $\alpha_1 = 30°$ for the left grain and $\alpha_2 = 10°$ for the right grain with the direction of temperature gradient has been analyzed in more details using PF and CA simulations [12]. In Fig 8 the blue line corresponds to the value given by the GL model and the red line corresponds to the value given by the FOG model. The central line of Figures 8 (West, Center and East) present the diverging grain boundary angle obtained with these two numerical methods as a function of the CA cell size and for $v_L = 0.086$ mm $\cdot$ s^{-1} and three values of the temperature gradient: (West) $G = 0.2375$ K $\cdot$ mm^{-1}, (Center) $G = 0.475$ K $\cdot$ mm^{-1}, and (East) $G = 1.9$ K $\cdot$ mm^{-1}. The angle given by the PF method (dashed line) is constant, with a reported variation only for the center configuration (gray window), $G = 0.475$ K $\cdot$ mm^{-1}. The angle given by the CA model (purple dots) varies continuously from the GL to the FOG value as cell size increases. This result has been explained by the fact that angle θ_D is linked to the secondary dendrite arm spacing preceding tertiary branching forming the grain boundary $\bar{\Lambda}$. Therefore, whereas this distance is correctly reproduced in PF simulations, it is cell size dependant in CA simulations, and values given by CA simulations are equal to the ones obtained with PF simulations if the cell size is equal to this physical spacing.

Simulations are reproduced using the CAPTN model. For this, two seeds with 5 μm initial branch length are placed at the bottom of a rectangular domain, the [1 0] branch of the left one (resp. right one) making an angle $\alpha_1 = 30°$ with the temperature gradient (resp. $\alpha_2 = 10°$). Fig 9 shows the solidification front at a given time for $G = 0.475$ K $\cdot$ mm^{-1}, $v_L = 0.086$ mm $\cdot$ s^{-1} and a cell size $l_{CA} = 0.2$ mm. The solute composition field in the liquid is presented as wireframe on the PTN mesh. As for Fig 5, a rectangular zone with fine mesh can be observed in front of each parabolic tip with an inclination corresponding to the growth direction of the tip. A coarser mesh is observed in the liquid located far from the solidification front and in the area where cells have been deallocated, i.e., with no remaining liquid neighboring cell. CA cells containing a growing polygon appear as black squares for the left grain and red squares for the right grain.

Fig 10 shows the needle network formed at the end of this simulation (a) and the corresponding cell structure (b). Black (resp. red) lines and cells are associated to the left grain (resp. right grain). The distance between highest tips of the two grains is
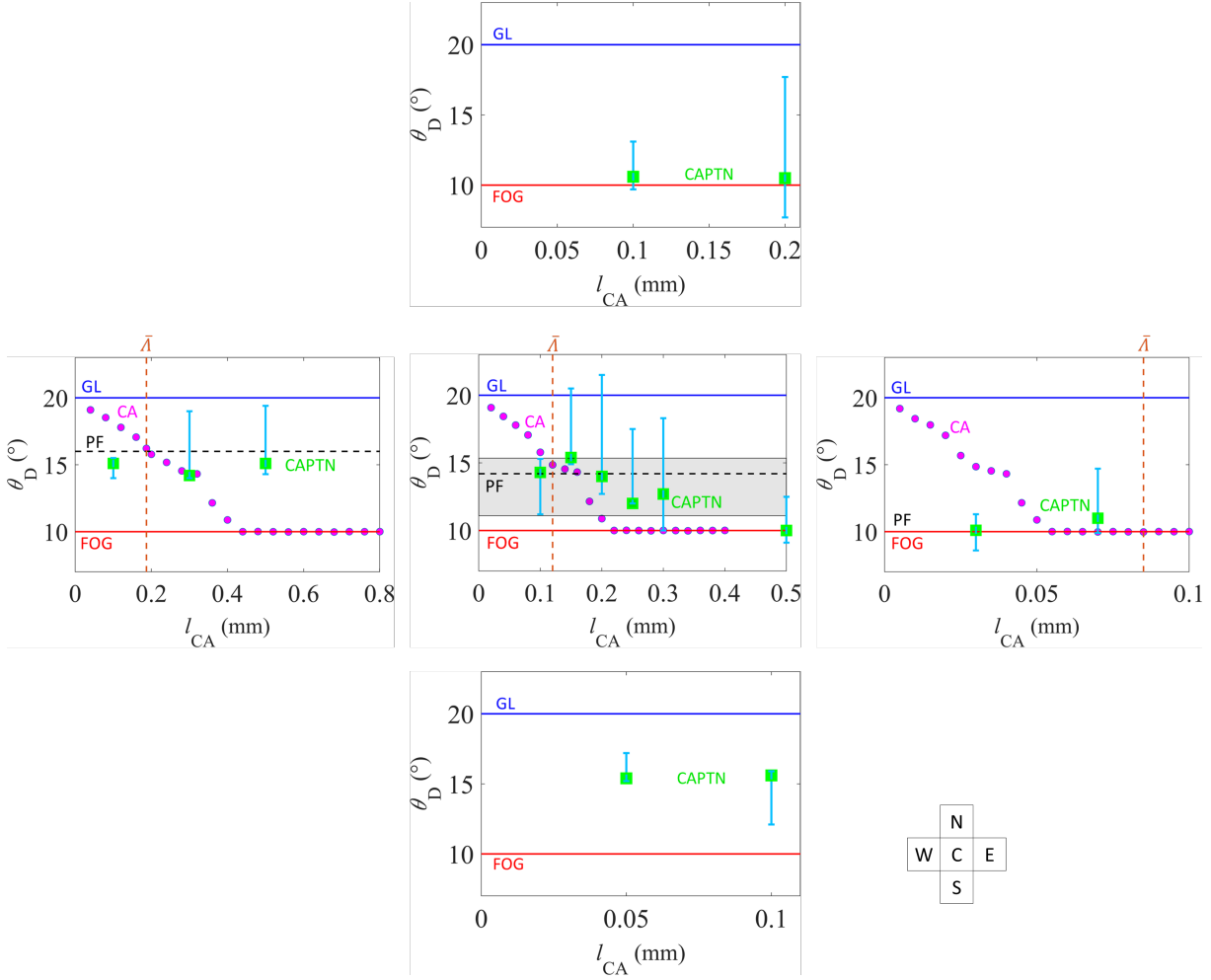
Figure 8: Evolution of the diverging grain boundary orientation angle θ_D according to l_{CA}. The blue and red lines are respectively the GL and the FOG models. Results of CAPTN simulations are presented as green squares and CA results [12] are presented as purple circles. The black dashed line is the phase field result, with variations reported as a gray zone [12]. The dashed orange line corresponds to the secondary dendrite arm spacing preceding tertiary branching. (Center) $G = 0.475\ \mathrm{K \cdot mm^{-1}}$ and $v_L = 0.086\ \mathrm{mm \cdot s^{-1}}$ (West) $G = 0.2375\ \mathrm{K \cdot mm^{-1}}$ and $v_L = 0.086\ \mathrm{mm \cdot s^{-1}}$ (East) $G = 1.9\ \mathrm{K \cdot mm^{-1}}$ and $v_L = 0.086\ \mathrm{mm \cdot s^{-1}}$ (North) $G = 0.475\ \mathrm{K \cdot mm^{-1}}$ and $v_L = 0.043\ \mathrm{mm \cdot s^{-1}}$ (South) $G = 0.475\ \mathrm{K \cdot mm^{-1}}$ and $v_L = 0.172\ \mathrm{mm \cdot s^{-1}}$.
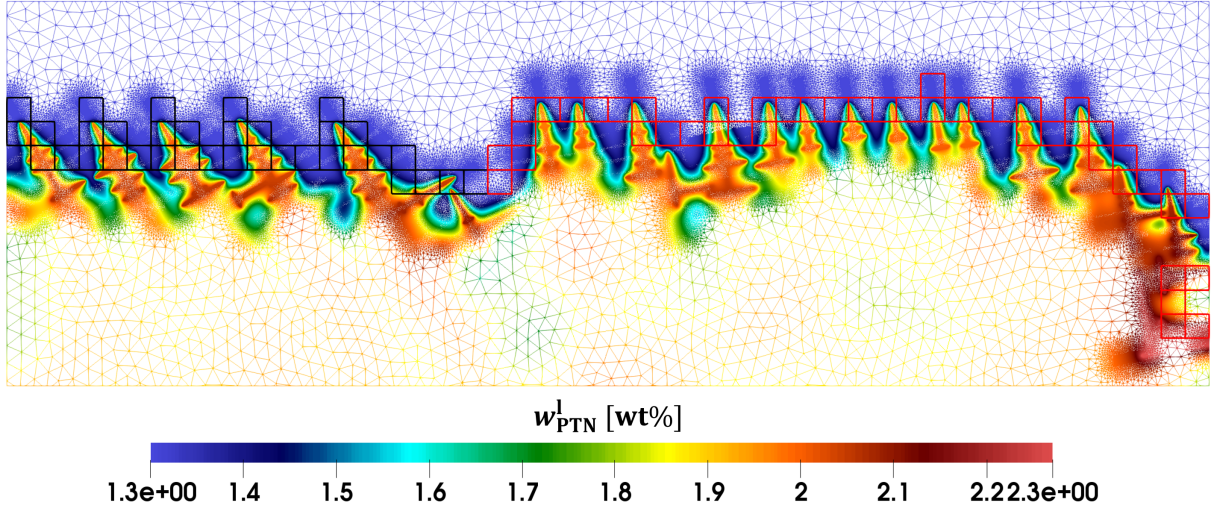
126

Figure 9: Wireframe of solute composition field in the liquid phase at the solidification front $t = 300$ s for the bi-crystal CAPTN simulation with $G = 0.475$ K $\cdot$ mm^{-1}, $v_L = 0.086$ mm $\cdot$ s^{-1} and $l_{CA} = 0.2$ mm. CA cells containing a growing polygon are represented as black squares for the left grain and red squares for the right grain. The domain width is 10 mm.

noted δ. This distance increases at the beginning of the simulation to reach a steady state value δ_{st}. The evolution of this distance is theoretically computed using velocities given by the Ivantsov growth law described in Section 3.1. It is obtained that the δ value reaches $99\%\delta_{st}$ at $t_{st} \approx 100$ s. The position of the solidification front at t_{st} is indicated as a horizontal orange dot line in Fig 10 and is located at a distance d_{st} from the bottom of the simulation domain. The angle of inclination between the grain boundary and the temperature gradient, θ_D, is measured by the inclination of the line between the position of the interface at d_{st} and at the end of the simulation (green dashed line on Fig 10). Two extreme angles are also measured for interfaces located above $2\,d_{st}$ (see the cyan lines on Fig 10).

Angles measured with the CAPTN method as a function of the CA cell size and for various couples (G, v_L) are reported in Fig 8 as green squares. In Fig 8 Center, it is observed that, contrary to CA simulations, the angle θ_D computed with the CAPTN model is not dependent on cell size, even for l_{CA} much higher than the one corresponding to the secondary dendrite arm spacing preceding tertiary branching. It is however observed that if cell size is too large to correctly reproduce solute interactions between branches, the CAPTN model retrieves the FOG limit (see Fig 8 Center). For cell size lower than this upper limit, values obtained are in good agreement with the one of the PF method no matter the value of l_{CA}. This result indicates that the CAPTN model reproduces the
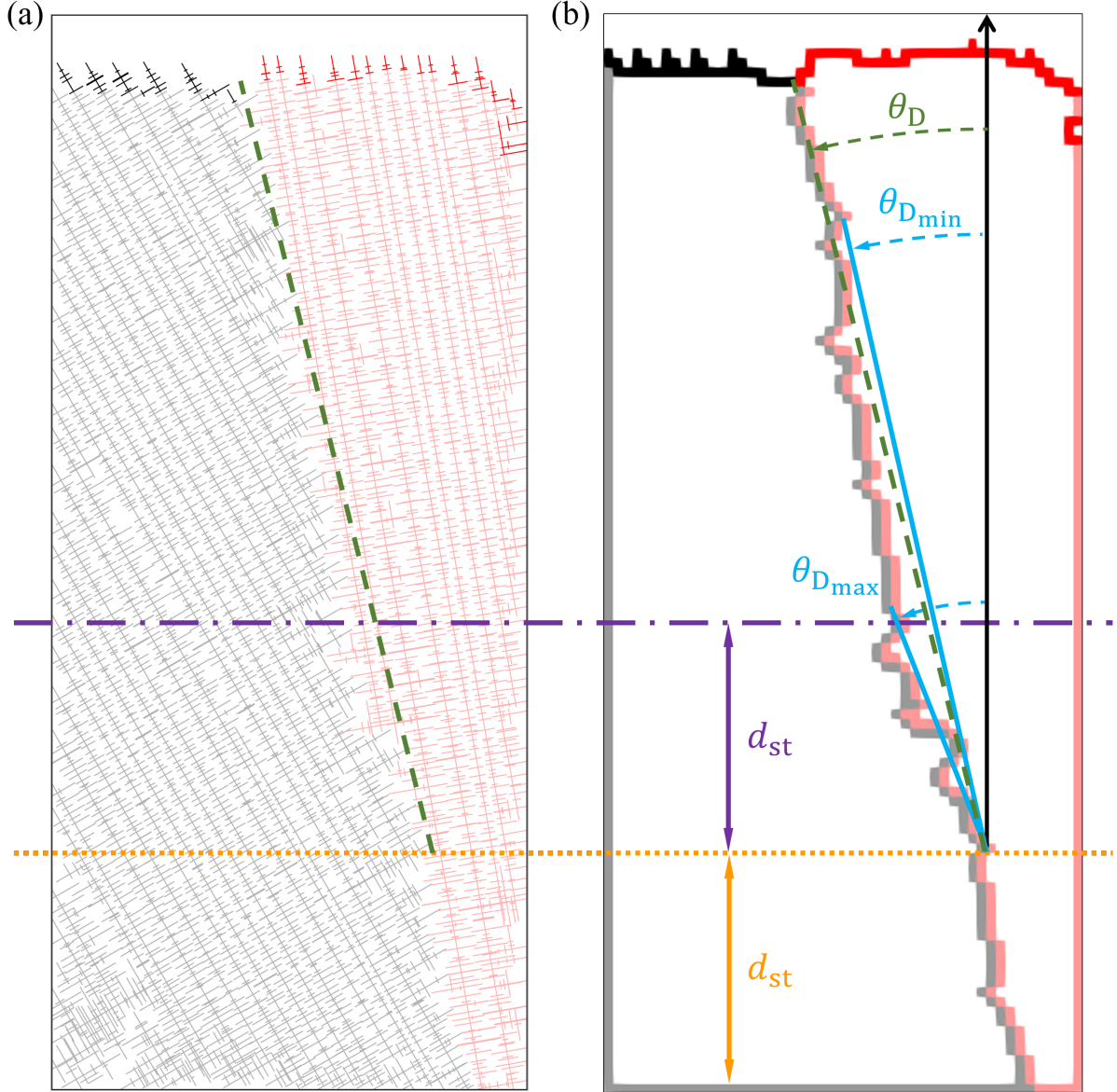
127

Figure 10: (a) Needle Network and (b) cell structure at the end of the CAPTN simulation $t = 300$ s for $G = 0.475$ K $\cdot$ mm^{-1}, $v_L = 0.086$ mm $\cdot$ s^{-1} and $l_{CA} = 0.2$ mm. The width of the domain is 10 mm. The black color is associated to the left grain and the red color to the right grain. The CA cells containing a growing polygon, drawn in Fig 9, are represented in full opacity, and other CA cells at the grain and domain boundaries are represented in lower opacity. The white area contained within the contour defined by the black (resp. red) cell belong to the left (resp. right) grain, while the white area at the top of the domain is liquid. In (a), the branches belonging to the CA cells containing a growing polygon are drawn in full opacity, and other branches are drawn in lower opacity.

128

$\bar{\Lambda}$ spacing, even for CA cell values much higher than this spacing. The minimum and maximum values of θ_D for a cell size lower than the $\bar{\Lambda}$ spacing are in excellent agreement with the range of values predicted by the PF simulations as they coincide with the range of the gray window. In addition, both models predict a decrease of θ_D as the temperature gradient increases for $v_L = 0.086$ mm $\cdot$ s^{-1}. This is verified in Fig 8 West, Center, and East. CAPTN simulations also predict an increase of θ_D as the isotherm velocity increases, as shown in Fig 8 North, Center, and South. These two tendencies lead to the profile of θ_D according to G/v_L displayed in Fig 11 (a) where the average θ_D value decreases from $\theta_D \simeq 15°$ at low G/v_L values to reach the FOG limit at $G/v_L \simeq 10$ K $\cdot$ s $\cdot$ mm^{-2}. The relation between θ_D and G/v_L can be approximated as

$$\frac{\theta_D - \theta_{FOG}}{\theta_{GL} - \theta_{FOG}} \propto \exp(-\beta \frac{G}{v_L}) \tag{4}$$

where θ_{GL} and θ_{FOG} are the GL and FOG limits, respectively, and $\beta > 0$. The value $\beta = 0.183$ is used in Fig 11 (a).

The step between stationary primary dendrite tips of two grains at steady state, δ_{st}, was identified as a main parameter for the control of the grain boundary orientation in Ref [28]. However, it can be observed on Fig 11 (a) that two identical values of G/v_L give similar values of θ_D but different values of δ_{st} (see Fig 11 (b)). Therefore, it seems that θ_D is a function of G/v_L rather than an function of δ_{st}, explaining the form chosen for Eq. 4. Possible relations between θ_D and $\bar{\Lambda}$ should be the topic of further investigations, following the findings reported in Ref [12].

4. Conclusions

This article presents advances on the CAPTN model which couples the cellular automation (CA) and the Parabolic Thick Needle (PTN) methods. Optimizations on the meshing strategy are presented which permit to reduce drastically computation time. A numerical parametric study is performed which shows that the model converges toward theoretical growth solutions as the thinness of the mesh and the size of the integration area are increased. This optimized CAPTN model is then evaluated on its ability to reproduce two physical quantities developed during directional growth in a constant temperature gradient G with a constant isotherm velocity v_L: the primary dendrite arm spacing λ_1 and the diverging grain boundary orientation angle θ_D between two grains of different orientations. The grain selection between primary branches and creation of new branches
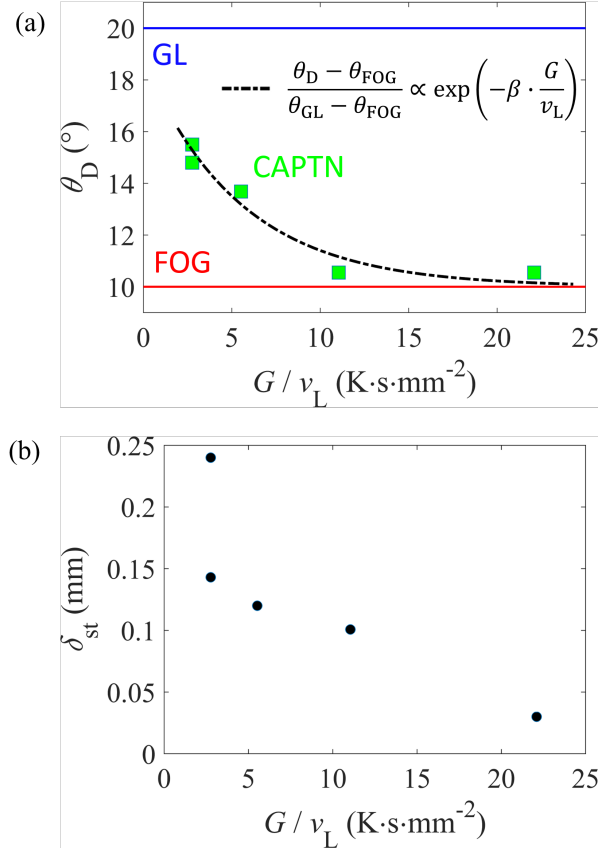
129

Figure 11: Evolution of (a) θ_D computed in CAPTN simulations and (b) δ_{st} computed by the Ivantsov growth law with G/v_L. In (a), the GL and FOG limits are indicated as blue and red lines respectively. The trend of θ_D is fitted by the mathematical formula $(\theta_D - \theta_{FOG})/(\theta_{GL} - \theta_{FOG}) \propto \exp(-\beta\,G/v_L)$, where θ_{GL} and θ_{FOG} are the GL and FOG limits, respectively, and $\beta > 0$.

from secondary and tertiary branches is well simulated as long as cell size is sufficiently small to model solute interactions between branches. In these conditions, simulations converge toward a distribution of primary branches which depends on the history of dendrite branches. This result is in agreement with the theory of Warren and Langer [23] and experimental results. Gradient and velocity dependencies on average values of these distributions have been compared with Hunt [24] and Kurz-Fisher [25] theories and are coherent with G^{-b} and v_L^{-c} power laws. The study on the grain boundary orientation angle has revealed that, contrary to the classical CA model, the angle obtained in CAPTN simulations does not depend on cell size for a large range of cell size. This angle has been computed for various gradients and isotherm velocities and is in good agreement with previous phase field studies [12]. Moreover, the diverging grain boundary orientation angle is found to be a monotonously decreasing function of the ratio G/v_L, and the trend can

130

be expressed by an exponential law. These promising validations and mesh optimizations will permit to extend the model to 3D simulations.

Acknowledgments

Appendix A. Diffusion length

A parabola of radius ρ_{tip} and velocity v_{tip} moves at steady state in the x direction in an infinite 2D domain. Cartesian (x, y) coordinates are defined in Fig A.12 along with (ξ, η) parabolic coordinates.
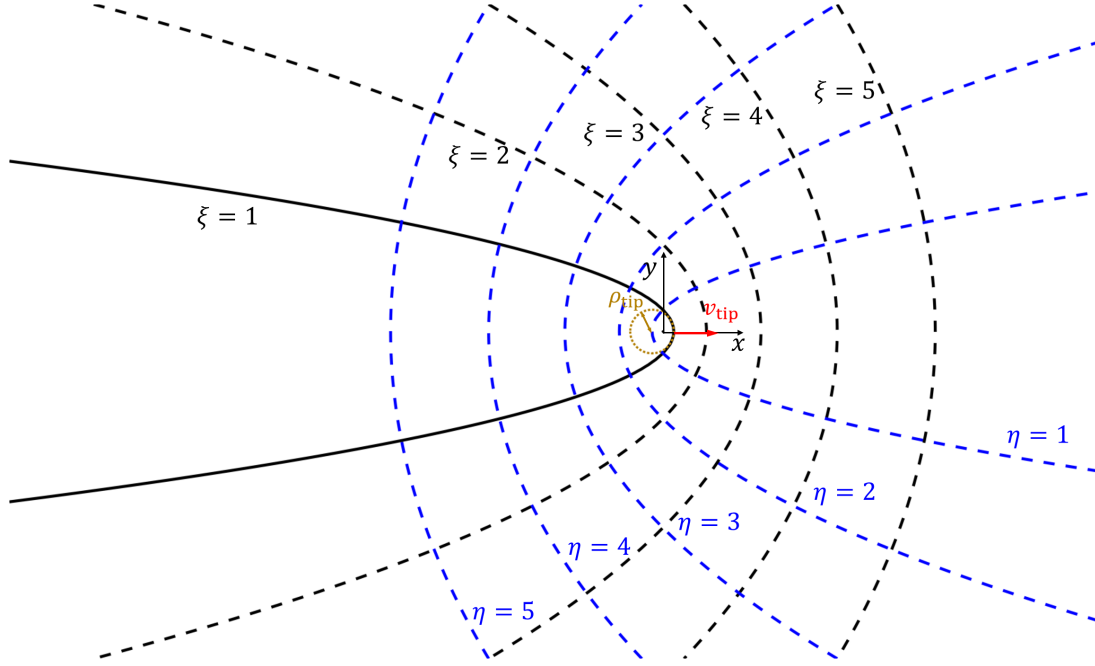
Figure A.12: Parabolic and Cartesian coordinates used for the calculation of the diffusion length

The relations between these two systems of coordinates is the following:

$$
\begin{array}{lll}
\text{Parabolic} & \rho_{\mathrm{tip}}\xi^2 = x + \sqrt{x^2 + y^2} & \rho_{\mathrm{tip}}\eta^2 = -x + \sqrt{x^2 + y^2} \\
\text{Cartesian} & x = \frac{\rho_{\mathrm{tip}}}{2}\left(\xi^2 - \eta^2\right) & y = \rho_{\mathrm{tip}}\xi\eta
\end{array}
\tag{A.1}
$$

In these steady state conditions, the composition field in the liquid is given by the Ivantsov solution [18]:

$$
w^{\mathrm{l}}(\xi) = w_0 + (1-k)w^{\mathrm{ls}}\sqrt{\pi\,\mathrm{Pe}} \cdot \mathrm{e}^{\mathrm{Pe}} \cdot \mathrm{erfc}(\xi\sqrt{\mathrm{Pe}})
\tag{A.2}
$$

131

with $\mathrm{Pe} = \rho_{\mathrm{tip}} v_{\mathrm{tip}} / 2 D^l$.

The diffusion length at the dendrite tip along its growing direction is defined as twice the intersection of the tangent of the composition along the x axis at the solid/liquid interface and the nominal composition w_0. From Eq. (A.2), the expression of the composition field on the x axis is derived:

$$w^l(x) = w_0 + (1-k)w^{\mathrm{ls}}\sqrt{\pi \mathrm{Pe}} \cdot e^{\mathrm{Pe}} \cdot \mathrm{erfc}(\sqrt{\mathrm{Pe} \cdot 2x/\rho_{\mathrm{tip}}}) \tag{A.3}$$

From Eq. (A.3), it is deduced that:

$$\left.\frac{\mathrm{d}w^l}{\mathrm{d}x}\right|_{x=\frac{\rho_{\mathrm{tip}}}{2}} = -2(1-k)w^{\mathrm{ls}}\,\mathrm{Pe}/\rho_{\mathrm{tip}} \tag{A.4}$$

Therefore, the diffusion length becomes

$$\delta_{\mathrm{d_{Iv}}} = \frac{w_0 - w^{\mathrm{ls}}}{-(1-k)w^{\mathrm{ls}}\,\mathrm{Pe}/\rho_{\mathrm{tip}}} \tag{A.5}$$

using the definition of the supersaturation Ω given in section 3.1, we obtain

$$\delta_{\mathrm{d_{Iv}}} = \frac{2\,\Omega\,D^l}{v_{\mathrm{tip}}} \tag{A.6}$$

References

[1] W. Kurz, M. Rappaz, and R. Trivedi. Progress in modelling solidification microstructures in metals and alloys. part II: dendrites from 2001 to 2018. *International Materials Reviews*, 66(1):30–76, 2021.

[2] D. Tourret and A. Karma. Multiscale dendritic needle network model of alloy solidification. *Acta materialia*, 61(17):6474–6491, 2013.

[3] D. Tourret and A. Karma. Three-dimensional dendritic needle network model for alloy solidification. *Acta Materialia*, 120:240–254, 2016.

[4] D. Tourret, M. M. Francois, and A. J. Clarke. Multiscale dendritic needle network model of alloy solidification with fluid flow. *Computational Materials Science*, 162:206–227, 2019.

[5] C.-H. Chen, A. M. Tabrizi, P.-A. Geslin, and A. Karma. Dendritic needle network modeling of the columnar-to-equiaxed transition. part II: three dimensional formulation, implementation and comparison with experiments. *Acta Materialia*, 202:463–477, 2021.

[6] M. Rappaz and Ch.-A. Gandin. Probabilistic modelling of microstructure formation in solidification processes. *Acta Metallurgica et Materialia*, 41(2):345–360, 1993.

[7] Ch.-A. Gandin and M. Rappaz. A coupled finite element-cellular automaton model for the prediction of dendritic grain structures in solidification processes. *Acta Metallurgica et Materialia*, 42(7):2233–2246, 1994.

[8] Ch.-A. Gandin, J.-L. Desbiolles, M. Rappaz, and P. Thevoz. A three-dimensional cellular automation-finite element model for the prediction of solidification grain structures. *Metallurgical and Materials Transactions A*, 30(12):3153–3165, 1999.

[9] T. Carozzani, H. Digonnet, and Ch.-A. Gandin. 3d cafe modeling of grain structures: Application to primary dendritic and secondary eutectic solidification. *Modeling and simulation in materials science and engineering*, 20(1):015010, 2012.

[10] T. Carozzani, Ch.-A. Gandin, H. Digonnet, M. Bellet, K. Zaidat, and Y. Fautrelle. Direct simulation of a solidification benchmark experiment. *Metallurgical and Materials Transactions A*, 44(2):873–887, 2013.

[11] R. Fleurisson, O. Senninger, G. Guillemot, and Ch.-A. Gandin. Hybrid cellular automaton-parabolic thick needle model for equiaxed dendritic solidification. *Journal of Materials Science & Technology*, 2022.

[12] E. Dorari, K. Ji, G. Guillemot, Ch.-A. Gandin, and A. Karma. Growth competition between columnar dendritic grains–the role of microstructural length scales. *Acta Materialia*, 223:117395, 2022.

[13] M. Berg, M. Kreveld, M. Overmars, and O. Schwarzkopf. Computational geometry. In *Computational geometry*, pages 1–17. Springer, 1997.

[14] D. Meagher. Geometric modeling using octree encoding. *Computer graphics and image processing*, 19(2):129–147, 1982.

[15] M.A. Chopra, M.E. Glicksman, and N.B. Singh. Dendritic solidification in binary alloys. *Metallurgical Transactions A*, 19(12):3087–3096, 1988.

[16] K. Somboonsuk, J.T. Mason, and R. Trivedi. Interdendritic spacing: part i. experimental studies. *Metallurgical and Materials Transactions A*, 15(6):967–975, 1984.

[17] H. Esaka. Dendrite growth and spacing in succinonitrile-acetone alloys. Technical report, EPFL, 1986.

[18] G.P. Ivantsov. Temperature field around a spherical, cylindrical, and needle-shaped crystal, growing in a pre-cooled melt. *Dokl. Akad. Nauk SSSR*, 58(4):567 – 569, 1947.

[19] Huang W., Geng X., and Zhou . Primary spacing selection of constrained dendritic growth. *Journal of Crystal Growth*, 134(1):105–115, 1993.

[20] S. H. Han and R. Trivedi. Primary spacing selection in directionally solidified alloys. *Acta Metallurgica et Materialia*, 42(1):25–41, 1994.

[21] W. Wang, P. D. Lee, and M. McLean. A model of solidification microstructures in nickel-based superalloys: predicting primary dendrite spacing selection. *Acta materialia*, 51(10):2971–2987, 2003.

[22] P.-A. Geslin, C.-H. Chen, A. M. Tabrizi, and A. Karma. Dendritic needle network modeling of the columnar-to-equiaxed transition. part i: two dimensional formulation and comparison with theory. *Acta Materialia*, 202:42–54, 2021.

[23] J. A. Warren and J. S. Langer. Stability of dendritic arrays. *Physical Review A*, 42(6):3518, 1990.

[24] J. D. Hunt. Solidification and casting of metals. *Metals Society, London*, 3:3–9, 1979.

[25] W. Kurz and D. J. Fisher. Dendrite growth at the limit of stability: tip radius and spacing. *Acta Metallurgica*, 29(1):11–20, 1981.

[26] D. Tourret and A. Karma. Growth competition of columnar dendritic grains: A phase-field study. *Acta Materialia*, 82:64–83, 2015.

133

[27] D. Tourret, Y. Song, A. J. Clarke, and A. Karma. Grain growth competition during thin-sample directional solidification of dendritic microstructures: A phase-field study. *Acta Materialia*, 122:220–235, 2017.

[28] A. Pineau, G. Guillemot, D. Tourret, A. Karma, and Ch.-A. Gandin. Growth competition between columnar dendritic grains–cellular automaton versus phase field modeling. *Acta Materialia*, 155:286–301, 2018.

[29] D. Walton and B. Chalmers. The origin of the preferred orientation in the columnar zone of ingots. *Trans. Metall. Soc. AIME*, 215:3–13, 1959.

Conclusion and perspective

Due to the influence of the microstructure on the properties of materials, numerical models aiming at predicting microstructures formed during solidification processes are always of academic and industrial interest and under development. The Columnar-to-Equiaxed Transition in SOLidification processing (CETSOL) project, which was launched in 1999, has for objective to improve our understanding of the Columnar-to-Equiaxed Transition (CET) in directionally solidified alloys under microgravity [6].

The Cellular Automaton – Finite Element (CAFE) model [48] was developed to predict the grain structure during solidification process in consideration of the resolution of energy and solute mass. However, it has appeared that as solute interaction between dendritic branches is approximate, the CAFE model is limited to qualitative prediction on the CET position in samples [7]. Therefore, its prediction on competitive dendritic growth should be improved [63, 64].

To overcome this limitation, in the frame of the CETSOL-5 phase, the coupling Cellular Automaton – Parabolic Thick Needle (CAPTN) method with resolution of energy and solute mass was performed by Fleurisson [14, 15] relying on the CAFE method [45]. The Parabolic Thick Needle (PTN) method [13] models the tip of a dendritic branch as a parabola in two dimensions or a paraboloid in three dimensions and calculates its morphology and kinetics based on the composition field in its vicinity and the solvability condition [20, 21]. It is relevant to predicting dendritic growth at both steady and unsteady state. The two-dimensional PTN method was implemented in a finite element library, and studies were dedicated to the influence of the PTN method parameters, as well as coupling the PTN method with the CAFE model [14, 15].

In the frame of the CETSOL-6 phase, this thesis aims to improve the efficiency of the CAPTN method, apply it for investigating the microstructures under directional solidification, and develop the three-dimensional CAPTN method.

Firstly, the computation efficiency of the PTN finite element implementation has been improved greatly. A new adaptive heterogeneous meshing strategy has been proposed for reducing the frequency of reconstruction of the mesh. The octree structure and orthogonal query method have been employed for seeking the nodes of mesh in a certain domain in an efficient way during the simulation. These numerical methods have been applied to the construction of the mesh, the setting of Dirichlet condition on the composition field, and the calculation of tip radius and velocity. The improved algorithms save tremendous amount of computational time, encouraging the application of the CAPTN method and its three-dimensional development.

Secondly, parametric studies on the PTN model have been carried out. By comparing the dendrite tip kinetics calculated by the original algorithms and the kinetics calculated by the improved algorithms in two dimensions, it has been proved that the improved PTN algorithms have no influence on the calculation of kinetics. It has however been observed that when the

integration distance is too large the kinetics is divergent. This phenomenon has been explained by mathematical deduction. For the three-dimensional PTN model, parametric studies on integration distance, minimum mesh size, time step, and radius of truncating cylinder have been carried out as well. Their conclusion is similar to that of two-dimensional model: in certain range, larger integration distance and smaller minimum mesh size improve the kinetics precision, time step has tiny influence on steady-state kinetics, and the truncating cylinder should not intersect with the integration area.

Thirdly, the CAPTN model has been improved and the three-dimensional CAPTN model has been evaluated in both steady and unsteady regimes. The improvements on the CAPTN model have acted on two aspects. In terms of the CA method, the activation of side branches has become more physical and more flexible: tertiary branches overlapping its primary branch have been eliminated, and it is possible to active a percentage of side branches. The physical branch length has been introduced into the CA method for selecting appropriate dendritic growth law. In terms of the PTN method, the interfacial liquidus composition in Dirichlet condition now depends on the local temperature of the node, and the criteria for reconstructing the mesh have been generalized for cases with multi-branches. The three-dimensional CAPTN model has been used to model an equiaxed grain growing at constant supersaturation. Grain orientation has no noticeable impact on the kinetics of primary branches. Side branches do have small impact on the kinetics of primary branches. The increase on the number of side branches yields larger requirement on computation resources and longer computational time. The three-dimensional CAPTN model has been evaluated by comparing its results with the results from the PTN method, the Dendritic Needle Network (DNN) method, and the Phase-Field (PF) method. For the simulation domain of the same size, the CAPTN model takes less time than the DNN model.

Fourthly, the two-dimensional CAPTN model has been applied for investigating the primary dendrite arm spacing of a single crystal and the grain boundary of bi-crystal under directional solidification with a constant temperature gradient G and a constant isotherm velocity v_{iso}. It has been shown that the CAPTN model can reproduce the grain selection between primary branches and creation of new branches from tertiary branches as long as the CA cell size is sufficiently small to model solute interactions between branches. For the single crystal, the CAPTN model has reproduced a distribution of primary dendrite arm spacing depending on the history of dendritic branches, and the average values of these distributions are coherent with the $G^{-b} v_{\text{iso}}^{-c}$ theoretical law. For the bi-crystal, for a large range of CA cell size, the diverging grain boundary orientation angles obtained by the CAPTN model are less dependent on the CA cell size than the classical CA method, and are in good agreement with previous PF studies [64]. It has also been found that this angle decreases with G/v_{iso}.

Despite the various efforts performed during the thesis to improve and optimize the two-dimensional and three-dimensional implementations of the CAPTN model, some difficulties remain to allow the prediction on grain structures of experiments of the CETSOL project and to study the CET.

- The orthogonal query could be more efficiency in the PTN method by reducing the orthogonal query range. Now the orthogonal query range is a square in two dimensions or a cube in three dimensions. Its creation is with the help of a circle in two dimensions or a sphere in three dimensions. Because a circle or a sphere is isotropic, it is simple to define its axis-parallel circumscribing square or cube as the orthogonal query range. The orthogonal query range can be certainly reduced to a more compact axis-parallel rectangle or cuboid by optimizing the algorithm, then less nodes will be reported as the results of orthogonal query, and the efficiency will be improved further.

- The criteria for reconstructing the PTN mesh (the finite element mesh used for the PTN method) could be optimized in the CAPTN method. There are two types of PTN mesh reconstruction. Local remeshing means to reconstruct only the mesh near the branch; total remeshing means to reconstruct the entire mesh of the domain. The idea is to use more local remeshings instead of total remeshings. In the multi-branch case, branches have different growing velocities. A variable could be introduced to each branch for recording the distance passed since its last local remeshing. If this distance is greater than a certain threshold, the local remeshing around this branch will be performed.

- In the PTN finite element implementation, the minimum mesh size $h_{\min}$, the integration distance a, and the radius of truncating cylinder r_{cyl} are all fixed for all branches. In the CAPTN model, branches have different morphologies and kinetics, and the difference may become greater in the cases with temperature gradient. It will be more relevant if the above-mentioned parameters are linked with physical characteristics. For example, $h_{\min}$ can be calculated based on the tip radius of each branch, which ensures good accuracy for calculation and avoids the use of very fine mesh for all branches. In this thesis, the integration distance is defined by the diffusion length at dendrite tip under Ivantsov solution, with the supersaturation corresponding to the steady-state growth. More generally, the integration distance could be defined by the diffusion length at dendrite tip under Ivantsov solution of the supersaturation of the tip. The definition of r_{cyl} is related to tip radius and integration distance, so it could be calculated for each branch as well.

With the technical improvements mentioned above, the CAPTN model can be further evaluated.

- The evaluation of the three-dimensional CAPTN model could be extended to columnar grains. The three-dimensional PF and DNN methods have produced results on columnar growth [58], which could be used as benchmarks.

- A first coupling of the two-dimensional CAPTN model to the resolution of energy and mass solute (called the CAPTN – FE model) has been performed [14, 15] before the improvements and developments presented in this thesis. This coupling should therefore be updated to take these improvements and developments into account. In

particular, a three-dimensional CAPTN – FE model is still to be developed in order to quantitatively predict the CET position in the samples solidified in the CETSOL project.

In spite of these limitations, we have shown that the CAPTN model is relevant to predicting dendritic grain structures both in two and three dimensions. The improvements in this thesis on the CAPTN method are encouraging for its further developments.

RÉSUMÉ

Les méthodes numériques de modélisation des microstructures formées lors de la solidification présentent un grand intérêt pour la recherche et les industries. La méthode Cellular Automaton – Parabolic Thick Needle (CAPTN) est une méthode numérique multi-échelle, qui couple la méthode automate cellulaire (CA) et la méthode Parabolic Thick Needle (PTN), pour simuler la croissance des grains dendritiques tout en tenant compte du champ de diffusion non stationnaire.

Cette thèse présente des avancées et des optimisations sur la méthode CAPTN. Une stratégie de maillage hétérogène adaptatif et la méthode de requête orthogonale avec la structure octree sont employées sur l'implémentation d'éléments finis de la méthode PTN pour augmenter l'efficacité de calcul. L'implémentation tridimensionnelle de la méthode PTN est réalisée et évaluée à travers les analyses de convergence des résultats de simulation vers des solutions théoriques en fonction de paramètres numériques. Les algorithmes de la méthode PTN et du couplage CAPTN sont aussi améliorés. Le modèle CAPTN tridimensionnel optimisé est évalué en modélisant un grain équiaxe croissant dans un domaine à une sursaturation constante. La cinétique obtenue par le modèle CAPTN est en bon accord avec la cinétique obtenue par le modèle Phase-Field (PF) et le modèle Dendritic Needle Network (DNN). Le modèle CAPTN bidimensionnel optimisé est évalué sur sa capacité à reproduire l'espacement des bras dendritiques primaires et l'angle d'orientation des joints de grains entre deux grains d'orientations différentes, développés en croissance directionnelle dans un gradient de température constant et une vitesse isotherme constante. Les simulations convergent vers une distribution des branches primaires qui dépend de l'histoire des branches dendritiques, en accord avec les observations expérimentales et la théorie. Contrairement au modèle CA classique, l'angle d'orientation des joints de grains obtenu dans les simulations CAPTN est stable avec la taille des cellules et en bon accord avec les études PF précédentes pour différents gradients de température.

MOTS CLÉS

Solidification, modélisation, multi-échelle, automate cellulaire, réseau d'aiguilles paraboliques, microstructure dendritique

ABSTRACT

Numerical methods for modeling microstructures formed during solidification are of great academic and industrial interest. The Cellular Automaton – Parabolic Thick Needle (CAPTN) method is a multiscale numerical method, which couples the Cellular Automaton (CA) and the Parabolic Thick Needle (PTN) methods, to simulate the growth of dendritic grains while accounting for non-steady diffusion fields.

This thesis presents advances and computing optimizations on the multiscale CAPTN method. An adaptive heterogeneous meshing strategy and the orthogonal query method with the octree structure are therefore employed on the finite element implementation of the PTN method for increasing computational efficiency. The three-dimensional implementation of the PTN method is performed and evaluated through the analyses of convergence of simulation results to theoretical solutions depending on numerical parameters. Algorithmic improvements on the PTN method and the CAPTN coupling are also performed. The optimized three-dimensional CAPTN model is evaluated by modeling an equiaxed grain growing under constant supersaturation. The kinetics obtained by the CAPTN model is in good agreement with the kinetics obtained by Phase-Field (PF) and Dendritic Needle Network (DNN) methods. The optimized two-dimensional CAPTN model is evaluated on its ability to reproduce two physical quantities developed during directional growth in a constant temperature gradient with constant isotherm velocity: the primary dendritic arm spacing and the grain boundary orientation angle between two grains of different orientations. Simulations converge toward a distribution of primary branches which depends on the history of the branching events, in agreement with experimental results and theory. Contrary to the classical CA model, the grain boundary orientation angle obtained in CAPTN simulations is stable with cell size and in good agreement with previous PF studies for various temperature gradients.

KEYWORDS

Solidification, modeling, multi-scale, Cellular Automaton, Parabolic Thick Needle, dendritic microstructure